Chitosan Nanoparticles for Nose-to-Brain Delivery of Biologics

---

Bettina Gabold

2023

Dissertation zur Erlangung des Doktorgrades

der Fakultät für Chemie und Pharmazie

der Ludwig-Maximilians-Universität München

Chitosan Nanoparticles for Nose-to-Brain Delivery of Biologics

Bettina Gabold (geb. Schwarz)

aus

München, Deutschland

2023

Erklärung und Eidesstattliche Versicherung

Erklärung

Diese Dissertation wurde im Sinne von §7 der Promotionsordnung vom 28. November 2011 von Frau Prof. Dr. Olivia M. Merkel betreut.

Eidesstattliche Versicherung

Diese Dissertation wurde eigenständig und ohne unerlaubte Hilfsmittel erarbeitet.

München, den 31.08.2023

Bettina Gabold

Dissertation eingereicht am: 31.08.2023

1. Gutachterin: Prof. Dr. Olivia M. Merkel

2. Gutachter: Prof. Dr. Gerhard Winter

Mündliche Prüfung am: 19.10.2023

Für meine Familie

In Liebe und Dankbarkeit

Table of Contents

Erklärung und Eidesstattliche Versicherung 3

Table of Contents 7

List of Abbreviations 11

Contribution to Publication 13

1 Contribution to Chapter I, 2.2.1 13

2 Contribution to Chapter I, 2.5.1 13

3 Contribution to Chapter II 13

4 Contribution to Chapter III 14

5 Contribution to Chapter IV 14

Chapter I - General Introduction 15

1 Neurological disorders and problems of brain targeting 15

2 Nose-to-brain delivery as alternative route 17

2.1 Editorial: Nose-to-Brain Delivery of Biologics 17

3 Nanoparticles in ntb drug delivery 21

4 Chitosan as drug delivery system 21

5 Air-Liquid Interface as suitable screening method 22

5.1 Air-Liquid Interface Cultures of the Healthy and Diseased Human Respiratory Tract: Promises, Challenges, and Future Directions 22

6 Aim of the Thesis 55

Chapter II – Microfluidic mixing as platform technology for production of chitosan nanoparticles loaded with different macromolecules 57

1 Graphical Abstract 57

2 Abstract 58

3 Introduction 58

4 Materials and methods 60

4.1 Materials....60
4.2 mRNA Synthesis....61
4.3 Chitosan nanoparticle preparation....62
4.4 Physicochemical characterization....65
4.5 Cell culture experiments....67
4.6 Statistical analysis....70
5 Results and discussion....70
5.1 Nanoparticle synthesis and characterization....70
5.2 Biotechnological drug loading in CS-based NPs....74
5.3 β-Galactosidase release study....75
5.4 Stability studies....77
5.5 Cell viability....79
5.6 Cellular uptake and gene knockdown....81
6 Conclusion....84
Chapter III – Transferrin-modified chitosan nanoparticles for targeted nose-to-brain delivery of proteins....85
1 Graphical Abstract....85
2 Key words....85
3 Abstract....86
4 Introduction....86
5 Materials and Methods....89
5.1 Materials....89
5.2 Modification of chitosan....90
5.3 Modification of transferrin....91
5.4 Nanoparticle preparation....92
5.5 Nanoparticle characterization....93
5.6 General cell culture....95

5.7 Co-culture model 96

5.8 Transferrin receptor expression 96

5.9 Cellular uptake 97

5.10 Statistical analysis 98

6 Results and Discussion 98

6.1 Modification of chitosan and transferrin 98

6.2 Nanoparticle characterization 102

6.3 Transferrin receptor expression 108

6.4 Cellular uptake 110

7 Conclusion 115

Chapter IV – Utilizing Chitosan Nanoparticles for the Delivery of Biologics to the Brain via Intranasal Route 117

1 Abstract 117

2 Introduction 117

3 Materials and Methods 120

3.1 Materials 120

3.2 Nanoparticle preparation 121

3.3 Size and surface charge measurement 122

3.4 Encapsulation efficiency 122

3.5 Scanning electron microscopy 123

3.6 Release kinetics 123

3.7 Mucus permeation 123

3.8 Fluorescence Correlation Spectroscopy (FCS) 124

3.9 Fluorescence Lifetime Imaging Microscopy (FLIM) and Single Particle Tracking (SPT) 125

3.10 Cell culture 127

3.11 Cell viability 127

3.12 Cellular uptake in liquid and ALI culture....128
3.13 Confocal microscopy....128
3.14 Nanoparticle permeability in ALI culture....130
3.15 Animal study....130
3.16 Statistical analysis....131
4 Results & Discussion....131
4.1 Physicochemical characterization....131
4.2 Mucus permeation....135
4.3 *In vitro* performance....142
4.4 *In vivo* experiments....147
5 Conclusion....149
Chapter V – Summary and Perspectives....151
Appendix....153
1 Supplementary information for Chapter II....153
2 Supplementary information for Chapter III....160
3 Supplementary information for Chapter IV....162
Bibliography....165
Acknowledgements....205
List of Publications....207

List of Abbreviations

3R	reduce, refine, replace
ACF	Autocorrelation function
AF488	Alexa Fluorophore 488
AFM	Atomic Force Microscopy
Al	alveolar
ALI	Air-Liquid Interface
ANF	Artificial nasal fluid
ANM	Artificial nasal mucus
ATTOGal	ATTO647N labeled b-galactosidase
BBB	blood-brain barrier
BCSFB	blood-cerebrospinal fluid barrier
bGal	β–Galactosidase
CF	cystic fibrosis
CNS	central nervous system
COPD	chronic obstructive pulmonary disease
CoV	Coronavirus
CS	chitosan
CuAAC	copper(I)-catalyzed azide-terminal alkyne cycloaddition
DAPI	4′,6-Diamidin-2-phenylindole
DBCO-NHS-ester	dibenzyl cyclooctyne-N-hydroxysuccinimide-ester
DLS	dynamic light scattering
DMSO	Dimethyl sulfoxide
DNA	Deoxyribonucleic Acid
EDC	1-ethyl-3-(3-dimethylaminopropyl) carbodiimide
EE	Encapsulation Efficiency
EMEM	Eagle's Minimum Essential Medium
ET	extrathoracic
FAM	fluorescein
FBS	Fetal Bovine Serum
FCS	fluorescence correlation spectroscopy
FLIM	fluorescence lifetime imaging microscopy
FRR	Flow Rate Ratio
G418	Geniticin
GFP	Green Fluorescent Protein
HAE	human airway epithelium
HLA-G	histocompatibility antigen G
HRV-C	human rhinovirus-C
ICP-OES	inductively coupled plasma optical emission spectroscopy
IgA	immunoglobulin A
IL-1α	interleukin-1α

IL-6	interleukin-6
LDA	Laser Doppler Anemometry
LDH	Lactate Dehydrogenase
LP	Lipofectamine
MCC	multilayered cell culture
MCE	mixed cellulose ester
MDR	multidrug resistance
MERS-CoV	Middle East respiratory syndrome coronavirus
MES	2-(N-morpholino)ethanesulfonic acid
MFI	median fluorescence intensity
mRNA	messenger Ribonucleic Acid
MTT	3-(4,5-dimethylthiazol-2-yl)-2,5-diphenyl-2H-tetrazolium bromide
NHS	N-hydroxysuccinimide
NP	nanoparticle
ntb	nose-to-brain
ONPG	ortho-nitrophenyl-ß-galactoside
PAM	PIE Analysis in MATLAB
PBS	phosphate-buffered saline
PCR	polymerase chain reaction
PDI	polydispersity index
RU	resonance unit
SARS-CoV	Severe acute respiratory syndrome coronavirus
SD	Standard Deviation
SEM	scanning electron microscopy
siRNA	small interference Ribonucleic Acid
siRNA GFP	siRNA targeted Green Fluorescent Protein
- siRNA	scrambled negative control siRNA
SPAAC	strainpromoted azide–alkyne cycloaddition
SPR	Surface Plasmon Resonance
SPT	Single particle tracking
TB	tracheobronchial
TEER	transepithelial electrical resistance
TEM	Transmission Electron Microscopy
Tf	Transferrin
TFR	Total Flow Rate
TfR-His	his-tagged transferrin receptor
TGF-β	transforming growth factor β
Th2	T-helper 2
TPP	pentasodium tripolyphosphate
VEGF	vascular endothelial growth factor

Contribution to Publication

1 Contribution to Chapter I, 2.2.1

Editorial: Nose to Brain Delivery of Biologics
Bettina Schwarz & Olivia M. Merkel

This chapter was published in the Journal Therapeutic Delivery, Vol. 10, No.4 in 2019. I performed the literature search and wrote the article.

2 Contribution to Chapter I, 2.5.1

Air-Liquid Interface Cultures of the Healthy and Diseased Human Respiratory Tract: Promises, Challenges, and Future Directions
Domizia Baldassi, Bettina Gabold, Olivia M. Merkel

This chapter was published as review article in the Journal Advanced NanoBiomed Research, Vol. 1, Issue 6 in 2021. Domizia Baldassi and I are joint first co-authors of the respective publication. We performed the literature search and wrote the article.

3 Contribution to Chapter II

Microfluidic mixing as platform technology for production of chitosan nanoparticles loaded with different macromolecules
Antonietta Greco, Bettina Gabold, Siyu Chen, Xiaoxuan Wang, Zehua Xu, Achim Hartschuh, Enrica Chiesa, Ida Genta, Christian L. Ried, Thomas Merdan, Olivia M. Merkel

This chapter was published as research paper in the European Journal of Pharmaceutics and Biopharmaceutics, Vol. 188 in 2023. Dr. Antonietta Greco and I are joint first co-authors of the respective publication. We performed most of the

experiments and wrote the article. mRNA was synthesized by Siyu Chen and AFM images were taken by Xiaoxuan Wang and Zehua Xu.

4 Contribution to Chapter III

Transferrin-modified chitosan nanoparticles for targeted nose-to-brain delivery

Bettina Gabold, Friederike Adams, Sophie Brameyer, Kirsten Jung, Christian L. Ried, Thomas Merdan, Olivia M. Merkel

This chapter was published as research article in the Journal of Drug Delivery and Translational Research, Vol. 13 in 2023. I am the first author of the respective publication, performed most of the experiments and wrote the article. Measurements of the SPR samples were performed by Dr. Sophie Brameyer and chemical synthesis and modifications were done with the help of Dr. Friederike Adams.

5 Contribution to Chapter IV

Utilizing Chitosan Nanoparticles for the Delivery of Biologics to the Brain via Intranasal Route

Bettina Gabold, Irene Gialdini, Igor Khalin, Antonietta Greco, Adrian Kromer, Xiaoxuan Wang, Lea-Adriana Barlang, Andreas Popp, Christian L. Ried, Thomas Merdan, Nikolaus Plesnila, Don C. Lamb, Olivia M. Merkel

I performed most of the experiments and wrote the chapter. Measurements of FLIM, SPT and FCS were performed by Irene Gialdini. Confocal images of the ALI culture sample were taken by Lea-Adriana Barlang. The *in vivo* experiments were conducted by Dr. Igor Khalin with sample preparation by Dr. Antonietta Greco and Adrian Kromer.

Chapter I - General Introduction

1 Neurological disorders and problems of brain targeting

Due to the progressive ageing of the European population, the prevalence, incidence and mortality of neurological disorders have increased over the last decades. According to a study from 2017, central nervous system (CNS) diseases are the third most common cause of premature death and disability in the EU with increasing numbers [1]. The development of adequate therapies for CNS disorders such as Alzheimer's, Parkinson's and brain cancer is especially challenging regarding different aspects. To this day, most therapeutic molecules need to be administered systemically, mostly orally or by intravenous injection. Consequently, these drugs have to cross the blood-brain barrier (BBB) to reach their target tissue.

The BBB is a semipermeable barrier composed of capillary endothelial cells that are strongly connected via tight junctions and adherens junctions (**Figure 1**). Therefore, paracellular transport of molecules through the BBB is prevented and transcellular transport is very limited [2]. Additionally, the BBB is closely associated with astrocytes, pericytes and microglia being essential for BBB induction and maintenance through the regulation of proliferation, migration, and vascular branching of brain endothelial cells [3]. Furthermore, the basal membrane provides additional structural support around the endothelial cells [4]. With a transendothelial electrical resistance around 1500 Ωcm^2, the BBB presents a strong resistance to movement of ions [5]. It is estimated that virtually all macromolecules and most of the low molecular weight drugs, especially the hydrophilic ones, are not able to permeate through the BBB [6]. Consequently, this leads to a very low bioavailability at the desired drug target site and, additionally, to side effects in non-targeted organs. However, most patients suffering from CNS disorders need chronic dosing and, therefore, it is considered that many drugs, useful for the treatment of neurological diseases, cannot unfold their potential due to the BBB [7]. Thus, alternative non-invasive ways are highly needed.

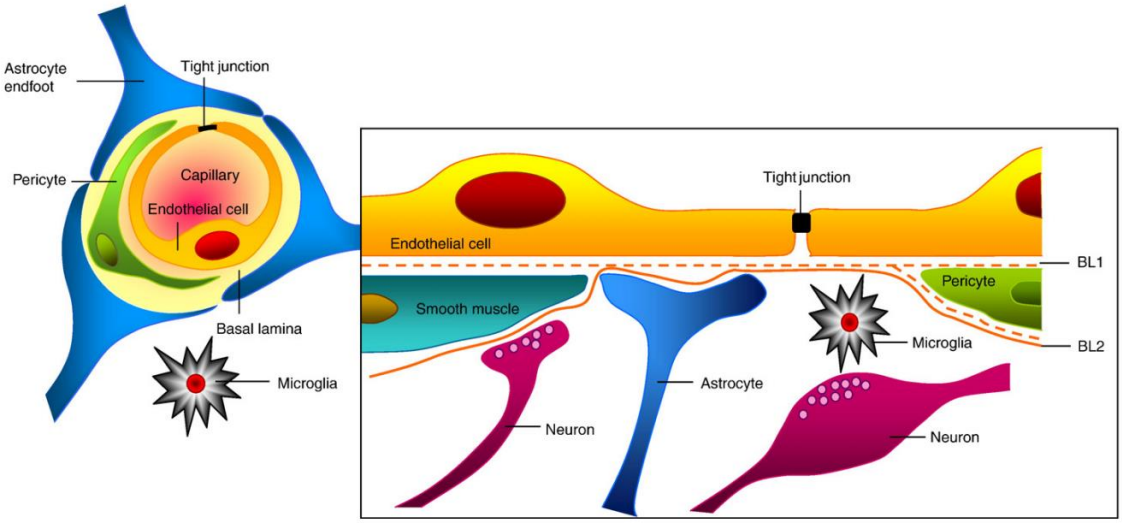

Figure 1. The cell associations at the BBB, where BL1 is basal lamina 1 and BL2 is basal lamina 2. Tight junctions are formed between cerebral endothelial cells sealing the paracellular diffusion pathway alongside the cells. (adapted with permission from Abbott et al.[8])

2 Nose-to-brain delivery as alternative route

2.1 Editorial: Nose-to-Brain Delivery of Biologics

Graphical Abstract

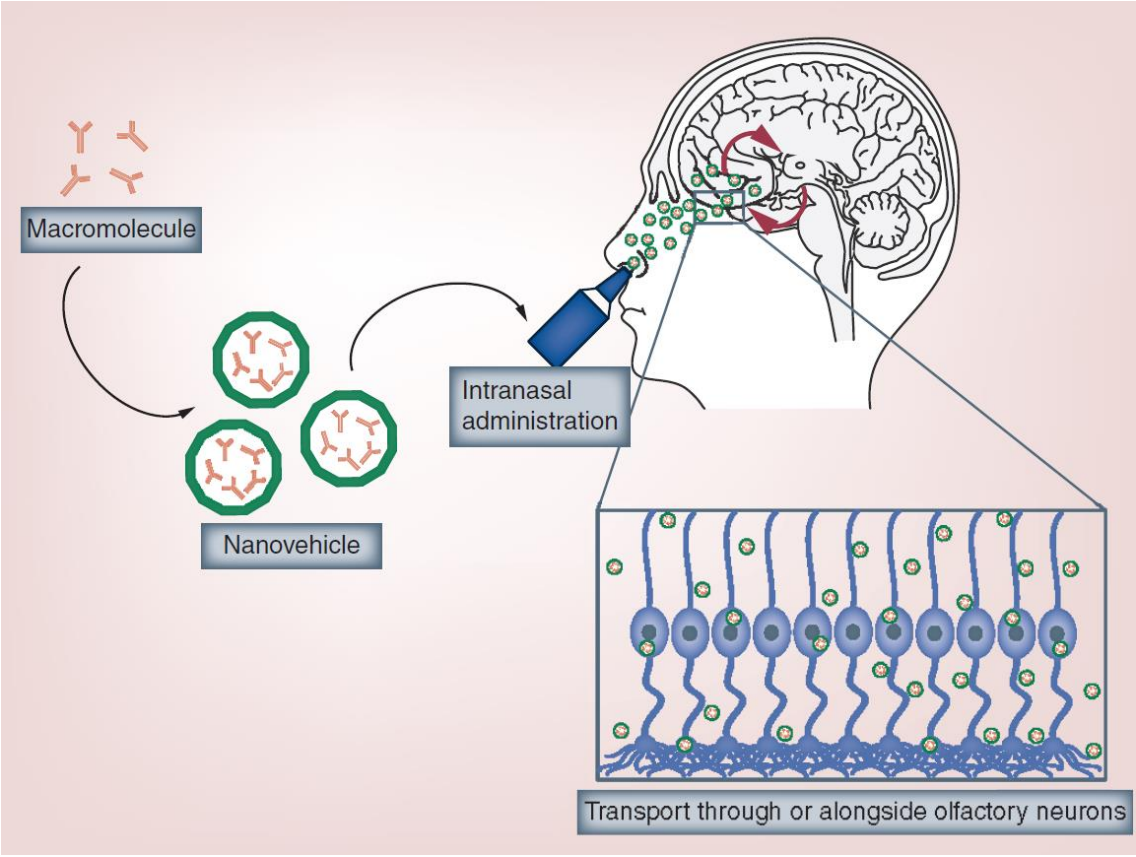

Keywords

CNS drug delivery, intranasal drug administration-biologics, nanocarriers, nose-to-brain delivery, olfactory epithelium, transport mechanisms

The prevalence, incidence and mortality of central nervous system (CNS) disorders have increased worldwide over the last decades. In 2015, CNS disorders were the second-leading cause of deaths accounting for 16.8% of global deaths. Additionally, the number of deaths from neurological disorders has increased by 36.7% between 1990 and 2015 with numbers still rising [9]. To this day, most of the therapeutic drugs intended for the treatment of CNS disorders, for example, Parkinson's and Alzheimer's diseases, are administered systemically and consequently, have to cross the blood–brain barrier (BBB). However, due to its selective permeability, the utilization of many novel therapeutic agents, especially macromolecules such as peptides and proteins, so-called biologics, is limited [10]. In contrast to systemic delivery, nose-to-brain (ntb) delivery presents a promising alternative enabling the delivery of therapeutic drugs to the CNS, while avoiding transport across the BBB. Compared with conventional drug-delivery approaches, ntb represents a non-invasive method, accessing the CNS directly through the olfactory or trigeminal nerve. Two decades ago, Frey was the first to report that horseradish peroxidase passes freely through intercellular junctions of the olfactory epithelium when administered intranasally reaching the olfactory bulbs of the CNS in 45–90 min in the rat and squirrel monkey [11]. Since then, the mechanisms of ntb delivery have been investigated extensively and the development of intranasal formulations for the therapy of CNS diseases has gained continued interest. The exact pathways and transport mechanisms by which drugs reach various regions of the CNS via the nasal passage have not yet been fully elucidated. The major pathway, however, is considered to be via the olfactory nerve, which arises in the olfactory region located at the upper part of the nasal cavity. Due to frequent contact with foreign noxious substances, the olfactory neurons regenerate every 3–4 weeks. Therefore, enzymes, proteins and transporters found in other epithelium may not be fully functional in the nasal passages. This turnover creates a 'leaky' barrier that drug molecules can easily pass through [12]. Furthermore, the olfactory ensheathing cells enveloping the olfactory neurons create continuous fluid-filled perineural channels that remain open despite regeneration of the neurons, leaving enough space for the passage of bigger molecules. Another important pathway for ntb delivery involves the trigeminal nerve which innervates the olfactory and respiratory mucosa in the nasal cavity to a certain extent and enters the CNS in the pons [13]. In general, transport of molecules from the nasal cavity to the origins of the nerves in the cerebrum and pons can occur extracellularly as well as intracellularly [14]. The intracellular pathway begins with

internalization of the drug by an olfactory neuron, trafficking along the axon inside the cell and finally being released via exocytosis. In the extracellular pathway, the drug crosses the nasal epithelium to the lamina propria and is then transported externally alongside the axon by bulk flow process. Irrespective of the type of pathway, the neuronal axons lead to the brain stem and from there the drug can distribute throughout the CNS [12]. However, it is difficult to tell which transport mechanism is predominant since isolating the different pathways from each other is very challenging. At large, the ntb delivery route holds various benefits compared with systemic administration. First of all, it is noninvasive, which reduces infection risks, increases patient compliance, especially compared with intrathecal administration, and thereby opens the possibility for patient self-administration. Due to the large surface area (human approximately 150 cm^2) and the rich vascular submucosa of the nasal cavity, drugs can be absorbed rapidly and exhibit a fast onset of action, avoiding first-pass metabolism [15]. Notably, ntb delivery is not limited to lipophilic or small-molecule drugs as is the BBB route. Clinical data have already demonstrated that macromolecules, for example, proteins or nucleic acids, and even cells or viruses are able to pass from the nose to the brain [16]. A cutting-edge study by Born et al. showed that the peptides melanocortin, vasopressin and insulin were detected in the cerebrospinal fluid within 30 min after intranasal administration in humans [17]. In general, insulin is one of the most studied biologics for its effects on the CNS. It has been demonstrated that, although it undergoes transcytosis at the BBB, intranasal administration leads to higher insulin levels in the brain compared with subcutaneous administration [18]. Due to the short distance, molecules reach the brain much faster after intranasal administration compared with systemic administration [17, 19]. However, ntb delivery also has its limitations. The upper parts of the nasal cavity are rather small and narrow, therefore, the dosage volume is restricted to maximum 400 µl [20]. The anatomy of individual nasal cavities is quite different forcing the formulation and administration techniques to be tailored to fit human interindividual variability. Furthermore, intranasally administered substances undergo rapid elimination by enzyme degradation, mucociliary clearance and drainage to the lower part of the pharynx [21]. Another unsolved issue is the delivery of hydrophilic and high molecular weight drugs because the permeation of the epithelial barrier via endocytosis usually depends on the hydrodynamic diameter. Hence, a suitable dosage form or targeting ligand enhancing bioavailability is needed. Several aspects need to be taken into account when

developing ntb formulations. For instance, the pH of the formulation should be similar to that of human nasal mucosa (pH 5.0 – 6.5) in order to avoid irritation [22]. Accordingly, tonicity and viscosity need to be adjusted. Excipients also need to be biocompatible and the formulation should be free of strong odors. Biologics, especially, are rapidly degraded by enzymes in the nasal mucosa and therefore need to be shielded. This can be done by introducing chemical modifications to the drug molecules or utilizing auxiliary agents either as formulation components or as co-administration agents [23, 24]. Additionally, there are many formulation-based approaches (i.e., micro- or nano-particulate systems) acting as CNS delivery platforms and allowing increased mucosal permeability and stability [25, 26]. The utilization of nanovehicle-based formulations can be indicated as a promising approach for efficient ntb delivery of biologics [27]. Drug transport through nasal mucosa can be facilitated by both polymer- and lipid-based formulations while protecting the payload from enzymatic degradation and increasing the residence time on the mucosal surface, thereby achieving higher drug concentrations at the site of interest. Moreover, nanocarriers can be tuned regarding physicochemical properties, appropriate excipients, drug loading, drug release rate, targeting ligands, biocompatibility/biodegradability, cytotoxicity, etc. [28]. Despite enormous advances in the field of CNS therapeutics in the last decades, efficient drug delivery is still challenging due to limitations presented by the BBB. Hence, exploiting the intranasal route as a potential strategy to circumvent the BBB presents an attractive option for future treatment of neurological disorders. In summary, advantages of ntb delivery include noninvasiveness, lower drug dosage compared with systemic administration, no systemic clearance, reduced risk of systemic toxicity and higher patient compliance. Although a number of studies have shown that biologics are able to reach the brain after intranasal administration, further research has to be conducted to develop a suitable formulation platform for this type of therapeutic agent. Designing better studies to elucidate the exact pathway or transport mechanism followed by the drug or formulation to reach the brain via intranasal administration is essential. Thereby, the development of new formulation strategies for improved treatment of neurological disorders can be facilitated. In conclusion, the intranasal administration route presents a promising option for the treatment of CNS disorders. However, the transport mechanism needs to be understood in terms of quality and quantity, and better *in vitro* and *in vivo* models are necessary to perform more relevant preclinical studies.

3 Nanoparticles in ntb drug delivery

As with other routes of administration, it has been shown that formulation design has a big impact on drug delivery and can help to overcome many of the barriers present in ntb delivery. The most limiting disadvantages of ntb delivery are the short residence time inside the nasal cavity due to mucociliary clearance, the rapid enzymatic degradation and the permeation of hydrophilic high molecular weight drugs [29]. In literature, many different types of formulations, such as solutions, emulsions, gels and nanoparticles, are reported to enhance ntb delivery of different types of molecules [30]. Especially for the delivery of delicate therapeutic drugs, such as nucleic acids or proteins, the contribution of nanoparticles (NPs) is crucial since they have been shown to provide many beneficial characteristics, including increased stability, mucoadhesion and enhanced absorption by passive or active targeting [28, 31]. At the same time, NPs can protect the therapeutic drugs from enzymatic degradation and prevent their extracellular transport by efflux transporters [6, 32, 33]. In the recent years, the field of nanotechnology with regards to ntb delivery has been extensively studied by researchers all over the world. This is the reason for a broad variety of different strategies and approaches regarding NP type, composition and possible adjuvants. In particular, polymeric nanocarriers have demonstrated a facilitated drug transport through nasal mucosa while protecting the cargo from enzymatic degradation and extending the residence time inside the nasal cavity resulting in increased drug concentration at the target site [34, 35].

4 Chitosan as drug delivery system

Among other polymers, chitosan (CS) has frequently been used for the preparation of NPs in ntb delivery. CS is a naturally derived linear co-polymer of β-(1-4)-linked D-glucosamine with a molecular structure constituted of a linear backbone linked through glycosidic bonds [36]. This polysaccharide has many basic amine groups, which are protonated and, thus, positively charged in most physiological fluids. Therefore, CS can generally be considered hydrophilic. However, the percentage and distribution of acetylated monomers has a critical effect on its solubility in aqueous media [37]. Because of these properties, CS exhibits interesting properties such as

mucoadhesiveness and the ability to open tight junctions [38]. It is currently known that CS shows biocompatibility, biodegradability and a concentration dependent cytotoxicity with a half maximal inhibitory concentration covering concentrations from 0.2 mg/mL to 2 mg/mL in the majority of cell models depending on the molecular weight and acetylation degree [39-41]. Furthermore, from a regulatory perspective it is noticeable that CS has FDA GRAS status and is already widely used as a dietary supplement and in the form of wound dressings [42]. Instant formation of CS NPs can be obtained by ionotropic gelation method with various polyanions such as tripolyphosphate. This method was first reported by Calvo et al. in 1997 and it can be used to produce CS NPs under simple and mild aqueous conditions [43]. Therefore, it is particularly suitable for the encapsulation of sensitive cargo such as proteins or nucleic acids. Additionally, the technique produces NPs with high loading efficiency and the capacity to control drug release [44].

5 Air-Liquid Interface as suitable screening method

5.1 Air-Liquid Interface Cultures of the Healthy and Diseased Human Respiratory Tract: Promises, Challenges, and Future Directions

5.1.1 Abstract

Air-liquid interface (ALI) culture models currently represent a valid instrument to recreate the typical aspects of the respiratory tract *in vitro* in both healthy and diseased state. They can help reducing the number of animal experiments, and hence support the 3R principle. This review discusses ALI cultures and cocultures derived from immortalized as well as primary cells, which are used to study the most common disorders of the respiratory tract, in terms of both pathophysiology and drug screening. The article displays ALI models used to simulate inflammatory lung diseases such as chronic obstructive pulmonary disease (COPD), asthma, cystic fibrosis, lung cancer, and viral infections. It also focuses on ALI cultures described in literature studying respiratory viruses such as SARS-CoV-2 causing the global Covid-19 pandemic at the time of writing this review. Additionally, commercially available models of ALI cultures are presented. Ultimately, the aim of this review is to provide a detailed overview of ALI

models currently available and to critically discuss them in the context of the most prevalent diseases of the respiratory tract.

5.1.2 Key words

Air-liquid interface, lung, pulmonary administration, respiratory tract, SARS Cov-2, 3D co-culture models

5.1.3 Introduction

Chronic respiratory inflammatory conditions observed in patients with asthma, cystic fibrosis (CF), and chronic obstructive pulmonary disease (COPD) are major causes for death and morbidity worldwide [45]. In addition, lung cancer and respiratory infections, including the global COVID-19 pandemic in 2020, are frequent causes of mortality. Therefore, more efficient treatment strategies are urgently sought for, particularly for diseases causing irreversible tissue destruction and loss of lung function. The complex cellular composition of the respiratory tract and its location at the air-liquid interface (ALI) hamper an accurate mimicking of the physiological situation. Various models have been applied in the past ranging from *in vitro* lung cell models to *in vivo* animal experiments [46]. In this field of research, animal models are routinely used since all *in vitro* models lack one or another aspect of lung anatomy or physiology, hampering validation of research results. Consequently, animal models are widely regarded as the sole reliable choice that is available. Yet, the anatomical differences between rodents and humans emphasize a substantial lack of functional homology regarding various biomolecules, drug deposition rates, and localization of particulate drug-delivery systems [47]. For example, the alveolar (Al) and the airway architecture show fundamental differences [48, 49]. Mice only have 6 to 8 levels of branching airways, whereas humans have up to 20 or more. Furthermore, mice do not have respiratory bronchioles comparable with humans, which are characterized by interruptions on their walls that project into the alveoli. They only have short terminal bronchioles opening straight into the Al ductules [50]. Therefore, interpretation of data derived from rodent models cannot easily be translated into the human context. Furthermore, the strong support for the reduce, refine, replace (3R) principle in experimental animal testing is constantly increasing [51]. These key facts have driven the development of alternative

in vitro cell culture methods aimed at mimicking the respiratory tract. Hereby, ALI models derived from the field of inhalation toxicology have been described as the most promising approach [52]. The most important characteristic of ALI culture is that the apical surface of cells is exposed to air, whereas the basal side is nourished by contact with liquid cell culture medium. This configuration allows cell differentiation toward a mucociliary phenotype, simulating *in vivo* conditions better than it is possible in conventional cell cultures. ALI models hence allow to obtain relevant data of the respiratory tract as they can be constructed from human-derived cells and are therefore capable to model scenarios close to *in vivo* conditions [53]. Another advantage is that drugs administered as aerosols and particles are not diluted or changed structurally by contact with cell culture medium before they impact on the epithelium differently from submerged models. Furthermore, dosing can be exactly controlled in contrast to *in vivo* administration, resulting in a better optimization of parameters *in vitro* and subsequently reduced amounts of experimental animals required in follow-up *in vivo* experiments. In addition, these lung models cannot only be used to help understand pathophysiological processes and conduct drug screening. They also support the mechanistic understanding of the interaction of xenobiotics at the cellular level in healthy and diseased tissue, complementing findings gained from *in vivo* studies. However, for many applications, ALI monoculture platforms fail to represent the cellular arrangement thoroughly, e.g., by lacking direct cell-cell interactions. Hence, coculture models constituted of more than one cell type are widely being developed [54]. For many applications, they are beneficial over ordinary ALI culture models because they provide a morphology, function, and intercellular interactions with enhanced resemblance to physiological *in vivo* conditions. This Review focuses on the different types of ALI cell culture models resembling the human respiratory tract including the commonly used cell types and applications. Herein, importance is given to models mimicking healthy as well as diseased states of the lung, e.g., in patients suffering from asthma, CF, or COPD. Especially advanced systems using multiple cell types or even culturing cells with viruses or bacteria for pathogen-host interaction studies will be presented in detail.

5.1.4 Anatomical and Cellular Structure of the Respiratory Tract

The respiratory tract is part of the respiratory system that also includes parts of the central nervous system, the chest wall, and the pulmonary circulation [55]. One can picture the respiratory tract as an upside-down tree with a complex network of bifurcations getting thinner and thinner with every branching step. Generally, the respiratory tract can be divided into three main regions: 1) the extrathoracic (ET) region which includes the oral and nasal cavity, the pharyngeal and laryngeal tract to the trachea entrance, 2) the tracheobronchial (TB) or conducting region expanding from the trachea down to the terminal bronchioles, and 3) the Al region responsible for the gas exchange [56]. Within the airways, several structural and cellular mechanisms protect the organ against harmful materials and potential pathogens. First, a continuous layer of epithelial cells lines the entire respiratory tree. These cells form tight-junction networks, building the specific structural integrity of the epithelial layer, and they are crucial for maintaining the normal functions of the respiratory system. Furthermore, the surfactant film coating the lower airways and the mucociliary escalator of the upper tract of the airways join forces to transport unwanted matter up the airways to be swallowed subsequently [57]. Also, a resident population of innate cells such as dendritic cells or macrophages inside and underneath the airway epithelium phagocytoses foreign material [58, 59]. Cell types present in the different regions alter from the conducting to the respiratory part of the airways, accommodating the respective specific functions and defense mechanisms (**Figure 2**). The ET epithelium constitutes predominantly of ciliated columnar cells and goblet cells, whereas the TB tract is lined by a pseudostratified, columnar epithelium consisting of goblet cells, basal cells, and ciliated cells, supporting the mucociliary clearance. Cuboidal ciliated cells and secretory Clara cells prevail in the epithelium of the bronchioles [60]. Apart from these tissue-specific epithelial cells, many nonepithelial migratory cells can be found such as mast cells, leukocytes, and lymphocytes. The Al region further down the respiratory system is constituted of Al type I and II pneumocytes forming the Al epithelium. Type I pneumocytes account for about 95% of the internal lung surface and are mainly responsible for gas exchange, whereas type II cells mediate many other functions such as regulation of the lung surfactant system, the Al fluid content, and secretion of antimicrobial and surface-active components. In addition, alveolar cells form the gas-exchange barrier by attaching to endothelial cells

via their basal membranes. In addition, resident alveolar macrophages remove inhaled debris.

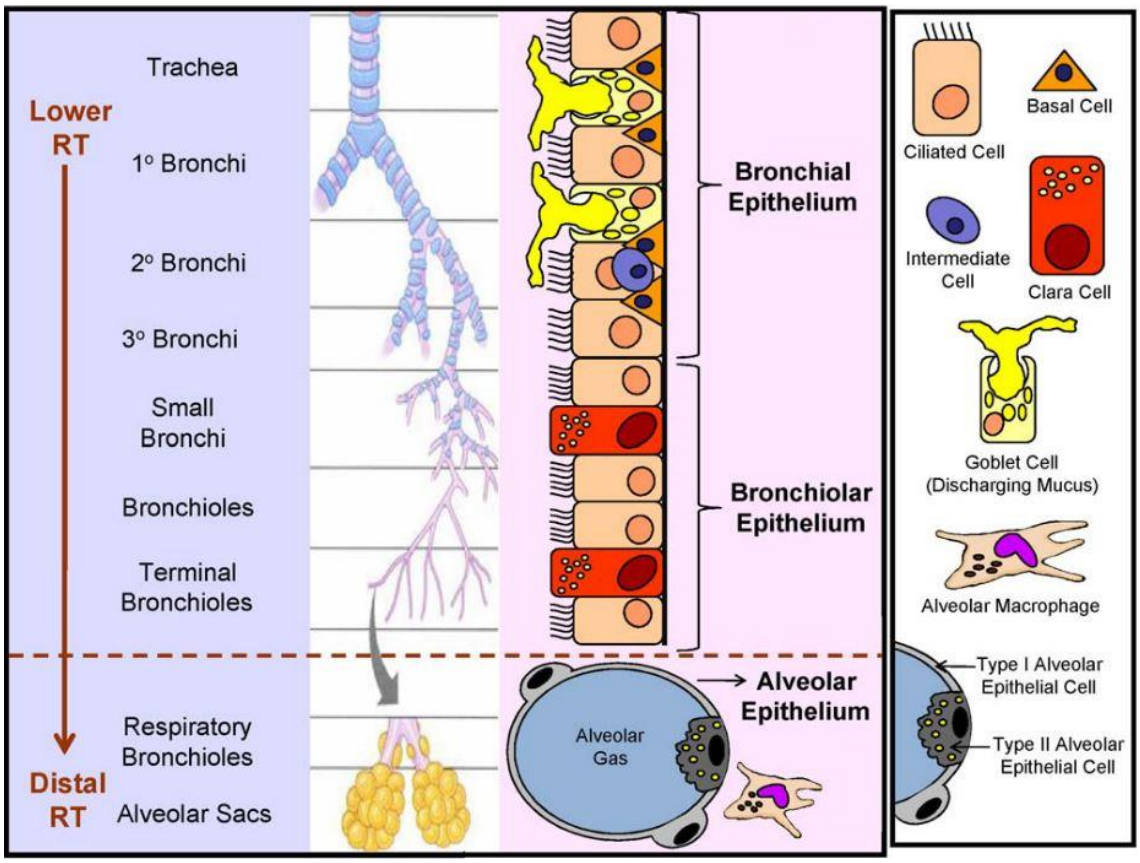

Figure 2. Principle cell types found alongside the human respiratory tract varying in functions and defense mechanisms. Reproduce with permission [61]. Copyright 2010, Elsevier.

5.1.5 Cellular Composition of ALI Models

In vitro cell culture systems offer controllable, adaptable, and reproducible models compared with *in vivo* and ex vivo systems. Numerous epithelial cell types have been grown at the ALI with the aim of mimicking distinct parts of the respiratory tract. Compared with submerged culture, differentiated cell morphology, altered biochemistry, and response to tested materials have been described, showing good resemblance to the actual *in vivo* situation. ALI models can be established with primary material or with immortalized cell lines, both offering pros and cons. In general, primary

cultures isolated directly from tissues represent a heterogeneous population of several different types of epithelial cells. Primary cells from patient populations suffering from respiratory diseases such as CF [62], asthma [63], and COPD [64] have been isolated for research purposes. Moreover, primary epithelial cells were used to study virus-host interactions [65]. Cells from different sections of the respiratory tract are cultured at ALI and can reproduce many features of the diseased state [66]. Each isolate, however, is unique, and therefore, it is impossible to completely reproduce it. Moreover, the isolation from normal human airway tissue comes with a limited number of cells [67]. Epithelial immortalized cell lines, as shown in **Table 1**, have the advantage of homogenous clonality with less phenotypic differences compared with primary cells, resulting in more stable cultures with easier handling. This is the reason why immortalized human cell lines are very commonly utilized in ALI cultures of the respiratory tract. However, it is important to emphasize that due to the transformation process and clonality, they can potentially lack important molecules that are usually encountered *in vivo*. In general, primary epithelial cells display a better representation of the native microenvironment and in principle are optimal candidates for simulating *in vivo* conditions. For the ET region of the respiratory system, only very few cell lines are suitable. The only immortalized cell line of human origin frequently used in nasal drug delivery research is the RPMI2650 cell line [68]. This epithelial cell line was obtained from an anaplastic squamous cell carcinoma of the human nasal septum and displays strong stability even after extended *in vitro* culturing without phenotype alteration, exhibiting superior differentiation under ALI conditions [69, 70]. RPMI2650 cells do not grow in polarized monolayers but in sheets of non-ciliated cells, and transepithelial electrical resistance (TEER) values range from 41 to 270 Ωcm^2 [68, 71]. Due to the lack of suitable immortalized cell lines of normal nasal tissue, many applications of drug delivery research use primary epithelial cells from nasal brushings or from nasal polyps [72, 73]. One of the most widely used human bronchial epithelial cell lines, 16HBE14o-, was established by transforming normal bronchial epithelial cells. They are used to mimic the TB region and have a cuboidal shape expressing tight-junction proteins and develop proper TEER values [74]. While there are conflicting reports whether this cell line is ciliated or not, it has been shown that 16HBE14o- cells express several transport proteins [75]. Furthermore, although bronchial epithelial cells can typically be found at an air interface, these cells sometimes fail to polarize under ALI conditions [76]. The exact mechanism or reason for this is currently still unknown but improvements in

culture conditions were shown to enable 16HBE14o- cell polarization at ALI, as it was shown for the RPMI 2650 cell line [69, 77]. Apart from 16HBE14o-, another cell line obtained from healthy human epithelial cells, the BEAS-2B cell line, is also commonly used. It is particularly described in coculture models to evaluate the influence of epithelial cells on cocultured immune cells after exposition to tobacco smoke or diesel exhaust [78, 79]. However, at the ALI, these cells do not appear to polarize, form tight junctions, or produce mucus and only reach very low TEER values of <100 Ωcm^2 [80]. Another extensively used cell line mimicking bronchial cells is the Calu-3 cell line derived from a bronchial epithelial adenocarcinoma [81]. This cell line shows an excellent polarized monolayer formation at ALI together with high levels of tight junction proteins and mucus production [82]. Depending on the culture conditions, TEER values of Calu-3 cells at ALI are usually bigger than 300 Ωcm^2, sometimes even exceeding 1000 Ωcm^2 [80]. However, also for this cell line the data for cilia expression appear to be contradictory, which might be related to the number of cell passages [81, 83, 84]. Due to high stability, robustness, *in vivo* resemblance, and easy culture, Calu-3 cells are often described as a suitable model for the respiratory epithelium [85]. The most commonly used alveolar cell line mimicking the AI region is the A549 cell line from human pulmonary adenocarcinoma. Many studies suggest that these cells are unable to polarize and lack functional tight junctions, although they seem to express certain tight-junction proteins such as occludin and E-cadherin [86]. Despite these limitations, the A549 cell line contains multilamellar cytoplasmic inclusion bodies typically seen in human alveolar type II cells [87]. These cells additionally release surfactant to reduce surface tension, similarly to what is observed *in vivo* [88, 89]. Therefore, A549 cells are still used in ALI coculture models, mostly in the presence of other epithelial cell lines to facilitate cell layer polarization but also together with immune cells and endothelial cells to mimic the alveolar barrier in the lung [90-92]. Besides A549, the NCI-H441 human alveolar cell line from lung adenocarcinoma has been utilized in several studies. This cell line has been described to have characteristics of both bronchiolar Clara cells and alveolar type II cells [93, 94]. It can form polarized monolayers with TEER values of around 300 Ωcm^2 and has mainly been used to study the air-blood barrier in co-cultures with endothelial cells [95, 96]. In general, the complex regulation mechanisms of airway responses to allergens, pathogens, and other antigens combined with the different cell types and cytokines present in the airways have a great influence on the microenvironment. Therefore, it is obvious that such a complex system cannot be

mimicked by just one cell type, and reproducing this microenvironment as a field of research is advancing continuously. Depending on which part of the respiratory tract and, above all, which disease should be analyzed, there are multiple options for designing a suitable model.

Table 1. Phenotypic characteristics of cell lines used in ALI cultures to mimic different parts of the respiratory tract.

Cell type	**Derivation**	**Phenotype**	**TEER [Ω·cm²]**	**Reference**
RPMI 2650	Nasal squamous cell carcinoma	Multilayered, non-ciliated, mucin expression, exhibiting tight junction formation	41-270	[71, 97]
16HBE14o-	Immortalized healthy tissue	Cuboidal monolayer, non-ciliated but microvilli present tight junction formation, transporter protein expression	~ 250	[77]
Calu-3	Adenocarcinoma	Columnar monolayer, mucin expression, tight junction formation	> 300	[82, 98, 99]
BEAS-2B	Immortalized healthy tissue	Monolayer formation, cytokine secretion, antioxidant expression,	< 100	[98]

		no mucin secretion or tight junction formation		
A549	Alveolar adenocarcinoma	Monolayer formation, membrane bound inclusion, alveolar type II-like, no polarization, no mucin secretion or tight junction formation	n.a.	[67, 88, 89]
NCI-H441	Papillary adenocarcinoma	Polarized monolayer formation, alveolar type II-like, Clara cell-like	~ 300	[95]

n.a. = not applicable.

5.1.6 ALI Models in Health and Disease State

Respiratory Viruses

It is estimated that 75% of all acute morbidities in developed countries are caused by acute respiratory diseases. The underlying reason for the majority of them is viruses. For the evaluation of virus-host interactions and the development of antiviral treatments, specific models capable of high-throughput screening in physiologically relevant conditions are required. In many other fields, animal experiments are used for this purpose but in virology, small animal models are often not suitable. Depending on the nature of the virus, some animal species are not susceptible to human viral infections or need virus adaption, thereby, potentially affecting viral pathogenicity. In many cases, the clinical state of the disease in humans is not reflected properly due to a lack of expression of specific human receptors. Therefore, it is advantageous to make efforts toward establishing advanced human *in vitro* models for a reliable analysis of virus-host interactions.

Immortalized human cell lines, such as Calu-3, are invaluable tools for the evaluation of virus replication cycles in lung epithelial cells [100]. However, the natural target cells of viruses in the respiratory tract are differentiated cells, whose characteristic features sometimes differ widely from immortalized cells. Therefore, the analysis of virus infections in continuous cell lines lacks important aspects of the viral pathogenesis. In the past years, models composed of well-differentiated epithelial cells from airway tissue have been established to assess respiratory virus infections under more clinically relevant terms. The cells are cultured under ALI conditions forming a monolayered, polarized, and differentiated epithelium [101]. This model closely resembles the airway epithelium *in vivo* regarding morphology and function, including mucus production and cilia movement [102]. For emerging respiratory viruses unable to proliferate in a traditional 2D submerged cell culture due to the lack of expression of several entry factors, ALI models greatly facilitate virus isolation and characterization [103, 104]. Ashraf et al. developed an ALI model to study the basic characteristics of human rhinovirus-C viruses (HRV–C) [105]. This subtype of HRV, which is considered the primary cause of common cold, has been circulating unnoticed due to the failure of culturing under submerged conditions. The group developed a model for growing HRV-C in an ALI culture of differentiated human sinus epithelial cells characterized by a pseudostratified morphology, cilia, and mucus-producing goblet cells. Thus, they were not only able to analyze the characteristics of clinical HRV-C but also compare the biological properties of different subtypes of rhinoviruses in the same cell culture system. Warner et al. strengthened the hypothesis that using physiologically relevant cell lines as well as a suitable cell culture model is fundamental. They used differentiated human airway epithelial (HAE) cells cultured under ALI conditions to evaluate the replication and innate immunity of rhinoviruses. With their experiments, they challenged older findings obtained from HeLa cells grown under conventional culture conditions [106]. Despite the potential advantages of primary cell-based models as discussed earlier, there are also some limitations. Ziegler et al. studied the susceptibility to the Epstein-Barr virus using an ALI model with primary bronchial epithelial cells [107]. Thereby, they detected significant donor differences. Their results suggest a significant impact of host variables to the susceptibility in the nasopharynx together with the type of EBV infection (productive or nonproductive). In conclusion, studying donor-dependent infection mechanisms as well as treatment responses, but also improving the robustness and reproducibility of *in vitro* models for interpretable

results represent a clinical need. Jonsdottir et al. established transgenic primary ALI cultures using lentiviral vectors, aiming at allowing for more combinations for virus-host interactions in different cell types and species [108]. They hypothesized that transgenesis would enable the study of viral and/or host factors, relevant for respiratory virus infections. They also expected that studying interactions between the virus and cells engineered for targeted gene knockdown or overexpression would allow the elucidation of specific mechanisms involved in virus-host interactions. This model in fact offers the potential for translation to animal cells so that viral pathogenesis can also be studied in other species in the future. Apart from testing different virus-host interactions, ALI models can also be utilized for the screening of different therapeutically relevant agents and their effectiveness on virus inactivation [109]. Especially for respiratory coronaviruses (CoV), an immediate unmet clinical need for broad-spectrum antiviral therapies was particularly emphasized by the 2020 Covid-19 pandemic. Originally, the importance of CoVs regarding human diseases was underrated, and therefore, at the beginning of the pandemic, no vaccine or general therapy was available to treat CoV-induced disease in humans. However, some strains of mainly zoonotic coronaviruses can enter new host species and spread there rapidly [110]. Both the Middle East respiratory syndrome CoV (MERS-CoV) and the severe acute respiratory syndrome CoV (SARS-CoV) have crossed the species barrier in the recent past, entered the human population, and resulted in severe diseases. In 2019, a novel human-infecting coronavirus (first provisionally named 2019-nCoV and later SARS-CoV-2) was first identified in Wuhan, in the Hubei province in China, and caused a worldwide pandemic, which is not yet under control by the time this Review is written [111]. Scientists were able to rapidly isolate the virus from the bronchial lavage fluid of patients suffering from SARS-CoV-2-mediated Covid-19 disease. They studied its biological characteristics using ALI models of primary human bronchial epithelial cells [112, 113]. Hence, polarized ALI cultures represented a valuable and high-throughput tool for rapidly gaining information on infection, replication, and pathogenesis of the new virus [114]. The thus obtained knowledge helped scientists and clinicians decide upon suitable containment measures for the population. At the time of writing this Review, two mRNA-based vaccines against SARS-CoV-2 were approved in a few countries [115, 116]. However, antiviral treatment options for patients with CoV infections are still very rare. Multiple therapeutic approaches are currently under development including commonly known antivirals, antibodies, interferons, vaccines,

and more recently also nucleic acid-based therapeutics [117-122]. For the evaluation of this broad variety and number of new therapeutic entities, more physiologically relevant *in vitro* models are needed including not only well-differentiated primary cells but also cocultures formed by more than a single cell type. One approach for a robust, high-throughput *in vitro* screening platform is presented by Gard et al. [65]. The group utilized an ALI cell-based model of human primary airway epithelial cells integrated into a high-throughput microfluidic platform (PREDICT96-ALI). This model can be used to study virus infections and has the potential to be used for fast and clinically relevant efficacy screening of different therapeutics. Nonetheless, to this day, only very few coculture models have been used for the analysis of virus-host interactions and possible therapies. Yoshikawa et al. cultured Calu-3 cells at the ALI to study the different functionalities of the apical and the basolateral domains in response to viral infection [123]. After virus inoculation of differentiated Calu-3 cells, the medium from both sides, apical and basolateral, was collected and incubated with dendritic cells or pulmonary macrophages to assess the potential of epithelial cytokines to modulate intrinsic factors of these cells. They showed an amplification of the early acute inflammatory response by both dendritic cells and pulmonary macrophages after infection of lung epithelial cells with SARS-CoV. In another study, a real ALI coculture model of the human respiratory tract was established by Blom et al. using human bronchial epithelial cells (16HBE14o-cell line), human monocyte-derived dendritic cells, and macrophage cultures [124]. Apart from establishing a reliable ALI coculture, they aimed to study the interplay between those three different cell types as well as interactions with biomimetic nanocarriers such as liposomes and virosomes, which show a promising opportunity for vaccines and/or drug delivery systems for antiviral therapeutics. Both studies underline the need for advanced ALI coculture models in the field of virology, not only with a differentiated epithelial layer but also in combination with different cell types that are present in the human lung tissue. With the implementation of such 3D *in vitro* models, scientists will be able to gain improved insights into virus-host interactions and obtain more reliable and translatable results regarding antiviral therapy, thereby, reducing animal experimentation to a minimum.

Cystic Fibrosis

CF represents one of the disorders involving the respiratory tract where ALI culture can help unveil the molecular processes of the disease and the search for new therapeutic approaches. In the Caucasian population, CF is the most prevalent autosomal recessive disease, involving about 100 000 people worldwide. It is a result of mutations in the CF transmembrane conductance regulator (CFTR) gene, which encodes the transmembrane protein responsible for transport of chloride and bicarbonate ions across epithelial cells [125]. Despite being a monogenic disease, about 2000 different mutations have been observed at the CFTR level, leading to different phenotypes and severity levels. The deletion of a phenylalanine in position 508 (ΔF508) is the most frequently encountered mutation, observed in about 70% of the CF population. The mutations result in a reduction of channel number, function or both, with severe consequences on the functionality of the affected tissues [126]. Although CF is a multiorgan disorder, the lung is the most affected. CFTR loss on the apical side of lung epithelium causes an imbalanced transport of ions and fluids across the cells, leading to unpaired mucociliary clearance, chronic inflammation, and recurring bacterial infections. Respiratory failure certainly represents the primary cause of death and morbidity [127]. After the discovery of the CFTR gene in 1989 [128], the understanding and treatment of CF greatly progressed in the past decades. This resulted in improved life quality and expectancy of the patients. The development of a mouse CFTR-knockout model helped identify many characteristics of CF. However, the CF mouse model lacked the development of spontaneous lung disease, which limited its use and pushed toward the development of alternative *in vivo* models in pigs and ferrets and *in vitro* models [129]. In the past two decades, polarized *in vitro* epithelial cultures have been fundamental for the progresses made in this field, especially for studying the role of CFTR in CF pathogenesis. Air-liquid interface culture systems are an ideal instrument for growing epithelial cells *in vitro*, as they allow the production of a differentiated airway epithelium including the main features found *in vivo*, particularly in terms of cellular differentiation, mucus secretion, and barrier function [130]. For this purpose, both secondary and primary cell lines have been used. Among the immortalized cell lines, models using CF, CFBE41o- cells, and non-CF cells, mostly 16HBE14o- and Calu-3, can be found. Calu-3 cells, in particular, are widely used due to their high transepithelial resistance, mucus secretion, and high expression of CFTR

protein [129]. Alternatively, CFBE41o- is a CF-immortalized cell line homozygous for ΔF508 deletion, therefore simulating the CF epithelium with high accuracy [131]. Despite the ease of use and accessibility, secondary cell lines are not representative of the great variety of scenarios found in CF epithelia, particularly in terms of CFTR variants. More appropriate patient-specific epithelial cell models have to be adopted. On this basis, primary cell lines are now considered the gold standard in CF research and are used for disease modeling as well as drug screening [62]. Primary HAE cells can be isolated from biopsy samples, lung explants, or cadavers and, after an expansion step, they can be seeded on transwell filters and grown at ALI. This process allows the generation of a pseudostratified epithelium with mucociliary morphology displaying the key physiologic functions of CF cells [132]. Moreover, it is possible to assess CFTR channel conductance through an Ussing chamber or patch clamping [133]. Recently, primary nasal epithelial cells have also been explored for ALI studies. These cells can overcome one of the major drawbacks of primary lung cells, namely, the limited accessibility associated with the invasive sampling methods. Nasal epithelial cells are obtained by noninvasive nasal brushing of patients and it was demonstrated that they show a polarization pattern well correlating with primary lung cells. They share similar growth and structural characteristics and, remarkably, also an analogous CFTR expression [134, 135]. The development of polarized primary CF epithelia played a significant role in the progress achieved by precision medicine in the context of CF. In particular, they strongly supported the development of CFTR modulators [136]. This class of drugs directly modulates the defective CFTR channel. They function either as CFTR potentiators by opening the channel present at the cell surface or as CFTR correctors by enhancing the transport of the protein to the cell membrane [137]. These therapeutics were a milestone in the treatment of CF, as they exert their action directly on the primary cause of the disease. However, they are not accessible to the entire CF population as they are mutation specific, meaning that they are effective only on specific CFTR mutations. The *in vitro* investigation of these modulators on patient-derived cells helped to discriminate the efficiency of each drug on the different genotypes. The potentiator Ivacaftor, for example, was shown to work on the G551D mutation [138], whereas the corrector Lumacaftor worked best on the ΔF508 mutation [139]. A wider study additionally showed the different effects of Lumacaftor on primary cells from patients with different genotypes, demonstrating the great potential of this airway model in the identification of patient-specific treatments [140]. Notably, Pranke

et al. demonstrated that the efficiency of CFTR modulators could also be evaluated on nasal epithelium by testing the effect of two CFTR correctors, Lumacaftor and Tezacaftor, on primary human bronchial and nasal cells. The results revealed only small response discrepancies in the two cell types, paving the way for using easily accessible nasal epithelial cells as predictors of CFTR modulators' effectiveness [141]. Apart from small-molecule drugs, ALI models can also be exploited to evaluate the ability of macromolecule-based therapies, including siRNA, to downregulate a target gene. In the context of CF, one example for a target is the epithelial sodium channel (ENaC), which is generally responsible for the transport of sodium. In CF, this channel is upregulated causing airway liquid depletion and thickened mucus. Manunta et al. were able to efficiently down-regulate ENaC expression on primary CF and non-CF cells grown in both submerged and ALI cultures. Interestingly, lower transfection efficiencies were observed in ALI cultures, reinforcing the importance of using advanced culture models to better mimic the *in vivo* situation [142]. This was confirmed by another study evidencing a similar behavior in CF cells cultured at ALI and in an *in vivo* mouse model in terms of dose regimen. In both systems, siRNA mediated a significantly higher ENaC knockdown after three repeated transfections compared with a single administration [143]. Coculture models, as already discussed, present a promising opportunity for further alignment between *in vitro* models and the complex *in vivo* situation. The addition of immune cells, in fact, greatly improves the imitation of the airway microenvironment [130]. In a study by d'Angelo et al., a triple coculture system was proposed for testing the cellular internalization and proinflammatory effect of an ENaC-targeted siRNA therapy. This model comprised 16HBE14o- cells as well as monocyte-derived macrophages from human blood and dendritic cells. Interestingly, in this study, the formulation was applied via nebulization through the Vitrocell Cloud system, thus increasing the resemblance to inhalation under *in vivo* conditions [144]. Moreover, coculture models have also contributed to shed light on another important aspect of CF, namely, bacterial infection of the airways. Staphylococcus aureus and Pseudomonas aeruginosa are the bacterial strains mainly involved in lung infections of patients with CF. Several studies showed that it is possible to cultivate both S. aureus [145, 146] and P. aeruginosa [147] on the apical side of polarized CF epithelial cells grown at ALI to observe the infection process, biofilm formation, and inflammatory responses. In this model, the bacterial infection can therefore be conducted under non-submerged conditions, providing a more natural condition for the infection process

(**Figure 3**) [148]. Using a more sophisticated method, Yonker et al. developed a model of inflamed mucosa by coculturing human airway basal cells and neutrophils. The group observed the migration of the latter in response to inflammation mediated by P. aeruginosa growth in the apical chamber of the Transwell filter [149]. Moreover, coculture of epithelial and bacterial cells can be very useful for testing the efficacy of antimicrobial agents. In case of P. aeruginosa, ALI cocultures were adopted to evaluate the ability of antibiotics [150], combination therapies [151], and antimicrobial peptides [152] to prevent bacterial infection while examining the consequences on human epithelial cells.

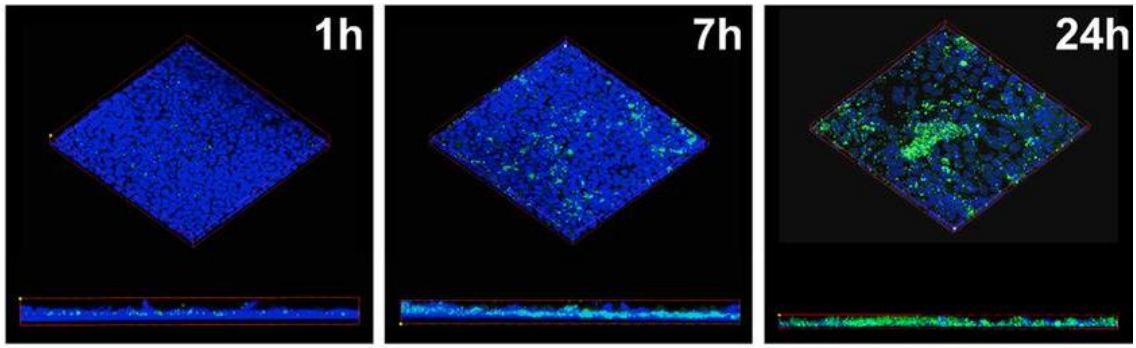

Figure 3. Polarized monolayers after infection with GFP-expressing *S. aureus* USA100 (green) and consecutively fixed and stained with Hoechst (blue) for confocal imaging at distinct time points. Reproduced under the terms and conditions of the Creative Commons Attribution 4.0 International License [146]. Copyright 2018, The Authors, published by the American Society for Microbiology.

Asthma

Asthma is a chronic lung illness with more than 300 million affected people worldwide, associated with a growing burden for healthcare systems of both industrialized and developing countries. The most prominent feature of asthma is a generalized inflammation of the upper airways resulting in recurrent episodes of coughing, wheezing, chest tightness, and dyspnoea [153]. In addition to a severe symptomatology, chronic inflammation has also serious consequences on lung structure and functionality, especially in terms of airway hyper-responsiveness,

obstruction, and remodeling as well as mucus hypersecretion [154]. The mechanisms behind the inflammatory status rely on inappropriate immunological responses to common-inhaled allergens, which trigger cytokine secretion by T-helper 2 (Th2) immune cells. The sustained release of inflammatory cytokines mediates a perpetuated inflammatory state [155]. Apart from Th2 cells, other immune cells such as eosinophils, mast cells, and dendritic cells are involved, defining asthma as an immunological disorder [156]. Indeed, asthma involves several cell types including epithelial cells, which represent the first line of defense and regulators of immune responses against the environmental factors. Activated epithelial cells secrete cytokines and chemokines that recruit dendritic cells, which are responsible for the following coordination of the inflammatory cascade. Airway epithelium functionality, however, is altered in the disease state [157]. Apart from the infiltration of immune cells, bronchial biopsies of asthmatic patients point out structural changes of airway epithelium in response to chronic inflammation. In addition to the increased number of mucus-secreting goblet cells and enhanced angiogenesis, they also display a remodeled, damaged epithelium missing tight and adherent junctions with consequent loss of apicobasal polarity [158]. This condition is strictly correlated with the breakdown of the defense mechanisms observed in asthma. The alterations of the airway epithelium make the development of suitable experimental models essential to comprehend the ongoing immunological and structural modifications and to identify possible therapeutic targets. Mouse models of allergic asthma have been widely used to investigate asthma-driving mechanisms and screen therapeutic agents. Nonetheless, they present anatomical as well as immunological discrepancies with human airways. As described above, mouse lungs differ in terms of lobar structure and branching pattern of the bronchi [49, 50]. Moreover, mice lack bronchodilatory nerves and the ability to cough, along with a different pattern of mediators secreted by mast cells [159]. The complex human *in vitro* and *ex vivo* systems now available embody a valid support to the well-established *in vivo* models. Epithelial cells grown at ALI can be used as a powerful tool to mimic the asthmatic epithelium *in vitro* with high similarity to the *in vivo* situation. The simplest way to reproduce the polarized epithelium at ALI for asthma studies is adopting common epithelial cell lines of the respiratory tract such as 16HBE14o-, BEAS-2B, and Calu-3. They are easily accessible and relatively simple to grow on Transwell supports. In addition, they express tight junctions, making them suitable for barrier function studies [159]. Stewart et al. evaluated different immortalized cell lines in comparison

with primary bronchial epithelial cells in terms of TEER values and marker expression. They observed that Calu3 cells featured a similar expression pattern of ZO-1, E-Cadherin, and MUC5AC to primary cells, although lacking a localized expression of β-tubulin [80]. Nonetheless, secondary cell lines lack the genetic features and the structural changes observed in asthmatic epithelium. The improvements achieved in primary cell extraction from bronchial biopsies allowed their implementation in asthma research as *ex vivo* models of airway epithelia. Primary cells from asthmatic patients show marked differences from the ones obtained from healthy individuals due to the increased secretion of inflammatory cytokines and mucus production. Furthermore, they retain a less differentiated phenotype with diminished capability to repair injuries [63]. In addition, they have disrupted tight junctions that reduce TEER values and increase permeability [160]. ALI cultures of asthmatic primary cells can therefore be considered a suitable model to depict the morphologic and inflammatory imbalances caused by chronic inflammation. Notably, these models retain the phenotypic differences typical of the disease state. Gras et al. confirmed that reconstituted bronchial epithelium from mild and severe asthma patients retains a trend in inflammatory marker expression and mucus production that varies in correlation with the severity of asthma [161]. Thanks to the high resemblance to the real-life condition, ALI culture of primary epithelial cells of the respiratory tract has been a valuable tool for the identification of novel drug targets and screening of alternative therapeutic options. They were, for instance, used for analyzing the role of transforming growth factor-β (TGF-β) [162] and histocompatibility antigen G (HLA-G) [163] in airway remodeling. Moreover, *in vitro* cultures of primary human cells from asthmatic patients are also exploited to detect novel subsets of asthmatic patients, as the recently identified interleukin-6-driven asthmatic group [164]. As mentioned above, this model system plays a crucial role in the preclinical investigation of novel therapeutic agents and for understanding the mechanisms of action of therapies already in use. β2-adrenoreceptor agonists, for example, together with corticosteroids, are first choices in the step-therapy approach for the management of asthma symptomatology. Holden et al. cultured primary cells as well as BEAS-2B cells at ALI as a simplified version of the respiratory tract to investigate the effect on inflammatory response of the β2-agonists in epithelial cells in combination with corticosteroids [165]. Potential anti-inflammatory agents were also screened using ALI culture. It was confirmed that one molecule inhibited nuclear factor κ-B2 (IKK2i), leading to a reduction of inflammatory mediators

in corticosteroid unresponsive epithelial cells [166], whereas an src-family kinase inhibitor was able to reduce TNF-α release, a key inflammatory mediator, and improved barrier properties of severe asthmatic ALI cultures [167]. Sexton et al. tested if a human monoclonal antibody inhibited a serine protease from the tissue kallikrein family in primary cultures of bronchial epithelial cells, which induces bronchoconstriction and mucus hypersecretion in the airways. The monoclonal antibody reduced the mucus secretion and the inflammatory burden. The results from ALI cultures showed that antibody treatment restored kallikrein expression and reduced mucus secretion. *In vivo* studies in a sheep asthma model emphasized that the monoclonal antibody decreased bronchoconstriction and hyper-responsiveness as well [168]. As already discussed in the context of CF, nasal primary epithelial cells offer a promising alternative to bronchial primary cells, thanks to their higher availability and effortless extraction procedure. A study comparing primary asthmatic nasal cells with non-asthmatic and bronchial cells demonstrated that the former express higher levels of typical mediators, which are commonly encountered in asthmatic patients, such as vascular endothelial growth factor (VEGF) and TGF-β. This observation strengthened the hypothesis that nasal epithelial cells are a suitable surrogate for primary lung epithelial cells [169]. Healey et al. utilized nasal epithelial cells from asthmatic donors in the preclinical testing of an siRNA-based therapy aimed at downregulating STAT-6 expression in epithelial cells, a gene involved in bronchial inflammation of asthma [170]. Similarly, Bequignon-et al. investigated the ability of a monoclonal antibody to bind the neonatal Fc receptor in human nasal epithelial cells as a potential administration route in asthma-related chronic rhinosinusitis [73]. Despite the advantages offered by this alternative source of primary cells, it is important to consider that they have some intrinsic differences in comparison with the bronchial ones that might affect the reliability of the results. It is therefore important to keep in mind the implications of choosing one or the other source of cells. The asthma research field has greatly benefited from ALI culture of epithelial cells. However, simple monoculture models cannot represent the complex cellular network typical of the disease state. Asthma is a multicellular disease involving epithelial cells as well as several immune cells. Coculture systems more closely represent the complexity encountered in asthmatic lungs as they bring together two or three different cell types on the same Transwell filter. Cocultures for asthma-related studies generally present lung epithelial cells, primary or immortalized, in the apical chamber of a Transwell to form a polarized

epithelium, whereas the basolateral chamber hosts a subtype of immune cells including dendritic cells [171], eosinophils [172], or T cells [173]. A coculture formed by primary epithelial cells and T cells was used by Wawrzyniak et al. to study the role of T cell-secreted cytokines and histone deacetylases on the integrity of the epithelial barrier integrity. They demonstrated a beneficial effect on barrier integrity after treatment with a histone deacetylase inhibitor [173]. Cocultures were also used to study airway remodeling in asthma, a typical feature of the disease. Haghi et al. developed an airway remodeling model by growing primary bronchial epithelial cells on the apical chamber and airway smooth muscle cells on the basolateral one [174]. In another study, Reeves et al. developed a coculture of primary human bronchial epithelial cells derived from asthmatic children and human lung fibroblasts to study the fibroblast-myofibroblast transition. They showed that it is possible to restore the healthy condition using a monoclonal antibody inhibiting TGF-β, a central factor involved in airway remodeling [175]. Triple cocultures would be an even more exemplary model of the asthmatic environment. However, studies exploiting this method are infrequent. A recent study by Paplinska-Goryca et al. provides a triple coculture model formed by primary epithelial cells, dendritic cells, and macrophages that might be helpful for better understanding the pathogenesis of asthma, thanks to the higher complexity of the system [176].

Lung Cancer

Lung cancer is the most prevalent cause of cancer-related deaths, both in men and also in women [177]. Therapeutic advancements of the past ten years are barely reflected in the small decline of lung cancer mortality. One reason is the histologic diversity of lung cancer including the three most common types: adenocarcinoma, squamous cell carcinoma, and small cell carcinoma, as well as several less-frequent types such as adenosquamous carcinoma and large-cell neuroendocrine carcinoma. Due to this high variability, it is necessary to examine the exact molecular mechanisms of each cellular type to further improve therapy options. Hereby, animal models are an important standard tool. Apart from known drawbacks such as high costs, species differences, and limited availability, ethical issues regarding the use of animals in tumor research are controversially discussed [178]. Therefore, also in this field, extensive research has been conducted in the past years to establish reliable and physiologically

relevant *in vitro* cell culture models, thereby, reducing the number of animals for experiments in tumor research and drug development. As conventional 2D cell cultures are not capable of mimicking the complex architecture and microenvironment of lung cancer *in vivo*, 3D cell cultures and cocultures contribute greatly to the knowledge of tumor cell pathophysiology and also for antitumor drug discovery [179]. Often, ALI systems are used to study the exact mechanisms of malignant transformations of different cell types because of their resemblance to the human lung physiology [180, 181]. ALI systems also serve as studies on how a specific signaling pathway can potentially be inhibited [182]. Horie et al. established a 3D co-culture model at the ALI using A549 cells and lung cancer-associated fibroblasts [183]. They found that fibroblasts enhanced A549 cell invasion into collagen gels, showing their tumor-promoting role through the production of instructive signals including growth factors and chemokines. Due to its aggressive nature and high mortality, it is especially important to improve the early detection and chemoprevention of lung cancer. However, the pathobiology of early stages is poorly understood. To this purpose, Correia et al. engineered an ALI culture of immortalized human bronchial epithelial cells overlaid on a fibroblast containing collagen layer to induce the activation of oncogenes [184]. They confirmed that deregulation of oncogene SOX2, under proper *in vivo* mimicking circumstances, leads to bronchial dysplasia. These findings are important steps forward toward the development of therapeutics used for primary and secondary chemoprevention [182]. The most frequently found 3D *in vitro* tumor models are lung cancer spheroids constituted of one or more cell types [185, 186]. Tumor spheroids are cell constructs that have self-organized to exhibit a 3D structure resembling the cancerous state. It was shown that genes expressed in 3D spheroids, especially the ones responsible for aggressive tumor growth, recapitulate the *in vivo* phenotype better than the respective 2D models [187]. Also, 3D models hold the potential to guide personalized medicine in the future, clearly demonstrating their superiority over conventional models [188]. However, particularly in lung cancer research, spheroid models have one critical disadvantage. Many of them lack air exposure and therefore do not reflect the physiological environment correctly. Subsequently, these cultures are unsuited models for testing the efficacy of aerosolized drugs. Meenach et al. compared lung tumor spheroids in air- as well as liquid-interface culture for treatment with paclitaxel-containing PEGylated phospholipid microparticles in the form of a dry powder [189]. For the cultivation at ALI conditions, A549 cells were

seeded on collagen-coated transmembrane inserts in a 24-well plate and then incubated for 24 h under submerged conditions. Subsequently, the medium on the apical side was discarded and spheroid formation was evident after 9 days. The group showed that IC50 values of paclitaxel can differ substantially between treatment of a tumor spheroid grown under submerged conditions and another one cultured at ALI conditions. Moreover, they stated that the data from ALI evaluation were reported in µg/dose, in contrary to the usual µM results; thereby, the patient dose in terms of mg/kg via direct inhalation of the drug can be easily determined. Gupta et al. developed a high-throughput model growing A549 lung adenocarcinoma cells as 3D spheroids at the air-liquid interface [190]. They found that, due to limited drug diffusion, the cytotoxic effect of paclitaxel in A549 ALI spheroids was only noticeable on the outer layer of the cell complex. However, the coadministration of a tumor-penetrating peptide enhanced paclitaxel penetration depth. These results emphasize the importance of air-grown 3D *in vitro* models not only to characterize tumor growth and microenvironment of different cell types but also to gain a deeper knowledge of the resistance mechanisms in lung cancer. Such models strongly improve efficacy and success of the screening process of chemotherapeutics and drug combinations and serve as a first step before conducting expensive *in vivo* preclinical or clinical studies. Apart from spheroids, other ALI models have been developed. Movia et al. used a multilayered cell culture (MCC) of A549 cells to study four anticancer drugs delivered by a clinical nebulizer as liquid aerosol [191]. Their results clearly demonstrated the advantages of this model: the biological complexity due to 3D architecture, closer resemblance to the patient status by modeling the multidrug resistance (MDR) observed in human patients, and applicability of aerosol administration methods due to ALI conditions. In a subsequent study, the group incorporated human fibroblasts into their MCC model to assess their role in MDR [192]. Indeed, cancer cell-fibroblast crosstalk led to a higher MDR than the one found in an ALI multilayered monocultures. These studies emphasize that a monoculture, even if it is 3D and under ALI conditions, still does not reflect the *in vivo* conditions sufficiently. Therefore, it is crucial to integrate several other key factors, such as immune cells, extracellular matrix, and genetic variability, into the *in vitro* platform in further studies. Zhang et al. assessed the impact of tumor microenvironment on bone marrow mesenchymal stem cells [193]. Conclusively, they found that an *in vitro* ALI lung cancer A549 microenvironment might induce stem cells to undergo alterations in cell proliferation, morphology, cytoskeleton, karyotype, and

migration ability. This study is an important example for the versatility and flexibility of advanced ALI *in vitro* models. In lung cancer research, they can be used for the evaluation of various therapeutic approaches by simply incorporating key factors of interest. Due to the versatile nature of lung cancer and the increasing development of MDR in tumors, new and innovative therapy options are constantly needed to improve therapeutic efficacy. In the past decade, nanotechnology emerged as a promising alternative and/or addition to conventional treatment strategies. When using these nanocarriers in pulmonary administration, the lung can be used as port of entry, limiting systemic distribution and avoiding first pass metabolism [194, 195]. Many attempts have been described in the literature to improve the delivery of already-approved chemotherapeutics, such as paclitaxel or doxorubicin, using nanocarriers [196-198]. Furthermore, nanocarriers are often used to encapsulate new therapeutic entities for lung cancer treatments such as nucleic acids [199] and also for co-delivery of different therapeutic agents [200]. The huge variety and number of combinations of delivery systems with already existing or new active pharmaceutical ingredients require testing in more complex and physiologically relevant *in vitro* models to assess and compare efficacy. Using 3D coculture systems, scientists can make reliable statements on penetration, efficacy, toxicity, and other characteristics of drug formulations, thereby reducing the amount of animal experiments drastically. Conclusively, the development of these advanced cell culture systems is crucial because in combination with organ-on-a-chip models and simulation approaches, they could potentially lead the way to animal-free research.

COPD

COPD, together with asthma, is considered as one of the chronic respiratory diseases displaying the highest impact on healthcare systems worldwide. Based on the World Health Organization report, it affects more than 250 million people around the world, with more than 90% of mortality in low- and middle-income countries [201]. COPD is triggered by persistent exposure to toxic gases and particles, where cigarette smoke exposure was identified as a central risk factor. Tobacco smoke, in fact, mediates an abnormal chronic inflammatory status, resulting in severe consequences on lung structure and functionality [202]. COPD affects small airways, lung parenchyma, as well as larger airways, and it is characterized by a progressive obstruction of the

airways that ultimately leads to lung failure. The clinical manifestations of COPD can be grouped into two major subsets, chronic bronchitis and emphysema, which affect large and distal airways, respectively. Chronic bronchitis is distinguished by chronic inflammation and remodeling of the large airways together with mucus secretion, whereas emphysema shows a progressive destruction of airway walls as well as loss of alveolar cells, which consequently impairs gas exchange [203]. The abnormal inflammatory response typical of COPD is linked to an enhanced presence of inflammatory cells in the airways, with neutrophils, macrophages, and CD8+ T-cells playing a prominent role. These cells secrete cytokines and chemokines including TNF-α, IL-1β, and IL-8, which mediate a perpetuated inflammatory condition [204]. Similar to asthma, bronchial epithelial cells retain a central function also in COPD. While at physiological conditions airway epithelium acts as a defensive barrier toward external agents, the alterations of the homeostatic environment driven by toxic agents cause severe modifications of epithelium structure and functionality. This is reflected particularly in terms of reduced mucociliary clearance and increased permeability to external factors. Therefore, lung epithelium faces increased permeability, reduced cilia beat ability, as well as decreased mucus clearance. Moreover, in this imbalanced status, epithelial cells are not only the target of inflammatory mediators, but they also secrete cytokines and chemokines that perpetuate and worsen the inflammatory status. The increased secretion of TGF-β and EGF, for example, is directly linked to fibrosis and mucus secretion [205]. Considering the central role played by epithelial cells in COPD, ALI models can grant deeper understanding of the disease-driving mechanisms as well as identification of novel therapeutic options. COPD is directly correlated with lung exposure to toxic pollutants such as tobacco smoke or diesel exhaust. Therefore, ALI cultures represent a straightforward tool mimicking the *in vivo* lung environment of the disease. Several studies have shown that after growing and differentiating cells at ALI, they can be exposed to cigarette smoke to obtain an *in vitro* system incorporating most of the effects observed also *in vivo*. Shamberger et al. demonstrated that cigarette smoke exposure of healthy human primary bronchial epithelial cells alters their differentiation and functionality. Apart from impairing the epithelial barrier integrity, it also affected cellular differentiation, resulting in an elevated number of mucus-secreting cells, whereas the number of ciliated cells decreased. These changes caused a mucus-rich lung environment [206]. Indeed, mucus hypersecretion is one of the main features of COPD. Culturing epithelial cells at ALI is essential to investigate this distinct

mucus hypersecretion trait of the disease [207], along with reduced mucus clearance by ciliated cells [208]. The effect of tobacco smoke on epithelial barrier integrity has also been explored in terms of tight-junction loosening [206] and airway remodeling [209]. Both factors are crucial for the pathophysiology of the disease and, similarly to the ones described above, their understanding was expanded by ALI cultures. Cells grown under this condition, in fact, form differentiated epithelia with different cellular subsets, such as ciliated cells, and can even secrete mucus, a condition not reproducible under submerged cultures. Recently, a new manufacturing method was established to grow primary small airway epithelial cells at the ALI. Small airways are the part of the airways mainly affected by chronic bronchitis. Gindele et al. showed that once primary cells from COPD patients were grown at ALI and exposed to cigarette smoke, their behavior well correlated with the *in vivo* conditions in terms of barrier integrity, mucus secretion, and cellular differentiation, making them a suitable tool for further COPD treatment studies [64]. The effect of cigarette smoke on barrier integrity is reflected also in an increased susceptibility to microbial infections [210]. Cocultures of epithelial cells grown at ALI and bacteria were developed along with exposure to cigarette smoke. Amatngalim et al. grew primary epithelial cells from COPD and non-COPD subjects at ALI and studied the different responses to Haemophilus influenzae after exposure to cigarette smoke. They observed that antibacterial activity was lower in primary cells from COPD patients and suppressed after cigarette smoke exposure [211]. To further improve the translatability of ALI-based systems in COPD research, efforts have been made toward the advancement of exposure systems for tobacco smoke. Azzopardi et al. used an aerosol exposure chamber to uniformly expose lung epithelial cells grown at ALI and used it to study the consequences on cellular viability and cytokine release after the aerosolization of tobacco smoke. This system allowed the investigation of tobacco effect on cells with various exposure regimens and exposure times that well correlate with real-life parameters [212]. In another study, primary COPD epithelial cells were exposed to diesel exhaust, another toxic agent responsible for triggering the disease, using a Vitrocell nebulization system. Instead of using suspended particles, this exposure system allowed to reproduce *in vitro* exposure conditions similar to the ones observed in everyday life [213]. As discussed above, coculture models can fill the rift between *in vitro* and *in vivo* models, thanks to more advanced cellular complexity. In COPD research, several studies have exploited coculture models to study the cellular networks involved in the disease. Ladjemi et al.

developed a coculture model formed by primary epithelial cells from COPD patients and B-cells. They used this system to test how the bronchial epithelium influenced the humoral response in the lung. Specifically, they observed the effect of interleukin 6 (IL-6) secreted by epithelial cells on immunoglobulin A (IgA) secretion by B cells, which is increased in COPD patients [214]. In another study, cocultures of respiratory epithelial cells and lung fibroblasts were established to understand the mechanisms behind airway remodeling and inflammation in COPD. The authors observed a stronger interleukin1 α (IL-1α)-mediated inflammation in cocultures exposed to cigarette extract, confirming the connection between smoke and inflammation [215]. An additional coculture model was established between primary small airway epithelial cells and macrophages to analyze the epithelial wound injury mechanisms in respiratory diseases [216]. COPD coculture models could therefore represent a useful tool to gain a deeper knowledge of the driving mechanisms of the disease as well as for *in vitro* screening of potential therapeutic agents. So far, most of the treatment-related studies were conducted using ALI cultures involving only a single cell line, mostly epithelial cells. The mucus-secreting cell line Calu-3, for example, was utilized to test the ability of simvastatin, a drug-mediating reduced mucus secretion of epithelial cells of COPD patients [217]. Calu-3 cells were also exposed to cigarette smoke extract to examine the ability of the antimicrobial peptide cathelicidin LL-37 to prevent the disruption of tight junctions. This effect was expected to reverse the impaired activity of the epithelium typical of COPD [218]. Another study investigated the impact of roflumilast, a phosphodiesterase inhibitor, on mucociliary clearance impairment. A Vitrocell nebulizer was used to nebulize cigarette smoke on primary human bronchial epithelial cells pretreated with rofumilast. An Ussing chamber was used to determine the recovery of mucociliary activity [219]. Primary cell-based ALI cultures were also used to test the potential of monoclonal antibody candidates to improve the COPD phenotype. ALI cells treated with an anti-TGF-β monoclonal antibody reversed the progressive dedifferentiation of the epithelium typical of the disease [208]. Monoclonal antibodies directed toward IL-1α and IL-1β decreased cigarette smoke-mediated airway inflammation in primary human bronchial epithelial cells [220]. Taken together, ALI models of mono- and coculture have been used in a variety of pharmacological and pharmacotherapeutic studies trying to understand and treat COPD better.

5.1.7 Commercially Available ALI Models

As described above in detail, there is an unmet urgent clinical need for standardized 3D *in vitro* ALI models of the respiratory tract to study toxicology and for efficient drug screening. Therefore, several companies have specialized in the fabrication of ALI models mimicking the morphology of healthy and diseased human tissue. Two of these models, available under the brand names MucilAir (Epithelix) and EpiAirway (MatTek Corporation), are made of primary human epithelial cells, which are freshly isolated from nasal or bronchial biopsies [221]. They can accurately reproduce the biophysiology of human airway epithelia comprising a functional mucociliary system and the secretion of mucus [222]. It was shown that both, MucilAir and EpiAirway models, express tight and adherent-junction proteins, as well as functional ABC drug efflux transporters [223, 224]. Hoffmann et al. showed similar permeability of 30 model substances when comparing MucilAir with nasal and bronchial epithelium in human tissue [225]. These findings confirm the match of these ALI models with major features of a normal human nasal and bronchial epithelium [226]. Hence, these models are widely used for toxicology studies, drug efficacy, and formulation screening (**Figure 4**) [227-230].

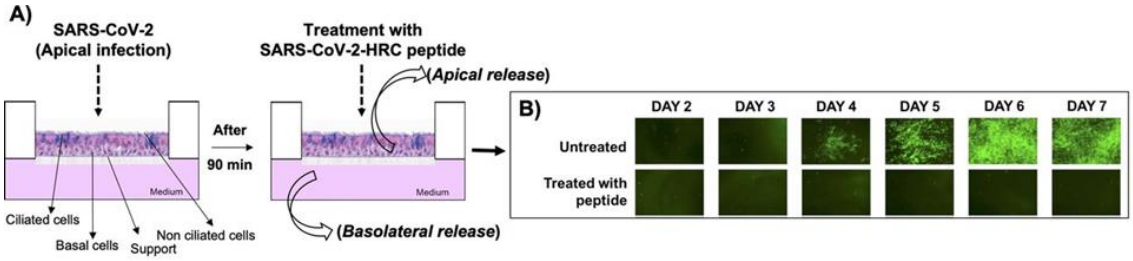

Figure 4. Cholesterol-conjugated peptides derived from SARS-CoV-2 block the SARS-CoV-2-mNeonGreen viral spread in HAE cells. A) Infection of HAE cells with SARS-CoV-2 (2000 PFU well^{-1} for a multiplicity of infection of ~ 0.02) for 90 min with subsequent addition of SARS-CoV-2 peptide. Collection of liquid from the apical or basolateral surfaces daily. B) Fluorescent virus is presented at the indicated days with or without peptide treatment. Adapted with permission [231]. Copyright 2020, American Society of Microbiology.

With two other models expressing a different phenotype, EpiAlveolar and SmallAir, scientists are additionally able to analyze the impact of different therapeutics on the lower respiratory tract [232, 233]. The two leading companies in this field, MatTek Corporation and Epithelix, recently also developed cocultures of ALI epithelial cells and fibroblasts (EpiAirway FT and MucilAir HF) for advanced analysis of cell interaction and better-mimicking *in vivo* conditions [234] [235]. These commercial models open various possibilities for further modifications with other cell types, bacteria, and viruses depending on the application. Outlaw et al. infected cells of the EpiAirway model with SARS CoV-2 to study the efficacy of a lipopeptide as virus entry inhibitor (**Figure 4**) [231]. As shown by Signer et al., MucilAir can readily be infected with different respiratory coronaviruses to evaluate the effect of new antiviral agents [236]. Another example to show the modularity of these systems is given by Mas et al. (Epithelix) [237, 238]. They combined a functional respiratory epithelium, primary lung fibroblasts, and proliferating tumor nodules from a KRAS-mutated non-small-cell lung cancer cell line. After confirming the biological relevance of this brand named OncoCilAir model regarding the *in vivo* situation, the group showed reduced growth of tumors when treated with MEK inhibitors and the standard anticancer agent docetaxel. Subsequently, this model has been used in a variety of other studies including specific tumor targeting and multiorgan chips [229, 239] (**Figure 5**). In general, organ-on-a-chip devices present the possibility to create artificial tissue microenvironments simulating those conditions found *in vivo*. This can also be used for mimicking lung functions involving a complex structure and fluid and solid mechanical stress [240, 241]. Zamprogno et al. established a lung-on-a-chip model to reconstitute the lung alveolar barrier. They used a hexagonal gold mesh with a suspended stretchable membrane to culture alveolar epithelial cells in ALI conditions mimicking physiological lung movement [242]. Huh et al. developed a microfluidic system replicating a functional unit of the living human lung [243]. Therefore, they constructed a compartmentalized microchannel system consisting of two chambers separated by a mesoporous elastomeric membrane. Human alveolar epithelial cells were seeded into the chambers and cultured at ALI including pulmonary microvascular endothelial cells. With this model, the group was able to simulate physiological breathing motions by stretching the mesoporous membrane. Although these particular techniques and execution are not yet optimized, there is already a microfluidic-based ALI lung model on the market. The company SynVivo developed a device containing a coculture of epithelial cells

embedded into vasculature comprising endothelial cells. Hereby, tight junctions are formed, functional cilia are built, and airway tubules form and transport mucus [244]. These examples including many more that can be found in literature demonstrate that lung-on-a-chip models are valid tools in pharmaceutical development [245].

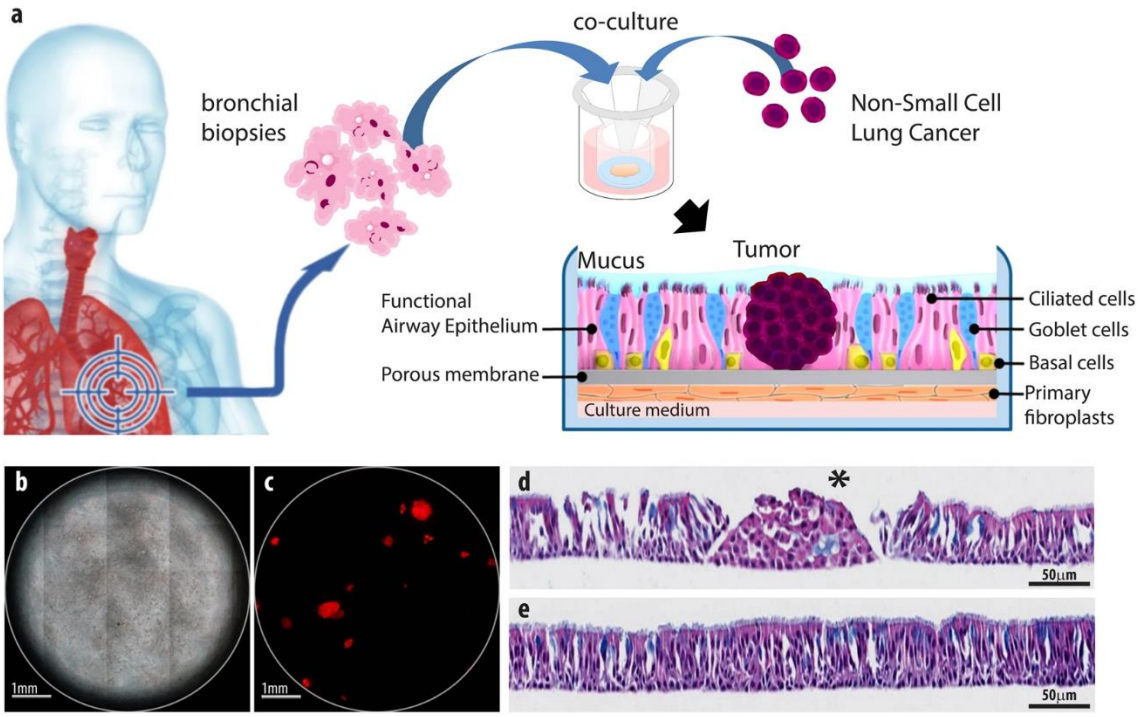

Figure 5. The OncoCilAir model. a) Scheme of lung cancer invasion of a healthy human airway modeled by OncoCilAir tissue. b) Phase contrast and c) fluorescence images of a human respiratory epithelium with EGFR tumor nodules (mRFP labeled) at the ALI. d,e) Haematoxylin eosin histological staining of differentiated functional regions of the airway, e) and with an array of non-polarized tumor cells, d, star) invading the epithelium d). Reproduced under the terms and conditions of the Creative Commons Attribution 4.0 International License [238]. Copyright 2017, The Authors, published by Springer Nature.

5.1.8 Aerosolization Systems

All the models described earlier demonstrate the possibility to mimic the exceptionally complex nature of the lung epithelium *in vitro* using ALI cultures. However, so far, the lack of high-throughput technology to obtain dosimetrically accurate aerosol-to- cell

drug delivery hampers the development of aerosolized inhalable therapeutics. Lenz et al. investigated the ALICECLOUD system, an aerosol-to-cell exposure system, with a vibrating mesh nebulizer developed for the use in standard multi-well plates [246]. The same group found that aerosolized drug delivery with the ALICE system results in ~8 µm-thin liquid layer, which is about 1000-fold lower than typical media heights under submerged cell culture conditions [247]. Therefore, it resembles the clinical conditions in the bronchial regime, making aerosolized drug delivery to ALI cells crucial for biokinetic studies. This system can be combined with coculture systems to examine the potential effect of particles in the lung using a sophisticated *in vitro* model [248].

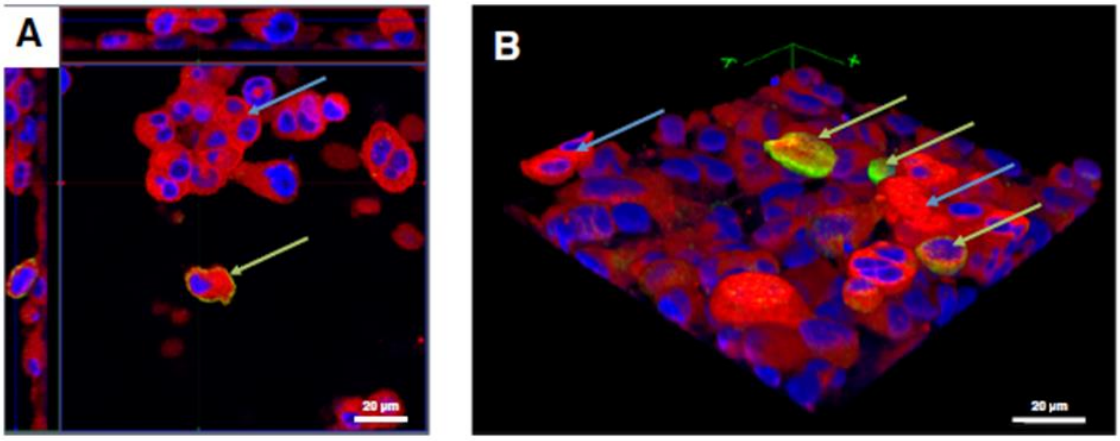

Figure 6. Z-stack image series for the analysis of THP-1 macrophage and HMC-1 cell distribution in the tetra-culture system of the apical compartment, analyzed via confocal laser scanning microscopy (CLSM). Cell membranes are stained with cell mask deep red dye (red), and cell nuclei are stained with DAPI (blue). Macrophage-like cells are counterstained with an anti-CD11b-antibody. A) x–y orthoslice. B) 3D image of the tetraculture based on the z-stack from (A). THP-1 (green arrows) and HMC-1 (blue arrows) cells are situated on top of the epithelial cells. EA.hy 926 cells were not present in the 3D reconstruction. Reproduced under the terms and conditions of the Creative Commons Attribution License [248]. Copyright 2013, The Authors, licensee BioMed Central Ltd.

Vitrocell Systems were among the first companies to offer a commercial version of this system. An interesting application of a tetraculture in combination with the Vitrocell system was investigated by Klein et al. regarding the effects of particle deposition on

the lung [248]. In this model, four different cell lines (epithelial cells, macrophages, mast cells, and endothelial cells) were grown on the same Transwell insert, demonstrating the potential offered by such ALI systems. Cells were grown on both sides of the insert to mimic *in vivo* cellular distribution (**Figure 6**). Another example of a commercially available aerosolization system is CULTEX from Cultex Technology. The company did not only develop an exposure system but also a computer-controlled long-term cultivation system [249, 250]. Using these two modules together allows prolonged ALI cultivation of normal human bronchial epithelial cells for a period of 38 days exhibiting *in vivo*-like differentiation characteristics for inhalation toxicological studies. The computer-controlled system can operate independently, reducing the risk of contamination and eliminating process variability. With the CULTEX aerosolization system, the particle or gas exposure takes place for 15-60 min under humid atmosphere at 37 °C. The device was extensively validated for the inhalation of airborne particles by Tsoutsoupoulos et al. [249]. After testing the aerosolization of 24 different substances, the results demonstrated the device to be robust, transferable, and predictive for *in vitro* screening. Other exposure systems with a limited number of users have also been described [251]. In addition, nebulizers can be used as well with the drawback of uncertain dose deposition after direct nebulization on top of ALI cultures. Many systems described in the literature need further modification for standardized particle deposition and dosimetry (**Figure 7**) [252-255].

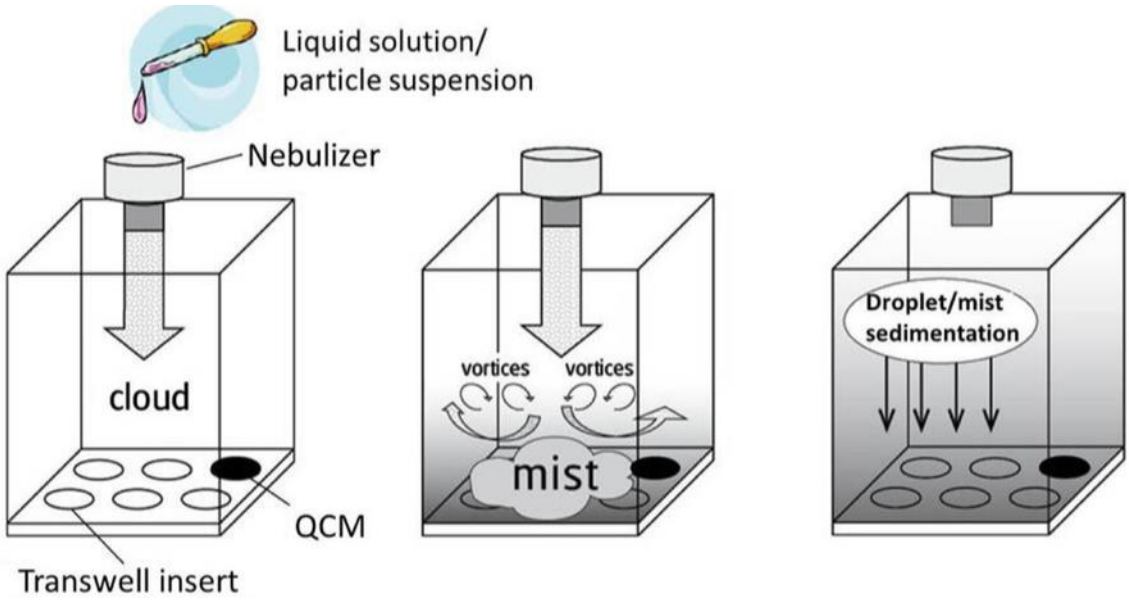

Figure 7. Scheme of the nebulization and sedimentation process of various solutions or suspensions using the VITROCELL Cloud 6 system with a quartz crystal microbalance (QCM). Phase 1: emission of droplet cloud from nebulizer. Phase 2: emitted cloud is transformed into a fine mist of droplets, which is distributed uniformly filling the chamber from bottom up. Phase 3: droplet deposition onto the cells via sedimentation. Reproduced under the terms and conditions of the Creative Commons Attribution 4.0 International License [256]. Copyright 2020, The Authors, published by Springer Nature.

5.1.9 Conclusion

In the past years, the need for alternatives to *in vivo* models to reduce, refine, and replace (3R) animal experiments has increased drastically. Furthermore, anatomical differences between commonly used laboratory animals, such as mice or rats, and humans lead to a significant lack of functional homology, especially regarding the respiratory tract. Modeling this part of the human body *in vitro* requires multiple considerations to simulate *in vivo* pathophysiology as closely as possible. In this Review, different *in vitro* air-liquid interface cultures mimicking the human respiratory tract were described in detail. The most frequently utilized cell lines representing different areas of the respiratory tract were discussed together with the possibilities of replacing these with human-derived primary cells. In addition, different approaches to

mimic diseases of the human respiratory tract, such as asthma, COPD, or viral infections, were discussed. These can be of great use in gaining deeper understanding of disease pathophysiology and in high-throughput drug screening to find new therapeutic options. Yet, the recreation of such a complex microenvironment *in vitro* using epithelial cells in combination with other cell types, such as immune cells, bacteria, or even viruses, is particularly challenging, leaving room for continuous progression in this field of research. Moreover, the broad variety of culture methods, cell sources, and exposure setups requires further evaluation of robustness, complexity, reproducibility, and ease of use of the *in vitro* setup. Until now, there is no golden standard cell model. However, a few companies have started commercializing validated and standardized ALI models from primary human respiratory epithelium. In conclusion, the use of the ALI culture technique, especially in coculture models, has the potential to result in significant advances in the development of more physiologically relevant tissue models for drug discovery and disease modeling, thereby reducing the number of experimental animals required in lung research.

6 Aim of the Thesis

The aim of this work was to develop and optimize a nanoparticle-based drug delivery system for successful nose-to-brain delivery of biologics such as proteins and nucleic acids. Therefore, an existing carrier system on the basis of the polysaccharide chitosan (CS) was chosen and nanoparticles (NPs) were prepared under mild conditions using ionotropic gelation method. For increased delivery efficiency, CS was chemically modified, and transferrin was covalently linked to the NP surface by azide-alkyne Huisgen cycloaddition. These NPs were fully characterized regarding physicochemical attributes such as size, zeta-potential, morphology and targeting ligand density. Further, the NPs were loaded with the model protein β-galactosidase (bGal) and their *in vitro* performance regarding targeted cellular uptake and permeability through nasal mucus and an epithelial cell layer cultured at the air-liquid-interface was compared. In order to increase reproducibility in the NP manufacturing process, a microfluidic mixing method was established for CS NP preparation. Different model compounds including siRNA, mRNA and bGal were encapsulated and release kinetics, cytotoxicity and cellular internalization was studied. Concludingly, the delivery of bGal loaded CS NPs was tested in an *in vivo* mouse model comparing intranasal and intravenous administration. Hereby, the amount of NPs and intact bGal delivered to the cerebrospinal fluid was measured 1 h after administration.

Chapter 1 of this thesis provides a general introduction briefly covering all relevant topics affecting the content of this work.

Chapter 2 describes the manufacturing of chitosan nanoparticles with the help of a microfluidic mixing system in order to establish an easily optimizable system for the encapsulation of different therapeutic molecules. Optimization of nanoparticle preparation by altering flow rates and concentrations as well as encapsulation of various macromolecules such as siRNA, mRNA and protein are described in detail.

Chapter 3 explains the possibility for surface modification of chitosan nanoparticles after particle preparation under mild conditions, so that the covalently linked targeting ligand can only be found on the nanoparticle surface and cargo is not damaged by the

chemical reaction conditions. In the presented study, transferrin is used as targeting ligand since the transferrin receptor is expressed in the nasal cavity, presenting a promising target for nose-to-brain delivery. Also, a dual targeting approach for the treatment of glioblastoma is suggested.

Chapter 4 deals with the overall potential of chitosan nanoparticles and transferrin decorated chitosan nanoparticles to act as efficient delivery systems for nose-to-brain delivery of biologics. For this purpose, both types of nanoparticles were studied regarding their physicochemical characteristics, their interaction with artificial nasal mucus and their transport through a nasal epithelial cell layer. Moreover, the ability of chitosan nanoparticles to reach the cerebrospinal fluid after intranasal administration was evaluated in an *in vivo* experiment.

Chapter 5 provides a concluding summary of the gathered findings in this work and also addresses the parameters that still need to be investigated in future studies.

Chapter II – Microfluidic mixing as platform technology for production of chitosan nanoparticles loaded with different macromolecules

1 Graphical Abstract

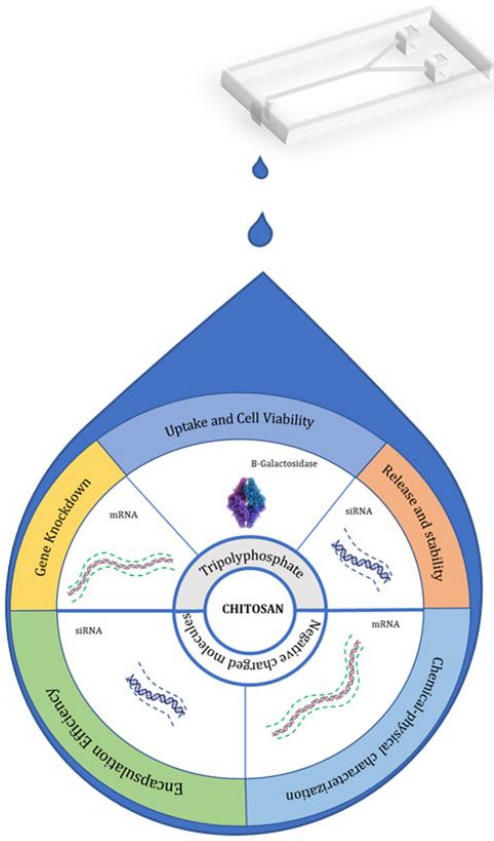

2 Abstract

In recent decades, biotechnological drugs have emerged as relevant therapeutic tools. However, therapeutic molecules can exert their activity only if properly formulated and delivered into the body. In this regard, nanosized drug delivery systems have been shown to provide protection, stability, and controlled release of payloads, increasing their therapeutic efficacy. In this work, a microfluidic mixing technique for the preparation of chitosan-based nanoparticles was established with the capability of easily exchanging macromolecular biological cargos such as the model protein β-Galactosidase, mRNA, and siRNA. The nanoparticles obtained showed hydrodynamic diameters ranging from 75 nm to 105 nm, low polydispersity of 0.15 to 0.22 and positive zeta potentials of 6 mV to 17 mV. All payloads were efficiently encapsulated (>80 %) and the well-known cytocompatibility of chitosan-based nanoparticles was confirmed. Cell culture studies demonstrated increased cellular internalization of loaded nano-formulations compared to free molecules as well as successful gene silencing with nano-formulated siRNA, suggesting the ability of these nanoparticles to escape the endosome.

3 Introduction

In recent years, the use of biotechnological drugs as therapeutic agents has become increasingly important as they have shown great therapeutic potential for a variety of diseases [257]. This class of molecules including peptides, proteins and nucleic acids offer advantages of high specificity, potency, and low toxicity compared to small molecules [258]. However, biodistribution and delivery issues impede the successful development of marketed products. Especially, the high molecular mass of biotechnological drugs presents major challenges as they are unable to passively diffuse across biological barriers. Therefore, intravenous and subcutaneous injections currently are the primary routes of administration. Besides, site-specific delivery, in particular to intracellular targets, has become a key challenge due to their poor membrane permeation. Consequently, appropriate delivery strategies are needed to successfully translate biotechnological drugs into the clinic [258, 259].

In this context, nanoparticle-based drug delivery platforms are one of the most studied

type of vehicles for overcoming pharmacokinetic limitations [260]. Combining their small size and biodegradable excipients, nanoparticles (NPs) exhibit numerous advantages such as increased bioavailability, cargo protection against premature degradation and targeted delivery [261]. There is a multitude of NPs found in the literature for the delivery of biotechnological drugs [262-265]. Polymeric NPs constituted of natural and synthetic polymers have gained interest due to their biocompatibility, biodegradability, stability, and ease of surface modification [266, 267]. Among these are chitosan (CS). CS is a polysaccharide of $\beta(1\rightarrow4)$ linked units of *N*-acetyl-D-glucosamine and D-glucosamine, which is generally obtained from the biopolymer chitin mainly found in insects, arachnids, and crustaceans[268]. Since it was first reported that CS can be used to produce NPs [269], many researchers have investigated this material in pharmaceutical studies [270-276].

Most commonly, CS NPs are prepared by bulk methods based on ionotropic gelation due to electrostatic interactions [43, 277]. Owing to its cationic character, CS readily forms NPs with an anionic counterpart such as pentasodium tripolyphosphate (TPP), thereby, encapsulating the desired cargo. Furthermore, NPs obtained from the interaction between CS and TPP (CS_{TPP} NPs) are promising for the delivery of sensitive macromolecules as they enable improved membrane permeation, controlled drug release, and cargo preservation due to the preparation under mild aqueous conditions [278]. However, when prepared by bulk mixing, CS_{TPP} NPs exhibit a high batch-to-batch variability due to the lack of control over electrostatic complexation. Additionally, the production rate is rather slow. Therefore, microfluidic mixing technique has proven to be a promising technology with the ability to overcome these drawbacks [279, 280]. In general, microfluidics can be defined as the science and technology of manipulating fluids in functional components, known as microfluidic chips, with small channels ranging from several micrometers to millimeters [281]. The biggest advantage is the accurate control over picoliter to nanoliter volumes within microscale dimension devices, thereby, allowing processes such as mixing, droplet generation and nanoprecipitation to be conducted in a particularly precise manner [282]. Microfluidic chips can be reproducibly fabricated in numerous geometrical architectures out of a variety of materials such as different polymers, glass, silicon, or paper [281]. To address current challenges in NPs formulation, microfluidic techniques were employed to prepare NPs with more controlled physical properties [283]. In a continuous flow

pattern, the local environment for particle formation can be strictly regulated leading to a reduction in batch-to-batch variability. Furthermore, scale-up is facilitated because process parameters optimized with a single microfluidic mixer device can easily be transferred to multi-mixer devices with identical geometries, increasing volume throughput and production. Especially for NPs preparation methods that are based on formation of electrostatic interactions and are, therefore, very sensitive to environmental changes such as mixing speed, droplet frequency and sample volume, microfluidic mixing leads to significantly higher reproducibility [284].

In this work, microfluidic mixing was utilized for the preparation of CS-based NPs with different macromolecules as cargo. The aim was to establish a method, that can be used as foundation for an easily optimizable and cost-effective production of CS-based NPs. This can serve as a reproducible and versatile platform to efficiently encapsulate (> 80 %) and safely deliver exchangeable hydrophilic biotechnological drugs such as proteins and nucleic acids, showing a size limit of approximately 100 nm to optimize the therapeutic activity and boost scale-up for industrial production.

4 Materials and methods

4.1 Materials

CS (5-20mPa·s, 0.5 % in 0.5 % Acetic Acid at 20 °C, 1526.464 g/mol, 85 % deacetylation degree, CAS 9012-76-4) was purchased from Tokyo Chemical Industries (4-10-1 Nihonbashi-honcho, Chuo-ku, Tokyo 103-0023). TPP, β-galactosidase (bGal) from Aspergillus oryzae, ortho-nitrophenyl-β-galactoside (ONPG), sodium acetate, sodium bicarbonate, sodium phosphate monobasic, sodium phosphate dibasic, magnesium sulfate, D-(+)-glucose, β-mercaptoethanol, acetic acid 100 %, dimethyl sulfoxide (DMSO), 3-(4,5-dimethylthiazol-2-yl)-2,5-diphenyl-2H-tetrazolium bromide (MTT), Lipofectamine™ Messenger MAX™ Reagent, Opti-MEM™, RPMI-1640 Medium, Fetal Bovine Serum (FBS), Penicillin-Streptomycin solution, Dulbecco's Phosphate Buffered Saline (PBS), trypsin-EDTA solution 0.25 %, geniticin (G418) disulfate solution, and RNase ZAP™ were obtained from Sigma-Aldrich (Taufkirchen, Germany). ATTO 647N was purchased from ATTO-TEC GmbH (Siegen, Germany). SYBR® Gold Nucleic Acid Gel Stain, AlexaFluor 488 (AF488), Lipofectamine™ 2000 transfection reagent, and HyClone trypan blue solution 0.4 % in phosphate-buffered

saline was purchased from Thermo Fisher Scientific (Hampton, NH, USA). CytoTox 96® Non-Radioactive Cytotoxicity Assay was supplied by Promega (Hilden, Germany). Scrambled siRNA
(5'-pCGUUAAUCGCGUAUAAUACGCGUat,
3'-CAGCAAUUAGCGCAUAUUAUGCGCAUAp)
were purchased from Integrated DNA Technologies (Leuven, Belgium).

4.2 mRNA Synthesis

The Cas9-2A-EGFP sequence from pSpCas9(BB)-2A-GFP (PX458) was amplified with Polymerase Chain Reaction (PCR) and purified by agarose gel extraction (QIAquick gel extraction kit from QIAGEN). Afterwards, the produced fragments were cloned to pJET1.2 blunt. The recombined plasmids were transformed into NEB 5-alpha competent *E. coli* according to the manufacturer's high efficiency transformation protocol for the NEB® 5-alpha Competent *E. coli* (C2987H/C2987I). *E. coli* were cultured on LB agarose medium plates at 37 ℃ for 24 h. Then, the bacteria clones were isolated from plates and tested by PCR, double digestion, and Sanger sequencing. Plasmids were isolated from *E. coli* culture by GenElute™ HP Plasmid Midiprep Kit. Subsequently, the plasmids were linearized by *Xba*I restriction enzyme for 4 h at 37°C and purified by GenElute™ PCR Clean-Up Kit in the next step. The Cas9-2A-EGFP mRNA was synthesized by HiScribe™ T7 High Yield RNA Synthesis Kit and capped by Vaccinia Capping System and mRNA Cap 2'-O-methyltransferase (New England Biolabs GmbH). Specifically, the linear DNA templates were incubated with T7 polymerase and NTPs at 37°C overnight. Afterwards, the products were treated by DNase I to remove the DNA templates, and then incubated with capping enzyme and cap 2'-O-methyltransferase at 37°C for 2 h. At last, the final products were purified by RNeasy Mini kit and verified by gel electrophoresis. The fluorescent mRNA, named AF405-mRNA, was produced by adding Aminoallyl-UTP-PEG5-AF405 (Jena Bioscience) to the NTPs mixture, and synthesis performed as reported above for Cas9-2A-EGFP. The fluorescence labelling efficiency was characterized by measuring the absorbance (260 nm) and the fluorescence (405 nm) followed by calculation of the dye-to-base ratio by the law of Lambert-Beer.

4.3 Chitosan nanoparticle preparation

All manufactured NP samples were prepared using the microfluidic mixing chip “Fluidic 186” (microfluidic ChipShop, Jena, Germany) with plastic connection tubing and adapters (microfluidic ChipShop, Jena, Germany) to guarantee a suitable flow. The channel dimensions of the S-shaped micromixer are 100 µm in depth and 200 µm in width. The mixing channel itself measures 217 mm in length enabling a prolonged co-flow of fluids. Two syringe pumps (LA-160, 6-Channel, RS232, Programmable from New Era Pump Systems, Inc., Farmingdale, NY, USA) and 3 mL NORM-JECT® luer-lock syringes (∅ 9.650 mm) were utilized for NP manufacturing.

CS_{TPP} NPs were prepared via ionotropic gelation method adapted from a well-established and previously published protocol [43]. Briefly, CS stock solution (1 mg/mL) was obtained by dissolving CS in 25 mM acetate buffer pH 5.0, while the bridging agent TPP was dissolved in highly purified water with a final concentration of 0.5 mg/mL.

For the preparation of CS_{TPP} NPs without cargo, CS stock solution (1 mg/mL) was diluted with acetate buffer pH 5.0 to reach the final concentration of 0.75 mg/mL; TPP stock solution (0.5 mg/mL) was diluted in highly purified water to obtain a final concentration of 0.15 mg/mL. Both solutions were injected separately into the diffusion mixer chip by setting the Total Flow Rate (TFR) to 0.50 mL/min and the Flow Rate Ratio (FRR) to 1 : 2.3, where CS was pumped at 0.15 mL/min, while TPP flow rate was 0.35 mL/min. The set parameters derive from preliminary optimization experiments reported in the Supplementary Info (**Figure S1**). For all experiments presented in this work, only two inlets of the microfluidic chip were used, while the remaining two inlets were blocked with blind plugs.

For the encapsulation of various macromolecules, manufacturing parameters were adjusted every time (**Table 2**). To obtain bGal CS_{TPP} NPs, the model protein bGal was dissolved in highly purified water at a concentration of 1 mg/mL and then diluted with TPP solution 0.15 mg/mL to attain a final concentration of 0.1 mg/mL. CS stock solution was diluted in 25 mM acetate buffer pH 5.0 to achieve a concentration of 0.75 mg/mL. TFR (0.5 mL/min) as well as the volume ratio between CS and bGal-TPP solutions (FRR 1 : 2.3) were kept constant throughout the manufacturing process. All experiments conducted to optimize the synthetic parameters for bGal CS_{TPP} NPs production are described in the supplementary info (**Figure S2**).

Table 2. Microfluidic parameters used for the CS-based NPs preparation.

Formulation	CS [mg/mL]	TPP [mg/mL]	TFR [mL/min]	FRR (Polymer : Payload)
bGal CSTPP NPs	0.75	0.15	0.5	1 : 2.3
siRNA CS NPs	0.034	-	0.5	1 : 2.3
siRNA CSTPP NPs	0.75	0.15	0.5	1 : 2.3
mRNA CS NPs	0.035	-	0.6	1 : 3
mRNA CSTPP NPs	0.96	0.05	0.6	1 : 3

For the preparation of nucleic acid loaded CS NPs, different N/P ratios, defined as the ratio between the CS amine groups (N) and the nucleic acids' phosphate groups (P), were considered.

Since siRNA is known to readily condensate with positively charged polymers [285], the preparation of NPs with and without TPP was investigated. For siRNA CS NPs production, siRNA was diluted in RNAse-free water to reach the concentration of 1 nmol/mL. Afterwards, siRNA CS NPs were prepared by examining different N/P ratios in a range from 1 to 7 (**Table S1** Supplementary info). Specifically, siRNA concentration and flow rate (FR) were kept constant at 1 nmol/mL and 0.350 mL/min,

respectively. CS flow was constant at 0.15 mL/min but the polymeric solution concentration was adjusted based on the N/P ratio to be prepared. Optimized siRNA CS NPs were produced by keeping the TFR constant at 0.5 mL/min and the FRR at 1 : 2.3 (CS 0.034 mg/mL : siRNA 1 nmol/mL) using the N/P ratio of 1.5.

The same N/P ratios (1 to 7) were tested for siRNA CS_{TPP} NPs by adding siRNA to TPP aqueous solution (0.15 mg/mL) (**Table S2** Supplementary data). This formulation was obtained by keeping the CS concentration (0.75 mg/mL) and FR (0.15 mL/min) as well as the TPP concentration (0.15 mg/mL) and FR (0.35 mL/min) constant throughout the manufacturing process. For the investigation of different N/P ratios, the amount of siRNA was modified. The best formulation was obtained at N/P ratio of 2 corresponding with the siRNA concentration of 250 pmol/mL.

Finally, CS NPs were investigated as nanoplatforms for mRNA delivery. mRNA CS NPs were obtained by taking advantage of the electrostatic complexation between the positive charges of CS and the negative charge of mRNA. Different N/P ratios in a range from 1.5 to 9 were investigated (Supplementary Data **Table S3**). Briefly, mRNA was dissolved in RNAse-free water to reach the final concentration of 0.005 mg/mL which was kept constant during the optimization process. CS was diluted in 25 mM acetate buffer pH 5.0 to achieve concentrations tailored to the N/P ratio to be prepared. Optimized mRNA CS NPs were synthesized at N/P ratio 5, with a TFR of 0.6 mL/min and FRR of 1 : 3 (CS 0.035 mg/mL : mRNA 0.005 mg/mL).

Similarly, mRNA CS_{TPP} NPs were obtained by maintaining mRNA concentration stable at 0.005 mg/mL diluted in TPP 0.05 mg/mL used as bridging agent for the NPs formulation to investigate its effect on NPs production and in cellular experiments. CS was diluted in 25 mM acetate buffer pH 5.0 to reach different concentrations according to the N/P ratio investigated ranging from 1.5 to 9 (Supplementary data **Table S4**). In detail, the concentration and the FR of mRNA-TPP solution were constant at 0.005 mg/mL and 0.45 mL/min, respectively. Concerning CS, the FR was constant at 0.15 mL/min but the concentration was tailored based on the N/P ratio to be obtained. Therefore, the optimized synthetic parameters to produce mRNA CS_{TPP} NPs were N/P 6.67, CS (0.96 mg/mL) with a FR of 0.15 mL/min, mRNA-TPP (0.005 mg/mL) FR at 0.45 mL/min, TRF 0.6 mL/min and FRR 1:3 (CS : mRNA TPP). All information related to the screening experiments is reported in the supplementary data (**Table S3** and **Table S4**).

4.4 Physicochemical characterization

4.4.1 Size and surface potential determination

Dynamic light scattering (DLS) measurements were performed to analyze hydrodynamic diameter and polydispersity index (PDI), whereas zeta potential values were obtained by laser Doppler anemometry (LDA). For DLS measurements, 100 µL of NPs suspension were added into a disposable micro-cuvette (Malvern Instruments, Malvern, UK). Sizes, as well as PDIs, were determined with a Zetasizer Nano ZS (Malvern Instruments) at 173° backscatter angle performing 15 runs three times per sample. Viscosity of 0.88 mPa·s and a refractive index of 1.33 were set for Zetasizer software data analysis. NPs were diluted with 600 µL 10 mM NaCl and transferred to a folded capillary cell (Malvern Instruments) performing three zeta potential measurements per sample using the same device.

4.4.2 Morphological characterization

The morphology and size of CS_{TPP} NPs was investigated by Atomic Force Microscope (AFM, DPN 5000, Nanoink,). The measurements were carried out by dropping 15 µL of CS NPs suspension diluted in water (1:100 v/v) onto a glass cover slip, which was dried overnight. The topography images (phase and error) were recorded in the Alternating Current (AC) imaging mode. The sizes of the NPs were determined by measuring the height of the NPs' cross-section using the software Gwyddion [286].

4.4.3 Encapsulation efficiency

Enzymatic assay

The percentage of bGal encapsulation efficiency (EE%) was determined with a modified version of an enzymatic activity assay [287, 288]. NPs were centrifuged for 1 h at 19,000 rpm and 4 °C and supernatants were used for an indirect analysis. Briefly, in a transparent 96-well plate, 50 µL of sample or of bGal standard solutions for a calibration curve were added to 116.66 µL of enzyme buffer containing 60 mM Na_2HPO_4, 60 mM NaH_2PO_4, 1 mM $MgSO_4$ and 0.27 % β-mercaptoethanol. For the

blank samples, 166.66 µL of enzyme buffer were used. The plate was equilibrated at 28 °C for 5 min in a plate reader (Tecan Group AG, Männedorf, Switzerland). Subsequently, 33.3 µL of ONPG with a concentration of 4 mg/mL in highly purified water, were added to each well. The enzymatic reaction was measured over 10 min, and the amount of encapsulated protein (EE%) was determined by the following equation:

$$EE\ [\%] = \left(1 - \frac{c_{free\ bGal}}{c_{max.\ bGal}}\right) * \mathbf{1}00\%. \quad [1]$$

where $c_{free\ bGal}$ is the measured amount of non-encapsulated bGal in the supernatant, and $c_{max.\ bGal}$ is the theoretic amount of bGal added in the experiment.

SYBR gold assay

Encapsulation efficiency of siRNA and mRNA was determined via SYBR gold assay. NP samples were manufactured with different N/P ratios, and 100 µL of each sample were added to a black 96-well plate. A calibration curve of siRNA or mRNA was obtained from standard solutions at known concentrations. Subsequently, 30 µL of 4x SYBR® Gold Nucleic Acid Gel Stain were added, and the well plate was incubated for 10 min in the dark. Measurements were conducted on a Tecan plate reader (Tecan Group AG, Männedorf, Switzerland) at an excitation wavelength of 485/20 nm and an emission wavelength of 520/20 nm. The amount of encapsulated nucleic acid (EE%) was calculated via the following equation:

$$EE\ [\%] = \left(1 - \frac{c_{free\ nucleic\ acid}}{c_{max.\ nucleic\ acid}}\right) * \mathbf{1}00\%. \quad [2]$$

Where $c_{free\ nucleic\ acid}$ is the measured amount of non-encapsulated nucleic acid, and $c_{max\ nucleic\ acid}$ is the theoretic amount of nucleic acid added in the experiment.

4.4.4 Release kinetics and stability studies

Release and stability studies of CS NPs loaded with bGal, siRNA or mRNA were conducted in two different media, namely 5 % glucose pH 7.4 or 25 mM acetate buffer

pH 5.7. Therefore, freshly prepared NPs were centrifuged on a 5 µL glycerol bed with a speed of 19,000 rpm at 4 °C for 1 h. The pellet was resuspended in the respective release media, and the tubes were incubated at 37 °C with 250 rpm shaking. At predetermined time points (0.5 h, 1 h, 2 h, 4 h, 6 h, 12 h, 24 h, 48 h, and 72 h for CS siRNA/mRNA loaded NPs with and without TPP, and 0.5 h, 1 h, 2 h, 4 h, 6 h, 12 h, and 24 h for CS bGal NPs) samples were drawn, centrifuged at 7,000 rpm and 4°C for 10 min before analysis of the supernatant. For bGal, the supernatant was analyzed with an enzymatic assay as described above. For siRNA and mRNA, SYBR Gold assay was used to examine the released amount.

4.5 Cell culture experiments

4.5.1 General culture conditions

Human epithelial lung carcinoma cell line H1299 (ATCC, Manassas, USA) was cultured in RPMI medium supplemented with 1 % penicillin/streptomycin and 10 % FBS. A modified version of this cell line expressing GFP protein, H1299-mEGFP, was cultured in RPMI-1640 medium supplemented with 2 mM L-glutamine, 10 % FBS, 1 % penicillin/streptomycin and 0.2 mg/mL geneticin (G418) [30]. The cell cultures were maintained at 37 °C in a > 95 % humidified atmosphere of 5 % CO_2 in air with media changes on alternate days. Once 80–100 % confluent, the cells were harvested with 0.25 % trypsin-EDTA and either sub-cultured in a 1:10 ratio or used for further experiments. H1299 were chosen as standard lung cell line for preliminary investigation of the NPs' biological activities.

4.5.2 Cell viability

For cell viability assessment via MTT assay, 5,000 H1299 cells per well were seeded in a 96-well plate 24 h prior to the experiment using phenol red-free RPMI-1640 medium. Cells were treated with either empty CS_{TPP} NPs and CS NPs loaded with bGal, siRNA and mRNA (with and without TPP) at different concentrations (30 µg/mL, 50 µg/mL, 100 µg/mL, 300 µg/mL, 600 µg/mL, 900 µg/mL, 1200 µg/mL) and incubated for 24 h at 37 °C, 5 % CO_2. Correspondingly, untreated cells were incubated as blank controls (− CTRL) while cells treated with 25 % of DMSO in the medium served as positive

control (+ CTRL); every sample was tested in triplicate. Subsequently, 10 µL of MTT solution with a concentration of 5 mg/mL in PBS was added to each well and incubated for 4 h at 37 °C, 5 % CO_2. Then, medium was removed and 100 µL DMSO were added to each well. The samples were incubated at room temperature in the dark for 30 min before measuring absorption at 570 nm using a Tecan plate reader (Tecan Group AG, Männedorf, Switzerland).

LDH release of treated cells was determined using the CytoTox-ONE Homogeneous Membrane Integrity Assay (Promega, Walldorf, Germany) according to the manufacturer's protocol. For this assay, 8,000 H1299 cells were seeded in a 96-well plate 24 h prior to transfection. Cells were treated with different concentrations of CS_{TPP} NPs, bGal CS_{TPP} NPs, siRNA CS_{TPP} NPs, siRNA CS NPs, mRNA CS_{TPP} NPs, mRNA CS NPs (30 µg/mL, 50 µg/mL, 100 µg/mL, 300 µg/mL, 600 µg/mL, 900 µg/mL, 1200 µg/mL) and incubated for 24 h at 37 °C, 5 % CO_2. Untreated cells were used as negative control (− CTRL) and cells treated with lysis buffer represent the positive control (+ CTRL) with complete LDH release. After 24 h of incubation, 100 µL of Cyto-Tox-ONE Reagent were added to each well, the plate was shaken shortly and incubated for 10 min. Afterwards, 50 µL of stop solution were added to each well, the plate was shaken shortly again, and fluorescence was recorded at the excitation wavelength of 560 nm and emission at 590 nm using a Tecan plate reader (Tecan Group AG, Männedorf, Switzerland).

4.5.3 Cellular uptake and transfection

H1299 cells were seeded in a 24-well plate at a density of 5×10^4 cells per well, 24 h prior to the experiment. In the next step, cells were treated with CS NPs containing the different cargos. For bGal, 60 µg were used with respect to loading efficiency. To follow the bGal CS_{TPP} NP uptake, the model protein was previously labeled with ATTO647N-NHS-ester. Briefly, 5 mg of bGal were dissolved in 1 mL PBS containing 0.2 M sodium bicarbonate solution at pH 9.0 (20:1 v/v). The mixture was incubated at room temperature in the dark for 1 h. The labeled protein was purified by gel filtration columns (Sephadex G-25 gel filtration PD 10 from GE Healthcare, Munich, Germany). NPs loaded with the labeled bGal were prepared as reported in Section "Chitosan nanoparticle preparation" and characterized as indicated in Section "Physicochemical characterization". Untreated cells were used as blank control, and every sample was

tested in triplicates. After 24 h of incubation at 37°C or 4°C, cells were washed with PBS, detached from the well plate with 0.25 % trypsin solution and transferred into 1.5 mL tubes. Afterwards, samples were centrifuged at 400 x g for 5 min. After removing the supernatant, cell pellets were washed with 500 µL of PBS. Then, cell suspensions were centrifuged and washed again before resuspension in 500 µL PBS containing 2 mM EDTA. Cellular uptake efficiency was assessed by flow cytometry using the Attune™ NxT Acoustic Focusing Cytometer (Thermo Fisher Scientific, Waltham, MA, USA). All cells were gated according to morphology based on forward/sideward scattering, and 10,000 events were evaluated per sample.

Similar experiments were performed using CS NPs containing AF488 labeled siRNA or AF405 labeled mRNA, each with and without TPP produced following the method described in Section “Chitosan nanoparticle preparation” and characterized as outlined in Section “Physicochemical characteristics”. For uptake experiments of AF488 siRNA, both siRNA CS_{TPP} NPs and siRNA CS NPs with a final siRNA concentration of 50 pmol were used. In contrast to bGal CS_{TPP} NPs experiments, wavelengths of 488 nm excitation and a 530/30 nm bandpass emission filter were used. After each measurement, the fluorescence of the samples was quenched with 1 % trypan blue and samples were remeasured. Hereby, intracellular uptake was distinguished from NPs present on the cell surface. For uptake experiments of AF405 mRNA, CS NPs with and without TPP with a final mRNA amount of 500 ng were utilized. Wavelengths of 405 nm excitation and a 421 nm bandpass emission filter were used.

4.5.4 Gene knockdown

For GFP protein knockdown, 20,000 H1299-mEGFP cells were seeded in a 24-well plate (Thermo Fisher Scientific) and incubated for 24 h. Afterwards, cells were transfected using polyplexes containing 50 pmol of either siRNA targeting GFP (siGFP) or scrambled negative control siRNA (− siRNA) and incubated in cell culture medium with or without 100 µM chloroquine (Sigma-Aldrich, Darmstadt, Germany). After 4 h, 500 µL of fresh RPMI-1640 medium were added, and cells were further incubated for 72 h. Finally, all samples were detached using trypsin, washed with PBS, and analyzed by flow cytometry as previously described.

4.6 Statistical analysis

All results are given as mean value ± standard deviation (SD). Statistical significance was investigated using one-way ANOVA and two-way ANOVA with Bonferroni's and Tukey's post hoc test. All statistical analyses were performed using GraphPad Prism version 9.2.0 for Windows (GraphPad Software, San Diego, CA, USA).

5 Results and discussion

The goal of this work was to investigate and simplify the production of CS-based NPs as versatile nanoplatforms for the delivery of different biologics using a microfluidic mixing technique. As a cationic polysaccharide, CS has the ability to gel when it interacts with polyanions such as TPP by inter- and intramolecular bonds allowing spontaneous formation of spherical and homogeneous nanosized structures regardless of the polysaccharide molecular weight [289, 290]. Due to the mild conditions, ionotropic gelation method has become the standard for the preparation of CS-based NPs, especially for the encapsulation of different macromolecules including proteins and nucleic acids [290, 291].

5.1 Nanoparticle synthesis and characterization

An essential parameter of the ionotropic gelation method for CS NPs synthesis involves an appropriate mixing between the acidic CS solution and the TPP solution. The microfluidic technique ensures a controlled mixing process of both solutions inside the microchannels warranting a precise and reproducible NP production. Moreover, this technique allows the modification of formulation parameters to manage the physicochemical properties of NPs, which are key factors for the drug delivery systems' performance. It is known that the size, size distribution, shape, and surface charge of NPs actively regulate the stability of the formulation, as well as its interaction with bioactive compounds, cellular uptake, and intracellular journey [280, 292-294]. All CS NPs investigated in this work were obtained by passive diffusion through a micromixing chip able to increase the interfacial areas and the contact time between the fluids, thereby, achieving an optimized consistent mixing process.

Preliminary experiments were performed to identify appropriate conditions for empty

CS_{TPP} NP formation, establishing suitable concentration ranges of each compound to obtain formulations with precise characteristics. CS concentrations were modified from 0.60 to 1 mg/mL, while TPP was kept constant at 0.15 mg/mL. Different polymer/crosslinker ratios were tested. Once the optimal concentration of CS was identified, different flow rates were tested to identify the best synthetic parameters. All preliminary results are reported in the supplementary data (**Figure S1**).

The best outcomes were obtained by setting the TFR to 0.5 mL/min and the FRR to 1 : 2.3 (CS : TPP) as stated in Section "Chitosan nanoparticle preparation". With these parameters, a NP mean diameter of 70.94 ± 0.39 nm with a PDI of 0.13 ± 0.01 and a surface charge of +14.38 ± 1.42 mV was obtained. Morphological analysis by AFM indicated that CS_{TPP} NPs exhibited a homogenous spherical shape and a smooth surface as expected for ionotropic gelation methodology (**Figure 8**). The images were recorded in the AC imaging mode in which the cantilever together with the AFM probe oscillates near its resonance frequency. The interaction between the AFM probe and the sample leads to a change of the amplitude of the oscillation. This change was detected and modulated with the feedback control unit to generate the height information on the topography image.

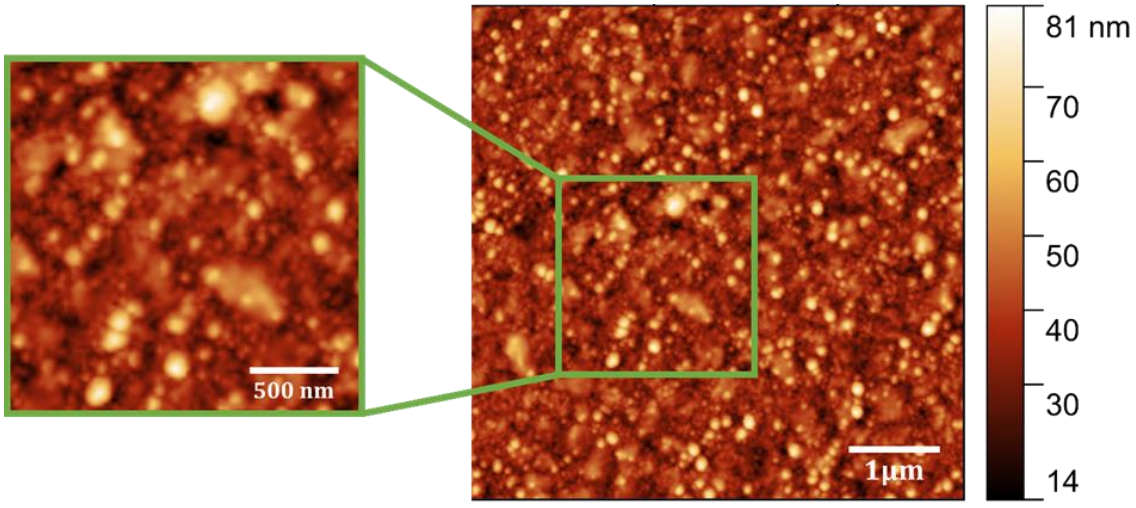

Figure 8. AFM topography image of empty CSTPP NPs with an image size of 5 µm × 5 µm. The scale bar on the right side indicates the height (nm). The green square outlines the image magnification 2 µm × 2 µm, scale bar set to 500 nm, for better analysis of NPs morphology.

The AFM probe contributes to the horizontal radius of the NPs on the images. Therefore, only the height was considered for the NPs' size evaluation. The height of NPs is distributed between 40 nm and 60 nm with the mean value of 50 nm. The smaller, but not statistically significant (*p value* 0.068), size of the NPs with respect to results obtained by DLS was attributed to the fact that DLS measures hydrodynamic diameters rather than actual sizes. Furthermore, samples are dried overnight, hence, shrinkage of NPs due to drying also contributes to the fact that smaller size values are obtained.

Based on the results obtained with empty CS_{TPP} NPs, a formulation containing the model protein bGal was developed. Proteins are known to be powerful therapeutic agents in medicine but, at the same time, their formulation is extremely complicated due to their sensitivity to chemical and physical changes [280, 293-295]. bGal was included in the TPP aqueous solution, testing four different bGal concentrations: 0.10 mg/mL, 0.15 mg/mL, 0.20 mg/mL, and 0.25 mg/mL (Supplementary data **Figure S2**). The best nanosized formulation was obtained with 0.10 mg/mL (applying the same synthesis parameters as for CS_{TPP} NPs) with a mean size of 77.80 ± 0.01 nm, a narrow distribution (PDI: 0.18 ± 0.01) and a positive surface charge (+16.90 ± 0.53 mV) (**Figure 9**). These outcomes corroborate that microfluidics-assisted ionotropic gelation represents an adequate method for protein formulation [290-293].

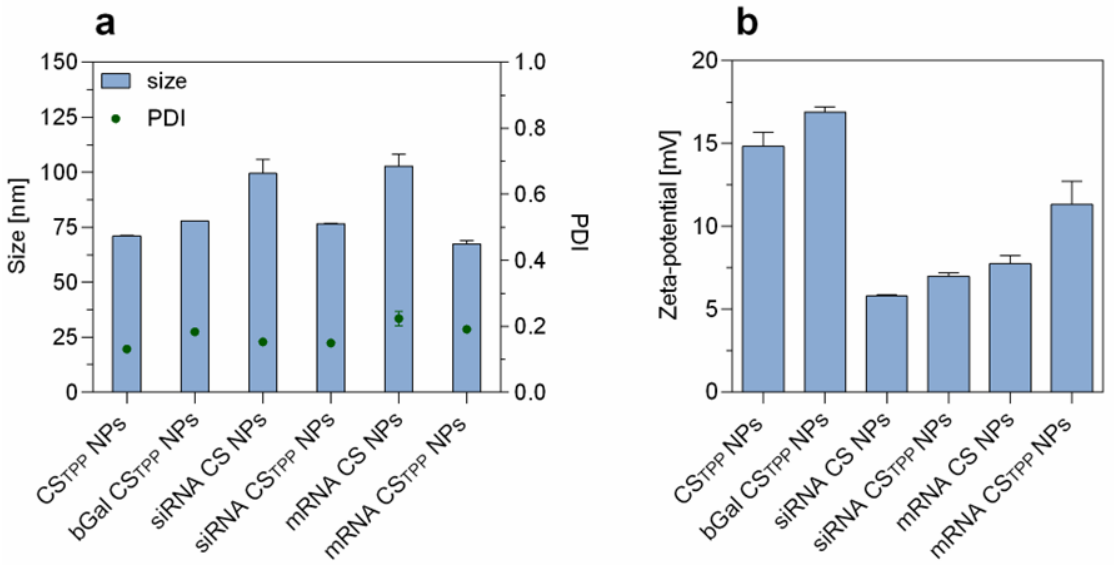

Figure 9. Physicochemical characterization results of CS-based NPs. (a) Hydrodynamic diameters (left y-axis), polydispersity indices (PDI, right y-axis) and (b)

zeta potentials of CSTPP NPs, bGal CSTPP NPs, siRNA CS NPs, siRNA CSTPP NPs, mRNA CS NPs, and mRNA CSTPP NPs all obtained by microfluidic technique. The outcomes represent mean ± SD, n = 3 independent batches.

Moreover, as suggested by different accounts in literature, CS-based NPs obtained by ionotropic gelation are valuable systems for the delivery of nucleic acids because of their good stability and enhanced and controlled gene transfection efficiency [290, 296-298]. Nucleic acids are recognized as powerful and versatile therapeutic tools for the treatment of a wide range of incurable or difficult to treat diseases [299]. However, nucleic acids are prone to rapid degradation by nucleases, and their formulation represents a major challenge [285, 299-301]. With this purpose, the formulation of model siRNA and model mRNA were studied aiming to test efficacy and versatility of CS-based NPs. The purpose was to exploit CS' capability to electrostatically interact with the phosphate group of siRNA and mRNA while investigating the structural and biological role of TPP.

In order to identify the optimal amount of polymers and siRNA, NPs at various N/P ratios were produced. Results are reported in **Table S1** of the supplementary data. The best siRNA CS NPs batch was obtained at N/P 1.5 yielding a mean diameter of 99.48 ± 9.89 nm, PDI of 0.15 ± 0.01, and zeta potential of +5.81 ± 0.77 mV (**Figure 9**). Regarding siRNA CS_{TPP} NPs, best results were detected at N/P 2 with a mean size of 77.64 ± 0.43 nm, PDI of 0.15 ± 0.001 and zeta potential of +6.99 ± 0.36 mV (**Table S2** of supplementary data).

For the mRNA (obtained as reported in section "mRNA synthesis", molecular weight of 1.7 x 10^6 g/mol), similar experiments for encapsulation in CS NPs were performed. Among all the results obtained (reported in **Table S3** and **Table S4** of supplementary data), mRNA CS NPs with N/P 5 (mean diameter: 104.72 ± 8.82 nm; PDI: 0.22 ± 0.05; zeta potential: +7.70 ± 1.12 mV) (**Figure 9**) and mRNA CS_{TPP} NPs with N/P 6.67 (mean diameter: 67.51 ± 3.34 nm; PDI: 0.19 ± 0.02 zeta potential: +11.33 ± 3.37 mV) (**Figure 9**) were chosen. To the best of our knowledge, for the first time, the impact of TPP on the physicochemical characteristics of mRNA-loaded CS NPs was investigated in this work. As widely known, TPP is a non-toxic polyanionic non-covalent crosslinker able to assist the formation of stable and homogeneous CS-based NPs [290-294]. The hydrodynamic diameter of NPs formed by CS and siRNA/mRNA, in the presence or

absence of TPP, discloses that TPP clearly had a strong impact on the NPs' size. Indeed, the results show that TPP is able to decrease the NPs mean size, in line with the scientific literature [296].

All CS-based formulations were close to or smaller than 100 nm, a very important feature in nanosized drug delivery systems field. NPs with a diameter bigger than 100 nm are susceptible to phagocytosis in the reticuloendothelial system [302, 303] while they are readily secreted by the kidneys at sizes smaller than 10 nm [302-305]. Therefore, NPs in the range size of 10-100 nm are ideal candidates to minimize clearance from the body. Accordingly, NPs within this size range have the capability to target many organs and overcome several physiological barriers [306]. Based on this knowledge, the NPs obtained in this work bear potential to deliver drugs to different parts of the body, therefore, increasing their versatility.

5.2 Biotechnological drug loading in CS-based NPs

To achieve the delivery of biotechnological drugs to a specific target, a successful approach is their efficient encapsulation in nanosized drug delivery systems [285]. As a general rule, ionic interactions between polymers and payload are broadly exploited to enhance NP drug loading [293]. The bGal amount encapsulated into CS_{TPP} NPs was evaluated by an enzymatic assay (Section "enzymatic assay") able to selectively detect the intact protein. The bGal CS_{TPP} NPs exhibited an EE of 89.86 ± 4.30 % corresponding to 157.3 ± 0.01 µg of bGal per batch (**Table 3**). Regardless of TPP use, both the model siRNA and mRNA showed satisfactory EE. SYBR Gold assays detected for siRNA CS NPs an EE of 98.14 ± 0.03 % corresponding to 1.78 ± 0.001 nmol in one batch. siRNA CS_{TPP} NPs showed a satisfactory EE of 99.19 ± 0.042 % (434 ± 1.28 pmol per batch) (**Table 3**). The different siRNA amounts encapsulated in the NPs with and without TPP derive from the intention to study the maximum capability of CS-based NPs to load siRNA and investigate the effect on the formulation's physicochemical features.

Table 3. EE (%) and loaded content of the CS-based NPs.

Formulation	EE (%)	Loaded content (µg per batch)
bGal CSTPP NPs	89.86 ± 4.30	157.3 ± 0.01
siRNA CS NPs	98.14 ± 0.03	29.98 ± 0.001
siRNA CSTPP NPs	99.19 ± 0.042	7.31 ± 1.28
mRNA CS NPs	94.72 ± 8.05	7.87 ± 0.09
mRNA CSTPP NPs	93.91 ± 0.19	7 ± 0.06

Similar results were obtained with the mRNA formulation, which showed an EE of 94.72 ± 8.05 % (7.87 ± 0.09 µg per batch) while for mRNA CS_{TPP} NPs the payload encapsulation was quantified as 93.91 ± 0.19 % (7 ± 0.06 µg per batch) (**Table 3**). The high EE results for all formulations can be attributed to the microfluidic technique known to improve the physicochemical characteristics of nanosized formulations [280, 293, 294].

5.3 β-Galactosidase release study

Protection of the payload and its controlled release are valuable parameters to evaluate the potential efficiency of CS-based formulations [285, 301]. In particular, the drug release from polymeric NPs depends on several factors such as the drug diffusion through the polymeric matrix wall, polymer erosion process or drug deposition on the NPs surface [267, 307, 308]. To explore the feasibility of CS NPs as drug delivery systems for therapeutic proteins, an *in vitro* release study of bGal CS_{TPP} NPs was performed using two different media, namely 5 % glucose pH 7.4 or 25 mM acetate

buffer pH 5.7 to simulate physiologic and the late endosomal compartment conditions, respectively. During the development of nanosized formulations, the investigation of NPs' behavior under simulated endosomal conditions is crucial. Endosomes are vesicular structures which typically entrap the nanosized drug delivery systems after endocytosis [309]. These intracellular vesicles are subject to a ripening process which includes acidification [309, 310]. In this regard, endosomes can merge with lysosomes, a subcellular compartment known for the enzymatic degradation of their content. Therefore, the endosomal entrapment of drug delivery systems could result in a loss of integrity and function. This represents a major hurdle for drug delivery which needs to be overcome by formulation design. NPs' physiochemical features can regulate and promote the endosomal escape to protect the payload from degradation [292, 311, 312]. **Figure 10** reports bGal release, monitored for 24 h, in the selected media. bGal CS_{TPP} NPs released all cargo within 6 h in 25 mM acetate buffer pH 5.7, and within 12 h when incubated in 5 % glucose pH 7.4. The faster bGal release in the acidic media can potentially be attributed to CS solubilization, decreasing NPs size and stability, therefore, allowing a faster protein release.

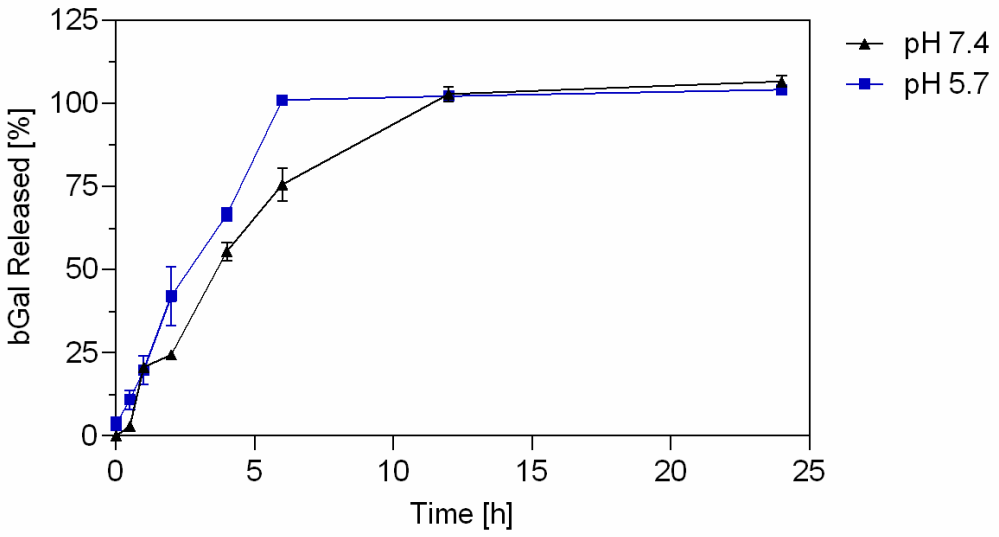

Figure 10. bGal *in vitro* release profiles form CS NPs in acetate buffer 25 mM pH 5.7 (blue line) and glucose 5 % pH 7.4 (black line) for 24 h at 37°C, to simulate the

endosomal and systemic physiologic environment respectively. The results represent the mean normalized bGal release values ± SD; n = 3 independent batches.

Figure 11 shows the stability of bGal CS_{TPP} NPs in terms of hydrodynamic diameter and polydispersity over the release period of 24 h. It is evident that the NP stability decreases faster in acidic environment compared to physiologic conditions. This is attributed to the increased solubility of CS in acidic medium. In general, stability of bGal CS_{TPP} NPs needs to be optimized as bGal was released in less than 10 h, questioning the suitability of CS NPs for intravenous drug delivery since this is associated with longer systemic circulation times. For obtaining prolonged release kinetics, one possibility is chemical modification or coating of CS NPs [257]. However, for some routes of administration such as nose-to-brain delivery, where NPs can reach the brain tissue already after 60 min, CS NPs can be favorable drug delivery systems, particularly for macromolecules such as proteins [258, 259].

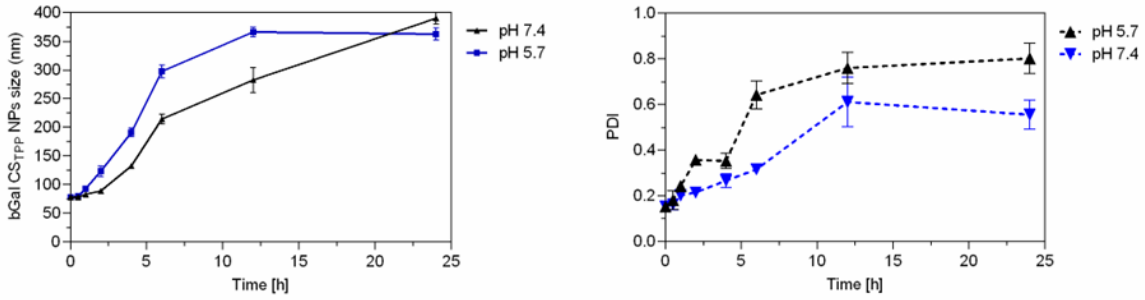

Figure 11. Stability of bGal CSTPP NPs over 24 h at physiologic and acidic pH. Left: Hydrodynamic diameters of bGal CSTPP NPs over time at pH 7.4 and pH 5.7. Right: Polydispersity Indices (PDIs) of bGal CSTPP NPs over time at pH 7.4 and pH 5.7. The results represent the mean values ± SD; n = 3 independent batches.

5.4 Stability studies

The stability of nucleic acid loaded CS NPs was evaluated by incubating the nanocarriers for specific periods of time at 37°C in 5 % glucose pH 7.4 or acetate buffer

25 mM pH 5.7, and detecting the payload released. In acidic conditions (pH 5.7), all NPs displayed acceptable stability, releasing less than 50 % of mRNA and siRNA over 72 h. Specifically, after 72 h of incubation mRNA CS NPs and mRNA CS_{TPP} NPs released 46.63 ± 0.07 % and 44.13 ± 0.92 % of mRNA, respectively. Thus, a similar behavior was observed for both mRNA formulations. For siRNA in acidic condition, a release of 7.70 ± 1.26 % for siRNA CS NPs was observed, while for siRNA CS_{TPP} NPs after 72 h of incubation the release was 30.03 ± 0.63 %. However, these values are obtained from the amount of released siRNA with respect to the encapsulation efficiency. The absolute amounts of siRNA released after 72 h of incubation from siRNA CS NPs and siRNA CS_{TPP} NPs resulted to be 137 pmol and 130 pmol, respectively. This behavior could be related to the lower negative charge density of TPP in acidic pH, therefore destabilizing the NPs [313, 314] confirming the NP behavior observed here (**Figure 12a**). At physiological conditions (glucose 5 % pH 7.4), the formulations were more stable than under acidic conditions. After 72 h of incubation, mRNA CS NPs and mRNA CS_{TPP} NPs released 37.40 ± 1.99 % and 39.88 ± 0.79 %, respectively. Noteworthy, siRNA CS NPs and siRNA CS_{TPP} NPs were stable under physiological conditions with 1.01 ± 0.18 % and 9.03 ± 0.39 % of siRNA released, respectively (**Figure 12b**). In general, these outcomes confirm the known stability of CS NPs [290, 296, 315]. Moreover, nucleic acid loaded CS NPs was evaluated by incubating the nanocarriers for 24 h at 37 °C in 5 % glucose pH 7.4 or acetate buffer 25 mM pH 5.7, and detecting the size and PDI; results confirm again the stability of CS NPs (**Figure S3** and **Figure S4** of the supplementary data).

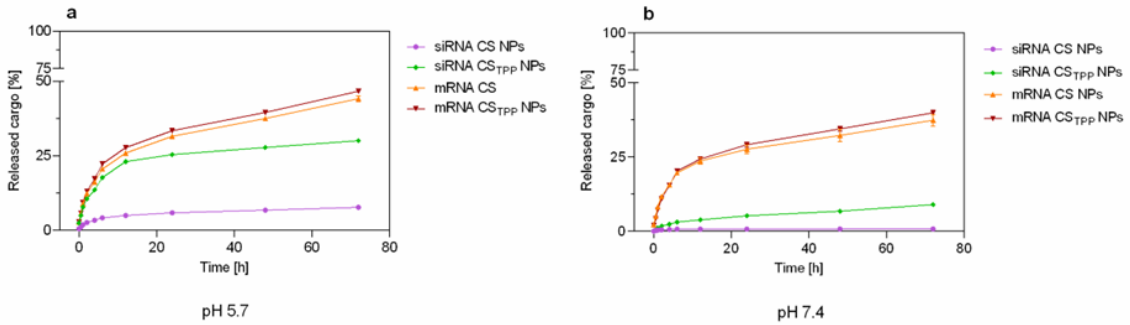

Figure 12. Stability profiles of siRNA CS NPs (violet line), siRNA CSTPP NPs (green line), mRNA CS NPs (orange line), and mRNA CSTPP NPs (red line) in (a) acetate buffer 25 mM pH 5.7 and (b) glucose 5 % pH 7.4 for 72 h at 37°C simulating the

endosomal and physiologic environment, respectively. The results represent the mean normalized absorbance values ± SD; n = 3 independent batches.

5.5 Cell viability

CS is widely recognized to be a biodegradable and biocompatible polymer exhibiting ideal characteristics to produce safe nanocarriers [316-318]. Nevertheless, one of the major drawbacks of cationic drug delivery systems is the cytotoxicity due to strong interaction with the negatively charged cell membrane bearing the risk for a potential loss of integrity [285, 319]. Therefore, cytotoxicity of all formulations was studied via MTT assay and LDH assay. NPs were tested at concentrations ranging from 30 - 1200 µg/mL after 24 h of incubation. The percentage of cellular viability was calculated in comparison to untreated cells. **Figure 13** reports that for all tested formulations the cell viability percentages, based on cellular metabolic activity, never dropped to 50 % (all the IC_{50} values were calculated and reported in **Figure S5** of the supplementary data). In more detail, at a concentration range of 30 - 100 µg/mL, cell viability was higher than 80 %. Testing a concentration of 300 µg/mL, a slight cytotoxic effect was detected for bGal CS_{TPP} NPs. In this regard, the superior cytotoxic profile of the bGal CS_{TPP} NPs compared to the other formulations studied here could be related to the highest positive surface charge (+16.90 ± 0.53 mV) which increases the electrostatic interactions with the cell membrane resulting in a greater endocytic uptake [285, 319]. With the exception of the siRNA CS NPs and siRNA CS_{TPP} NPs, all the formulations tested at the concentration of 600 µg/mL resulted in cell viability lower than 80 %. Finally, all the formulations studied at the concentration 900 - 1200 µg/mL showed a clear impact on the cellular metabolic activity registering a viability from 78 to 56 % respect the untreated cells (– CRTL).

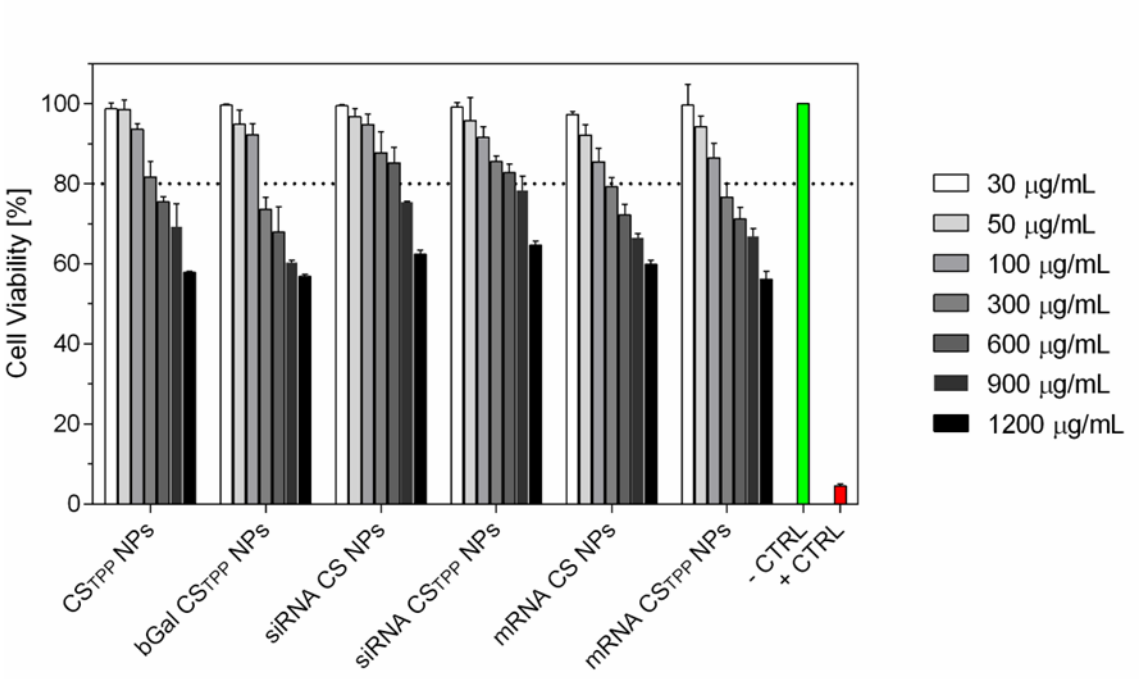

Figure 13. Cell viability outcomes obtained analyzing the cellular metabolic activity by MTT assay. The CS-based NPs concentrations tested were in the range of 30 – 1200 µg/mL. Results are shown as mean ± SD as percentage of viable cells in comparison to untreated cells (– CTRL) representing 100 % viability, n = 3.

For a complete overview of the effect of CS-based NPs on H1299 cellular membrane integrity, LDH assays were carried out applying the same conditions as used for MTT assays. The percentage of released LDH was obtained from the comparison with a positive control (+ CTRL) (100 % LDH release) for each formulation. For all tested formulations, LDH increased with concentration and exceeded 25 % of LDH release at concentrations between 300 and 900 µg/mL (**Figure 7**). These results corroborate the observations from the MTT assays. In conclusion, these findings confirm the well-known biocompatibility of CS-based NPs [315]. For further experiments, the NP concentrations used were within the range of cytocompatibility.

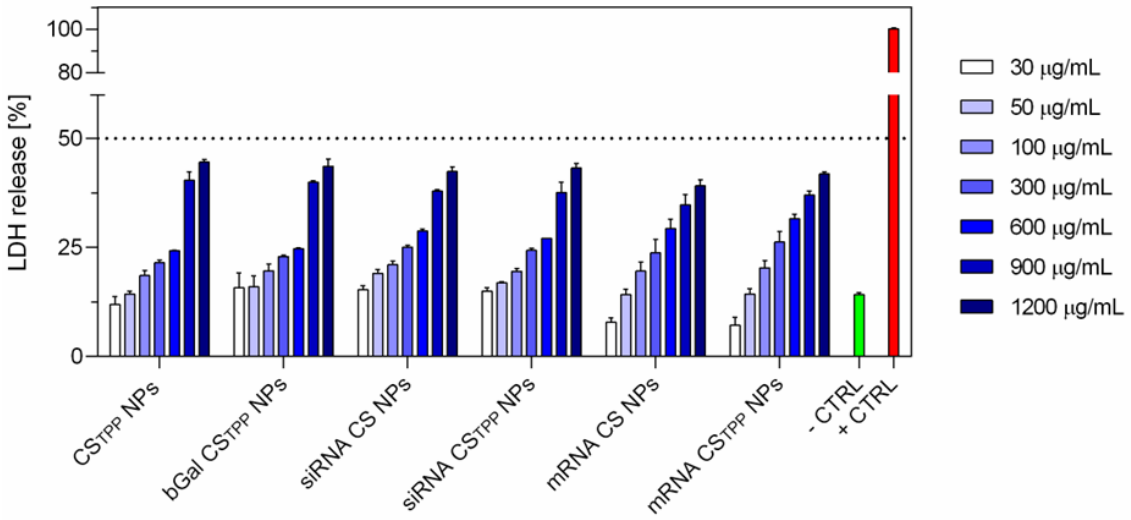

Figure 14. Cell membrane integrity was studied by LDH assay testing different CS-based NPs (30 – 1200 µg/mL). Results are shown as mean ± SD as percentage of LDH release in comparison to cells treated with lysis buffer (+ CTRL) representing 100 % LDH release; − CTRL represent untreated cells (n = 3).

5.6 Cellular uptake and gene knockdown

Cellular uptake of CS NPs with different cargos was evaluated by flow cytometry. In this study the NPs investigated were loaded with a labeled payload to allow their detection by flow cytometry. All NPs showed physicochemical features identical to the corresponding non-labeled formulations (results reported in section “Nanoparticle synthesis and characterization”). As illustrated in **Figure 15a**, which displays the MFI of ATTO647N-labeled bGal, internalization of the protein significantly increased after encapsulation into NPs. While free protein is also taken up into the cells, these results are not significantly different from untreated cells, and the recorded fluorescence intensity of cells treated with encapsulated protein is more than 10-fold higher compared to samples incubated with free protein. Among all tested CS NPs and cargo combinations, bGal CS_{TPP} NPs exhibited the highest zeta potential values (**Figure 9b**). Therefore, the interaction between the positively charged NPs and the negatively charged cell surface is rather strong, leading to fast cell surface saturation with CS

NPs. Hence, the overall uptake process is slowed down by this interaction. Although it is known that CS NP internalization is mediated by different endocytic pathways involving clathrin- and caveolae-mediated endocytosis as well as micropinocytosis [320, 321], it is hypothesized that after 24 h only a distinct amount of NPs is internalized into the cells while the rest still adheres to the cell surface due to strong interactions. Hence, in this particular case a lower NP dose could be enough to achieve a therapeutic effect. However, these hypotheses need to be confirmed in future experiments.

Figure 15b shows cellular uptake of siRNA loaded CS NPs with and without TPP. As expected, free siRNA was not internalized into H1299 cells, whereas all tested types of siRNA CS-based NPs improved the uptake efficiency significantly. Furthermore, NPs without TPP performed better (p value ≤ 0.05) than the ones containing the bridging agent, although simple siRNA CS NPs exhibited larger hydrodynamic diameters and no significant difference in zeta potential between the two formulations was observed (**Figure 9**). However, as demonstrated in **Figure 12**, siRNA CS NPs revealed increased stability in both 5 % glucose pH 7.4 and acetate buffer pH 5.7 compared to CS_{TPP} NPs. This discrepancy in stability might lead to a premature release of siRNA in culture medium and, thus, a decreased cellular uptake of CS_{TPP} NPs. After confirming the internalization of siRNA-loaded NPs, the degree of gene silencing in EGFP-expressing H1299 cells was evaluated using anti-EGFP siRNA (siGFP), non-targeting siRNA as negative control (− siRNA CS NPs) and commercially available lipofectamine (LP) as gold standard for transfections. Results are presented in **Figure 15d** and given as percentage referring to untreated cells as 100 %. Neither free siGFP, nor − siRNA CS NPs achieved a silencing effect, whereas treatment with both siRNA CS NPs with and without TPP resulted in significant gene knockdown.

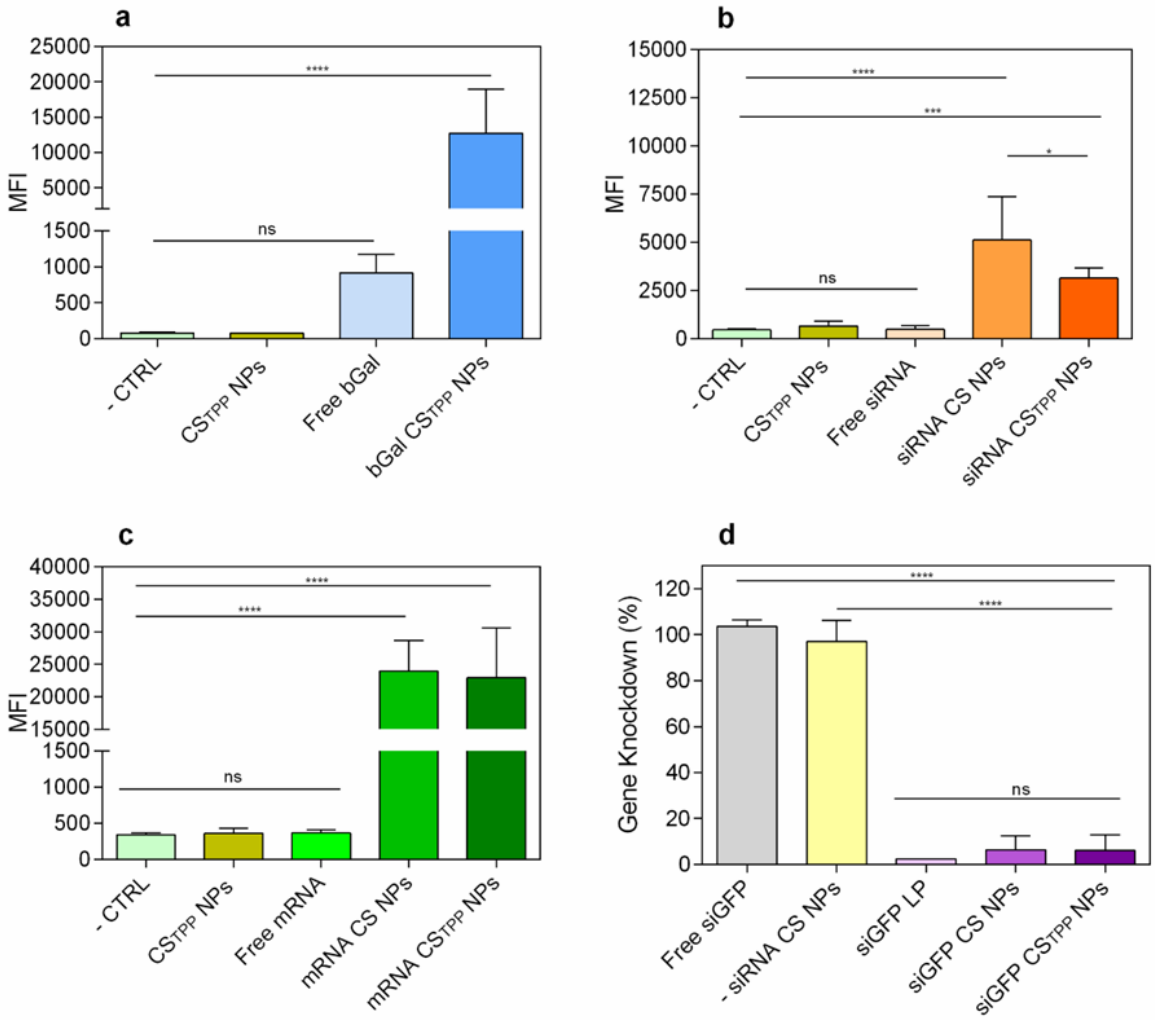

Figure 15. Cellular uptake of CS-based NPs and gene silencing of nucleic acid-loaded CS NPs in H1299 cells. (a) Cellular uptake study of free bGal and bGal CS_{TPP} NPs (60 µg of free protein and encapsulated protein were studied); (b) Cellular uptake study of free siRNA, siRNA CS NPs, and siRNA CS_{TPP} NPs (50 pmol of free and encapsulated siGFP were used); (c) Cellular uptake study of free EGFP-encoding mRNA, mRNA CS NPs, and mRNA CS_{TPP} NPs (500 ng of free and encapsulated fluorescent AF405-mRNA were studied). In all cellular uptake studies – CTRL represents the untreated cells. (d) eGFP knockdown mediated by siGFP CS NPs or siGFP CS_{TPP} NPs was studied in comparison to Lipofectamine lipoplexes (siGFP LP), free siGFP and – siRNA CS NPs as control (50 pmol siGFP free or encapsulated). The statistical analysis was performed by one-way ANOVA with Tukey's test. * p value <

0.05; *** p value < 0.005; **** p value < 0.0001. All the results are mean values ± SD of three independent experiments.

Results of mRNA CS NPs are displayed in **Figure 15c**. A fluorescent mRNA was used to evaluate cellular internalization into H1299 cells after 24 h. Empty NPs as well as free mRNA showed no cellular uptake compared to untreated cells. From these results it can already be concluded that a suitable delivery system is needed for successful intracellular mRNA delivery as already stated in literature [322, 323]. Encapsulation into CS NPs generally led to an increase in cellular internalization (**Figure 15c**). Surprisingly, there was no significant difference between NPs with and without TPP in the formulation, although NPs without TPP exhibited bigger sizes and lower zeta potential values compared to NPs containing TPP. Since uptake of CS NPs can be mediated by different pathways, similar results can be obtained with mRNA CS NPs independent of their size.
Overall, these results demonstrate the suitability of CS NPs produced via microfluidic mixing to serve as a formulation platform for different types of biological macromolecules. Values from cellular uptake and gene knockdown are in good correspondence with results of CS NPs found in literature [321, 324, 325].

6 Conclusion

Biotechnological drugs are recognized as novel therapeutic molecules with interesting biological properties for therapeutic applications. In this work, the versatility of a CS nanoplatform was investigated for the delivery of protein, siRNA, and mRNA. By exploiting the microfluidic technique, homogeneous and stable CS-based NPs were obtained. All payloads were efficiently encapsulated, and the results confirmed the nanoplatform's power to control protein and RNA release as well as to protect nucleic acids from degradation. The well-known cytocompatibility of CS-based NPs was confirmed. Cellular uptake studies showed an enhanced internalization of the nano-formulations with respect to the free molecules providing successful gene knockdown. In conclusion, this study demonstrated the eligibility of CS-based NPs produced via microfluidic mixing as versatile, affordable, and efficient nanosized platform for delivery of biological macromolecules.

Chapter III – Transferrin-modified chitosan nanoparticles for targeted nose-to-brain delivery of proteins

1 Graphical Abstract

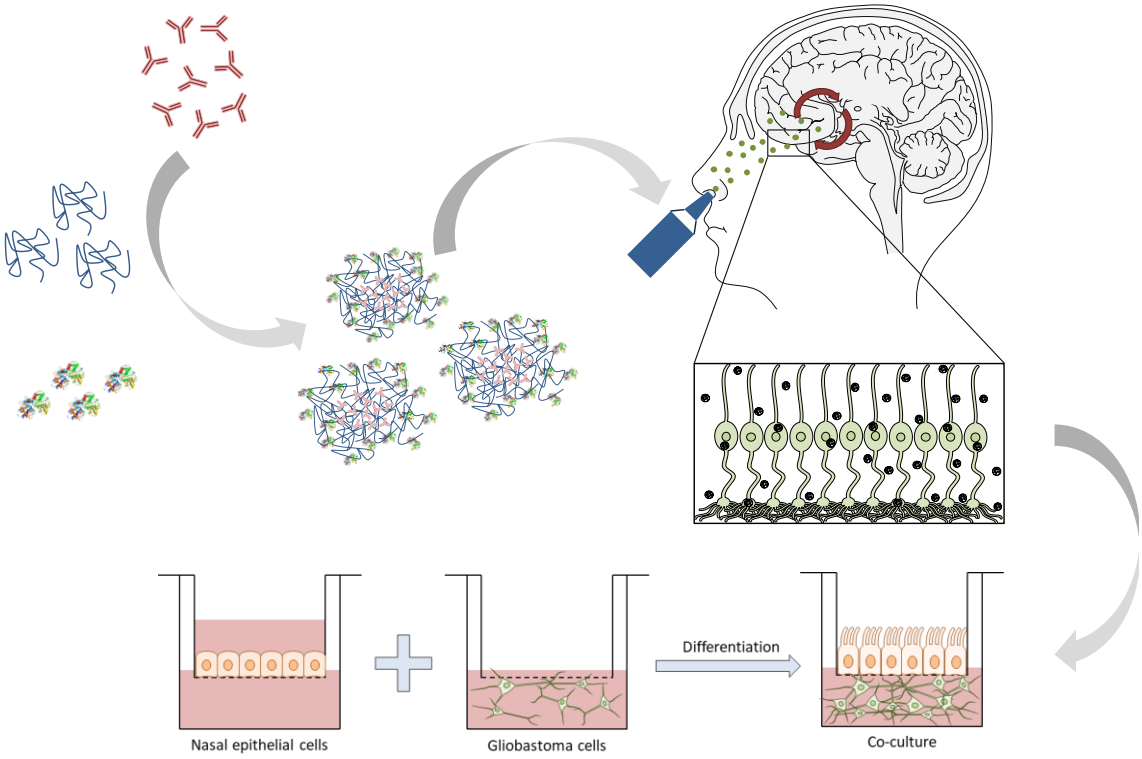

2 Key words

Chitosan nanoparticles; Transferrin receptor; Nose-to-brain; Brain delivery; Glioblastoma

3 Abstract

Nose-to-brain delivery presents a promising alternative route compared to classical blood–brain barrier passage, especially for the delivery of high molecular weight drugs. In general, macromolecules are rapidly degraded in physiological environment. Therefore, nanoparticulate systems can be used to protect biomolecules from premature degradation. Furthermore, targeting ligands on the surface of nanoparticles are able to improve bioavailability by enhancing cellular uptake due to specific binding and longer residence time. In this work, transferrin-decorated chitosan nanoparticles are used to evaluate the passage of a model protein through the nasal epithelial barrier *in vitro*. It was demonstrated that strain-promoted azide–alkyne cycloaddition reaction can be utilized to attach a functional group to both transferrin and chitosan enabling a rapid covalent surface-conjugation under mild reaction conditions after chitosan nanoparticle preparation. The intactness of transferrin and its binding efficiency were confirmed via SDS-PAGE and SPR measurements. Resulting transferrin-decorated nanoparticles exhibited a size of about 110–150 nm with a positive surface potential. Nanoparticles with the highest amount of surface bound targeting ligand also displayed the highest cellular uptake into a human nasal epithelial cell line (RPMI 2650). In an air–liquid interface co-culture model with glioblastoma cells (U87), transferrin-decorated nanoparticles showed a faster passage through the epithelial cell layer as well as increased cellular uptake into glioblastoma cells. These findings demonstrate the beneficial characteristics of a specific targeting ligand. With this chemical and technological formulation concept, a variety of targeting ligands can be attached to the surface after nanoparticle formation while maintaining cargo integrity.

4 Introduction

Diseases of the central nervous system (CNS) such as Parkinson’s, Alzheimer’s and brain cancer present a major health burden worldwide. A study from 2017 found that neurological disorders are the third most common cause of premature death and disability in the EU with prevalence being likely to increase due to the progressive ageing of the European population [1]. Adequate treatments for CNS disorders are challenging to develop regarding different aspects. The major obstacle for administered

drugs is transit through the blood-brain-barrier (BBB) or the blood-cerebrospinal fluid barrier (BCSFB) to reach the brain tissue [8]. Macromolecules such as proteins or nucleic acids, which represent an increasing fraction in the therapeutic landscape, are particularly limited in their ability to cross the BBB [326]. Although a variety of technological approaches have been investigated over the last decades trying to facilitate macromolecular drug transport into the brain, such accomplishments remained elusive [327-329]. Nose-to-brain (NtB) delivery presents an alternative route to reach the brain and, thus, gaining increasing interest over the past years. The advantages include non-invasiveness and rapid onset of action due to highly vascularized nasal mucosa. Furthermore, NtB is a direct route avoiding first-pass-metabolism and circumventing the BBB [330]. It has been reported that drugs deposited on the olfactory region inside the nasal cavity can be delivered directly to brain tissue via olfactory or trigeminal nerve endings [331]. In particular, Reger et al. demonstrated the verbal memory improvement of Alzheimer disease patients after intranasally administering insulin without systemic side effects [332]. However, NtB delivery also has its limitations, especially for macromolecules sensitive to rapid degradation. When administered intranasally, many substances undergo fast elimination by enzymatic degradation, mucociliary clearance and drainage to the lower part of the pharynx [21].In this context, nanotechnology emerged to be a promising strategy for NtB delivery enhancement of therapeutic biomolecules [333, 334]. The cargo is protected against degrading effects of extracellular enzymes, and membrane efflux pumps may be bypassed [334]. Consequently, drug transport can be improved significantly after intranasal administration compared to administration of free drug [335, 336]. Further, nanoparticle characteristics can be adjusted towards increased adherence to the mucus-covered epithelial cell layer promoting transport through tissue [273]. Chitosan nanoparticles (CS NPs) are one of these formulations, which are very attractive for NtB delivery due to chitosan's biocompatibility, biodegradability and mucoadhesion [37, 337]. In general, chitosan is the principal derivative of chitin, a structural component of the exoskeleton of crustacea and insects, and is usually obtained by alkaline deacetylation [338]. Its sugar backbone is constituted of β-1,4-linked glucosamine with a low degree of *N*-acetylation. The cationic character together with the presence of reactive functional groups make chitosan a very attractive polymer to use in controlled-release technologies [339-342]. CS NPs are already well

established and can be prepared under mild conditions, e.g. via ionotropic gelation with a bridging agent in aqueous conditions [43]. Although, until now, chitosan nanoparticles have mostly been used for NtB delivery of small molecules, aforementioned advantages make them particularly suitable for sensitive cargos such as proteins or nucleic acids [343, 344].

In general, substances administered intranasally can be transported to the CNS via different pathways, namely via intracellular, paracellular and transcellular mechanisms [345]. In the intracellular or transcellular olfactory nerve pathway, the substance is taken up by pinocytosis and endocytosis into the olfactory sensory neurons and transported alongside the axon to the olfactory bulb [12]. From there, the molecules can disperse throughout the brain. In the olfactory epithelium pathway, the substance is absorbed into the lamina propria before entering the CNS through the gaps surrounding the olfactory nerve tract [346, 347]. Substances can also be absorbed by lymphatic vessels or local blood vessels. However, most molecules are translocated through the perineural space via bulk flow to the subarachnoid space from the brain [12].

However, the olfactory region accounts for only about 5-10% of the total surface area inside the human nasal cavity [27, 348, 349]. The remaining area is covered by respiratory epithelia. Since olfactory nerves can only be found in the olfactory region, this is the main target site for NtB formulations. Because of the small and hard-to-reach target area located at the upper end of the nasal cavity, several targeting moieties have been studied to enhance the efficacy and specificity of NtB delivery, such as different lectins [336, 350, 351], lactoferrin [352-354] or cell-penetrating peptides [355-357]. Among these, lactoferrin is one of the most frequently used targeting moieties incorporated on the nanoparticle surface due to high expression levels of the lactoferrin receptor in neurons and brain endothelial cells [358]. Surface modification of PEG-PCL nanoparticles with lactoferrin led to an enhanced accumulation in the brain compared to non-modified nanoparticles according to an *in vivo* fluorescence imaging study by Liu et al. [352]. In this study, transferrin (Tf) was utilized as targeting ligand. On the one hand, the transferrin receptor is known to be expressed in human nasal cavity and, thus, it represents a promising targeting ligand [359, 360]. On the other hand, proliferating cells and cells that have undergone malignant transformation, such as in glioblastoma multiforme, show an overexpression of transferrin receptor to regulate the amount of iron for metabolic needs. Therefore, a dual targeting effect can be achieved

when using transferrin as surface ligand on nanoparticles [361, 362]. In general, transferrin belongs to the same protein family as lactoferrin and is an iron-binding glycoprotein of about 80 kDa, which is involved in cellular iron acquisition [363]. Cells recognize Tf via receptor-mediated endocytosis, while only the holo-form (diferric Tf with two binding sites occupied) and not the apo-form shows strong receptor-binding [364]. Naturally, proteins exhibit many primary amine groups representing suitable binding sites for linker attachment. In general, surface modification of protein-loaded NP after preparation is not trivial. A very powerful tool for bioconjugation is represented by a set of biorthogonal chemical reactions referred to as 'click' reactions, which are usually characterized by fast reaction speed, easy handling, versatility, regioselectivity and high product yields [365, 366]. The most commonly used reaction is the copper(I)-catalyzed azide-terminal alkyne cycloaddition (CuAAC) reaction [367]. However, the use of this conjugation method has been restricted in biomedical applications due to toxicity concerns of the copper catalyst and the need for additional purification steps [368]. The strain-promoted azide–alkyne cycloaddition (SPAAC) reaction of azides with strained cyclooctynes presents a promising alternative because it proceeds without a copper catalyst. With this method, a functional group can be attached to both transferrin and chitosan enabling a rapid covalent surface-conjugation under mild reaction conditions after CS NP preparation.

Here we report the chemical modification, preparation, characterization and *in vitro* evaluation of chitosan nanoparticles with human holo-transferrin as surface targeting ligand for a possible application in NtB delivery.

5 Materials and Methods

5.1 Materials

Chitosan (5-20 mPa·s, 0.5 % in 0.5 % Acetic Acid at 20 °C, deacetylation degree of 85 %) was purchased from TCI Chemical Industry Co., LTD (Tokio, Japan). Ethyl 5-bromovalerate, 1-ethyl-3-(3-dimethylaminopropyl)carbodiimide (EDC), N-hydroxysuccinimide(NHS), DMSO, 2-(N-morpholino)ethanesulfonic acid (MES), human

holo-transferrin expressed in rice, pentasodium-tripolyphosphate (TPP), β-galactosidase (bGal) from *Aspergillus oryzae*, 2-nitrophenyl ß-D-galactopyranoside (ONPG), EMEM (Eagle's Minimum Essential Medium), L-glutamine, penicillin/streptomycin, fetal bovine serum (FBS), human glioblastoma cell line U87, DMEM (Dulbecco's Modified Eagle Medium), epidermal growth factor, insulin, hydrocortisone, trypsin-EDTA, and other routine chemicals were obtained from Sigma-Aldrich (Taufkirchen, Germany) and used as received. Dibenzyl cyclooctyne-N-hydroxysuccinimide-ester (DBCO-NHS-ester) and fluorescein (FAM) azide were acquired from Lumiprobe GmbH (Hannover, Germany). ATTO647N-NHS dye was bought from ATTO-TEC GmbH (Siegen, Germany). His-tagged transferrin receptor (TfR-His) was purchased from Sino Biological Inc. (Beijing, P.R. China). Human nasal squamous carcinoma cell line RPMI 2650 were obtained from Cell Lines Services (Eppelheim, Germany) and human breast epithelial cells MCF-10A from ATCC (Manassas, USA). Air-liquid interface (ALI) differentiation medium was bought from Lonza (Basel, Switzerland). Anti-human CD71 (PE, clone OKT 9, eBioscience™) and anti-mouse IgG1 (PE, clone M1-14D12, eBioscience™) were purchased from Thermo Fisher Scientific (Waltham, MA, USA). Biacore His-capture kit was obtained from Cytvia (Marlborough, MA, USA).

5.2 Modification of chitosan

The precursor for the click reaction, azide-modified chitosan was prepared according to literature [369]. In brief, an amidation of chitosan with 5-azidopentanoic acid in the presence of EDC/NHS was performed. For this reaction, 5-azidopentanoic acid was synthetized according to literature [370]. In a 25 mL round bottom flask, 2.50 mg of ethyl 5-bromovalerate (11.9 mmol, 1 equiv.) were dissolved in 6.25 mL DMSO and consecutively 3.07 g sodium azide (47.7 mmol, 4 equiv.) were added while stirring. The reaction mixture was stirred for 24 h at 100 °C. After cooling, the brown suspension was treated with 100 mL water. Then, the solution was extracted with ethyl ether (4 x 50 mL) and the combined organic phase was concentrated to approx. 30 mL *in vacuo*. This solution was diluted with 30 mL of 1 M $NaOH_{(aq)}$ and the mixture was stirred overnight at room temperature. After washing the solution with ethyl ether (3 x 20 mL), it was acidified to pH 1 with $HCl_{(conc)}$. The product was extracted with ethyl ether (3 x 20 mL). The combined organic phases were dried over $MgSO_4$, filtered and the solvent

was removed *in vacuo*. 1.29 g of 5-azidopentanoic acid were obtained as a yellow liquid (yield 52 wt%). For the amidation of chitosan with 5-azidopentanoic acid, 0.50 g chitosan (2.73 mmol, 1.0 equiv.) and 0.39 g 5-azidopentanoic acid (2.73 mmol, 1.0 equiv.) were dissolved in 50 mL MES buffer and the reaction mixture was stirred for 5 h at room temperature. Then the solution was degassed with nitrogen for 30 min. Afterwards, 1-ethyl-3-(3-dimethyl aminopropyl) carbodiimide (EDC, 1.57 g, 2.73 mmol, 1.0 equiv.) and *N*-hydroxysuccinimide (NHS, 2.83 g, 24.6 mmol, 9.0 equiv.) were gradually added to the flask within 20 min and left to react while stirring for 16 h. The polymer solution was dialyzed (MWCO 6-8 kDa) against distilled water for 6 days at 4 °C to remove impurities and freeze-dried afterwards. Azide-functionalized Chitosan (0.47 g, yield 53 wt%) was obtained as a slightly yellow powder.

5.3 Modification of transferrin

Human holo-Tf expressed in rice was used for the modification with an alkyne group. For each batch, 30 mg Tf (0.38 µmol, 1.0 equiv.) were dissolved in 900 µL of 50 mM phosphate buffer pH 8. In another glass vial, 1.64 mg of dibenzyl cyclooctyne-*N*-hydroxysuccinimide-ester (DBCO-NHS-ester, 3.8 µmol, 10 equiv.) were dissolved in 100 µL DMSO and then added to the Tf solution. The reaction mixture was stirred overnight at 300 rpm at 4°C. Afterwards, the conjugate was purified using a Sephadex G-25 pre-packed PD-10 column and freeze-dried subsequently. As product, 25.2 mg of alkyne-functionalized Tf (yield 79.5 wt%) were obtained as a slightly red powder. For the analysis of the conjugation reaction, IR spectra were recorded. Furthermore, the apparent weight of the protein and successful modification for use in click chemistry were evaluated by SDS-PAGE. In brief, fluorescein (FAM) azide was used as a fluorescent click-partner for the alkyne-modified Tf. Briefly, 10 µl of FAM azide (5 mg/mL, 0.075 mM, 3.75 equiv.) solution in DMSO and 100 µL sodium ascorbate solution (5 mM) was added to 1 mL of alkyne modified Tf (1 mg/mL, 0.02 mM, 1.0 equiv.) in water while gently shaking the vial. The reaction mixture was incubated at room temperature in the dark for 2 h without shaking. For the verification of covalent linkage and intactness of protein an SDS-PAGE was performed using a Novex WedgeWell 8-16% Tris-Glycine Gel (1.0 mm x 12 well). Unmodified holo-Tf was used as control. The gel was stained with Coomassie blue and analyzed with a ChemiDoc

imager (Bio-Rad Laboratories, Inc., Feldkirchen, Germany). Subsequently, the gel was destained and analyzed again under UV-light to visualize fluorescent bands.

5.4 Nanoparticle preparation

5.4.1 Preparation of chitosan nanoparticles

Chitosan nanoparticles were prepared via ionotropic gelation method according to a well-established and previously published protocol [43]. Briefly, 5 mg chitosan (CS) were dissolved in 5 mL of 25 mM acetate buffer pH 5.0 while stirring overnight. Pentasodium-tripolyphosphate (TPP), which has anionic character and, therefore, serves as a bridging agent in CS NP preparation, was dissolved in highly purified water with a final concentration of 1 mg/mL. Both solutions were filtered through a 0.22 µm mixed-cellulose-ester (MCE) filter. Subsequently, 2 mL of TPP solution were quickly added to the chitosan solution while stirring at 1000 rpm. The suspension turned slightly opaque, indicating successful nanoparticle formation, and was left stirring for 2 h. Nanoparticles were centrifuged on a 20 µL glycerol bed at 10,000 rpm and at 4°C for 45 min. The supernatant was removed. For loaded nanoparticles, 2 mg of β-galactosidase (bGal) or ATTO647N-labeled β-galactosidase (ATTOGal) were added to the TPP solution before mixing with chitosan. Labeling of β-galactosidase with ATTO647N was performed according to the manufacturer's protocol using a 2-fold molar excess of dye. Briefly, ATTO647N-NHS dye in DMSO was added to an aqueous protein solution at a concentration of 5 mg/mL and incubated for 1 h at room temperature. Afterwards, the protein-dye-conjugate was purified using a Sephadex G25 column.

5.4.2 Preparation of transferrin-decorated chitosan nanoparticles

For the preparation of transferrin-decorated chitosan nanoparticles, azide-modified CS was mixed in a 1:1 weight ratio with regular CS to a final concentration of 1 mg/mL in 25 mM acetate buffer pH 5.0 (CS mixture). Alkyne-modified Tf was dissolved in highly purified water at different concentrations (1, 2, 2.5, 4, and 5 mg/mL). CS mixture was filtered through a 0.45 µm MCE filter. TPP and bGal were dissolved in highly purified water at a concentration of 1 mg/mL each. After adding the bridging agent TPP and

protein to the CS solution, the dispersion was stirred for 1 h before adding 1 mL of alkyne-modified Tf in the respective concentration. This reaction mixture was stirred for 1 h at 1000 rpm. Then, the nanoparticles were centrifuged at 10,000 x g for 45 min on a 20 µL glycerol bed, and the supernatant was removed.

5.5 Nanoparticle characterization

5.5.1 Size and zeta-potential determination

For evaluation of hydrodynamic diameter and polydispersity index (PDI), dynamic light scattering was used, and laser Doppler anemometry was applied for zeta potential analysis. 100 µL of NPs resuspended in highly purified water were added into a disposable micro-cuvette (Malvern Instruments, Malvern, UK) and size as well as PDI was determined with a Zetasizer Nano ZS (Malvern Instruments) at 173° backscatter angle performing 15 runs three times per sample. Viscosity of 0.88 mPa·s and a refractive index of 1.33 were set for data analysis using the Zetasizer software. NPs were then diluted with 900 µL 10 mM NaCl, and 700 µL of NP suspension were transferred to a folded capillary cell (Malvern Instruments) to perform three zeta potential measurements per sample using the same device.

5.5.2 Encapsulation of model protein

For the determination of encapsulation efficiency, a modified version of β-galactosidase assay was conducted to assess enzymatic activity [287, 288, 371]. This analysis was performed indirectly and, thus, supernatants after centrifugation were used. Briefly, 8.33 µL of supernatant was added to 158.33 µL enzyme buffer containing 60 mM Na_2HPO_4, 60 mM NaH_2PO_4, 1 mM $MgSO_4$ and 0.27 % β-mercaptoethanol, in a transparent 96-well plate. For the blank reference, 167.66 µL of enzyme buffer were used. For generating a calibration curve, the same procedure as for samples with varying known concentrations of bGal was applied. The plate was equilibrated at 28 °C for 5 min in a plate reader (Tecan Group AG, Männedorf, Switzerland). Then, 33.3 µL of 2-nitrophenyl β-D-galactopyranoside (ONPG) with a concentration of 4 mg/mL in highly purified water, were added to each well. The enzymatic reaction was measured

for 10 min. The amount of encapsulated protein was determined by the following equation:

$$EE\ [\%] = \left(1 - \frac{c_{free\ bGal}}{c_{max.\ bGal}}\right) * \mathbf{1}00\%. \qquad [1]$$

5.5.3 Determination of bound transferrin

Nanoparticles were lyophilized with an Epsilon 2-6D LSCPlus (Martin Christ Gefriertrocknungsanlagen GmbH, Osterode am Harz, Germany) under following conditions: Primary drying at -50°C for 4 h and then, secondary drying at -20°C for 42 h, 5°C for 4 h and 25°C for 12 h under vacuum (0.09 mbar). Lyophilized samples were used for the analysis of Tf binding efficiency on nanoparticle surface. Inductively coupled plasma optical emission spectroscopy (ICP-OES) was used to determine the iron amount of surface bound Tf. Lyophilized modified Tf was used as reference. 10 mg of lyophilized nanoparticles were weighed into a glass vial, acidified with 0.5 mL HNO_3 (69 %) and 1.5 mL HCl (37 %) and heated in a laboratory microwave at 185 °C for 30 min. Samples were measured using a Varian Vista RL CCD Simultaneous ICP-OES.

5.5.4 Transferrin receptor binding

The binding affinities of the prepared Tf-decorated CS NPs to His-tagged transferrin receptor (TfR-His) were investigated by Surface Plasmon Resonance (SPR) spectroscopy. HBS buffer (10 mM HEPES pH 7.4, 150 mM NaCl, 0.005 % (v/v) Tween 20) was used as running buffer for all measurements. Tf-decorated nanoparticles were prepared as described above, redispersed in HBS buffer and hydrodynamic diameters were measured to ensure no alterations caused by the high salt conditions (**Figure S7**). For comparison, free human holo-Tf and alkyne modified holo-Tf were dissolved in HBS buffer. SPR assays were performed in a Biacore T200 device using CM5 Series S carboxymethyl dextran sensor chips coated with anti-His-Tag antibodies from the Biacore His-capture kit. Briefly, the chips were equilibrated with HBS buffer until the dextran matrix was swollen. Afterwards, two flow cells of the sensor chip were activated with a 1:1 mixture of N-ethyl-N-(3-dimethylaminopropyl) carbodiimide hydrochloride and N-hydroxysuccinimide according to the standard amine coupling

protocol. A final concentration of 50 µg/mL anti-His-Tag antibody in 10 mM acetate buffer pH 4.5 was loaded onto both flow cells using a contact time of 420 s for gaining a density of approximately 10,000 resonance units (RU) on the surface. By injection of 1 M ethanolamine/HCl pH 8.0 free binding sites of the flow cells were saturated. Preparation of chip surfaces was carried out at a flow rate of 10 µL/min. For interaction analysis, TfR-His (30 ng) was captured onto one flow cell using a contact time of 60 s at a constant flow rate of 10 µL/min. This resulted in a capture density of approximately 200-300 RU of TfR-His. Nanoparticles with five different amounts of transferrin (1, 2, 2.5, 4, and 5 mg) were injected onto both flow cells using an association time of 240 s and a dissociation time of 600 s. The flow rate was kept constant at 30 µL/min. As control, a similar concentration of chitosan was injected. The chip was regenerated after each cycle by removing TfR-His completely from the surface using 10 mM glycine pH 1.5 for 60 s at a flow rate of 30 µL/min. To address the binding affinities of free human holo-Tf and modified Tf, SPR assays were performed as described above using these concentrations (1, 10, 25, 50, 2 x 100, 500, and 1000 nM) of free human holo-transferrin or alkyne modified holo-transferrin, respectively. All experiments were performed at 25°C. Sensorgrams were recorded using the Biacore T200 Control software 2.0.2 and analyzed with the Biacore T200 Evaluation software 3.1. The surface of flow cell 1 was not coated with TfR-His and used to obtain blank sensorgrams for subtraction of the bulk refractive index background. The referenced sensorgrams were normalized to a baseline of 0. Peaks in the sensorgrams at the beginning and the end of the injection are due to the run-time difference between the flow cells for each chip. For the calculation of K_D values, steady state affinity curves were used, and the kinetics were fitted assuming a 1:1 binding model using the Biacore T200 Evaluation Software 3.1.

5.6 General cell culture

Human nasal squamous carcinoma cell line RPMI 2650 was cultured in EMEM (Eagle's Minimum Essential Medium) supplemented with 1 mM sodium pyruvate, 0.1 mM non-essential amino acids, 2 mM L-glutamine, 1% penicillin/streptomycin and 10% fetal bovine serum (FBS). Human glioblastoma cell line U87 was cultured in EMEM containing 1% penicillin/streptomycin and 10% FBS and human breast epithelial cells

MCF-10A were cultured in DMEM (Dulbecco's Modified Eagle Medium) supplemented with 10% FBS, 1% penicillin/streptomycin, 20 ng/ml epidermal growth factor, 10 µg/ml insulin and 0.5 mg/ml hydrocortisone. The cell cultures were maintained at 37 °C in a >95% humidified atmosphere of 5% CO_2 in air with media changes on alternate days. Once 80–100% confluent, the cells were harvested with 0.25% trypsin-EDTA for further experiments.

5.7 Co-culture model

A co-culture model of RPMI2650 and U87 cells was established. First, RPMI2650 cells were cultured at the air-liquid interface (ALI). Hence, they were seeded on PET Transwell™ membrane inserts (1 µm pore size, ∅ 0.33 cm, Corning, NY, USA) with a density of 4 x 10^5 cells/cm^2. Air-lift was performed after 24 h by removing the medium from the apical compartment and replacing the medium on the basolateral compartment with ALI differentiation medium. TEER values of RPMI2650 cell layers were determined every 4-5 days to determine cell monolayer integrity using an epithelial voltohmmeter (EVOM2, WPI, Sarasota, FL, USA) with a chamber electrode (EndOhm, WPI). For the measurement, 700 µL of regular culture medium were added to the electrode chamber and 150 µL to the apical side compartment of the insert. The measured TEER values were corrected by subtracting the mean resistance of blank porous membranes. After 21 days of culture at 37 °C and 5% CO2, cells showed steady TEER values and were used for further experiments. After 20 days U87 cells were seeded with a density of 5 x 10^4 cells/well in a 24-well plate. On day 21, the Transwell™ insert containing RPMI2650 cells at ALI were placed into the 24-well plate containing U87 cells. The medium was changed and consisted of 90% ALI medium and 10% U87 medium. The co-culture was incubated at 37 °C in a >95% humidified atmosphere of 5% CO_2 for 4 h before using it for experiments.

5.8 Transferrin receptor expression

For validation, whether the used cell line is suitable for targeting with Tf decorated CS NPs, the endogenous transferrin receptor 1 (CD71) expression levels were determined for each cell line. Hereby, MCF-10A cells were used as negative control. In general, cells were harvested following trypsinization and resuspended in PBS at 10^5 cells/mL in

triplicate for CD71, isotype control and unstained samples. After incubation with the respective PE-labeled antibodies, samples were washed twice with PBS, and the median fluorescence intensity (MFI) was quantified using an Attune Nxt flow cytometer (Thermo Fisher Scientific, Waltham, MA, USA) with a 488 nm excitation laser and a 574/26 nm emission filter. All cells were gated according to morphology based on forward/sideward scattering, and 10,000 events were evaluated per sample.
This experiment was repeated with RPMI2650 cells cultured under ALI conditions to confirm the presence of CD71 at the ALI in comparison to regular liquid culture.

5.9 Cellular uptake

ATTOGal loaded CS NPs with different amounts of surface-bound Tf (1, 2, 2.5, 4, and 5 mg) were used for the analysis of cellular uptake. RPMI2650 cells were seeded in a density of 5 x 10^4 cells/well in a 24-well plate. After 24 h incubation, they were treated with the different NP samples at a concentration of 0.1 mg/mL. After additional 4 h, cells were harvested via trypsinization, washed twice with PBS before resuspension in 400 µL PBS containing 2 mM EDTA and analysis via flow cytometry using 637 nm excitation and 670/14 nm emission filter. All cells were gated according to morphology based on forward/sideward scattering, and 10,000 events were evaluated per sample.

For the evaluation of NP passage through an epithelial cell layer, cells in co-culture were treated with NP at a concentration of 0.1 mg/mL. Hereby, free ATTOGal was compared to ATTOGal loaded CS NPs and Tf-decorated nanoparticles. One half of the samples was incubated at 37 °C and the other half at 4 °C to distinguish between actual uptake and adhesion to the cell surface. After 24 h, cells were harvested and washed three times before resuspension in 400 µL PBS containing 2 mM EDTA. Samples were analyzed via flow cytometry with 637 nm excitation and 670/14 nm emission filter. All cells were gated according to morphology based on forward/sideward scattering, and 10,000 events were evaluated per sample.

5.10 Statistical analysis

All results are given as mean value ± standard deviation (SD) of three individual experiments unless stated otherwise. Statistical significance was investigated using one-way ANOVA and two-way ANOVA with Bonferroni's and Tukey's posthoc post-test. All statistical analysis was performed using GraphPad Prism version 9.2.0 for Windows (GraphPad Software, San Diego, CA, USA, www.graphpad.com).

6 Results and Discussion

Specific targeting of cells in the olfactory region with NPs is hypothesized to improve intranasal protein delivery to the brain, thereby, offering a promising alternative to conventional delivery over BBB. The targeting ligand should be covalently linked and solely bound on the NP surface in order to obtain a defined morphology, keep particle size as small as possible and protect the encapsulated cargo [372, 373]. For this purpose, both CS and Tf were chemically modified according to previously published protocols introducing functional groups capable of undergoing a Huisgen-type SPAAC reaction [369, 370, 374].

6.1 Modification of chitosan and transferrin

In general, Huisgen-type cycloadditions are Cu^{1}-catalyzed if a propargyl group is used [375]. For a copper-free 'click' reaction between chitosan NPs and targeting ligand, the ring-strained alkyne derivative DBCO was chosen as functional group for transferrin (**Figure S8**) [376, 377]. By using this reaction type, it was possible to modify the NP surface after NP formation while preserving the cargo. For the preparation of Tf-decorated CS NPs, chemical modifications of both CS and Tf were performed (**Figure 16**). The aim was to create a covalent, stable bond between the targeting ligand and the nanoparticles [377-379].

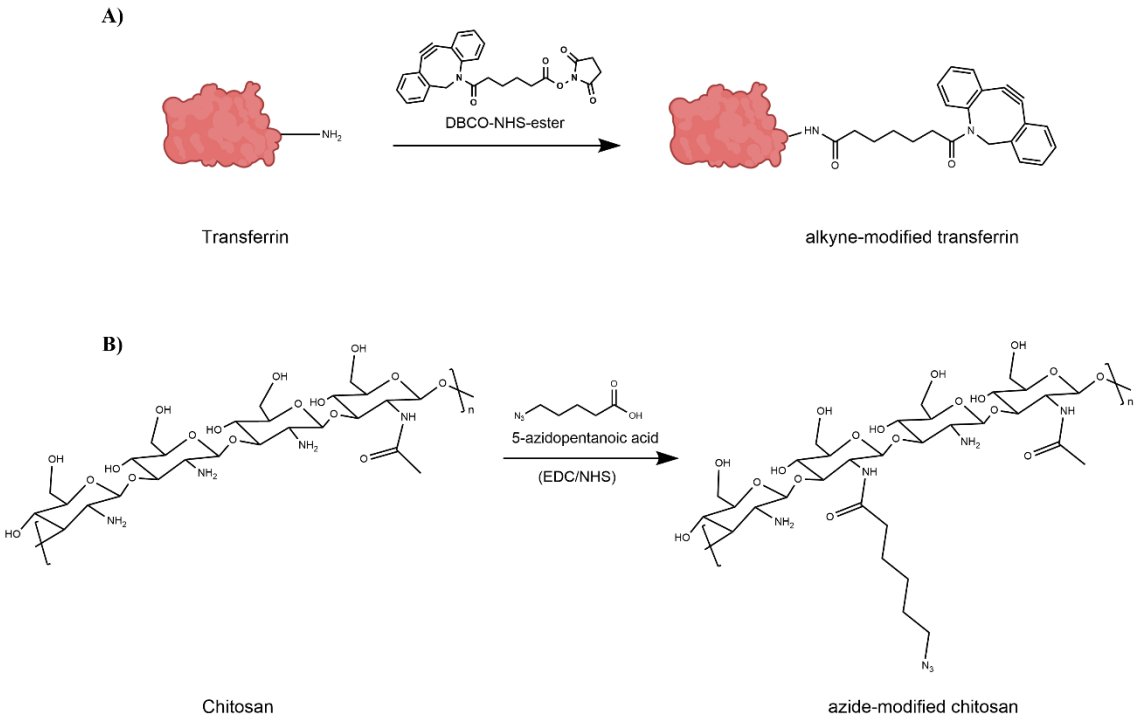

Figure 16. Chemical modification of transferrin and chitosan in order to introduce functional groups capable of undergoing click-reaction. A) Modification of transferrin with DBCO-NHS-ester in the presence of EDC/NHS for generation of an alkyne functional group. B) Modification of chitosan with 5-azidopentanoic acid for introducing azide functional groups.

Therefore, azide-modified CS was prepared by amidation with 5-azidopentanoic acid in the presence of EDC/NHS. EDC can initiate the formation of an amide linkage between 5-azidopentanoic acid and CS by activating the carboxyl group and forming a reactive O-acylisourea intermediate, which spontaneously reacts with primary amines. However, this intermediate is not very stable in aqueous solutions. Thus, NHS is added and being activated by EDC, increasing stability of the reactive intermediate [380, 381]. This 2-step coupling allows for an efficient conjugation to primary amines under physiologic conditions. The IR spectra of unmodified CS, 5-azidopentanoic acid and azide-modified CS reveal the appearance of an absorbance around a wave number of 2100 cm^{-1} in the azide-modified CS spectrum, which is characteristic for a terminal azide group (**Figure 17**) [382]. These results are supported by ^{1}H-NMR spectra shown

in **Figure 17**. The appearance of new signals and the splitting of protons suggest a coupling of 5-azidopentanoic acid to some of the amino repetition units in CS. These results indicate a successful CS modification.

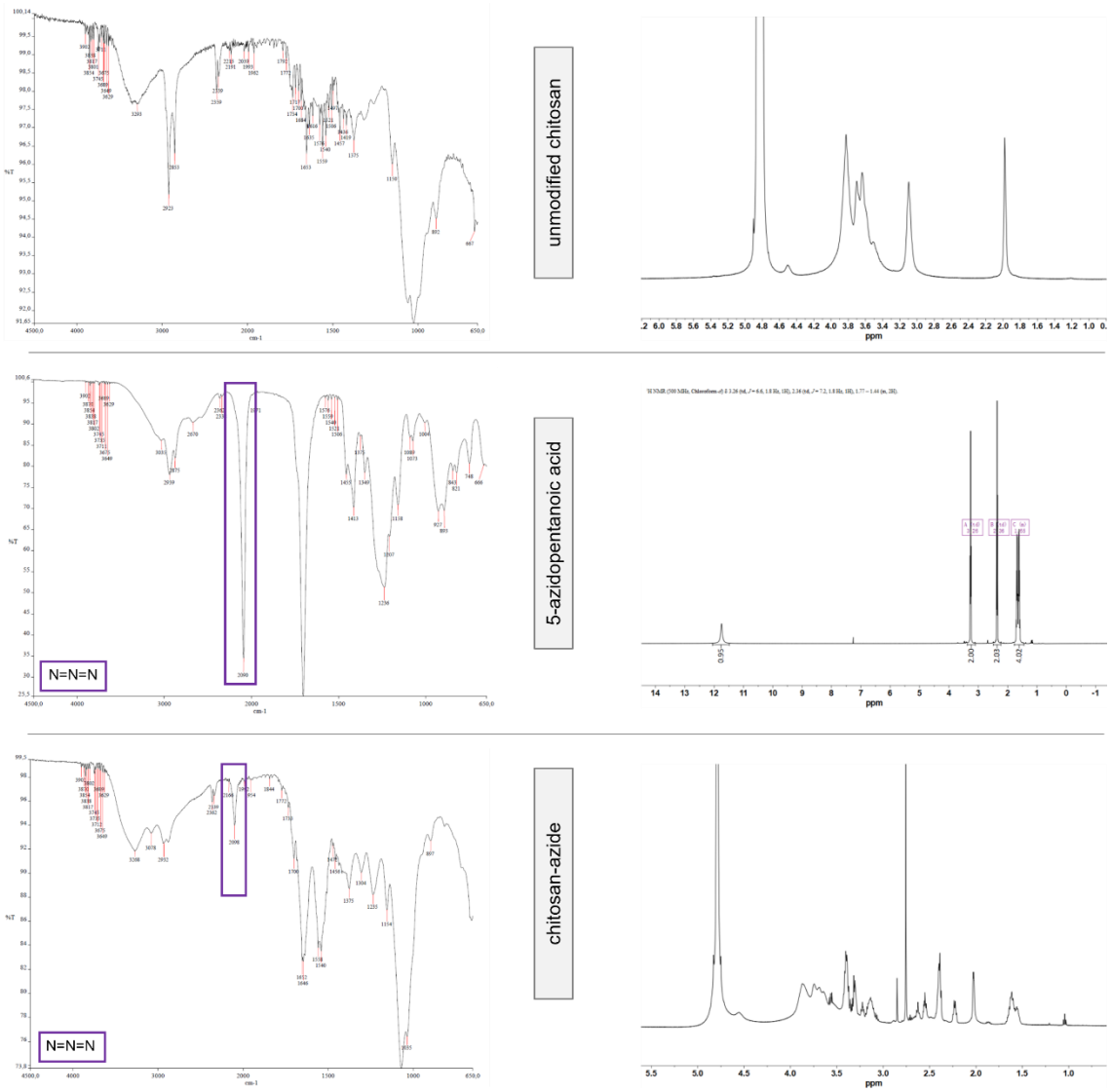

Figure 17. Analytics of chitosan after chemical modification. Right: IR spectra of unmodified chitosan, 5-azidopentanoic acid, and azide-chitosan. Left: ^{1}H-NMR spectra of unmodified chitosan, 5-azidopentanoic acid, and azide-chitosan recorded in $CDCl_3$.

Tf was modified using DBCO-NHS-ester. This NHS-ester activated DBCO reacts with primary amines in physiologic to slightly alkaline conditions yielding stable amide bonds (**Figure 16**) [374]. The resulting alkyne-modified Tf was first analyzed after click-

reaction with FAM-azide by IR and SDS-PAGE. IR measurements revealed that the spectrum of unmodified holo-Tf corresponds to literature-reported Tf spectra (**Figure S6**) [383]. However, a difference between Tf and alkyne-modified Tf was not observed. Additionally, the characteristic resonances of DBCO at 1700 cm^{-1} and 754 cm^{-1} were too weak to be detected with this technique [384]. Therefore, another method was used to analyze whether modification of Tf was successful. First, modified Tf was reacted with FAM-azide, a fluorescent click-reaction partner, for 2 h at room temperature. Unmodified Tf was used as control. Subsequently, SDS-PAGE experiments were performed with this reaction mixture, and the protein bands were visualized using Coomassie blue. In a second step, UV light was used to detect the fluorescent click partner. The Coomassie staining in **Figure 18A** shows that the protein bands of alkyne-Tf are similar to the ones of unmodified Tf, suggesting protein integrity after chemical alteration [378, 385]. Evidence for successful modification is shown in **Figure 18B**. Due to the click-reaction with FAM-azide, the band of modified transferrin becomes visible under UV light together with the excess of fluorescent reaction partner at the bottom of the gel. Fluorescent bands show the same molecular weight as seen for the bands in Coomassie staining. This confirms that indeed it is modified-Tf that lights up due to the fluorescent label. Importantly, the fluorescence in the control sample can only be detected at the bottom of the gel, confirming that a conjugation did not take place with unmodified holo-Tf.

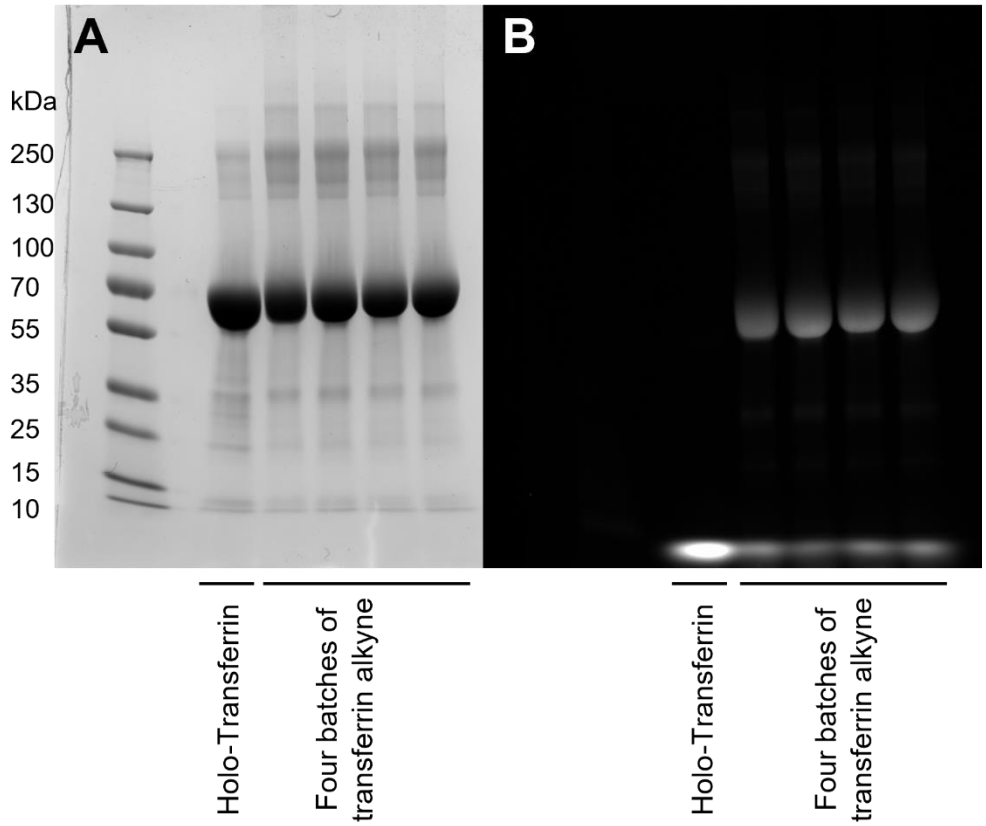

Figure 18. Alkyne-modified transferrin can be covalently modified by SPAAC as demonstrated by analysis via gel electrophoresis. Comparison of alkyne modified Tf and holo-Tf with Coomassie staining A and with gel visualization B under UV-light after click-reaction with FAM-azide.

6.2 Nanoparticle characterization

The advantages of attaching the targeting ligand after NP preparation are, on the one hand, the protection of the cargo due to reduced interactions with the ligand. On the other hand, the NP size is smaller since ligand molecules can solely be found on the NP surface. A NP size between 100-150 nm together with a positive surface potential are stated to be suitable characteristics for nose-to-brain delivery [386, 387]. As mucopolysaccharides are negatively charged, the positive NP surface charge is responsible for their mucoadhesive effect [270, 388]. Hence, after nanoparticle preparation via ionotropic gelation [43], hydrodynamic diameter, polydispersity index and zeta potential were determined (**Table 4**). Chitosan nanoparticles without targeting

ligand showed a size of about 120 nm, while an increase in size and also PDI was observed for Tf-decorated CS NPs. This is attributed to the Tf molecules bound on the NP surface having a molecular weight of about 80 kDa each and, therefore, increasing the hydrodynamic diameter of CS NPs. However, these Tf CS NPs showed higher PDI values suggesting a less homogenous sample. A possible explanation is the NP preparation via ionotropic gelation method in which it is not possible to exactly control the NP formation. As a result, there are different numbers of free Tf binding sites on the surface leading to a non-homogenous targeting ligand distribution. Additionally, Tf-decorated NPs exhibited a decreased zeta-potential. It has been reported that Tf shields the positive surface charge of NPs, indicating successful attachment of targeting ligand on the NP surface [389]. Furthermore, the encapsulation efficiency of bGal was determined by an enzymatic assay as described above. CS NPs without ligand tend to exhibit a slightly higher encapsulation efficiency than Tf-decorated NPs which may be attributed to the number of overall charges in the CS molecule being decreased after chemical modification. Yet, within this sample size, this trend is not significant. Notably, an increase in added Tf amount does not have a significant impact on neither NP size or zeta-potential nor encapsulation efficiency. However, PDI values tend to increase with higher Tf concentrations suggesting lower sample homogeneity. This may originate from different amounts of Tf of NP surface, which are unevenly distributed.

Table 4. Evaluation of physicochemical characteristics of chitosan NPs without surface ligand and transferrin decorated chitosan NPs measuring hydrodynamic diameter, ζ-potential, and encapsulation efficiency of bGal (values are given in mean ± SD.; n = 3).

Transferrin conc. [mg/mL]	Size [nm]	PDI	ζ-potential [mV]	Encapsulation efficiency [%]
0	120 ± 11	0.194 ± 0.023	24.1 ± 2.9	63 ± 8
1	126± 14	0.211 ± 0.067	18.9 ± 2.1	54 ± 7
2	132± 16	0.222 ± 0.081	17.0 ± 2.7	54 ± 7
2.5	131± 21	0.235 ± 0.056	16.4 ± 1.4	55 ± 11
4	140 ± 17	0.227 ± 0.045	15.7 ± 1.6	51 ± 4
5	142± 23	0.251 ± 0.091	16.4 ± 2.2	47 ± 14

For the determination of Tf amount bound on the NP surface, the samples were analyzed using ICP-OES. The iron content of NP samples was detected and compared to free modified holo-Tf. The amount of surface-bound Tf was calculated with respect to the initially utilized amount of Tf during NP formation. **Figure 19** shows different amounts of initially utilized Tf with their respective iron content after NP preparation. The analysis revealed that a 1:1 ratio between modified CS and modified Tf (corresponding to 2.5 mg of Tf in **Figure 19**) leads to a binding efficiency of less than 5

%. After optimizing the ratio to 1:1.6 (corresponding to 4 mg of Tf in **Figure 19**), binding efficiency was improved to about 10%. Furthermore, there is no linear correlation since using an excess amount of Tf did not lead to clearly increasing surface binding.

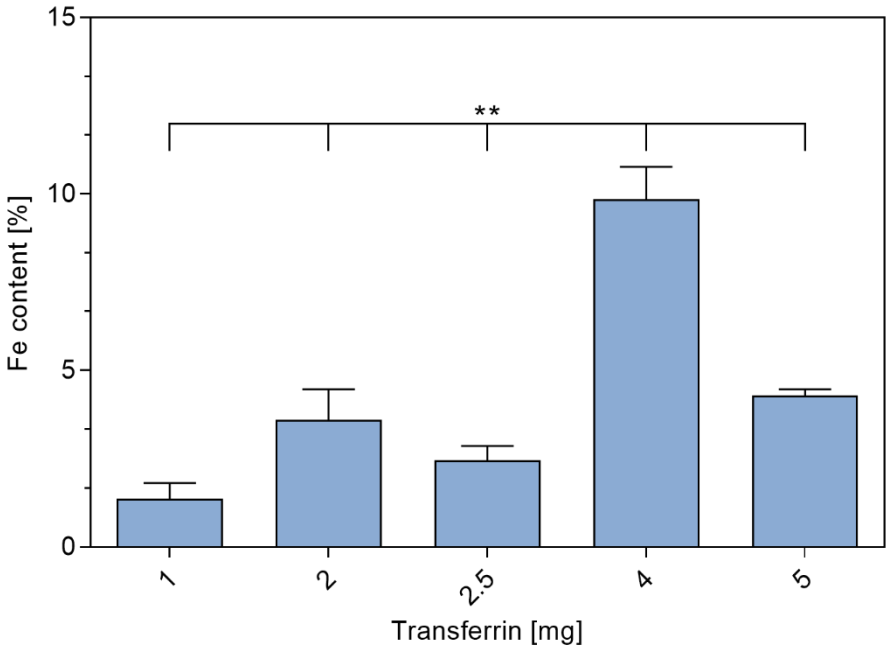

Figure 19. Iron content of transferrin-decorated chitosan nanoparticles using different amounts of transferrin in NP preparation (data points mean ± SD; n = 3; one-way ANOVA; one asterisk "*", $p < 0.05$; two asterisks "**", $p < 0.01$; three asterisks "***", $p < 0.005$).

SPR measurements were used to determine binding affinity and kinetics of the interaction between plain and Tf-decorated CS NPs, respectively, with the transferrin receptor. Therefore, the His-tagged TfR was captured onto a sensor chip with anti-His-Tag antibodies on the surface before adding the NP samples. As positive control, free holo-Tf and free holo-Tf alkyne were injected in similar concentrations. A clear overall binding affinity of free holo-Tf to the TfR was detected with a K_D value of 1.40 nM, which is in agreement with the published K_D values in the range of 1-3 nM (**Figure 20A)**) [390-393]. Furthermore, free holo-Tf binding was characterized by an association rate of $k_a = 2.88 \cdot 10^5$ /M·s and showed a dissociation rate of $k_d = 5.474 \cdot 10^{-4} s^{-1}$. The

binding affinity of alkyne transferrin seems to be similar with an overall K_D value of 1.47 · 10^{-9} M, an association rate of k_a = 3.84 · 10^5 and a dissociation rate of k_d = 5.66 · 10^{-4} s^{-1} (**Figure 20B)**). These findings confirm that chemical modification of Tf does not impair the binding behavior to TfR. Together with SDS-PAGE results, SPR measurements confirm the structural integrity of alkyne-modified Tf. For comparison of NPs with different amounts of Tf immobilized on the surface, the samples were injected onto the biosensor chip one after the other keeping a constant concentration of 1 mg/mL Tf. Differences in binding behavior were evident, where an increased interaction was observed with increasing surface amount of Tf per NP. Although binding affinities of NPs to the TfR could not be determined due to the adhesiveness of CS to the biosensor chip, a comparison between different amounts of surface-bound Tf revealed consistency with ICP-OES measurements. The sample with the highest degree of Tf-modification also showed the highest receptor-binding response. In general, NP samples did not reach saturation but exhibited a linear correlation curve suggesting that the observed binding is not specific but still evident (**Figure 20C)**).

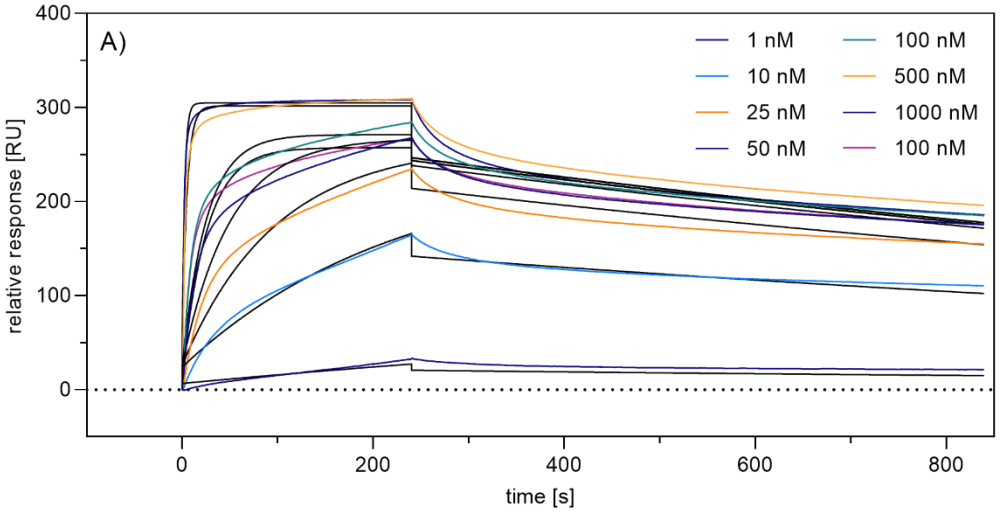
A)
1 nM
10 nM
25 nM
50 nM
100 nM
500 nM
1000 nM
100 nM
relative response [RU]
time [s]

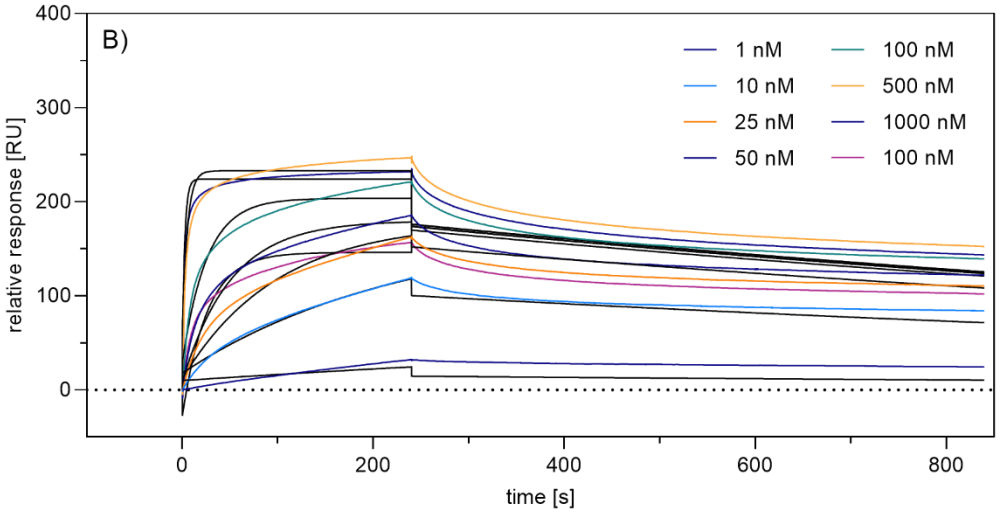
B)
1 nM
10 nM
25 nM
50 nM
100 nM
500 nM
1000 nM
100 nM
relative response [RU]
time [s]

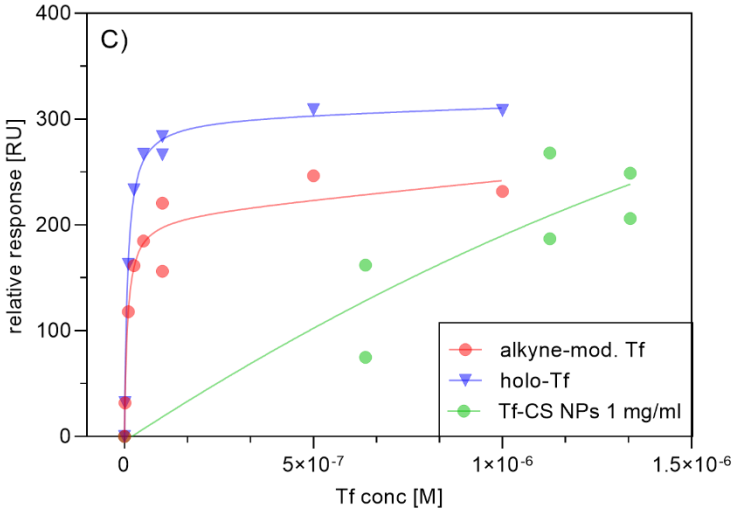
C)
alkyne-mod. Tf
holo-Tf
Tf-CS NPs 1 mg/ml
relative response [RU]
Tf conc [M]

Figure 20. Binding of free holotransferrin, free modified holo-transferrin, and transferrindecorated CS NPs was analyzed by SPR spectroscopy. The transferrin receptor (TfR) was captured via His-tag onto a CM5 sensor chip coated with anti-His antibody, and different concentrations of analytes were tested. A) Human holo-transferrin in different concentrations (1–1000 nM). B) Alkyne modified holo-transferrin in different concentrations. C) CS NPs with different surface-bound transferrin amounts (1, 2, 2.5, 4, and 5 mg/mL). The plots are representatives of three independently performed experiments. Black lines in panels A and B represent the fit of a 1:1 binding model (RU, response unit).

6.3 Transferrin receptor expression

Although there is already evidence in literature that TfR is expressed in both cell lines used to mimic NtB delivery (RPMI2650 and U87 cells), handling, passage number and also cell line source might have an influence on cellular quality and characteristics [394, 395]. Therefore, TfR expression was examined by comparison with a breast epithelial cell line expressing too low levels of TfR for detection via flow cytometry [396]. Therefore, RPMI2650 cells, U87 cells and MCF-10A cells (negative control) were incubated with fluorescently labeled anti-CD71 antibody and an IgG isotype control antibody and analyzed via flow cytometry (**Figure 21**). As expected, media fluorescence intensity (MFI) values of epithelial breast cancer cell line MCF-10A did not differ between cells incubated with anti-CD71 or isotype control, suggesting no detectable TfR expression. Both, U87 and RPMI2650 cells, showed a significant TfR expression on the cell surface. Additionally, the expression level of U87 exceeded the one of RPMI2650.

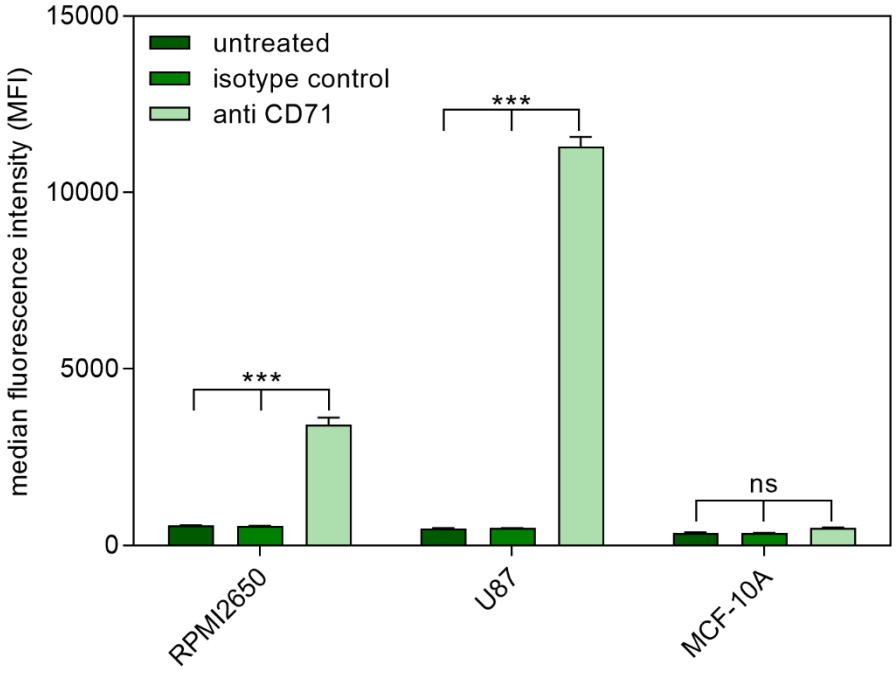

Figure 21. Transferrin receptor (CD71) expression of RPMI 2650 cells, U87 cells, and MCF-10A cells in liquid culture as measured by flow cytometry and compared to an isotype control and as well as untreated cells. Results are presented as median fluorescence intensity (data points indicate mean ± SD, n = 3; two-way ANOVA with Bonferroni's post-test; ns, not significant; one asterisk "*", $p < 0.05$; two asterisks "**", $p < 0.01$; three asterisks "***", $p < 0.005$).

Apart from more intricate techniques such as microfluidic 3D cell culture, air-liquid interface culture models of the respiratory tract are currently the most promising *in vitro* approach to mimic *in vivo* conditions in rather high-throughput experiments [240, 397, 398]. The most important characteristic of this model is that cells are cultured on a supporting membrane, so that the apical side is exposed to air while the basolateral side is in contact with nourishing medium. For the respiratory tract, this configuration grants cell differentiation towards a mucociliary phenotype resulting, for example, in the formation of tight junctions, the production of cilia and mucus [69, 70, 399]. RPMI2650 cells are known to change morphology when cultured at ALI [68]. Therefore, their ability to retain CD71 expression levels at ALI after 21 days of culture was examined. The results confirm that after ALI cultivation, the cells still express TfR

on the cell surface (**Figure 22**). However, the expression levels are lower than in liquid culture, but still significantly increased compared to the isotype control and untreated sample. Due to the change in cell morphology at ALI, the apical and the basolateral side differ considerably from each other. We hypothesize that the TfR might only be expressed on the apical side leading to decreased TfR expression levels. As an overall result, the chosen cell lines are suitable for cellular uptake experiments with Tf as targeting ligand in liquid as well as ALI culture.

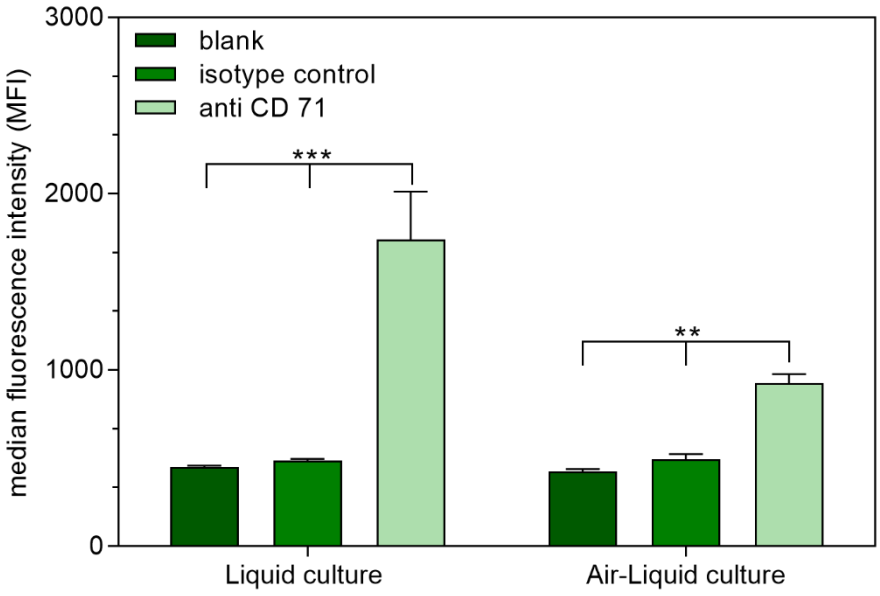

Figure 22. Transferrin receptor expression of RPMI 2650 cells cultured at ALI as measured by flow cytometry and compared to an isotype control as well as untreated cells. Results are presented as median fluorescence intensity (data points indicate mean ± SD, n = 3; two-way ANOVA with Tukey's post-test; one asterisk "*", $p < 0.05$; two asterisks "**", $p < 0.01$; three asterisks "***", $p < 0.005$).

6.4 Cellular uptake

In general, cationic materials such as CS can non-specifically interact with negatively charged cell membranes provoking adsorptive endocytosis [400, 401]. This non-targeted uptake could potentially interfere with the desired uptake into the olfactory region of the nasal cavity. It has already been demonstrated that cellular uptake is

strongly dependent on surface ligand density [402]. Therefore, cellular uptake of Tf-decorated, ATTOGal loaded nanoparticles in liquid culture of RPMI2650 cells was evaluated via flow cytometry. Up to now, the RPMI 2650 cell line is the only cell line used as a nasal model [68]. However, it does not mimic nasal epithelium completely and further studies with excised nasal mucosa should be performed to accurately clarify the exact molecular mechanisms of NP uptake. Nonetheless, this cell line is widely used as tool for preclinical screening studies for nasal epithelial passage of different molecules and NPs [72]. The cells are fast and easy to culture and yield reproducible results [68]. ALI culture of RPMI2650 cells is suitable to assess general passage through epithelial cell layers exhibiting tight junctions and important ABC-transporters [70, 399].Therefore, they were used in this work to assess the differences between simple CS NPs and Tf-decorated NPs.

In the cellular uptake experiment, free ATTOGal and unmodified CS NPs were compared to NP samples with different amounts of Tf on the surface (**Figure 23**). All NP samples exhibited an enhanced cellular uptake compared to free bGal. Furthermore, addition of Tf-decorated CS NPs with the highest degree of Tf modification showed the biggest increase in cellular uptake. Although there is no evident correlation between utilized Tf amount and cellular uptake, there is a trend of uptake enhancement with increasing amounts of bound Tf. Taking into account the results from ICP-OES measurements (**Figure 19**), it is evident that the cellular uptake corresponds to the amount of Tf bound on the NP surface. This also explains the decrease of cellular uptake for the sample with 5 mg Tf compared to NPs prepared with 4 mg Tf. In the former NP formulation less surface-bound Tf is available in comparison to the latter although the initially used Tf feed was higher. Conclusively, NPs with 4 mg of Tf, which exhibited the highest overall amount of surface-bound Tf, showed the best cellular uptake.

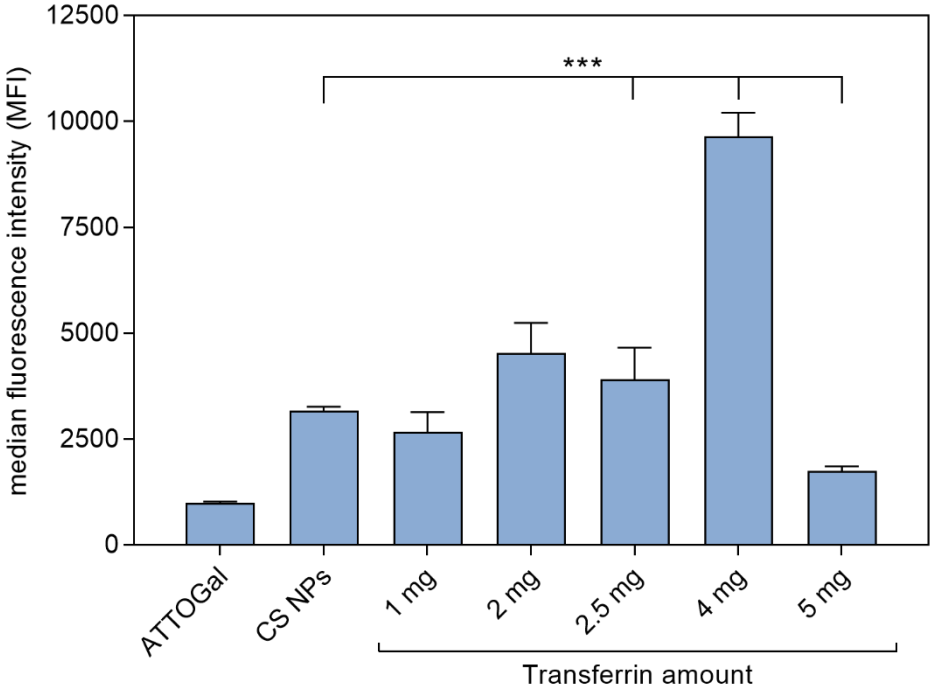

Figure 23. Cellular uptake of ATTOGal loaded transferrin-decorated CS NPs in liquid culture of RPMI 2650 nasal epithelial cells as measured by flow cytometry and compared to CS NPs without transferrin as well as free ATTOGal. Results are presented as median fluorescence intensity (data points indicate mean ± SD, n = 3; two-way ANOVA with Tukey's post-test; one asterisk "*", $p < 0.05$; two asterisks "**", $p < 0.01$; three asterisks "***", $p < 0.005$).

Hence, for cellular uptake into the co-culture model CS NPs with 4 mg of modified Tf were prepared. This co-culture was used to evaluate not only the passage through an epithelial cell layer at the air-liquid interface but also the subsequent uptake into cells found in brain tissue. Therefore, human nasal epithelial cells RPMI2650 were cultured on a Transwell™ membrane insert and incubated for 21 days until the TEER values were > 50 Ωcm^2 [68]. This TEER value guarantees cell layer integrity and tight junction formation suggesting full cell differentiation [69, 399, 403]. Consecutively, the insert holding the differentiated cells was added to a 24-well plate containing human glioblastoma cells (U87) cells at the bottom of the well (**Figure 24**).

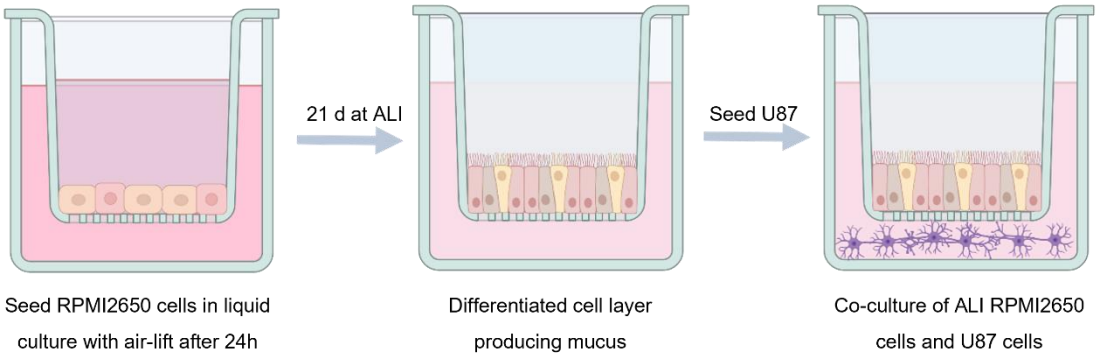

Figure 24. Schematic illustration of co-culture preparation using nasal epithelial cell line RPMI 2650 and glioblastoma cell line U87.

This co-culture model was then treated with NP samples and incubated for 24 h. TEER was measured at different time points throughout the cellular uptake experiment to ensure cell monolayer integrity. The free ATTOGal sample showed a slight, not significant decrease after 4 h and remained constant for the rest of the uptake experiment. As chitosan is known for being able to open tight junctions to a certain extent, an initial decrease in TEER of about 7 Ω/cm^2 was observed for both NP samples [404]. Afterwards, TEER values remained constant suggesting an integer cell layer with no signs of cytotoxicity. **Figure 25** shows the MFIs of both cell lines. Free ATTOGal was compared to ATTOGal-loaded CS NPs and Tf-decorated NPs. At 24 h post treatment the free protein can be mainly found in the U87 cells suggesting a rapid passage through the epithelial cell layer. Encapsulation of ATTOGal into CS NPs also led to an efficient uptake into U87 cells. However, after 24 h, a significant amount of NPs was still found in the RPMI2650 cell layer. This may be attributed to different reasons. The presence of mucus slows down NPs more than the much smaller protein. Additionally, receptor-mediated transcytosis is a rather slow process, so that a considerable amount of NPs has not yet passed the epithelial layer after 24 h. Attaching Tf on the NP surface seemed to improve the cellular uptake into both types of cells. However, this trend was not significant. The amount of Tf in relative comparison to CS is only about 10% resulting in a rather low number of targeting ligands on the NP surface. This number can be increased by addition of more modified CS in the NP preparation process. However, parameters have to be optimized for

every new blend ratio since particle size, PDI and zeta-potential can vary drastically (data not shown). Another hypothesis explaining the low cellular uptake of Tf-decorated CS NPs is that of valency. We have recently described how monovalent ligands cannot fully outcompete multivalent ones [405]. Yet, it was also described that for Tf-mediated endocytosis size is more important than multivalency [406]. The reason is that clathrin-mediated uptake and transcytosis, which is the predominant pathway of internalization for Tf, is limited by the size of natural clathrin-coated pits (~ 100-150 nm) [407]. Hence, adjusting the formulation regarding both parameters will presumably result in improved uptake behavior [408]. Nonetheless, it was successfully shown that Tf-decorated CS NPs are able to cross the epithelial barrier *in vitro*, retain their targeting function and be taken up into therapeutically relevant target cells. Despite the results obtained in this study, further evaluation on the best transport pathway for NtB delivery has to be conducted, in particular regarding transport time and delivery of therapeutic concentrations.

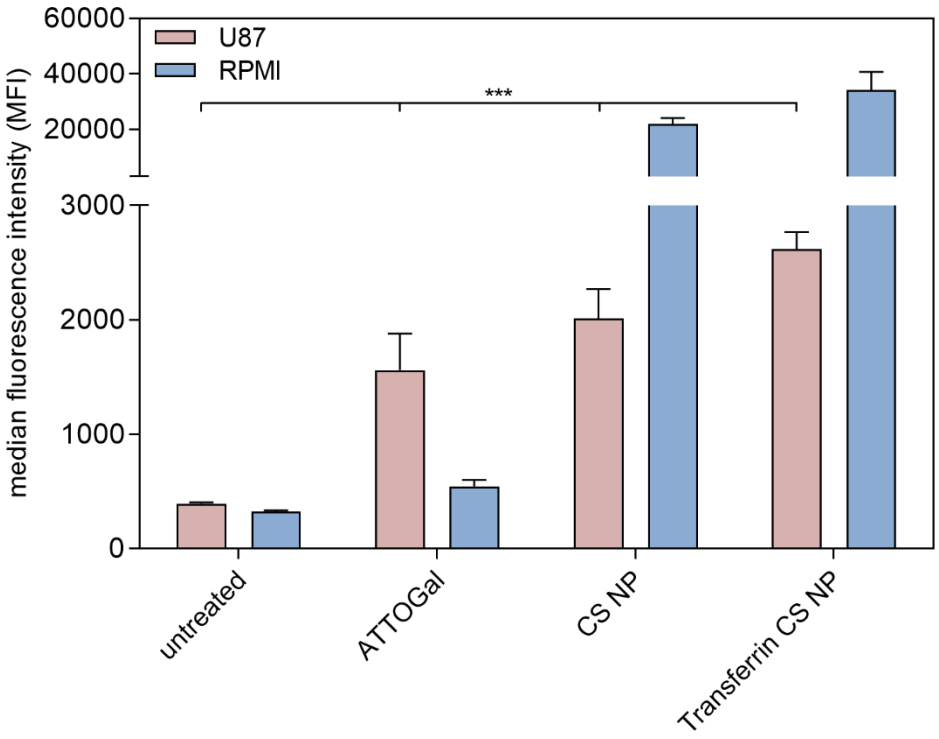

Figure 25. Cellular uptake of ATTOGal, loaded transferrin decorated CS NPs into a co-culture of U87 glioblastoma cells and ALI RPMI 2650 nasal epithelial cells as measured by flow cytometry and compared to ATTOGal loaded CS NPs without transferrin and

free ATTOGal. Results are presented as median fluorescence intensity (datapoints indicate mean ± SD, n = 3; two-way ANOVA with Bonferroni's posttest; one asterisk "*", $p < 0.05$; two asterisks "**", $p < 0.01$; three asterisks "***", $p < 0.005$).

7 Conclusion

Targeting the brain still is an especially challenging task due to the presence of the BBB [14]. Here, nose-to-brain delivery presents a promising alternative for direct drug delivery to brain tissue by circumventing the BBB, especially for biomolecules such as proteins or nucleic acids, which are recently growing in number for therapeutic use [7, 409] [14, 347]. Amongst other materials, CS NPs have shown great potential for intranasal administration, mainly because of their mucoadhesive and tight junction-opening properties [28, 334, 410]. For improved and specific drug delivery, NPs are often decorated with targeting ligands facilitating cell entry [411]. In this work, the aim was to create a concept for protein loaded CS NPs with a surface bound targeting ligand that can easily be exchanged according to the therapeutic need. For this study, Tf was chosen as proof-of-concept targeting ligand since it is already well studied and the transferrin receptor can be exploited as target for nose-to-brain delivery. After introducing and analyzing functional groups to enable a versatile copper-free click chemistry, we have successfully prepared Tf-decorated CS NPs. With this method, a variety of targeting ligands can be attached to the surface after NP formation leading to smaller and more defined formulations. We also demonstrated that these NPs were specifically internalized by cells expressing TfR via receptor-mediated endocytosis. Hereby, we were able to tune the amount of surface ligands resulting in different binding behaviors. Furthermore, this system might be relevant in nose-to-brain delivery of proteins by passage through a mucus-producing epithelial cell layer with consecutive uptake into potential target cells. However, this hypothesis has to be proven in further studies, potentially on excised nasal mucosa, together with a more detailed analysis of which transport mechanism can be favorable for NtB delivery. Nonetheless, Tf-decorated CS NPs produced via copper-free click reaction offer an auspicious platform with easily interchangeable surface ligands for the targeted delivery of macromolecules.

Chapter IV – Utilizing Chitosan Nanoparticles for the Delivery of Biologics to the Brain via Intranasal Route

1 Abstract

Due to its selective permeability, the blood-brain-barrier presents a major hurdle in brain targeted drug delivery, especially for macromolecules such as proteins or nucleic acids. Nose-to-brain delivery offers a promising opportunity for drug delivery via the olfactory and trigeminal pathway resulting in effective concentrations in the brain tissue and central nervous system when compared to systemic delivery. In this study, polymeric nanoparticles constituted of chitosan, which were further chemically modified and decorated with transferrin as targeting ligand, were utilized to examine the nose-to-brain delivery of proteins. The synthetized chitosan nanoparticles and transferrin decorated chitosan nanoparticles were evaluated for their physicochemical characteristics, release kinetics, cellular uptake and permeability through an epithelial cell layer. The ability of the nanosystem to reach the central nervous system after intranasal administration was assessed using fluorescently labeled nanoparticles containing the model protein β-galactosidase. The results suggest that chitosan nanoparticles can be used for successful delivery of intact proteins to the brain.

2 Introduction

Over the last decades, the prevalence and mortality of central nervous system (CNS) disorders have increased, becoming a major health burden worldwide. In 2017, neurological disorders were the third most common cause of premature disability and death in the EU [1]. Due to the progressive ageing of the European population, this incidence is likely to increase in the future. To this day, CNS disorders such as Parkinson's or Alzheimer's disease are mostly treated with therapeutic drugs that need

to be administered systemically and, therefore, have to transit through the blood-brain-barrier (BBB) or blood-cerebrospinal-fluid (BCSFB) to reach the brain tissue [8]. However, due to the selective permeability of the BBB, the administration of novel therapeutic drugs, such as proteins or nucleic acids, is limited [10]. Despite enormous technological advances in the field of CNS therapeutics that have been investigated over the past years to enhance drug transport to the brain, particularly for macromolecules, many of these approaches still remain elusive due to the limitations presented by the BBB [327-329]. In this context, intranasal administration of drugs with consecutive uptake into brain tissue represents a promising and attractive option for future treatment of neurological disorders [412]. This so-called nose-to-brain (ntb) delivery gained increased interest over the past years because it enables the transport of therapeutic drugs to the CNS, while avoiding to cross the BBB or BCSFB [14, 330].

Compared to conventional drug delivery approaches, ntb delivery offers various benefits [345]. First, it is a noninvasive method accessing the CNS directly via the olfactory or the trigeminal nerve after drug deposition on the olfactory epithelium [331]. It can reduce infection risks, especially in comparison with intrathecal or intravenous administration. Therefore, it increases patient compliance and opens the possibility for self-administration. Second, the large surface area of the nasal cavity (approx. 150 cm^2 in humans) with its rich vascular submucosa and the short distance from the nose to the brain enable fast drug absorption and rapid onset of action, thereby, avoiding first-pass-metabolism in the liver [15, 17, 19].

Importantly and in contrast to the BBB route, ntb delivery is not limited to small molecules or lipophilic drugs. Macromolecules such as peptides, proteins and nucleic acids, but also big particulates, e.g. cells or viruses, can successfully be delivered from nose to brain as has been demonstrated by clinical data [16, 332]. However, ntb delivery also has its disadvantages and limitations. Although the surface area of the nasal cavity is quite large, the upper parts are small and narrow. Yet, the target region constituted of the olfactory epithelium with olfactory nerve endings is located in these upper parts of the nasal cavity. Therefore, the dosage volume is restricted to a maximum of 400 µL [20]. Moreover, anatomical differences demand for tailored formulations and administration techniques to overcome inter-individual variability.

Another concern is that intranasally administered drugs, especially proteins and nucleic acids, can undergo rapid enzymatic degradation, mucociliary clearance, and drainage to the lower parts of the pharynx [21]. Further, the permeation of the epithelial barrier inside the nasal cavity via endocytosis generally depends on the hydrodynamic diameter. Therefore, the delivery of hydrophilic and high molecular drugs is limited. Consequently, a suitable dosage form is needed for efficient ntb delivery of macromolecules. In this regard, nanotechnology-based formulations emerged to be promising strategy for efficient ntb delivery of therapeutic biomolecules [27, 333, 334].

Both polymer- and lipid-based nano-formulations can be utilized to bypass membrane efflux pumps and protect the payload against extracellular enzymes [24, 334]. Further, residence time on the mucosal surface can be increased leading to higher drug concentrations at the site of interest. Hence, drug transport efficiency after intranasal administration can be improved significantly with the use of nanotechnology compared to administration of the free drug [335, 336]. A big advantage of nanocarriers is their ability to be tuned regarding physicochemical properties, drug loading and release rate, targeting ligands, appropriate excipients for biocompatibility and biodegradability.

One of the most attractive formulations for ntb delivery are polymeric nanoparticles (NPs) constituted of chitosan (CS), in particular because of their biocompatibility, biodegradability and mucoadhesion [37, 273, 337, 344, 410]. Chitosan, produced via alkaline deacetylation of chitins, is a polysaccharide consisting of a sugar backbone of β-1,4-linked glucosamine with a low degree of N-acetylation [338]. Due to its cationic character together with the presence of reactive functional groups, CS is an auspicious polymer for controlled-release technologies [339, 341, 342]. CS NPs can be prepared by a variety of techniques such as nanoprecipitation, sieving method, coacervation, emulsion, ionotropic gelation method or reverse micellar method [413]. In this study, CS NPs were prepared via ionotropic gelation under mild aqueous conditions using a bridging agent [43]. Due to the aforementioned advantages, CS NPs are particularly suitable for intranasal CNS delivery of fragile cargo such as proteins, peptides or nucleic acids, although they have mostly been used for the delivery of small molecules in the past [343, 344].

Furthermore, it has been demonstrated that the utilization of targeting ligands can enhance the efficacy and specificity of ntb delivery because the target area located at the upper end of the nasal cavity is particularly hard to reach. Here, specific surface ligands can increase residence time at the target area and, hence, reduce mucociliary clearance resulting in higher efficacy compared to non-targeted delivery [336, 354, 355]. In this work, transferrin (Tf) was explored as potential targeting ligand on the surface of CS NP as a well-known glycoprotein targeting Tf-receptors, which are widely expressed inside the human nasal cavity [359, 360]. Cells can recognize Tf, which triggers receptor-mediated endocytosis leading to longer residence times of NPs in the epithelium [364]. The many primary amine groups in proteins such as Tf render them susceptible to chemical modifications and suitable for linker attachment. For bioconjugation of Tf on the surface of CS NP, a copper-free click reaction method was used as described previously [271].

Here, we report the preparation as well as physicochemical, *in vitro* and *in vivo* characterization of CS NPs with and without Tf as targeting ligand as potential drug delivery system for ntb delivery of proteins.

3 Materials and Methods

3.1 Materials

Chitosan (5-20 mPa·s, 0.5 % in 0.5 % Acetic Acid at 20 °C, deacetylation degree of 85 %) was purchased from TCI Chemical Industry Co., LTD (Tokio, Japan). Ethyl 5-bromovalerate, 1-ethyl-3-(3-dimethylaminopropyl)carbodiimide (EDC), N-hydroxysuccinimide(NHS), DMSO, 2-(N-morpholino)ethanesulfonic acid (MES), human holo-transferrin expressed in rice, pentasodium-tripolyphosphate (TPP), β-galactosidase (βGal) from Aspergillus oryzae, 2-nitrophenyl ß-D-galactopyranoside (ONPG), EMEM (Eagle's Minimum Essential Medium), L-glutamine, penicillin/streptomycin, fetal bovine serum (FBS), DMEM (Dulbecco's Modified Eagle Medium), Dulbecco's Phosphate Buffered Saline (PBS), epidermal growth factor, insulin, hydrocortisone, trypsin-EDTA, D-(+)-glucose, β-mercaptoethanol, acetic acid 100%, and other routine chemicals were obtained from Sigma-Aldrich (Taufkirchen, Germany) and used as received. ATTO647N-NHS dye and ATTORho6G-alkyne dye

were bought from ATTO-TEC GmbH (Siegen, Germany). The human nasal squamous carcinoma cell line RPMI 2650 was obtained from Cell Lines Services (Eppelheim, Germany). Air-liquid interface (ALI) differentiation medium was bought from Lonza (Basel, Switzerland).

3.2 Nanoparticle preparation

Preparation of chitosan nanoparticles was conducted via ionotropic gelation method according to a previously published and well-established protocol [43]. In brief, 5 mg chitosan (CS) were dissolved in 5 mL of 25 mM acetate buffer pH 5.0 while stirring overnight. Pentasodium-tripolyphosphate (TPP) was dissolved in highly purified water with a final concentration of 1 mg/mL. Due to its anionic character, TPP serves as a bridging agent to the positive charges of chitosan during NP preparation. Both solutions were filtered through a 0.22 µm mixed-cellulose-ester filter. While stirring at 1000 rpm, 2 mL of TPP solution were quickly added to the chitosan solution and stirred for 2 h. Successful nanoparticle formation was indicated by a slightly opaque suspension color. Subsequently, nanoparticles (NPs) were centrifuged on a 20 µL glycerol bed with a speed of 10,000 rpm at 4°C for 45 minutes. Afterwards, the supernatant was removed and stored for analysis of encapsulation efficiency. Loaded nanoparticles were obtained by addition of 2 mg β-galactosidase (βGal) or ATTO647N labeled β-galactosidase (ATTOGal) to the TPP solution before mixing with chitosan. Fluorescent labeling of β-galactosidase with ATTO647N dye was performed according to the manufacturer's protocol using a 2-fold molar excess of dye. Briefly, βGal solution with a concentration of 5 mg/mL was reacted with ATTO647N-NHS dye in DMSO for 1 h at room temperature. Then, the protein-dye-conjugate was purified using a Sephadex G25 column. Preparation of transferrin decorated chitosan nanoparticles (Tf-CS NPs) was conducted according to protocols described earlier [271]. Briefly, azide-modified CS was mixed in a 1:1 weight ratio with regular CS to a final concentration of 1 mg/mL in 25 mM acetate buffer pH 5.0 (CS mixture). Alkyne-modified transferrin was dissolved in highly purified water at a concentration of 4 mg/mL. CS mixture was filtered through a 0.45 µm mixed-cellulose-ester filter. TPP and βGal, or ATTOGal respectively, were dissolved in highly purified water at a concentration of 1 mg/mL each. After adding the bridging agent TPP and protein to the CS solution, the dispersion was stirred for 1 hour

before adding 1 mL of alkyne-modified transferrin. This reaction mixture was stirred for another hour at 1000 rpm. Then the nanoparticles were centrifuged at 10,000 x g for 45 min on a 20 µL glycerol bed and the supernatant was removed.

3.3 Size and surface charge measurement

Hydrodynamic diameter and polydispersity index (PDI) was examined by dynamic light scattering, whereas laser Doppler anemometry was applied for zeta potential analysis. A volume of 100 µL of NPs resuspended in highly purified water was added into a disposable micro-cuvette (Malvern Instruments, Malvern, UK). Then, hydrodynamic diameter as well as PDI was determined with a Zetasizer Nano ZS (Malvern Instruments) at 173° backscatter angle running 15 runs three times per sample. Viscosity of 0.88 mPa*s and a refractive index of 1.33 were considered for Zetasizer software data analysis. Subsequently, NPs were diluted with 900 µL 10 mM NaCl, and 700 µL of this suspension were transferred to a folded capillary cell (Malvern Instruments) to perform three zeta potential measurements per sample using the same device.

3.4 Encapsulation efficiency

A modified version of a previously published ß-galactosidase assay was conducted to assess enzymatic activity and, thereby, determine encapsulation efficiency [287, 288, 371]. For this analysis, supernatants after centrifugation were used. Briefly, in a transparent 96-well plate 8.33 µL of supernatant was added to 158.33 µL enzyme buffer containing 60 mM Na_2HPO_4, 60 mM NaH_2PO_4, 1 mM $MgSO_4$ and 0.27% ß-mercaptoethanol. For measurement of blank samples, 167.66 µL of enzyme buffer were used. A calibration curve was generated based on known concentrations of βGal following the same procedure as for samples. First, the plate was equilibrated at 28°C for 5 min in a plate reader (Tecan Group AG, Männedorf, Switzerland). Then, 33.3 µL of 2-nitrophenyl ß-D-galactopyranoside (ONPG) with a concentration of 4 mg/mL in highly purified water were added to each well. The enzymatic reaction was recorded for 10 min. The amount of encapsulated protein was determined by

$$EE\ [\%] = \left(1 - \frac{c_{free\ bGal}}{c_{max.\ bGal}}\right) * 100\%. \quad [1]$$

3.5 Scanning electron microscopy

The morphological structure of chitosan nanoparticles was observed via scanning electron microscopy (SEM). The SEM images were recorded using a FEI Helios G3 UC scanning electron microscope equipped with an EDX-detector and a focused ion beam and operated at an applied voltage of 5.0 kV. Samples were prepared by dropping freshly manufactured nanoparticles on aluminum sample holders. After drying under compressed air, samples were covered with a carbon layer before analysis.

3.6 Release kinetics

Release studies of βGal loaded CS NPs and Tf-CS NPs were conducted using 5% glucose and artificial nasal fluid (ANF) as two different media. ANF was prepared according to literature and contained sodium chloride (8.77 mg/mL), potassium chloride (2.98 mg/mL) and calcium chloride dihydrate (0.59 mg/mL) in highly purified water [388]. After preparation, NPs were redispersed in 3 mL of the respective media and placed into an orbital shaking incubator at 37°C and 250 rpm shaking. At scheduled time points (15 min, 30 min, 45 min, 1 h, 1.5 h, 2 h, 3 h, 4 h, 5 h, 6 h), 125 µL of sample was drawn and replaced with fresh media. The samples together with known βGal concentrations for the generation of a calibration curve were measured with the same enzymatic assay as was used for the determination of encapsulation efficiency. Empty NPs were used as blank control.

3.7 Mucus permeation

For the assessment of NP permeation through mucus, artificial nasal mucus (ANM) was prepared by adding 0.5% (w/v) of mucin to ANF. In the next step, 50 µL of ANM were added on top of a fresh Transwell™ membrane insert (8 µm pore size, ∅ 0.33 cm, Corning, NY, USA). The basolateral chamber was filled with 300 µL of

PBS. Subsequently, CS NPs or Tf-CS NPs redispersed in PBS were added on top of the mucus layer at a concentration of 0.1 mg/mL. At distinct time points, the PBS was removed from the basolateral chamber and replaced with fresh PBS. The samples were analyzed for ATTOGal fluorescence in a plate reader (Tecan Group AG, Männedorf, Switzerland) at an excitation wavelength of 620/20 nm and an emission wavelength of 664/20 nm. As a control, NP permeation was also assessed on membranes without ANM. The percentage of NP permeation was calculated by dividing the mean fluorescence intensity (MFI) of the samples at a distinct time points by the MFI of the control sample at the same time point.

3.8 Fluorescence Correlation Spectroscopy (FCS)

NPs containing ATTOGal were prepared as described above. Prior to imaging, NPs were resuspended in 2 mL of ANF and then further diluted in ANF or ANM. As controls, ATTO647-NHS and β-Gal-ATTO647N solutions were prepared in both ANF and ANM. Next, 20-30 µL of each sample was added to an 8-well LabTek I slide (VWR, Radnor, USA). The FCS measurements were performed on an in-house-built laser scanning confocal microscope as described elsewhere [414] with a 60X water immersion objective (Plan Apo 60x WI/NA 1.27, Nikon). A 635 nm pulsed diode laser (LDH-P-C-635M, PicoQuant) was used for excitation at a laser power of 4.5 µW before the objective. The fluorescence emission was separated from the excitation pathway with a quad-line 405/488/561/635 beamsplitter (Semrock, West Hernietta, USA) and detected with an avalanche photodiode detector (APD) (Count® Single Photon Counting Module, Laser Components) after a 635 nm longpass (AHF Analysentechnik, Tübingen, Germany) emission filter. The alignment of the system was routinely checked by measuring an aqueous solution of ATTO655-COOH with FCS.

The FCS data were acquired for 5-15 min by recording the emitted photons with the APD on a time-correlated single-photon-counting card (TCSPC, SPC-150 Becker and Hickl, Berlin, Germany) and then analyzed with PIE Analysis in MATLAB (PAM) [415]. Depending on the sample, the autocorrelation functions (ACFs) were fit with a diffusion model containing up to three diffusional components. A 3D Gaussian focus shape is assumed, yielding an ACF given by:

$$G(\tau) = \frac{\gamma}{(A_1 + A_2)^2}\left\{\left[A_1\left(1 + \frac{4D_1\tau}{\omega_r^2}\right)^{-1}\left(1 + \frac{4D_1\tau}{\omega_z^2}\right)^{-\frac{1}{2}}\right] + \left[A_2\left(1 + \frac{4D_2\tau}{\omega_r^2}\right)^{-1}\left(1 + \frac{4D_2\tau}{\omega_z^2}\right)^{-\frac{1}{2}}\right]\right\}\left(1 + \frac{T}{1-T}e^{\tau/\tau_T}\right). \quad [2]$$

where τ is the time lag of the correlation, D_i represents the diffusion coefficient of the species *i* and the lateral and axial focus sizes are indicated with ω_r and ω_z, respectively, (i.e. the distance between the center of the focal volume and the lateral or axial position where the intensity has decayed by $1/e^2$). For a 3D Gaussian distribution, the shape factor γ is $2^{-3/2}$. N_T represents the total number of fluorescent molecules in the observation volume. f_i represents the amplitude of each species and would be equal to the fraction of each species if they have equal brightnesses. In this case, $f_i = \frac{N_i}{N_T}$, where N_i is the number of molecules of species *i* and $N_T = N_1 + N_2 + N_3$. When the brightness of each species is not equal, as is the case here, the relative brightness of each species needs to be taken into account in the analyses to make an accurate quantification of N_i [416].

3.9 Fluorescence Lifetime Imaging Microscopy (FLIM) and Single Particle Tracking (SPT)

The FLIM measurements were performed on the same laser scanning confocal microscope described in the FCS section. For imaging, a 100×100 µm area is divided into 300 lines and scanned with a frame time of 1s. The raw photon data were analyzed frame-wise via the phasor approach [417] using PAM. The phasor approach is a graphical way to analyze fluorescence lifetime decays. For each pixel of an image with coordinates (*i,j*), the sine and cosine Fourier components are calculated and contribute to the phasor coordinates *g* and *s* according to the following equations:

$$s_{i,j}(\omega) = \frac{1}{M_{Inst}} \cdot \int_0^T I_{i,j}(t) \cdot \sin(\omega t - \Phi_{Inst}) dt \Big/ \int_0^T I_{i,j}(t) dt, \quad [3]$$

$$g_{i,j}(\omega) = \frac{1}{M_{Inst}} \cdot \int_0^T I_{i,j}(t) \cdot \cos(\omega t - \Phi_{Inst}) dt \Big/ \int_0^T I_{i,j}(t) dt, \quad [4]$$

where $I_{i,j}(t)$ is the photon counts at time bin *t* from the TCSPC data of the corresponding pixel (*i,j*). The frequency ω corresponds to 2π/ T, with T being the repetition timescale of the lifetime decay histogram (here 25 ns). The correction factors Φ_{Inst} and M_{Inst} account respectively for the phase shift and the demodulation caused by the instrument response function and are calculated from a calibration measurement of a sample with known lifetime (Atto647N, 3.5 ns, Atto-Tec).

From the two phasor coordinates *s* and *g*, the phase (τ_φ) and modulation (τ_m) lifetime can be determined according to:

$$\tau_\varphi(\omega) = \frac{1}{\omega} \cdot \frac{s}{g}, \quad [5]$$

$$\tau_m(\omega) = \frac{1}{\omega} \cdot \sqrt{\frac{1}{g^2 + s^2} - 1.} \quad [6]$$

The arithmetic average of the phase and modulation lifetimes was used to calculate an apparent lifetime for every pixel.

After extracting the pixel-wise lifetime information, particle detection and tracking was then performed in PAM. First, a wavelet transformation algorithm was used to segment and track single particles, using the same intensity, size and eccentricity filter for all the

samples [418]. Then, for each particle, an intensity-weighted lifetime average was calculated to obtain the particle-wise lifetime value.

3.10 Cell culture

The human nasal squamous carcinoma cell line RPMI 2650 was cultured in EMEM (Eagle's Minimum Essential Medium) supplemented with 1 mM sodium pyruvate, 0.1 mM non-essential amino acids, 2 mM L-glutamine, 1% penicillin/streptomycin and 10% fetal bovine serum (FBS). The cell cultures were maintained at 37°C in a >95% humidified atmosphere of 5% CO_2 with media changes on alternate days. Once 80–100% confluent, the cells were harvested with 0.25% trypsin-EDTA for further experiments.

Additionally, RPMI2650 cells were cultured at the air-liquid interface (ALI). Therefore, they were seeded on PET Transwell™ membrane inserts (1 µm pore size, ∅ 0.33 cm, Corning, NY, USA) with a density of 4 x 10^5 cells/cm^2. After 24 h air-lift was performed by removing the medium from the apical compartment and replacing the medium on the basolateral compartment with ALI differentiation medium. Transepithelial electrical resistance (TEER) values of RPMI2650 cell layers were measured every 4-5 days to evaluate cell monolayer integrity using an epithelial voltohmmeter (EVOM2, WPI, Sarasota, FL, USA) with a chamber electrode (EndOhm, WPI). For the measurement, 700 µL of regular culture medium were added to the electrode chamber and 150 µL to the apical compartment of the insert. The obtained TEER values were corrected by subtracting the mean resistance of blank porous PET membranes. After incubation for 21 days at 37°C and 5% CO_2, cells exhibited steady TEER values and were used for further experiments.

3.11 Cell viability

For cell viability assessment via MTT assay, RPMI2650 cells were seeded in a 96-well plate with a density of 5 x 10^3 cells/well 24 h prior to the experiment using phenol red free EMEM medium. Cells were treated either with different concentrations (25 µg/mL, 50 µg/mL, 100 µg/mL) of empty or βGal loaded CS NPs and Tf-CS NPs, and incubated for 24 h at 37°C, 5% CO_2. Correspondingly, untreated cells were incubated as blank

controls and every sample was analyzed in triplicate. Subsequently, 10 µL of MTT solution with a concentration of 5 mg/mL in PBS was added to each well. After an incubation time of 4 h at 37°C and 5% CO_2, medium was removed and 100 µL DMSO were added to each well. Samples were incubated at room temperature in the dark for 30 min before measuring absorption at 570 nm using a Tecan plate reader (Tecan Group AG, Männedorf, Switzerland).

3.12 Cellular uptake in liquid and ALI culture

Cellular uptake experiments were conducted with RPMI2650 cells in liquid and ALI culture. For liquid culture uptake, RPMI2650 cells were seeded in a density of 5 x 10^4 cells/well in a 24-well plate. After 24 h incubation at 37°C they were treated with free ATTOGal, empty CS NPs, ATTOGal loaded CS NPs, or Tf-CS samples, respectively, at a concentration of 0.1 mg/mL. ALI cultures were treated analogously. Hereby, one half of the samples was incubated at 37°C and the other half at 4°C to distinguish between active uptake and adhesion to the cell surface. After 4 h incubation, cells were harvested via trypsinization, washed twice with PBS before resuspension in 400 µL PBS containing 2 mM EDTA. Samples were analyzed via flow cytometry using 637 nm excitation and a 670/14 nm emission filter. All cells were gated according to morphology based on forward/sideward scattering, and 10,000 events were evaluated per sample.

3.13 Confocal microscopy

For the analysis of NP uptake into ALI culture by confocal imaging, ALI cells were treated with ATTOGal loaded CS NPs and Tf-CS NPs at a concentration of 0.1 mg/mL and incubated for 4 h at 37°C, 5% CO_2. In between all following steps, cells were washed twice with PBS. First, cells were fixed on the apical and basolateral side with 4% paraformaldehyde in PBS for 15 min. Afterwards, Transwell™ insert membranes were cut out with a scalpel and cells were permeabilized with PBS containing 0.3% Tween20 for 10 min. Then, unspecific binding sites were blocked by 60 min incubation with a solution of bovine serum albumin (blocking buffer) and only afterwards the antibody against zona occludens 1 (ZO-1) protein at a concentration of 10 µg/mL was added and incubated for another 60 min. Next, the cytoskeleton was visualized using

rhodamine labeled phalloidin (1:40 dilution of stock solution in blocking buffer), which was incubated with the cells for 40 min. Finally, 4′,6′-diamidino-2-phenylindole (DAPI) was added to cells at a final concentration of 0.5 µg/mL in blocking buffer and incubated for another 10 min. All cells were washed with PBS and mounted using FluoSave reagent prior to analysis with a SP8 inverted scanning confocal microscope (Leica Camera, Wetzlar, Germany).

Furthermore, ALI cultures treated with CS NPs for 4 h were embedded in Cryomatrix™ medium on dry ice to obtain cross sections for improved analysis of cellular uptake. For this procedure, the circular membranes were cut out of the Transwell™ support and the basolateral side was embedded in Cryomatrix™ medium. Afterwards, RPMI2650 cells on the apical side were covered with the same embedding medium on dry ice and stored at -80°C until further processing. Cryosections with a thickness of 7 µm were obtained using a Kryostat CM3050S (Leica Biosystems, Nussloch, Germany). These sections were dried for 4 h on glass slides and then fixed with ice cold methanol and acetone (1:1) for 10 min. Slides were washed three times for 5 min with cold wash buffer (medac diagnostika, Wedel, Germany) while shaking. Subsequently, unspecific binding sites were blocked with blocking buffer for 20 min before incubation with the primary antibody in wash buffer containing 1% bovine serum albumin for 1 h. Glass slides were washed again three times for 5 min with cold wash buffer before treatment with a 1:500 dilution of a fluorescence conjugated secondary antibody in wash buffer containing 1% bovine serum albumin for 30 min in the dark. Afterwards, sections were washed again three times for 5 min with cold wash buffer while shaking. Finally, the slides were counterstained and embedded with ProLong™ Gold Antifade Mountant including DAPI solution overnight in the dark. For control sections, only secondary antibody was used. Fluorescence imaging was performed using a laser scanning confocal microscope LSM700 with the Axio Imager 2 and the Software ZEN 2.3 lite (Carl Zeiss, Wetzlar, Germany). Images were taken with a Zeiss 63x oil immersion objective. Z-Stack images were obtained by taking 2D images in 0.045 µm intervals. In total 24-2D sectional images were captured along the z-axis with the Zeiss 63x oil immersion objective. The pictures and Z-Stack dataset were analyzed, aligned, and modified regarding contrast and intensity, using ZEN 2.3 lite (blue edition). Nucleus staining (DAPI) was illustrated with the emission color blue, Alexa Fluor 488 was

shown in green, while the NP-conjugated with ATTO647N were shown in magenta. Scale bars were added using the free software ImageJ.

3.14 Nanoparticle permeability in ALI culture

For the evaluation of NP passage through the epithelial cell layer, RPMI2650 cells at the ALI were treated with NPs at a concentration of 0.1 mg/mL. Free ATTOGal was compared to ATTOGal loaded CS NPs and Tf-CS NPs. In the basolateral chamber, 300 µL PBS were used as acceptor medium. At distinct time points (15 min, 30 min, 45 min, 1 h, 1.5 h, 2 h, 3 h, 4 h, 5 h, 6 h, 9 h, 12 h and 24 h), the acceptor medium was removed and replaced with fresh PBS. Samples were analyzed for ATTOGal fluorescence in a plate reader (Tecan Group AG, Männedorf, Switzerland) at an excitation wavelength of 620/20 nm and an emission wavelength of 664/20 nm together with an ATTOGal calibration curve. An empty Transwell insert without cells was used as control for NP permeation and the percentage was calculated by defining this control sample as 100% unhindered permeation.

3.15 Animal study

All animal experiments were performed on male C57Bl/6N mice of 6-8 weeks age from Charles River Laboratories (Wilmington, MA, USA) and conducted in accordance with institutional guidelines and approved by the Government of Upper Bavaria. In these experiments, only CS NPs without targeting ligand were used to assess general CS NPs transport into brain tissue. Therefore, CS NPs were labeled with ATTORho6G-alkyne dye according to the manufacturer's protocol. In order to perform intranasal delivery, mice were anesthetized with 4% isoflurane and treated with the labeled CS-NPs intranasally by instilling a total of 25 µL CS NPs in 5 µL increments in alternating nostrils. Mice treated with the same volume of PBS were used as control. For intravenous administration, 25 µL of NP suspension were injected into the tail vein of the mice. After an incubation time of 1 h, mice were anesthetized by an intra-peritoneal injection of medetomidine (0.5 mg/kg), fentanyl (0.05 mg/kg), and midazolam (5 mg/kg) (MMF) (140/10 mg/kg body weight, WDT, Bayer, Leverkusen, Germany), the head was fixed, and an incision was cut into the back of the neck. A small glass capillary was

inserted into the incision in between the first vertebra, and CSF was collected and immediately placed in the -20C° freezer.

3.16 Statistical analysis

All results are given as mean value ± standard deviation (SD) of three individual experiments unless stated otherwise. Statistical significance was analyzed using one-way ANOVA and two-way ANOVA with Bonferroni's and Tukey's posthoc post-test. All statistical analysis was performed using GraphPad Prism version 9.2.0 for Windows (GraphPad Software, San Diego, CA, USA, www.graphpad.com).

4 Results & Discussion

4.1 Physicochemical characterization

Chitosan nanoparticles were prepared via ionotropic gelation method following a previously established protocol [43]. Nanoparticles are formed via electrostatic interactions between positively charged chitosan polymer and the negatively charged bridging agent TPP. This preparation method was chosen because of its mild conditions. In this technique, two aqueous solutions are mixed at ambient temperature while stirring without using organic solvents or sonication. This is especially relevant for the encapsulation of proteins, which can be very labile and sensitive to various stress factors [419]. Numerous formulations were prepared with different chitosan, TPP and protein concentrations to establish preparation conditions for generating NPs with the desired physicochemical characteristics such as size, size distribution, surface potential, encapsulation efficiency and morphology (data not shown). According to Mistry et al., NPs used for ntb delivery should display a size of 100-150 nm with a positive surface potential [386]. Hence, NPs can be transported even through the smallest axons (∅ 100 nm) and have a longer residence time inside the nasal cavity due to an adhesive interaction with the negatively charged mucopolysaccharides [420]. In this regard, optimal CS NPs were formed when the CS/TPP ratio was 5.0 (w/w) which corresponds very well to the optimal ratio of 3–5 for chitosan/TPP (w/w) found by

Calvo et al. [43, 44]. When using excessively lower or higher CS/TPP ratios, either a clear solution was observed indicating almost no particle formation, or larger NPs with low colloidal stability leading to aggregation were obtained. One specific CS NP formulation was selected for successive studies displaying a narrow size distribution and high colloidal stability (**Table 5**). Furthermore, it is known that targeting ligands on the NP surface can improve cellular uptake and NP transport through the epithelial barrier [336, 354, 355]. In this study, transferrin was utilized as a targeting ligand and CS NPs were modified according to a previously established and published protocol [271]. Strain-promoted azide-alkyne cycloaddition reaction was used to attach Tf covalently to the surface of NPs. After chemical modifications to chitosan and transferrin, transferrin was linked to chitosan after particle formation [378, 421, 422]. This formulation was previously optimized to meet the requirements of ntb delivery [271]. The optimal ligand density was determined to be approximately 10 wt% in relation to the NPs. **Table 5** displays the physicochemical characteristics of protein loaded CS NPs and Tf-CS NPs. Both types of NPs show relatively small particle sizes of $<$ 150 nm with narrow size distributions. As expected, Tf-CS NPs are slightly bigger due to the additional macromolecule on the NP surface. Furthermore, they both exhibit positive zeta-potentials deriving from the molar difference between CS and TPP. The decreased zeta-potential of TF-CS NPs can be explained by the ability of transferrin to shield the overall positive charge of CS NPs as is also known for poly(ethylene) glycol decorated nanocarriers [389, 423, 424]. For determination of the encapsulation efficiency, a specific enzymatic reaction of βGal was used. Thus, the assay confirmed that the amount of detected protein was functional after the NP preparation and purification procedure. Both types of NPs showed similar protein encapsulation efficiencies of approximately 50-60% (**Table 5**). Scanning electron microscopy validated the results obtained via dynamic light scattering (**Figure 26**). Although CS NPs showed fusion and aggregation upon air-drying, single particles showed sizes of 120-150 nm with a narrow distribution. Additionally, both NP types exhibited a round shape and smooth morphology.

Table 5. Physicochemical characteristics of βGal loaded CS NPs and Tf-CS NPs (values are given in mean ± SD; n = 3).

	Size [nm]	**PDI**	**ζ-potential [mV]**	**Encapsulation efficiency [%]**
CS NPs	120 ± 16	0.196 ± 0.021	21.9 ± 1.8	61 ± 9
Tf-CS NPs	142 ± 21	0.224 ± 0.047	16.1 ± 2.2	53 ± 6

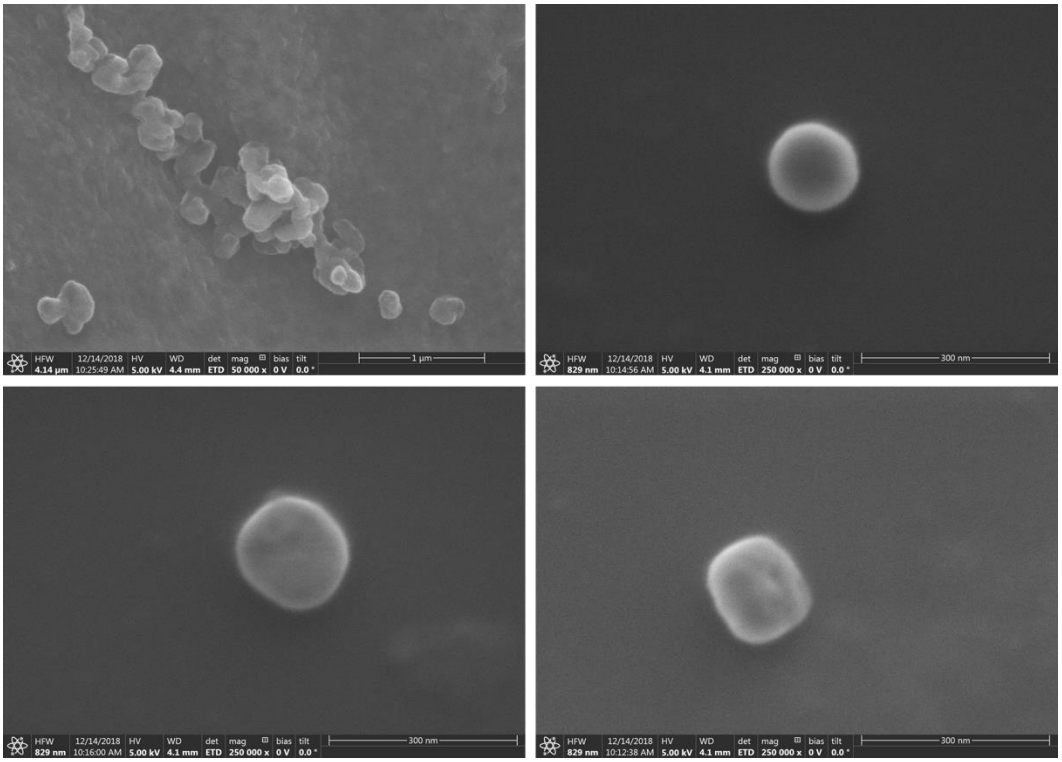

Figure 26. Scanning electron microscopy pictures of freshly prepared chitosan nanoparticles. Top left: Overview of dried CS NPs at a scale of 1 µm. Top right: Picture of a dried single CS NP for the assessment of morphology and smoothness with a scale bar of 300 nm. Bottom: Pictures of dried single Tf-CS NPs for the assessment of morphology and smoothness with a scale bar of 300 nm.

Release studies of βGal loaded CS NPs and Tf-CS NPs were conducted in 5% glucose and artificial nasal fluid to simulate a salt-free and a salt-rich condition. Notably, almost no burst release was observed for both particle types in the two tested media (**Figure 27**). In 5% glucose, a continuous release of βGal over time reaches 50% after approximately 1 h and 100% after about 6 h of incubation at 37°C and shaking. Addition of transferrin on the NP surface did not have an impact on the release kinetics. In ANF, βGal release from CS NPs was a bit faster compared to 5% glucose, especially in the beginning, reaching 50% release after 45 min. A value of 100% release was reached after about 6 h and is comparable to the data obtained in 5% glucose. Tf-CS NPs displayed a much slower βGal release in ANF compared to both CS NPs and to the release in 5% glucose, reaching 50% only after 4 h and just about 70% after 6 h of incubation. This observation is most likely attributed to the shielding characteristic of Tf on the NP surface. Nanoparticle modifications with Tf have been described to yield stealth-like properties, rendering particles less prone to colloidal instability in high salt dispersants [389, 425]. βGal

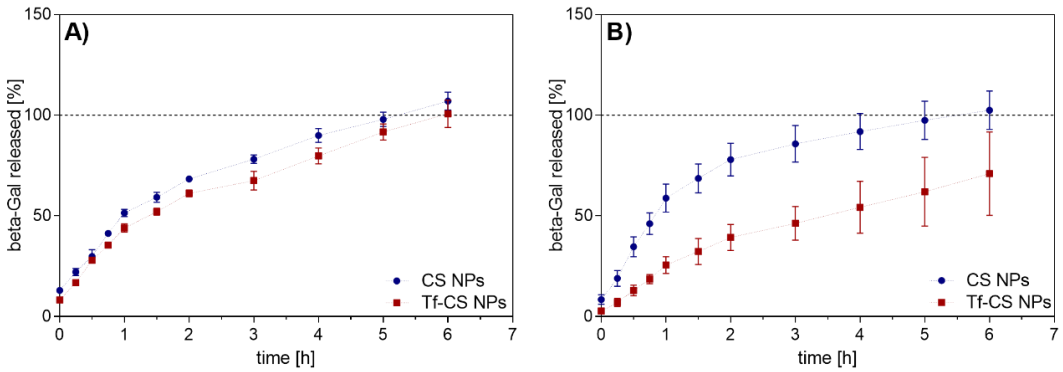

Figure 27. Release kinetics of βGal loaded CS NPs and Tf-CS-NPs over a time period of 6 h in A) 5% glucose and B) artificial nasal fluid. (values are given in mean ± SD; n = 3).

4.2 Mucus permeation

Human nasal mucosa naturally produces a substantial amount of nasal mucus in the physiological healthy state, protecting the nasal mucosa from drying out and trapping unwanted substances [426]. In general, mucus is a viscoelastic gel with mucin as the major component. The term “mucin” comprises a family of high molecular weight, heavily glycosylated proteins secreted mainly by goblet cells and seromucous glands at the apical epithelium [21]. Due to their large size (2 – 50 MDa) and complex structure, mucins exhibit a complicated colloidal behavior involving different types of interactions, and their disposition to form aggregates [427]. Human nasal mucus mainly consists of water (95%) together with mucin (0.5 - 2%), other proteins (~1%), lipids (~1%) and high salt concentrations and typically has a lower viscosity compared to mucus from the lower respiratory tract [428-430]. Depending on the intranasal location, mucus is propelled in different directions and with different speeds by the synchronized beating of surface cilia. This results in different mucus turnover times for respiratory (about 10 min) and olfactory epithelia (up to several days) [349, 431]. Consequently, in some parts of the nasal cavity, nanoparticles can face rapid mucociliary clearance. Additionally, they can also be trapped by mucus due to electrostatic, hydrophobic and hydrogen bond interactions with mucins or by physical entrapment of NPs that are larger than the typical mucus network mesh size (∅ 100 – 200 nm) [432, 433]. Therefore, understanding the exact behavior of CS NPs in mucus is crucial for successful drug delivery. In a first experiment, NP permeation through a mucus layer was assessed. Hence, artificial nasal mucus was added on the apical side of a Transwell™ membrane insert while PBS was filled in the basolateral chamber. Accordingly, permeation of ATTOGal loaded into CS NPs or Tf-CS NPs was tracked over time via fluorescence of the labeled protein. As a control regarding membrane retention alone, the permeation through empty membranes was recorded. As **Figure 28** shows, both types of NPs are restrained by the ANM compared to permeation without mucus. However, the cumulative amounts of NPs passing through the mucus layer converge over time. These findings demonstrate that chitosan nanoparticles with a size of 120 – 150 nm can pass the mucus network mesh stating that NP permeation is hindered but not blocked. The mucoadhesive properties of chitosan are widely known [337, 338, 434, 435]. They are mainly attributed to the positively charged amine

groups. During the addition of TPP as bridging agent during nanoparticle preparation, electrostatic interactions between the positively charged amine groups and negatively charged phosphate groups are formed. Hence, a decreased number of free amine groups is available for interaction with negatively charged mucins. Furthermore, addition of transferrin as targeting ligand on the NP surface shields positive charges, presumably leading to further decreased electrostatic interactions [389]. However, the mucus permeation rate of CS NPs and Tf-CS NPs is very similar (**Figure 28C**). A slight difference can only be seen after 3 h. This is explained by the fact that the actual amount of transferrin on the NP surface is rather low (10 wt% with regard to NP weight). While this amount of modification seems enough for enhanced colloidal stability of the particles (**Figure 27B**), the reduction in surface potential might not be pronounced enough for significantly reduced mucus interaction. For PEGylation, for example, it is reported that only a very dense layer of low molecular weight PEG is able to shield NPs and increase their mucopenetration [436, 437]. Hereby, the molecular weight of PEG as well as the degree of surface coverage can influence the mucus transport rate immensely. In summary, the mucus permeation assay provides evidence for both permeation as well as the interaction of NPs with mucus. However, these results should be taken as an estimate since the mucus thickness in this assay is calculated to be approximately 1 mm due to its viscosity, while the thickness of physiologic human mucus is between 5 - 100 µm [438]. Therefore, fluorescence correlation spectroscopy (FCS) in combination with fluorescence lifetime imaging microscopy (FLIM) and single particle tracking (SPT) were performed to study the interaction of ATTOGal loaded CS NPs and Tf-CS NPs with ANM in detail.

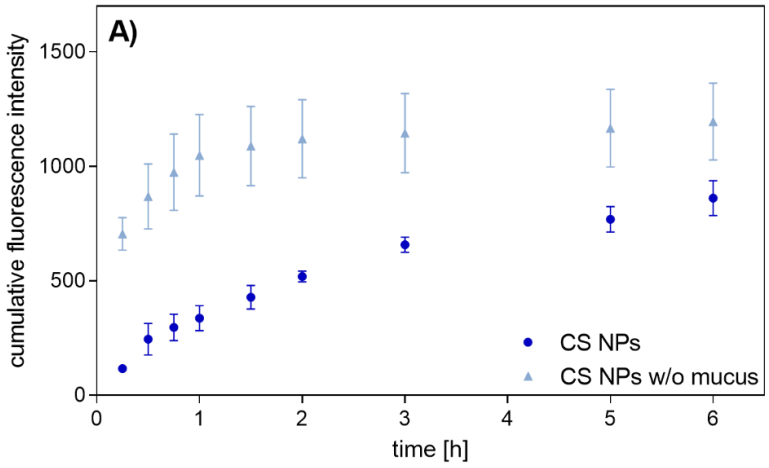
A)
cumulative fluorescence intensity
1500
1000
500
0
0
1
2
3
4
5
6
time [h]
CS NPs
CS NPs w/o mucus

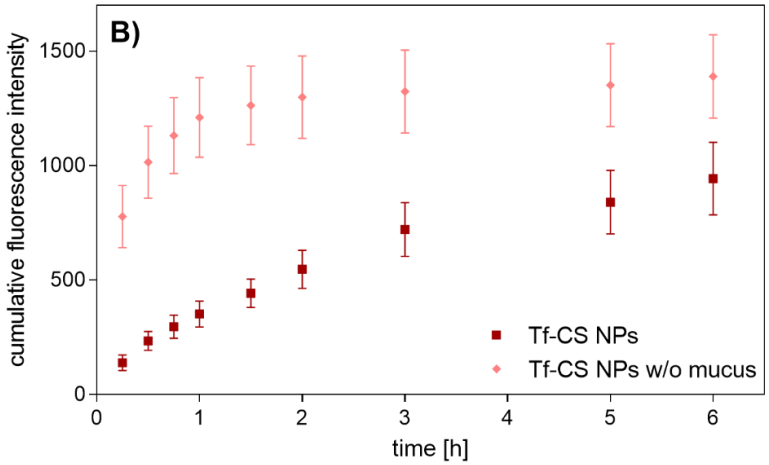
B)
cumulative fluorescence intensity
1500
1000
500
0
0
1
2
3
4
5
6
time [h]
Tf-CS NPs
Tf-CS NPs w/o mucus

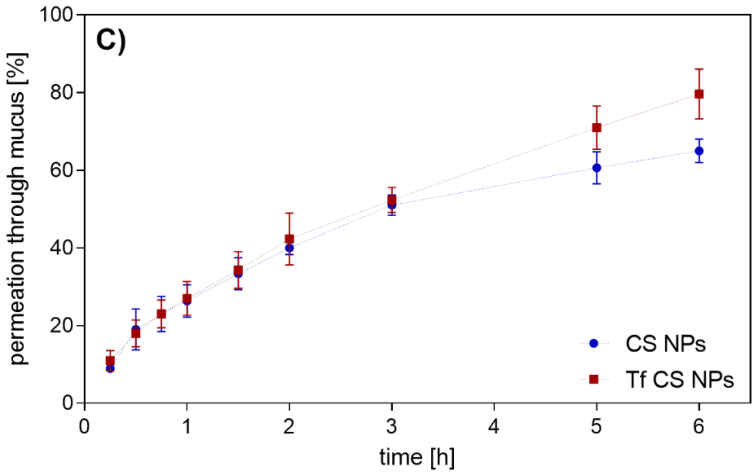
C)
permeation through mucus [%]
100
80
60
40
20
0
0
1
2
3
4
5
6
time [h]
CS NPs
Tf CS NPs

Figure 28. Permeation of CS NPs and Tf-CS NPs through artificial nasal mucus. A) Permeation rate of CS NPs through ANM coated membrane (dark blue) and permeation through the support membrane only (light blue), both presented as cumulative fluorescence intensity. B) Permeation rate of Tf-CS NPs through ANM coated membrane (dark red) and permeation through the support membrane only (light red), both presented as cumulative fluorescence intensity. C) CS NPs and Tf-CS NPs passing through an ANF coated membrane over time calculated as percentage of the control (support membrane only). (values are given in mean ± SD; n = 3)

For FCS experiments, ATTOGal loaded CS NPs and Tf-CS NPs were freshly prepared and dispersed either in ANF or ANM prior to analysis.

Figure 29 displays FCS curves of both types of NPs and free ATTOGal in ANF (A) and two types of ANM containing either 0.5% mucin (B) or 1% mucin (C). In ANF, the free protein curve was fit with two components, a fast component (D = 321 µm^2/s), indicating the presence of free dye in solution and one representing the protein (D = 34 µm^2/s). Fitting of the ACFs for both types of NPs required three components, indicating the presence of a small amount of free dye, free protein released from the NPs and intact particles. However, since the diffusion coefficients (D) of NPs (D = 1.4 µm^2/s for CS NPs; D = 1.0 µm^2/s for Tf-CS NPs), the free protein and the free dye differ substantially from each other, the individual components can be retrieved from the fit to the ACF (**Table S5**). From literature, it is known that NPs prepared by ionotropic gelation method show good stability regarding protein encapsulation [439, 440]. Here, the observation of a species with a diffusion component around 1 µm^2/s suggests that some protein is still encapsulated within the NPs. However, for the FCS curves in ANM (0.5 % mucin and 1% mucin), there is no substantial difference between both types of NPs and free protein. All three curves show a very fast component, attributed to free dye, a second slower but highly variable component (D = 7-38 µm^2/s) and a third very slow diffusional component (D = 0.08-0.50 µm^2/s) (**Table S5**). For all samples, i.e. ATTOGal, CS NPs and Tf-CS NPs, the second component can be attributed to free protein since it has a value compatible with the ATTOGal in ANF and the slower diffusion can be explained by the higher viscosity of ANM or the formation of small sized aggregates. This indicates that both NPs are unstable and release some protein. The third, slow component is more difficult to interpret. For the ATTOGal sample, this very slow component is most likely due to aggregates of free protein and mucins. This

is supported by the absence of this component for free ATTOGal in ANF (**Figure S9 and Table S5**). However, for the NPs samples, it is unclear whether this component can be attributed to NPs diffusion, slowed by the viscosity of the mucus, or due to the same protein-mucin aggregates present in the ATTOGal sample. Thus, based on diffusion alone, we cannot distinguish to the possibilities. Furthermore, we noticed that measurements in the presence of mucin are difficult as the amount of mucin-protein aggregation is variable, as can be seen by comparing the FCS curves of free ATTOGal in 0.5% mucin from four independent experiments.

Therefore, to try to distinguish between intact NPs and protein-mucin aggregates, fluorescence lifetime imaging microscopy (FLIM) was performed. These experiments were performed in ANM with 0.5% of mucin to limit the technical challenges of the highly viscous ANM. The results of the FLIM analysis are shown in XXX. For experiments with ATTOGal alone in ANM, a fluorescence lifetime around 3.5 ns was measured (typical for ATTO647N) with no lifetimes lower than 2.8 ns were observed (***Figure 30***, top panels) and incubation of ATTOGal for two hours in ANM did not affect its lifetime distribution (***Figure S9***). When the protein is incorporated into the NPs, some quenching occurs and a distribution of lifetimes is observed. FLIM of both types of NPs in ANM was analyzed after 0 min, 30 min, 60 min and 120 min. Free ATTOGal in ANM and NPs in ANF at time 0 were used as controls. A dotted vertical line is shown at a fluorescence lifetime of 2.8 ns, separating potential freely diffusing aggregates from encapsulated proteins. This means that lifetimes clearly below 2.8 ns can be attributed to NPs, while above 2.8 ns could be due to either protein aggregates or encapsulated proteins. For CS NPs in ANF, FLIM analysis confirms that at least 91% of ATTOGal remain encapsulated. In ANM, this ratio changes to 64% of clearly encapsulated ATTOGal for CS NPs and up to 36% of free ATTOGal. Within the first 30 min, the fraction of NPs decreases by another 20% but stays stable throughout the rest of the experiment. For Tf-CS NPs dispersed in ANF, the lifetime distribution contains a significant fraction with a long lifetime. It is known that addition of Tf loosens the particle structure, which would lead to less quenching of the fluorescently labeled βGal. In general, the NP preparation method of ionotropic gelation relies on the interactions between the positively charged amine groups of CS and the negatively charged phosphate groups of TPP. For Tf-attachment, CS was modified chemically on

approximately one third of the amine groups. Therefore, less free amines are available to undergo electrostatic interactions with the phosphate groups, causing a loosening in particle structure. As we did not detect a high fraction of released βGal in ANF from FCS measurements (**Figure 29**), we attribute this longer lifetime component to less quenching of the fluorophore. After dispersion of Tf-CS NPs in ANM, the fraction of particles with a fluorescence lifetime below 2.8 ns drops from 39% to only 26% within 30 minutes but then remains stable. Hence, a good fraction (~2/3rds) of the Tf-CS NPs remain stable, at least for two hours, in ANM.

In general, analyzing and predicting NP stability in mucus is challenging. The passage of both types of NPs through a thin ANM layer did not differ significantly. The mucus permeation experiment did not reflect the exact physiological conditions due to higher mucus thickness, although it has been widely used [441, 442]. FCS analysis showed good stability of both NP types in ANF but was difficult to interpret in ANM. Measurement of the fluorescence lifetime supports the interpretation that CS NPs are stable in ANF and ANM. For Tf-CS NPs, the drop in the slow lifetime component suggests some protein release corresponding to the respective FCS data. However, as only about 1/3rd of Tf-CS NPs seem to dissociate during the first 30 min, they can also be considered stable to some extent.

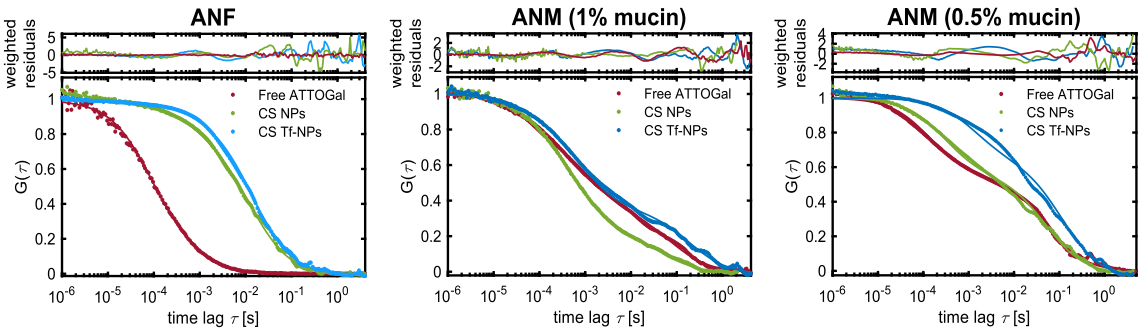

Figure 29. Diffusion of CS NPs in ANF and ANM. Representative ACFs of CS NPs prepared with ATTOGal in (A) ANF and artificial mucus composed of ANF supplemented with (B) 1% mucin and (C) 0.5% mucin. The ACF of free ATTOGal is reported as control.

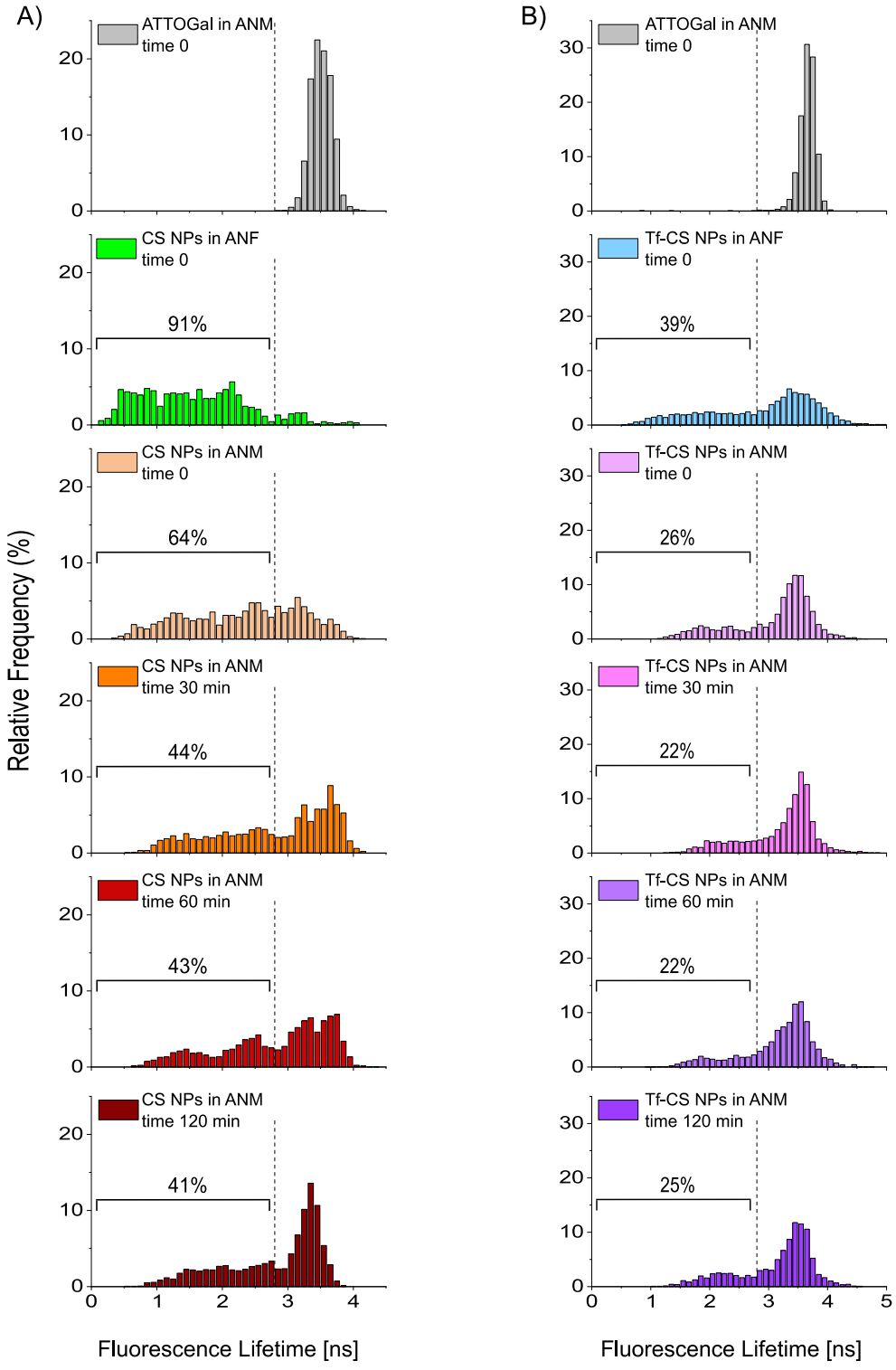
A)
B)
ATTOGal in ANM
time 0
CS NPs in ANF
time 0
91%
CS NPs in ANM
time 0
64%
CS NPs in ANM
time 30 min
44%
CS NPs in ANM
time 60 min
43%
CS NPs in ANM
time 120 min
41%
Tf-CS NPs in ANF
time 0
39%
Tf-CS NPs in ANM
time 0
26%
Tf-CS NPs in ANM
time 30 min
22%
Tf-CS NPs in ANM
time 60 min
22%
Tf-CS NPs in ANM
time 120 min
25%
Relative Frequency (%)
Fluorescence Lifetime [ns]
Fluorescence Lifetime [ns]

Figure 30. Fluorescence lifetime of ATTOGal CS NPs and Tf-CS NPs. Histograms of fluorescence lifetimes of (A) CS NPs and (B) Tf-CS NPs in ANM at different time points, indicated in the panels. The lifetime histogram of the protein aggregates in ANM are reported as reference on the top panel. Dotted lines indicate a fluorescence lifetime of 2.8 ns, i.e., the lowest lifetime value obtained for protein aggregates in mucus. The percentage of particles with lifetime values lower than 2.8 ns is indicated in each panel. The histograms were compiled from 3 independent experimental replicates.

4.3 *In vitro* performance

The safety of chitosan as a pharmaceutical excipient as well as in the form of nanoparticles has already been studied and discussed extensively [443-445]. Nonetheless, the cytotoxicity of CS NPs on RPMI2650 cells at concentrations relevant for this work was evaluated via an MTT assay. Cells were incubated with empty and βGal loaded CS NPs and Tf-CS NPs at three different concentrations. The results confirm the biological safety for all tested samples (**Figure 31**).

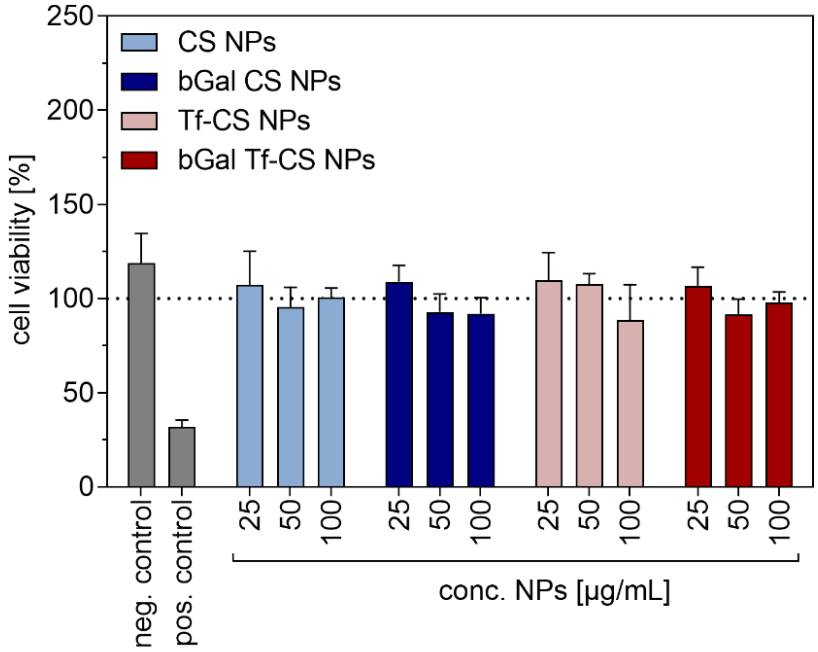

Figure 31. Cell viability of RPMI2650 cells as determined via an MTT assay. Different concentrations (25 µg/mL, 50 µg/mL, 100 µg/mL) of empty and βGal loaded CS NPs

and Tf-CS NPs were presented to the cells and the percentage of viable cells after 24 h are shown. Cells used as negative control were treated with PBS and the positive control was treated with 10% DMSO (values are given in mean ± SD; n = 3).

The cellular internalization of ATTOGal loaded CS NPs and Tf-CS NPs on the human nasal epithelial cell line RPMI2650 was evaluated using flow cytometry. Cells cultured under conventional conditions were compared to cells cultured at the air-liquid interface (ALI). ALI cell culture models represent a valid tool for replicating typical characteristics of the human respiratory tract [397]. They can serve as a promising alternative to refine settings and samples used in animal experiments, complying to the 3R principle. Furthermore, it has to be kept in mind that anatomical differences exist between rodents, which are the most commonly used laboratory animal model, and humans [345]. As an example, the surface area of the respiratory region in rodents accounts for about 50% of the total surface while, in humans, it covers almost 90% of the nasal cavity [15, 446]. Therefore, it is advisable to perform first screening experiments in suitable *in vitro* models before selecting distinct samples for *in vivo* verification. Additionally, *in vivo* experiments should be planned deliberately and all mentioned factors need to be considered when translating the results towards the human situation [447]. Consequently, ALI models are a valuable instrument for screening of drug delivery systems and for narrowing down formulations used *in vivo*. In this experiment, RPMI2650 were cultured on Transwell™ inserts where the apical medium was removed after an incubation time of 24 h. With this so-called airlift and a change of medium in the basolateral chamber, cells start differentiation to a pseudostratified epithelium producing mucus. TEER values were measured every other day and only samples with a value > 50 Ω cm^2 were used for experiments [68]. **Figure 32** shows cellular uptake of NPs in liquid and in ALI culture. As expected, there was no significant cellular uptake of the free protein in both culture types. Encapsulation into CS NPs increased uptake significantly, and even more when attaching transferrin as a targeting ligand. However, the absolute values in ALI culture were not as high as in liquid culture, underlining the impact of mucus on NP transport. As discussed for **Figure 28**, NP permeation is delayed by mucus and, therefore, after 4 h of incubation, less NPs have reached the epithelial cell layer in ALI culture. Furthermore, in previous work, we demonstrated that the transferrin receptor is still expressed at the ALI but not as

strongly as in liquid culture [271]. This is presumably another reason for the decreased uptake values of Tf-CS NPs in ALI culture.

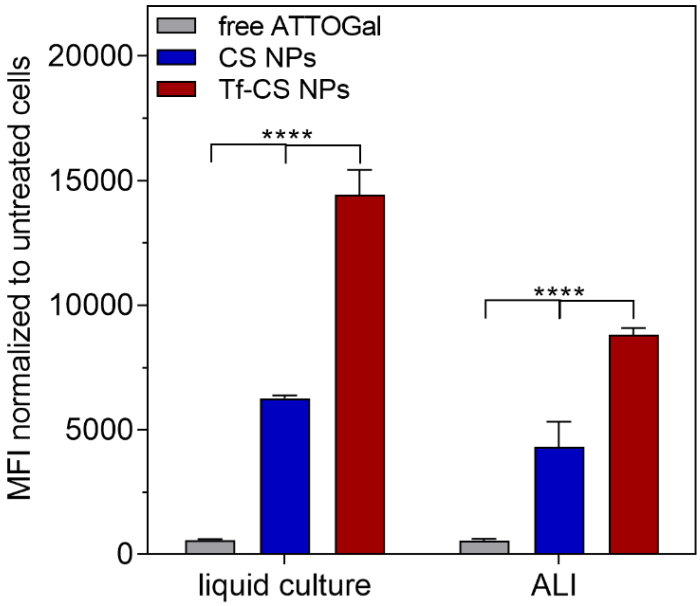

Figure 32. NP uptake into RPMI2650 cells in liquid culture as well as ALI. Comparison of mean fluorescence intensity (MFI) of free ATTOGal with ATTOGal loaded CS NPs and Tf-CS NPs (values are given in mean ± SD; n = 3; Two-way ANOVA, *, $p \leq 0.05$; **, $p \leq 0.01$; ***, $p \leq 0.001$; ****, $p \leq 0.0001$).

For a better understanding of NP passage through the epithelial cell layer, confocal microscopy images were acquired. First, formation of tight junctions as well as cell differentiation by mucus production for RPMI2650 cells cultured at ALI was demonstrated (**Figure S11**). For the experiments, ALI cultures were treated with ATTOGal loaded CS NPs and Tf-CS NPs for 4 h before staining with phalloidin-rhodamine for the cytoskeleton and DAPI for cell nuclei. **Figure 33** illustrates the different NP treatments and resulting effects on cellular uptake in an orthogonal view of a z-stack image. Blue areas depict cell nuclei while red staining reflects the cytoskeleton and yellow staining is attributed to the incorporated ATTOGal protein. **Figure 33A** depicts ATTOGal loaded into Tf-CS NPs and **Figure 33B** For better visualization, protein signals are marked with white arrows. More yellow fluorescent signals can be observed with Tf-CS NPs. Furthermore, after 4 h, the signals of Tf-CS

NPs can be found more towards the basolateral side indicating a faster transport through the epithelial cell layer compared to CS NPs without a targeting ligand. These findings support the results of the cellular uptake presented in **Figure 32**. Consequently, attachment of transferrin on the NP surface leads to receptor mediated endocytosis, which is mainly clathrin-mediated as extensively shown in literature [448-451]. However, the mechanism by which CS NPs are transported through the epithelial cell layer is still elusive. Chitosan alone, as well as in the form of NPs, is known to have the ability to open tight junctions in endothelial and epithelial cell layers to a certain extent, so a paracellular route is imaginable [452, 453]. Additionally, a substantial amount of CS NPs is internalized via endocytosis. **Figure 34** shows a cross-section of CS NP treated ALI culture where nuclei are displayed in blue, CS NPs in pink and clathrin in green. After 4 h of incubation, the majority of CS NPs are still localized towards the apical side of the cell layer. This observation is in good correspondence with the permeation kinetic obtained with the mucus permeation assay (**Figure 28C**). Consequently, the retardation of NPs by mucus leads to a lag time for NPs to reach the epithelial layer and to be internalized by the cells. Furthermore, CS NPs are not co-localized with clathrin, suggesting that the mechanism of endocytosis is rather caveolae-mediated or via macropinocytosis. This theory is supported by the study of El Leithy et al. using different inhibitors to assess the exact uptake mechanism of folic acid-CS NPs into Caco-2 cells [454]. Interestingly, they found that CS NP internalization is mediated by different mechanisms such as caveolae, micropinocytosis and microtubular-mediated endocytosis. However, clathrin-mediated endocytosis did not seem to play an important role. Garaiova et al. stated that chitosan nanoparticles are internalized into HeLa cells through different endocytic pathways involving, to a small extent, clathrin-dependent endocytosis [320]. Several other studies also confirm that cellular internalization of CS NPs is not mediated only by one endocytic pathway [321, 455, 456].

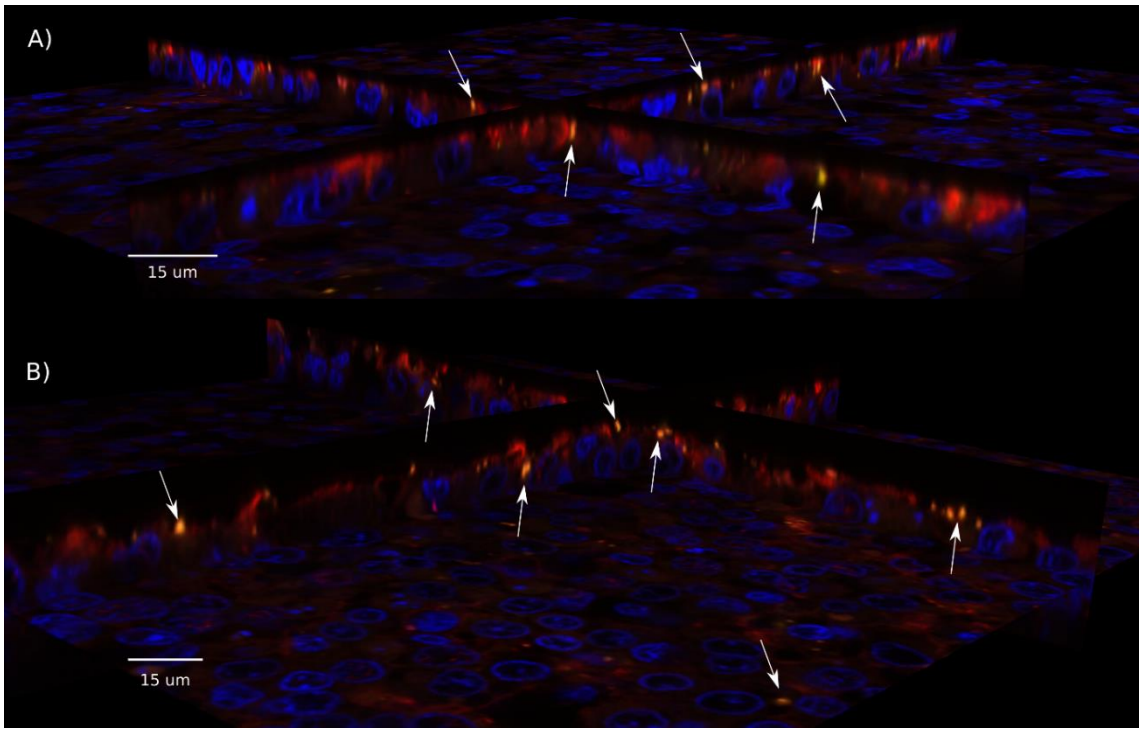

Figure 33. Z-stack confocal images of ALI cultured RPMI2650 cells after 4 h incubation with NPs. Cell nuclei were stained with DAPI (blue), the cytoskeleton with rhodamine (red) and ATTOGal loaded NPs are shown in yellow (indicated by white arrows). A) Tf-CS NPs and B) CS NPs.

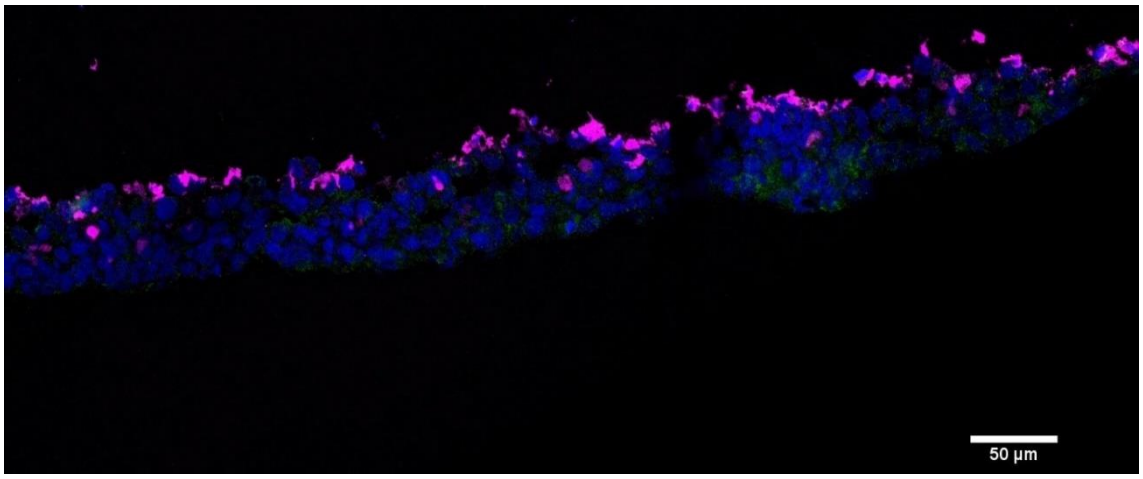

Figure 34. Confocal image of embedded ALI cultured RPMI2650 cells treated with CS NPs (pink) for 4 h. Cell nuclei were stained with DAPI (blue), clathrin was stained with a specific primary antibody and an Alexa Fluor 488 labeled secondary antibody (green).

For successful delivery from the nose to brain tissue, NP passage through the epithelial cell layer is crucial. Hence, CS NP and Tf-CS NP permeation through nasal epithelial cells cultured at the ALI was evaluated over a period of 24 h and results are shown in **Figure 35**. For both NPs, a substantial amount of protein was transported through the epithelial cell layer over time. In the beginning, no difference was detectable between the two types of NPs. However, after approximately 20 h, a non-significant trend of slightly faster Tf-CS NP permeation compared to CS NPs was observed. After 24 h, Tf-CS NP transported 77% ± 10% of the total protein load, and CS NP 54% ± 24%, when compared to the control sample without cells corresponding to 100% permeation.

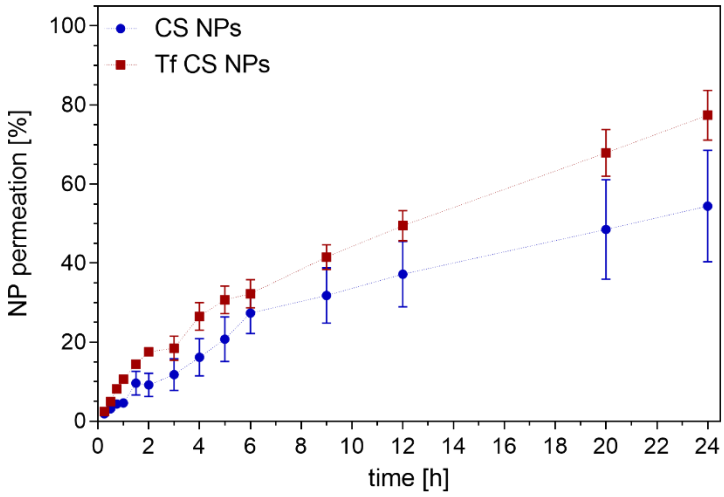

Figure 35. Permeability of CS NPs (blue) and Tf-CS NPs (red) through a mucus covered cell layer of ALI cultured RPMI2650 cells over 24 h (values are given as mean ± SD; n = 3).

4.4 *In vivo* experiments

Mouse experiments were performed to assess the general CNS availability of CS NPs. In this experiment, only ATTORho6G-labeled CS NPs without transferrin were used as Tf-CS NPs displayed less stability in mucus. Mice were anesthetized with 4%

isoflurane and treated with the labeled CS-NPs intranasally by intranasal instillation. As a control, PBS was used. For intravenous administration, NPs were injected into the tail vein of the mice. After 1 h, CSF was collected under anesthesia, and CSF samples were measured for fluorescence in a plate reader. Here, control CSF was spiked with known amounts of labeled CS-NPs in order to assess the amount of NPs that reached the CSF. **Figure 36** shows that 1 h after treatment, approximately 15% of the administered NPs and 5.5% of the administered βGal can be found in the CSF. In comparison, after i.v. administration, neither NPs, nor βGal were detected in the CSF. It has been widely shown that drugs were detectable in the brain tissue already after 30 min to 1 h post-administration [457-460]. Hence, the chosen time point of 1 h gave a sufficient impression of the deliverable amount of NPs to the CSF. The amount of βGal in CSF was measured via an enzymatic assay as described above. Since only chemically and structurally intact βGal can undergo the enzymatic reaction, this assay demonstrates that the detected protein is not affected during the preparation, administration and *in vivo* transport process. In future experiments, a pharmacokinetic study with multiple time points should be conducted to assess the exact concentration curve of βGal loaded CS NPs and to understand the trafficking into CSF.

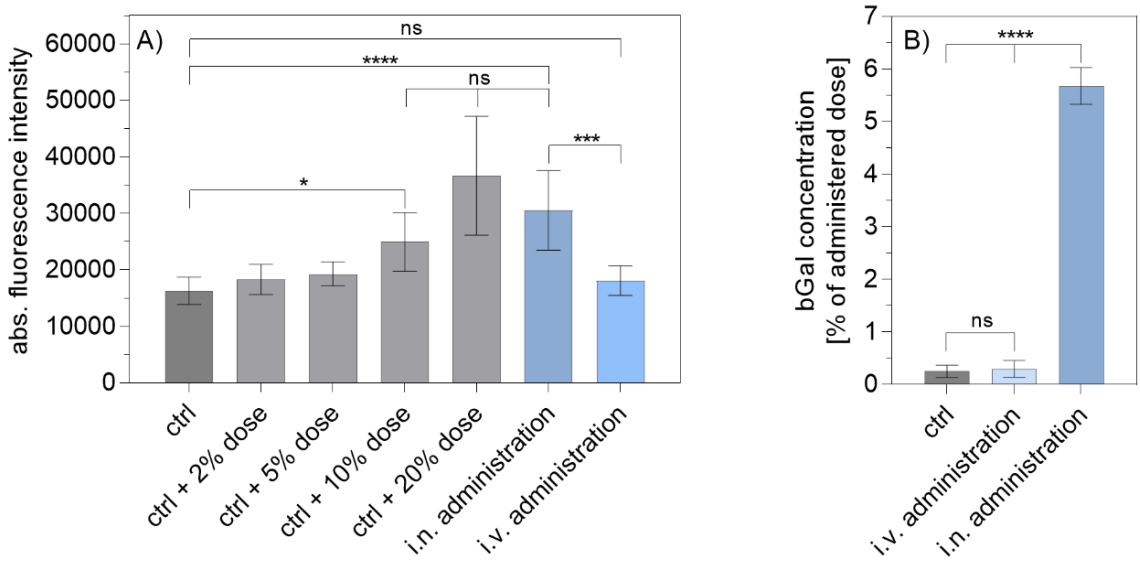

Figure 36. Comparison of intranasal and intravenous administration of CS NPs in mice after 1 h. A) Measurement of fluorescence intensity of the CSF control spiked with 2%, 5%, 10% and 20% of the administered dose and CSF samples after i.n. and i.v. administration; B) Determination of βGal concentration with respect to the administered dose in CSF samples after i.n. and i.v. administration compared to the control (values are given as mean ± SD; n = 3; One-way ANOVA with Tukey's test, *, $p \leq 0.05$; **, $p \leq 0.01$; ***, $p \leq 0.001$; ****, $p \leq 0.0001$)

5 Conclusion

Historically, intranasal drug delivery was only used for allergies or other local treatments. In the last decades, however, the potential of the nasal route to deliver therapeutics to the CNS has gained a lot of interest [345, 461]. Nasal drug delivery to the brain offers many advantages over standard systemic delivery approaches such as noninvasiveness, lower drug dosage compared with systemic administration, no systemic clearance, reduced risk of systemic toxicity and higher patient compliance. Although a number of studies have shown that biologics are able to reach the brain after intranasal administration, suitable formulation platforms are needed for this type of therapeutic agents to prevent premature enzymatic degradation [17, 334]. In this work, CS NPs with and without Tf as a surface targeting ligand were prepared for ntb delivery

of macromolecules. The targeting ligand on the surface of CS NPs can easily be exchanged due to the modular nature of the functionalized nanocarriers, demonstrating the variability of this drug delivery system. It was demonstrated that the mild conditions of ionotropic gelation method led to stable NPs with a good protein encapsulation efficiency and physicochemical characteristics beneficial for ntb delivery. Furthermore, CS NPs were able to cross the mucus covered nasal epithelial cell layer, be transported to the CSF and deliver the intact protein. Although further studies, especially with relevant therapeutic drugs, are needed to assess the therapeutic efficacy of this nanosystem, the results highlight modified CS NPs as a promising formulation to deliver sensitive macromolecules such as therapeutic antibodies to the brain tissue following intranasal administration.

Chapter V – Summary and Perspectives

Within this work, chitosan nanoparticles loaded with biological macromolecules were evaluated as potential drug delivery systems for ntb delivery to patients suffering from neurological diseases. As many newly developed drugs for targeting neurological disorders such as Alzheimer's or Parkinson's disease are macromolecules, they show limited permeability across the BBB in order to reach the brain tissue. Therefore, ntb delivery can be utilized as promising alternative route. Despite numerous advantages such as non-invasiveness, avoidance of first-pass metabolism, rapid onset of action and increased patient compliance, it also has its limitations. Among them, rapid enzymatic degradation of the therapeutic drug as well as low transport efficiency leading to low drug concentration at the target site, are the major obstacles. In this regard, nanotechnology can be used to encapsulate the cargo and facilitate achieving therapeutic drug levels in the brain tissue. Especially chitosan nanoparticles have proven to be promising for transmucosal drug delivery through the epithelial barrier as chitosan is known to exhibit mucoadhesive effects and tight junction opening properties. Furthermore, CS NPs can be prepared under relatively mild conditions and without the use of organic solvents preventing premature degradation of sensitive cargo. Therefore, they are a suitable carrier system for biological macromolecules such as proteins or nucleic acids.

The feasibility of using chitosan nanoparticles as a vehicle for the delivery of macromolecules, particularly proteins, was studied in this work. Within the course of the study, the NP manufacturing process was optimized using a microfluidic mixing technique. This approach improves scalability of the process and, thus, eases potential commercial use of the drug delivery system. It was shown that microfluidic mixing led to reproducible NPs where potential therapeutic macromolecules can easily be changed with minor process modifications leading to similar physicochemical characteristics. Sensitive cargo such as protein, siRNA and mRNA remained intact during manufacturing process and was successfully released from CS NPs in *in vitro* experiments. Therefore, CS NPs can be used as a platform for the transport of numerous cargos sensitive to degradation. Supportive of this conclusion, it was demonstrated that CS NPs could easily be modified on their surface providing the

possibility to attach ligands for more specific and targeted transport. More specifically, NP surface was chemically modified by covalently attaching a functional group capable of undergoing a so-called copper-free “click-reaction” with the targeting ligand, also containing a specific functional group. This chemical modification can be performed under mild hydrophilic conditions after NP formation, not harming the NP structure or sensitive cargo. Furthermore, surface ligands are easily exchangeable depending on the desired target. These characteristics make the CS NPs a modular system that can be adapted to specific drug delivery needs. In an ALI co-culture model, it was demonstrated that surface-modified CS NPs show an increased cellular uptake into nasal epithelial cells, transcytosis and, subsequently, uptake into glioblastoma cells. This demonstrates that by choosing the right surface ligand a dual-targeting effect can be achieved. Ultimately, the ability of CS NPs to successfully cross the nasal epithelial barrier and be transported into brain tissue was confirmed in an *in vivo* mouse experiment. Compared to intravenous administration, a significant amount of CS NPs was found in the CSF 1h after the formulation was administered intranasally.

Conclusively, the results described within this work display the potential of CS NPs to function as effective drug delivery systems in ntb delivery while circumventing the BBB. They can easily be prepared in a scalable microfluidic manufacturing process, be modified under mild conditions, and are capable of transporting sensitive cargo into the brain tissue. There are still some aspects that need to be investigated in more detail in future experiments. Therapeutic molecules, e.g. monoclonal antibodies, should be loaded into CS NPs in order to prove therapeutic efficacy after ntb transport. Also, different targeting ligands must be studied to improve transport specificity. Another important topic that should be addressed in further studies is finding a suitable delivery device that is capable of transporting the NP formulation to the upper end of the nasal cavity into the olfactory region increasing the efficacy of ntb delivery while reducing systemic effects.

Despite the need for further optimization and evaluation, the gathered findings may play a role in bridging the gap of NPs for therapeutic use and might help to bring ntb delivery closer from bench to bedside.

Appendix

1 Supplementary information for Chapter II

Table S1. Size, PDI and Zeta-potential of siRNA CS NPs made using different N/P ratios. TFR 0.5 mL/min, FRR (CS : siRNA) 1 : 2.3. siRNA concentration was kept constant at 1 nmol/mL, while CS concentration was adjusted based on the N/P ratio to be investigated. Results represent the mean ± SD; n = 3 independent batches. The formulation selected for further studies is highlighted in grey.

N/P	Size ± Std. Dev. [nm]	PDI ± Std. Dev.	Zeta-Potential ± Std. Dev. [mV]
1	91.52 ± 0.78	0.29 ± 0.030	+2.96 ± 0.61
1.5	99.48 ± 9.89	0.15 ± 0.010	+5.81 ± 0.77
2	109.77 ± 0.61	0.35 ± 0.010	+4.18 ± 0.39
4	82.68 ± 0.49	0.26 ± 0.004	+4.24 ± 1.07
5	92.10 ± 10.76	0.35 ± 0.070	+4.44 ± 1.16
6	97.75 ± 4.53	0.45 ± 0.030	+5.56 ± 1.35
7	124.80 ± 1.39	0.44 ± 0.020	+5.57 ± 0.53

Table S2. Size, PDI and Zeta-potential of siRNA CS_{TPP} NPs made using different N/P ratios. TFR 0.5 mL/min, FRR (CS : siRNA TPP) 1 : 2.3. CS and TPP concentrations were kept constant at 0.75 mg/mL and 0.15 mg/mL respectively; siRNA amount was modified based on the N/P ratio to be studied. Results represent the mean ± SD; n = 3 independent batches. The formulation selected for further studies is highlighted in grey.

N/P	Size ± Std. Dev. [nm]	PDI ± Std. Dev.	Zeta-Potential ± Std. Dev. [mV]
1	66.12 ± 3.51	0.23 ± 0.007	+2.67 ± 1.96
1.5	67.15 ± 2.47	0.27 ± 0.080	+3.91 ± 1.72
2	77.64 ± 0.43	0.15 ± 0.001	+6.99 ± 0.36
4	80.42 ± 1.92	0.21 ± 0.030	+7.91 ± 1.83
5	84.99 ± 0.75	0.23 ± 0.020	+7.24 ± 0.73
6	89.38 ± 3.85	0.39 ± 0.010	+8.18 ±2.36
7	123.82 ± 9.47	0.35 ± 0.040	+9.45 ± 3.19

Table S3. Size, PDI and Zeta-potential of mRNA CS NPs made using different N/P ratios. TFR 0.6 mL/min, FRR (CS : mRNA) 1 : 3. mRNA concentration was constant at 0.005 mg/mL, while CS concentration was adjusted based on the N/P ratio to be investigated. Results represent the mean ± SD; n = 3 independent batches. The formulation selected for further studies is highlighted in grey.

N/P	Size ± Std. Dev. [nm]	PDI ± Std. Dev.	Zeta-Potential ± Std. Dev. [mV]
1.33	143.30 ± 0.10	0.34 ± 0.010	+1.15 ± 0.36
1.60	122.23 ± 1.67	0.34 ± 0.010	+2.15 ± 1.74
2.22	149.37 ± 0.57	0.26 ± 0.010	+3.16 ± 1.98
4	135.37 ± 7.62	0.40 ± 0.080	+5.89 ± 2.36
5	104.72 ± 8.82	0.22 ± 0.050	+7.70 ± 1.12
7	166.57 ± 1.17	0.24 ± 0.010	+4.75 ± 3.81
8.33	116.33 ± 3.65	0.36 ± 0.070	+3.32 ± 0.24

Table S4. Size, PDI and Zeta-potential of mRNA CS_{TPP} NPs made using different N/P ratios. TFR 0.6 mL/min, FRR (CS : mRNA) 1 : 3. miRNA and TPP concentrations were kept constant at 0.005 mg/mL and 0.05 mg/mL, respectively, while CS concentration was adjusted based on the N/P ratio to be investigated. Results represent the mean ± SD; n = 3 independent batches. The formulation selected for further studies is highlighted in grey.

N/P	Size ± Std. Dev. [nm]	PDI ± Std. Dev.	Zeta-Potential ± Std. Dev. [mV]
1.5	137.13 ± 1.96	0.34 ± 0.010	+2.46 ± 1.92
1.78	120.70 ± 1.99	0.26 ± 0.010	+2.87 ± 1.24
4	142.00 ± 1.40	0.26 ± 0.010	+3.72 ± 0.78
6	76.64 ± 0.43	0.149 ± 0.010	+6.24 ± 1.31
6.67	67.51 ± 3.34	0.19 ± 0.020	+11.33 ± 3.37
8	78.43 ± 0.31	0.24 ± 0.010	+10.64 ± 1.36
9	144.65 ± 3.65	0.25 ± 0.030	+10.93 ± 3.31

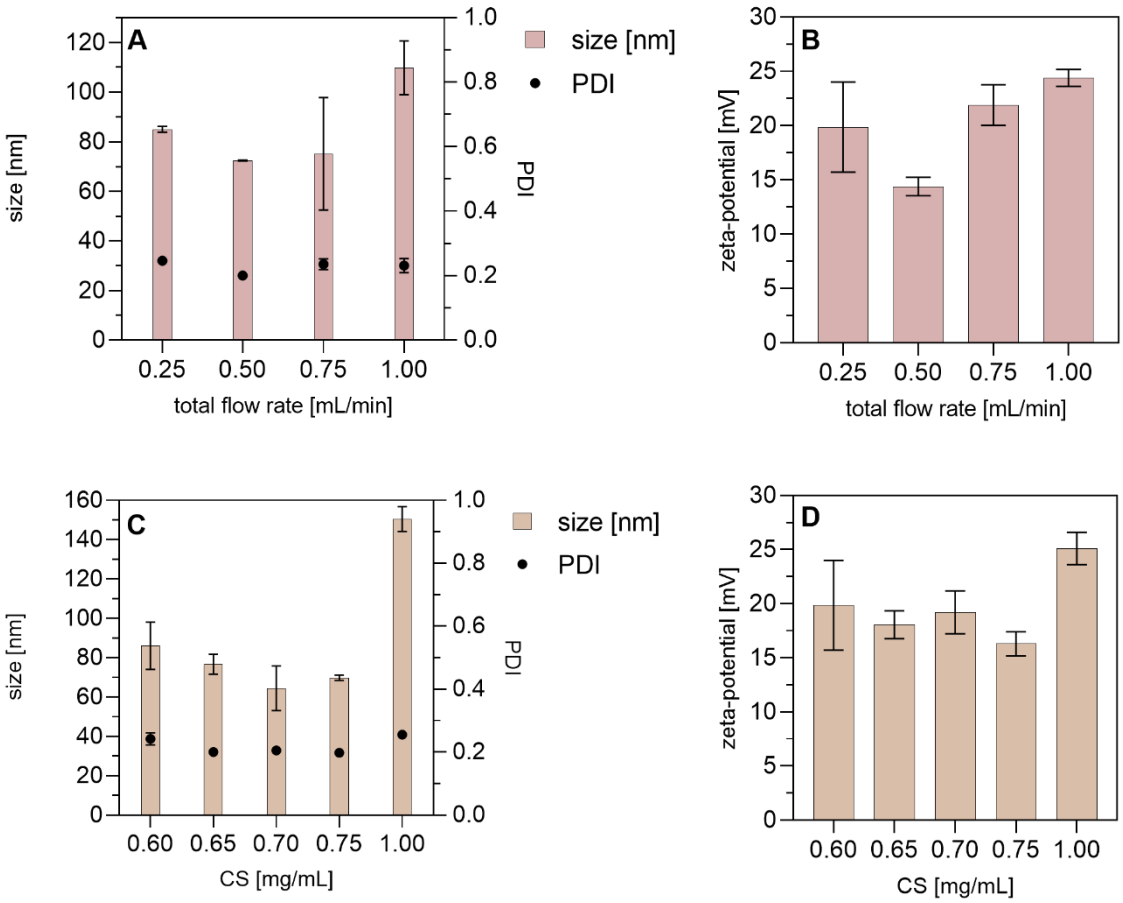

Figure S1. Physicochemical characterization results of empty CS_{TPP} NPs optimization by variation of CS concentration and total flow rate. **A-B)** CS_{TPP} NPs with a CS concentration of 0.75 mg/mL and a TPP concentration of 0.15 mg/mL reached the smallest size of about 75 nm and a zeta-potential of 14 mV at a total flow rate of 0.50 mL/min;

C-D) CS_{TPP} NPs with a fixed total flow rate of 0.50 mL/min and a fixed TPP concentration of 0.15 mg/mL showed the most favorable size (75 nm) and zeta-potential (16 mV) at a CS concentration of 0.75 mg/mL (Results represent mean ± SD, n = 3 independent batches).

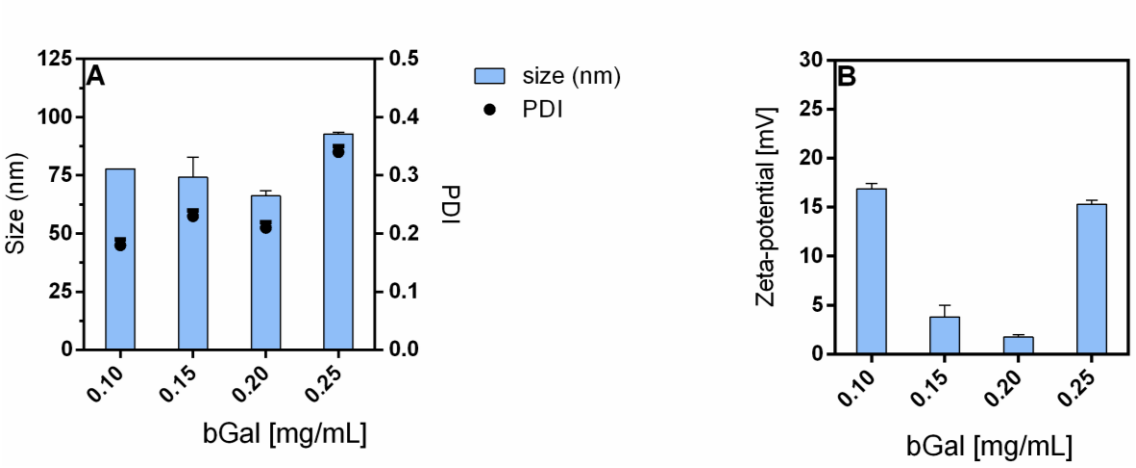

Figure S2. Results of bGal CS_{TPP} NPs optimization by variation of bGal concentration. bGal was diluted in 0.15 mg/mL of TPP to reach the final concentration of 0.10 mg/mL, 0.15 mg/mL, 0.20 mg/mL, and 0.25 mg/mL. CS concentration was constant at 0.75 mg/mL. The best results were obtained at a bGal concentration of 0.10 mg/mL with mean size of 77.80 ± 0.01 nm (**A)** left y-axis), PDI of 0.18 ± 0.01 (**A)** right y-axis), and zeta potential of +16.90 ± 0.53 mV (**B)**). Results represent mean ± SD, n = 3 independent batches.

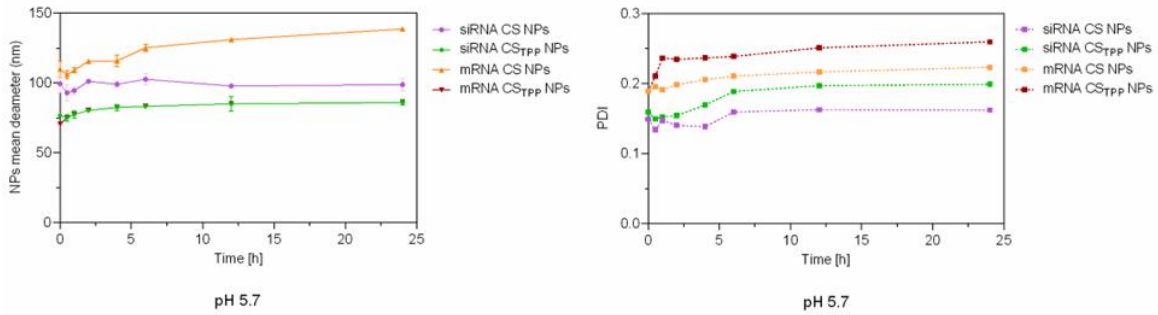

Figure S3. Stability profiles in terms of size (left) and PDI (right) of siRNA CS NPs (violet line), siRNA CS_{TPP} NPs (green line), mRNA CS NPs (orange line), and mRNA CS_{TPP} NPs (red line) in acetate buffer 25 mM pH 5.7 for 24 h at 37 °C simulating the endosomal environment. The results represent the mean normalized absorbance values ± SD; n = 3 independent batches.

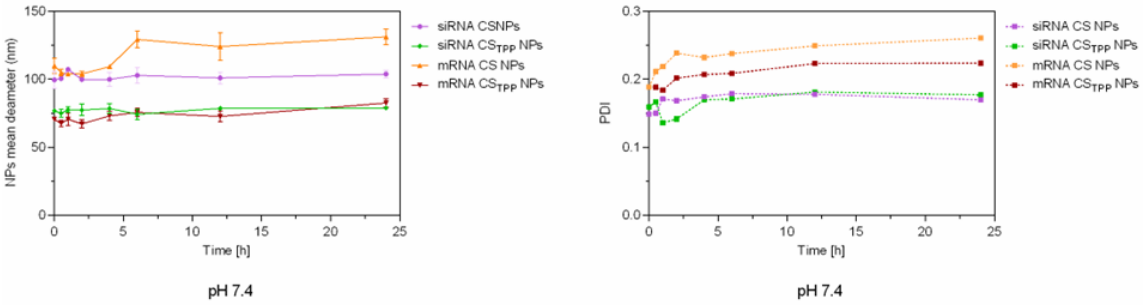

Figure S4. Stability profiles in terms of size (left) and PDI (right) of siRNA CS NPs (violet line), siRNA CS_{TPP} NPs (green line), mRNA CS NPs (orange line), and mRNA CS_{TPP} NPs (red line) in Glucose 5% pH 7.4 for 24 h at 37 °C simulating the physiologic environment. The results represent the mean normalized absorbance values ± SD; n = 3 independent batches.

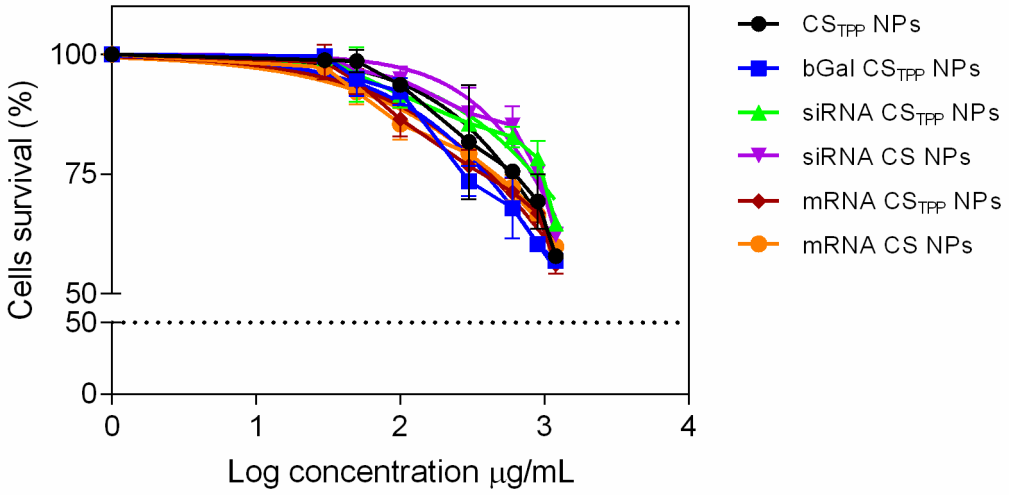

Figure S5. Dose-response curve and half maximal inhibitory concentration (IC_{50}) values of CS_{TPP} NPs (black line), bGal CS_{TPP} NPs (blue line), siRNA CS_{TPP} NPs (green line), siRNA CS NPs (violet line), mRNA CS_{TPP} NPs (red line), and mRNA CS NPs (orange line). The concentrations tested were in the range of 30 – 1200 µg/mL. The IC_{50} values were: 1860 µg/mL (R^2 = 0.90) for CS_{TPP} NPs, 1528 µg/mL (R^2 = 0.95), for bGal CS_{TPP} NPs 3349 µg/mL (R^2 = 0.90) for siRNA CS_{TPP} NPs, 2111 µg/mL (R^2 = 0.92), for siRNA CS NPs, 1967 µg/mL (R^2 = 0.95) for mRNA CS_{TPP} NPs, and 2429

µg/mL (R^2 = 0.97) for mRNA CS NPs (orange line). Results are shown as mean ± SD as a percentage of viable cells in comparison to untreated cells representing 100 % viability, n = 3.

2 Supplementary information for Chapter III

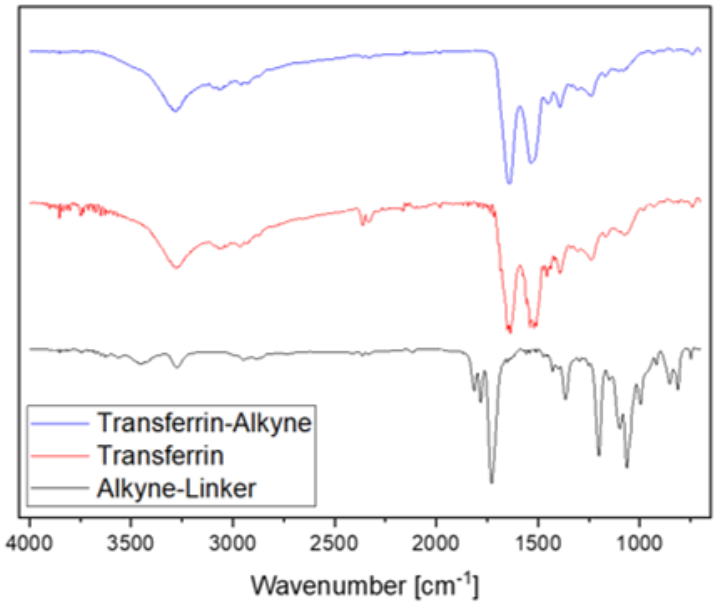

Figure S6. IR spectra of holo-transferrin, alkyne-modified transferrin and DBCO-NHS-linker.

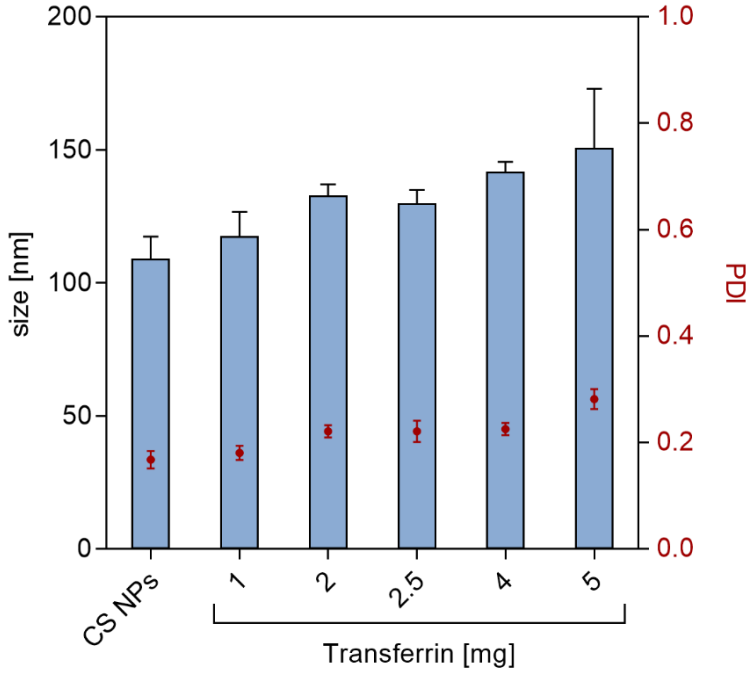

Figure S7. Hydrodynamic diameters and PDI values of transferrin-decorated CS NPs in HBS buffer as used for SPR measurements (Datapoints indicate mean ± SD, n = 3).

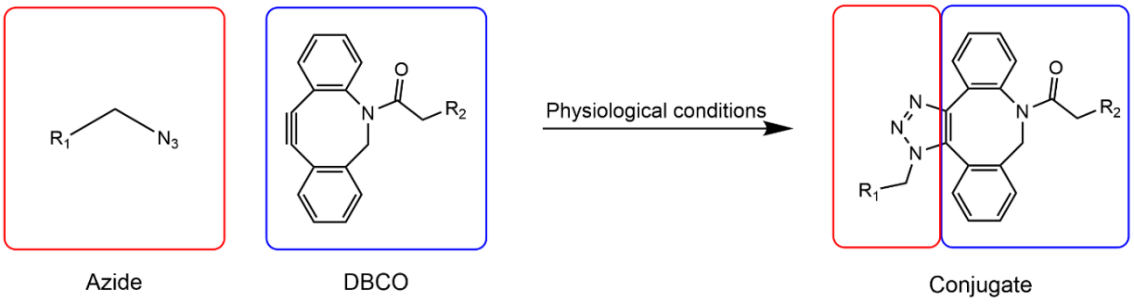

Figure S8. Schematic representation of SPAAC ligation reaction.

3 Supplementary information for Chapter IV

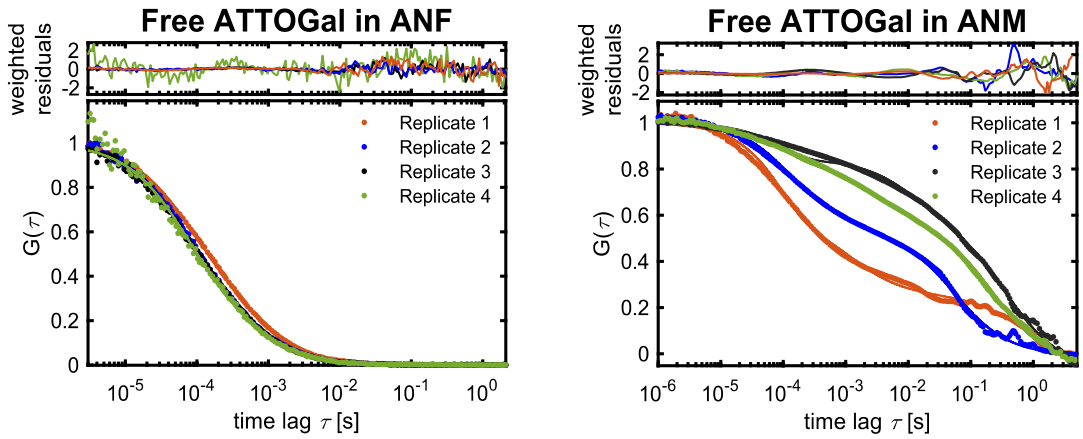

Figure S9. Diffusion of ATTO647N-labelled βGal in ANF and ANM. The ACFs of ATTOGal in (A) ANF and (B) ANM (0.5% mucin) for four independent replicates are depicted.

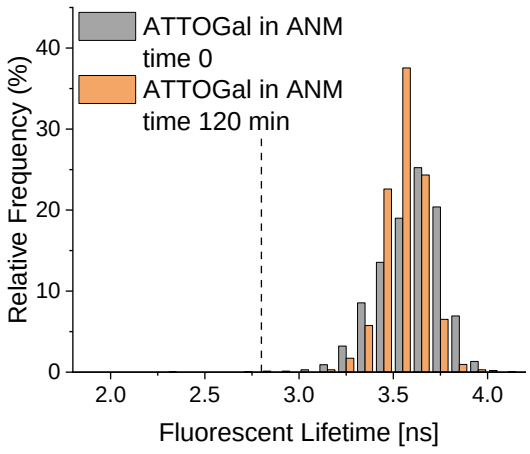

Figure S10. Fluorescence lifetime of ATTOGal in ANM (0.5% mucin) at time 0 min and 120 min. Dotted lines indicate a fluorescence lifetime of 2.8 ns. The histograms were compiled from at least 3 independent experimental replicates.

Table S5. Diffusion of ATTO47N dye, ATTOGal, and ATTOGal loaded CS NPs and Tf-CS NPs in ANF and ANM (0.5% mucin). The mean ± SD of the values obtained from n independent FCS measurements as indicated in the last column. The autocorrelation function was fit using a 1- or 2-component diffusion model with a triplet fraction. N1 and N2 are the relative amplitudes of the component that show the diffusion coefficient D1 or D2, respectively. Note that, for the samples in mucus, the slow diffusion coefficients are attributed to mucin-induced aggregates. In addition, the high SD are caused by the highly variable and unpredictable size and behavior of the mucin-induced aggregates with the labeled molecules, as can be seen in supplementary **Figure S9**.

	Species 1 Free dye		**Species 2 Free protein/small aggregates**		**Species 3 Intact NPs and/or large protein/mucin aggregates**		
	Mean f_1 ± SD	**Mean D_1 ± SD ($\mu m^2/s$)**	**Mean f_2 ± SD**	**Mean D_2 ± SD ($\mu m^2/s$)**	**Mean f_3 ± SD**	**Mean D_3 ± SD ($\mu m^2/s$)**	**n**
ATTO647N, ANF	1	321.19 ± 10.54	-	-	-	-	3
ATTOGal, ANF	0.69 ± 0.20	321 (fixed)	0.31 ± 0.20	33.69 ± 4.06	-	-	5
CS NPs, ANF	0.04 ± 0.02	321 (fixed)	0.10 ± 0.04	34 (fixed)	0.86 ± 0.04	1.37 ± 0.42	6
Tf-CS NPs, ANF	0	321 (fixed)	0.16 ± 0.08	34 (fixed)	0.84 ± 0.08	1.02 ± 0.59	3
ATTO647N, ANM (0.5% mucin)	0.23 ± 0.14	321 (fixed)	0.12 ± 0.07	7.72 (globally fixed)	0.64 ± 0.20	0.20 ± 0.13	3
ATTOGal, ANM (0.5% mucin)	0.30 ± 0.14	321 (fixed)	0.22 ± 0.05	15.05 ± 15.64	0.48 ± 0.13	0.15 ± 0.18	4
CS NPs, ANM (0.5% mucin)	0.25 ± 0.08	321 (fixed)	0.37 ± 0.08	20.23 ± 9.27	0.38 ± 0.16	0.24 ± 0.23	2
Tf-CS NPs, ANM (0.5% mucin)	0.16 ± 0.04	321 (fixed)	0.29 ± 0.09	7.80 ± 4.93	0.55 ± 0.04	0.08±0.04	4
ATTOGal, ANM (1% mucin)	0.33	321 (fixed)	3.34	14.43	0.33	0.30	1
CS NPs, ANM (1% mucin)	0.22	321 (fixed)	0.56	38.05	0.22	0.50	1
Tf-CS NPs, ANM (1% mucin)	0.20	321 (fixed)	0.46	23.10	0.35	0.12	1

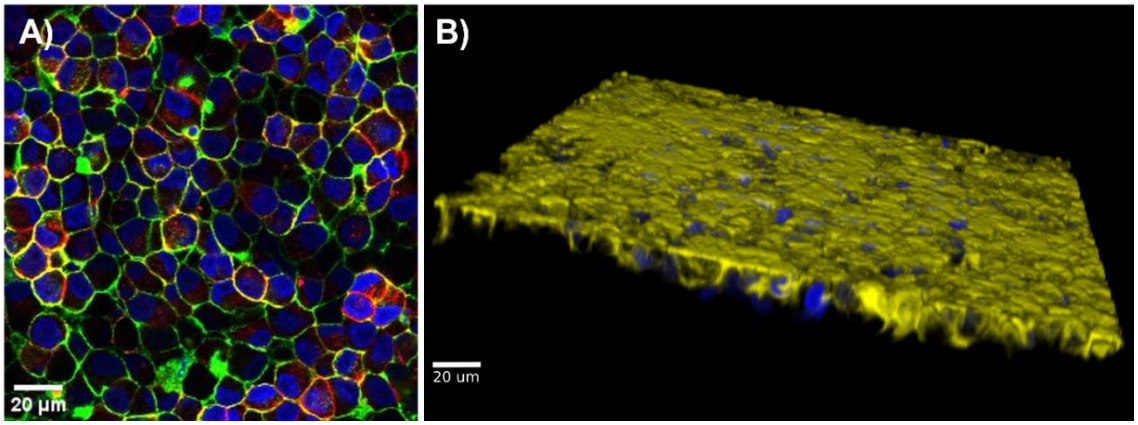

Figure S11. Confocal images of RPMI2650 cells cultured at ALI. A) Cell nuclei are stained with DAPI (blue), the cytoskeleton with rhodamine (red) and the ZO-1 proteins with a specific AlexaFluor488 labeled antibody (green). B) 3D-Image of the cell layer at the ALI. Cell nuclei are stained with DAPI (blue), mucus is stained with AlexaFluor488 labeled wheat germ agglutinin (yellow).

Bibliography

1. Deuschl, G., et al., *The burden of neurological diseases in Europe: an analysis for the Global Burden of Disease Study 2017.* Lancet Public Health, 2020. **5**(10): p. e551-e567.

2. Bors, L.A. and F. Erdő, *Overcoming the Blood–Brain Barrier. Challenges and Tricks for CNS Drug Delivery.* Scientia Pharmaceutica, 2019. **87**(1): p. 6.

3. De Bock, M., et al., *A new angle on blood–CNS interfaces: A role for connexins?* FEBS Letters, 2014. **588**(8): p. 1259-1270.

4. Sharif, Y., et al., *Blood brain barrier: A review of its anatomy and physiology in health and disease.* Clinical Anatomy, 2018. **31**(6): p. 812-823.

5. Crone, C. and O. Christensen, *Electrical resistance of a capillary endothelium.* Journal of General Physiology, 1981. **77**(4): p. 349-371.

6. Pires, P.C. and A.O. Santos, *Nanosystems in nose-to-brain drug delivery: A review of non-clinical brain targeting studies.* Journal of Controlled Release, 2018. **270**: p. 89-100.

7. Pardridge, W.M., *The blood-brain barrier: Bottleneck in brain drug development.* NeuroRX, 2005. **2**(1): p. 3-14.

8. Abbott, N.J., et al., *Structure and function of the blood–brain barrier.* Neurobiology of Disease, 2010. **37**(1): p. 13-25.

9. Feigin, V.L., et al., *Global, regional, and national burden of neurological disorders during 1990–2015: a systematic analysis for the Global Burden of Disease Study 2015.* The Lancet Neurology, 2017. **16**(11): p. 877-897.

10. Begley, D.J., *Delivery of therapeutic agents to the central nervous system: the problems and the possibilities.* Pharmacology & Therapeutics, 2004. **104**(1): p. 29-45.

11. Frey, W., *Neurologic agents for nasal administration to the brain.* World Intellectual Property Organization, 1991. **5**: p. 89.

12. Crowe, T.P., et al., *Mechanism of intranasal drug delivery directly to the brain.* Life Sciences, 2018. **195**: p. 44-52.

13. Silver, W.L. and T.E. Finger, *The anatomical and electrophysiological basis of peripheral nasal trigeminal chemoreception.* Annals of the New York Academy of Sciences, 2009. **1170**(1): p. 202-205.

14. Lochhead, J.J. and R.G. Thorne, *Intranasal Drug Delivery to the Brain*, in *Drug Delivery to the Brain: Physiological Concepts, Methodologies and Approaches*, M. Hammarlund-Udenaes, E.C.M. de Lange, and R.G. Thorne, Editors. 2014, Springer New York: New York, NY. p. 401-431.

15. Mygind, N. and R. Dahl, *Anatomy, physiology and function of the nasal cavities in health and disease.* Advanced drug delivery reviews, 1998. **29**(1-2): p. 3-12.

16. Lochhead, J.J. and R.G. Thorne, *Intranasal delivery of biologics to the central nervous system.* Advanced Drug Delivery Reviews, 2012. **64**(7): p. 614-628.

17. Born, J., et al., *Sniffing neuropeptides: a transnasal approach to the human brain.* Nature Neuroscience, 2002. **5**: p. 514.

18. Francis, G.J., et al., *Intranasal insulin prevents cognitive decline, cerebral atrophy and white matter changes in murine type I diabetic encephalopathy.* Brain, 2008. **131**(12): p. 3311.

19. Mischley, L.K., et al., *Central nervous system uptake of intranasal glutathione in Parkinson's disease.* Npj Parkinson'S Disease, 2016. **2**: p. 16002.

20. Mittal, D., et al., *Insights into direct nose to brain delivery: current status and future perspective.* Drug Delivery, 2014. **21**(2): p. 75-86.

21. Lai, S.K., Y.-Y. Wang, and J. Hanes, *Mucus-penetrating nanoparticles for drug and gene delivery to mucosal tissues.* Advanced Drug Delivery Reviews, 2009. **61**(2): p. 158-171.

22. Arora, P., S. Sharma, and S. Garg, *Permeability issues in nasal drug delivery.* Drug Discovery Today, 2002. **7**(18): p. 967-975.

23. Kabanov, A.V., *Brain delivery of proteins via their fatty acid and block copolymer modifications AU - Yi, Xiang.* Journal of Drug Targeting, 2013. **21**(10): p. 940-955.

24. Oliveira, P., et al., *Drug-metabolizing Enzymes and Efflux Transporters in Nasal Epithelium: Influence on the Bioavailability of Intranasally Administered Drugs.* Current Drug Metabolism, 2016. **17**(7): p. 628-647.

25. Gartziandia, O., et al., *Chitosan coated nanostructured lipid carriers for brain delivery of proteins by intranasal administration.* Colloids and Surfaces B: Biointerfaces, 2015. **134**(Supplement C): p. 304-313.

26. Rassu, G., et al., *Nose-to-brain delivery of BACE1 siRNA loaded in solid lipid nanoparticles for Alzheimer's therapy.* Colloids and Surfaces B: Biointerfaces, 2017. **152**: p. 296-301.

27. Bourganis, V., et al., *Recent advances in carrier mediated nose-to-brain delivery of pharmaceutics.* European Journal of Pharmaceutics and Biopharmaceutics, 2018. **128**: p. 337-362.

28. Samaridou, E. and M.J. Alonso, *Nose-to-brain peptide delivery – The potential of nanotechnology.* Bioorganic & Medicinal Chemistry, 2017.

29. Sastri, K.T., et al., *Nanocarrier facilitated drug delivery to the brain through intranasal route: A promising approach to transcend bio-obstacles and alleviate neurodegenerative conditions.* Journal of Drug Delivery Science and Technology, 2022. **75**: p. 103656.

30. Warnken, Z.N., et al., *Formulation and device design to increase nose to brain drug delivery.* Journal of Drug Delivery Science and Technology, 2016. **35**: p. 213-222.

31. Kozlovskaya, L., M. Abou-Kaoud, and D. Stepensky, *Quantitative analysis of drug delivery to the brain via nasal route.* Journal of Controlled Release, 2014. **189**(Supplement C): p. 133-140.

32. Qian, S., Q. Wang, and Z. Zuo, *Improved brain uptake of peptide-based CNS drugs via alternative routes of administrations of its nanocarrier delivery systems: a promising strategy for CNS targeting delivery of peptides.* Expert Opinion on Drug Metabolism & Toxicology, 2014. **10**(11): p. 1491-1508.

33. Costa, C.P., et al., *Intranasal delivery of nanostructured lipid carriers, solid lipid nanoparticles and nanoemulsions: A current overview of in vivo studies.* Acta Pharmaceutica Sinica B, 2021. **11**(4): p. 925-940.

34. Ozsoy, Y., S. Gungor, and E. Cevher, *Nasal Delivery of High Molecular Weight Drugs.* Molecules, 2009. **14**(9): p. 3754-3779.

35. Kammona, O. and C. Kiparissides, *Recent advances in nanocarrier-based mucosal delivery of biomolecules.* Journal of Controlled Release, 2012. **161**(3): p. 781-794.

36. Dutta, P.K., J. Dutta, and V. Tripathi, *Chitin and chitosan: Chemistry, properties and applications.* 2004.

37. Garcia-Fuentes, M. and M.J. Alonso, *Chitosan-based drug nanocarriers: Where do we stand?* Journal of Controlled Release, 2012. **161**(2): p. 496-504.

38. Csaba, N., M. Garcia-Fuentes, and M.J. Alonso, *The performance of nanocarriers for transmucosal drug delivery.* Expert Opinion on Drug Delivery, 2006. **3**(4): p. 463-478.

39. Kean, T. and M. Thanou, *Biodegradation, biodistribution and toxicity of chitosan.* Advanced Drug Delivery Reviews, 2010. **62**(1): p. 3-11.

40. Opanasopit, P., et al., *Effect of Salt Forms and Molecular Weight of Chitosans on In Vitro Permeability Enhancement in Intestinal Epithelial Cells (Caco-2).* Pharmaceutical Development and Technology, 2007. **12**(5): p. 447-455.

41. Bernkop-Schnürch, A., M. Hornof, and D. Guggi, *Thiolated chitosans.* European Journal of Pharmaceutics and Biopharmaceutics, 2004. **57**(1): p. 9-17.

42. Boateng, J.S., et al., *Wound Healing Dressings and Drug Delivery Systems: A Review.* Journal of Pharmaceutical Sciences, 2008. **97**(8): p. 2892-2923.

43. Calvo, P., et al., *Novel hydrophilic chitosan-polyethylene oxide nanoparticles as protein carriers.* Journal of Applied Polymer Science, 1997. **63**(1): p. 125-132.

44. Calvo, P., et al., *Chitosan and Chitosan/Ethylene Oxide-Propylene Oxide Block Copolymer Nanoparticles as Novel Carriers for Proteins and Vaccines.* Pharmaceutical Research, 1997. **14**(10): p. 1431-1436.

45. Wang, H., et al., *Global, regional, and national life expectancy, all-cause mortality, and cause-specific mortality for 249 causes of death, 1980–2015: a systematic analysis for the Global Burden of Disease Study 2015.* The lancet, 2016. **388**(10053): p. 1459-1544.

46. BeruBe, K., et al., *In vitro models of inhalation toxicity and disease.* Alternatives to laboratory animals, 2009. **37**(1): p. 89-141.

47. Spits, H. and J. Villaudy, *Modeling human lung infections in mice.* Nature Biotechnology, 2019. **37**(10): p. 1129-1130.

48. Shapiro, S.D., *Animal Models of Asthma.* American Journal of Respiratory and Critical Care Medicine, 2006. **174**(11): p. 1171-1173.

49. Ware, L.B., *Modeling human lung disease in animals.* American Journal of Physiology-Lung Cellular and Molecular Physiology, 2008. **294**(2): p. L149-L150.

50. Bal, H. and N. Ghoshal, *Morphology of the terminal bronchiolar region of common laboratory mammals.* Laboratory animals, 1988. **22**(1): p. 76-82.

51. Van Patter, L.E. and C. Blattner, *Advancing ethical principles for non-invasive, respectful research with nonhuman animal participants.* society & animals, 2020. **28**(2): p. 171-190.

52. Lacroix, G., et al., *Air–liquid interface in vitro models for respiratory toxicology research: consensus workshop and recommendations.* Applied in vitro toxicology, 2018. **4**(2): p. 91-106.

53. Dvorak, A., et al., *Do airway epithelium air–liquid cultures represent the in vivo airway epithelium transcriptome?* American journal of respiratory cell and molecular biology, 2011. **44**(4): p. 465-473.

54. Chary, A., et al., *An in vitro coculture system for the detection of sensitization following aerosol exposure.* ALTEX-Alternatives to animal experimentation, 2019. **36**(3): p. 403-418.

55. Person, A. and M.L. Mintz, *Anatomy and physiology of the respiratory tract.* Disorders of the respiratory tract: common challenges in primary care, 2006: p. 11-15.

56. Leslie, K.O., M.R. Wick, and M.L. Smith, *Practical Pulmonary Pathology: A Diagnostic Approach E-Book: A Volume in the Pattern Recognition Series*. 2017: Elsevier Health Sciences.

57. Schürch, S., et al., *Surfactant displaces particles toward the epithelium in airways and alveoli.* Respiration physiology, 1990. **80**(1): p. 17-32.

58. Holt, P., M. Schon-Hegrad, and P. McMenamin, *Dendritic cells in the respiratory tract.* International reviews of immunology, 1990. **6**(2-3): p. 139-149.

59. Lehnert, B.E., *Pulmonary and thoracic macrophage subpopulations and clearance of particles from the lung.* Environmental health perspectives, 1992. **97**: p. 17-46.

60. McDowell, E.M., et al., *The respiratory epithelium. I. Human bronchus.* Journal of the National Cancer Institute, 1978. **61**(2): p. 539-549.

61. Berube, K.A., et al., *Human primary bronchial lung cell constructs: the new respiratory models.* Toxicology, 2010. **278**(3): p. 311-318.

62. Awatade, N.T., et al., *Human primary epithelial cell models: promising tools in the era of cystic fibrosis personalized medicine.* Frontiers in Pharmacology, 2018. **9**: p. 1429.

63. Papazian, D., P.A. Würtzen, and S.W. Hansen, *Polarized airway epithelial models for immunological co-culture studies.* International archives of allergy and immunology, 2016. **170**(1): p. 1-21.

64. Gindele, J.A., et al., *Intermittent exposure to whole cigarette smoke alters the differentiation of primary small airway epithelial cells in the air-liquid interface culture.* Scientific Reports, 2020. **10**(1): p. 6257.

65. Gard, A., et al., *High-Throughput Human Primary Cell-Based Airway Model for Evaluating Influenza.* Coronavirus, or other Respiratory Viruses &lt, 2020.

66. Tilley, B.-G.H., et al., *The air-liquid interface and use of primary cell cultures.* Am J Physiol Lung Cell Mol Physiol, 2011. **300**: p. L25-L31.

67. Rothen-Rutishauser, B., et al., *In vitro models of the human epithelial airway barrier to study the toxic potential of particulate matter.* Expert opinion on drug metabolism & toxicology, 2008. **4**(8): p. 1075-1089.

68. Kreft, M.E., et al., *The Characterization of the Human Nasal Epithelial Cell Line RPMI 2650 Under Different Culture Conditions and Their Optimization for an Appropriate in vitro Nasal Model.* Pharmaceutical Research, 2015. **32**(2): p. 665-679.

69. Mercier, C., N. Perek, and X. Delavenne, *Is RPMI 2650 a Suitable In Vitro Nasal Model for Drug Transport Studies?* European Journal of Drug Metabolism and Pharmacokinetics, 2018. **43**(1): p. 13-24.

70. Sibinovska, N., S. Žakelj, and K. Kristan, *Suitability of RPMI 2650 cell models for nasal drug permeability prediction.* European Journal of Pharmaceutics and Biopharmaceutics, 2019. **145**: p. 85-95.

71. Reichl, S. and K. Becker, *Cultivation of RPMI 2650 cells as an in-vitro model for human transmucosal nasal drug absorption studies: optimization of selected culture conditions.* Journal of Pharmacy and Pharmacology, 2012. **64**(11): p. 1621-1630.

72. Schlachet, I. and A. Sosnik, *Mixed Mucoadhesive Amphiphilic Polymeric Nanoparticles Cross a Model of Nasal Septum Epithelium in Vitro.* ACS Applied Materials & Interfaces, 2019.

73. Bequignon, E., et al., *FcRn-dependent transcytosis of monoclonal antibody in human nasal epithelial cells in vitro: a prerequisite for a new delivery route for therapy?* International journal of molecular sciences, 2019. **20**(6): p. 1379.

74. Forbes, B., *Human airway epithelial cell lines for in vitro drug transport and metabolism studies.* Pharmaceutical science & technology today, 2000. **3**(1): p. 18-27.

75. Ehrhardt, C., et al., *16HBE14o-human bronchial epithelial cell layers express P-glycoprotein, lung resistance-related protein, and caveolin-1.* Pharmaceutical research, 2003. **20**: p. 545-551.

76. Ehrhardt, C., et al., *Influence of apical fluid volume on the development of functional intercellular junctions in the human epithelial cell line 16HBE14o–: implications for the use of this cell line as an in vitro model for bronchial drug absorption studies.* Cell and tissue research, 2002. **308**: p. 391-400.

77. Forbes, B., et al., *The human bronchial epithelial cell line 16HBE14o− as a model system of the airways for studying drug transport.* International journal of pharmaceutics, 2003. **257**(1-2): p. 161-167.

78. Bleck, B., et al., *Diesel exhaust particle-exposed human bronchial epithelial cells induce dendritic cell maturation.* The Journal of Immunology, 2006. **176**(12): p. 7431-7437.

79. Mayer, A.K., et al., *Airway epithelial cells modify immune responses by inducing an anti-inflammatory microenvironment.* European journal of immunology, 2008. **38**(6): p. 1689-1699.

80. Stewart, C.E., et al., *Evaluation of differentiated human bronchial epithelial cell culture systems for asthma research.* Journal of allergy, 2012. **2012**.

81. Patel, J., et al., *Transport of HIV-protease inhibitors across 1α, 25di-hydroxy vitamin D 3-treated Calu-3 cell monolayers: modulation of P-glycoprotein activity.* Pharmaceutical research, 2002. **19**: p. 1696-1703.

82. Grainger, C.I., et al., *Culture of Calu-3 cells at the air interface provides a representative model of the airway epithelial barrier.* Pharmaceutical research, 2006. **23**: p. 1482-1490.

83. Fiegel, J., et al., *Large porous particle impingement on lung epithelial cell monolayers—toward improved particle characterization in the lung.* Pharmaceutical research, 2003. **20**: p. 788-796.

84. Shen, B., et al., *Calu-3: a human airway epithelial cell line that shows cAMP-dependent Cl-secretion.* American Journal of Physiology-Lung Cellular and Molecular Physiology, 1994. **266**(5): p. L493-L501.

85. Braakhuis, H.M., et al., *An air-liquid interface bronchial epithelial model for realistic, repeated inhalation exposure to airborne particles for toxicity testing.* JoVE (Journal of Visualized Experiments), 2020(159): p. e61210.

86. Caraballo, J.C., et al., *Ambient particulate matter affects occludin distribution and increases alveolar transepithelial electrical conductance.* Respirology, 2011. **16**(2): p. 340-349.

87. Lieber, M., *Smith B, Szakal A, Nelson-Rees W, and Todaro G.* A continuous tumor-cell line from a human lung carcinoma with properties of type II alveolar epithelial cells. Int J Cancer, 1976. **17**: p. 62-70.

88. Blank, F., et al., *An optimized in vitro model of the respiratory tract wall to study particle cell interactions.* Journal of aerosol medicine : the official journal of the International Society for Aerosols in Medicine, 2006. **19**(3): p. 392-405.

89. Öhlinger, K., et al., *Air-liquid interface culture changes surface properties of A549 cells.* Toxicology in vitro : an international journal published in association with BIBRA, 2019. **60**(NA): p. 369-382.

90. Wang, Y., et al., *Comparison of in vitro toxicity of aerosolized engineered nanomaterials using air-liquid interface mono-culture and co-culture models.* NanoImpact, 2020. **18**(NA): p. 100215-NA.

91. Cappellini, F., et al., *Dry Generation of CeO2 Nanoparticles and Deposition onto a Co-Culture of A549 and THP-1 Cells in Air-Liquid Interface-Dosimetry Considerations and Comparison to Submerged Exposure.* Nanomaterials (Basel, Switzerland), 2020. **10**(4): p. 618-NA.

92. Lehmann, A.D., et al., *An in vitro triple cell co-culture model with primary cells mimicking the human alveolar epithelial barrier.* European journal of pharmaceutics and biopharmaceutics : official journal of Arbeitsgemeinschaft fur Pharmazeutische Verfahrenstechnik e.V, 2010. **77**(3): p. 398-406.

93. Zhang, L., J.A. Whitsett, and B.R. Stripp, *Regulation of Clara cell secretory protein gene transcription by thyroid transcription factor-1.* Biochimica et biophysica acta, 1997. **1350**(3): p. 359-367.

94. Rehan, V.K., et al., *1α,25-Dihydroxy-3-epi-vitamin D3, a natural metabolite of 1α,25-dihydroxy vitamin D3: production and biological activity studies in pulmonary alveolar type II cells.* Molecular genetics and metabolism, 2002. **76**(1): p. 46-56.

95. Woollhead, A.M. and D.L. Baines, *Forskolin-induced cell shrinkage and apical translocation of functional enhanced green fluorescent protein-human αENaC in H441 lung epithelial cell monolayers.* The Journal of biological chemistry, 2005. **281**(8): p. 5158-5168.

96. Papritz, M., et al., *Side-specific effects by cadmium exposure: Apical and basolateral treatment in a coculture model of the blood-air barrier.* Toxicology and applied pharmacology, 2010. **245**(3): p. 361-369.

97. Kreft, M.E., et al., *The characterization of the human nasal epithelial cell line RPMI 2650 under different culture conditions and their optimization for an appropriate in vitro nasal model.* Pharmaceutical research, 2015. **32**: p. 665-679.

98. Stewart, C.E., et al., *Evaluation of Differentiated Human Bronchial Epithelial Cell Culture Systems for Asthma Research.* Journal of allergy, 2012. **2012**(NA): p. 943982-943982.

99. Sibinovska, N., et al., *Suitability and functional characterization of two Calu-3 cell models for prediction of drug permeability across the airway epithelial barrier.* International journal of pharmaceutics, 2020. **585**(NA): p. 119484-NA.

100. Josset, L., et al., *Cell Host Response to Infection with Novel Human Coronavirus EMC Predicts Potential Antivirals and Important Differences with SARS Coronavirus.* mBio, 2013. **4**(3): p. 1-11.

101. Qian, Z., et al., *Innate Immune Response of Human Alveolar Type II Cells Infected with Severe Acute Respiratory Syndrome–Coronavirus.* American journal of respiratory cell and molecular biology, 2013. **48**(6): p. 742-748.

102. Gray, T.E., et al., *Mucociliary differentiation of serially passaged normal human tracheobronchial epithelial cells.* American journal of respiratory cell and molecular biology, 1996. **14**(1): p. 104-112.

103. Sungnak, W., et al., *SARS-CoV-2 entry factors are highly expressed in nasal epithelial cells together with innate immune genes.* Nature medicine, 2020. **26**(5): p. 681-687.

104. Abo, K.M., et al., *Human iPSC-derived alveolar and airway epithelial cells can be cultured at air-liquid interface and express SARS-CoV-2 host factors.* bioRxiv, 2020: p. 2020.06.03.132639.

105. Ashraf, S., et al., *Biological characteristics and propagation of human rhinovirus-C in differentiated sinus epithelial cells.* Virology, 2012. **436**(1): p. 143-149.

106. Warner, S.M., et al., *Rhinovirus replication and innate immunity in highly differentiated human airway epithelial cells.* Respiratory research, 2019. **20**(1): p. 150-150.

107. Ziegler, P., et al., *A three-dimensional Air-Liquid Interface Culture Model for the Study of Epstein-Barr virus Infection in the Nasopharynx.* bioRxiv, 2020: p. 2020.08.31.272096.

108. Jonsdottir, H.R., et al., *Establishment of primary transgenic human airway epithelial cell cultures to study respiratory virus–host interactions.* Viruses, 2019. **11**(8): p. 747.

109. Jonsdottir, H.R. and R. Dijkman, *Coronaviruses and the human airway: a universal system for virus-host interaction studies.* Virology journal, 2016. **13**(1): p. 24-24.

110. de Wit, E., et al., *SARS and MERS: recent insights into emerging coronaviruses.* Nature reviews. Microbiology, 2016. **14**(8): p. 523-534.

111. Wang, C., et al., *A novel coronavirus outbreak of global health concern.* Lancet (London, England), 2020. **395**(10223): p. 470-473.

112. Zhu, N., et al., *A Novel Coronavirus from Patients with Pneumonia in China, 2019.* The New England journal of medicine, 2020. **382**(8): p. 727-733.

113. Lu, R., et al., *Genomic characterisation and epidemiology of 2019 novel coronavirus: implications for virus origins and receptor binding.* Lancet (London, England), 2020. **395**(10224): p. 565-574.

114. Ravindra, N.G., et al., *Single-cell longitudinal analysis of SARS-CoV-2 infection in human airway epithelium.* bioRxiv, 2020.

115. Polack, F.P., et al., *Safety and Efficacy of the BNT162b2 mRNA Covid-19 Vaccine.* The New England journal of medicine, 2020. **383**(27): p. 2603-2615.

116. Jackson, L.A., et al., *An mRNA Vaccine against SARS-CoV-2 — Preliminary Report.* The New England journal of medicine, 2020. **383**(20): p. 1920-1931.

117. Sheahan, T.P., et al., *Broad-spectrum antiviral GS-5734 inhibits both epidemic and zoonotic coronaviruses.* Science translational medicine, 2017. **9**(396): p. NA-NA.

118. Jiang, L., et al., *Potent neutralization of MERS-CoV by human neutralizing monoclonal antibodies to the viral spike glycoprotein.* Science translational medicine, 2014. **6**(234): p. 3008140-NA.

119. Lundin, A., et al., *Targeting membrane-bound viral RNA synthesis reveals potent inhibition of diverse coronaviruses including the middle East respiratory syndrome virus.* PLoS pathogens, 2014. **10**(5): p. e1004166-NA.

120. Shalhoub, S., et al., *IFN-α2a or IFN-β1a in combination with ribavirin to treat Middle East respiratory syndrome coronavirus pneumonia: a retrospective study.* The Journal of antimicrobial chemotherapy, 2015. **70**(7): p. 2129-2132.

121. Liu, R., et al., *A recombinant VSV-vectored MERS-CoV vaccine induces neutralizing antibody and T cell responses in rhesus monkeys after single dose immunization.* Antiviral research, 2018. **150**: p. 30-38.

122. de Wilde, A.H., et al., *A Kinome-Wide Small Interfering RNA Screen Identifies Proviral and Antiviral Host Factors in Severe Acute Respiratory Syndrome Coronavirus Replication, Including Double-Stranded RNA-Activated Protein Kinase and Early Secretory Pathway Proteins.* Journal of virology, 2015. **89**(16): p. 8318-8333.

123. Yoshikawa, T., et al., *Severe Acute Respiratory Syndrome (SARS) Coronavirus-Induced Lung Epithelial Cytokines Exacerbate SARS Pathogenesis by Modulating Intrinsic Functions of Monocyte-Derived Macrophages and Dendritic Cells.* Journal of virology, 2008. **83**(7): p. 3039-3048.

124. Blom, R.A., et al., *A triple co-culture model of the human respiratory tract to study immune-modulatory effects of liposomes and virosomes.* PLoS One, 2016. **11**(9): p. e0163539.

125. Boucher, R.C., *An overview of the pathogenesis of cystic fibrosis lung disease.* Advanced drug delivery reviews, 2002. **54**(11): p. 1359-1371.

126. Ratjen, F., et al., *Cystic fibrosis.* Nature reviews. Disease primers, 2015. **1**(1): p. 15010-NA.

127. Stoltz, D.A., D.K. Meyerholz, and M.J. Welsh, *Origins of Cystic Fibrosis Lung Disease.* The New England journal of medicine, 2015. **372**(4): p. 351-362.

128. Riordan, J.R., et al., *Identification of the cystic fibrosis gene: cloning and characterization of complementary DNA.* Science (New York, N.Y.), 1989. **245**(4922): p. 1066-1073.

129. Rosen, B.H., et al., *Animal and model systems for studying cystic fibrosis.* Journal of cystic fibrosis : official journal of the European Cystic Fibrosis Society, 2017. **17**(2): p. S28-S34.

130. Castellani, S., et al., *Human Cellular Models for the Investigation of Lung Inflammation and Mucus Production in Cystic Fibrosis.* Analytical cellular pathology (Amsterdam), 2018. **2018**(NA): p. 3839803-3839803.

131. Ehrhardt, C., et al., *Towards an in vitro model of cystic fibrosis small airway epithelium: characterisation of the human bronchial epithelial cell line CFBE41o.* Cell and tissue research, 2005. **323**(3): p. 405-415.

132. Randell, S.H., et al., *Primary epithelial cell models for cystic fibrosis research.* Methods in molecular biology (Clifton, N.J.), 2011. **742**(NA): p. 285-310.

133. Mou, H., K. Brazauskas, and J. Rajagopal, *Personalized medicine for cystic fibrosis: establishing human model systems.* Pediatric pulmonology, 2015. **50**(S40): p. S14-23.

134. Schögler, A., et al., *Characterization of pediatric cystic fibrosis airway epithelial cell cultures at the air-liquid interface obtained by non-invasive nasal cytology brush sampling.* Respiratory research, 2017. **18**(1): p. 215-215.

135. Brewington, J.J., et al., *Brushed nasal epithelial cells are a surrogate for bronchial epithelial CFTR studies.* JCI insight, 2018. **3**(13): p. NA-NA.

136. Martiniano, S.L., S.D. Sagel, and E.T. Zemanick, *Cystic fibrosis: a model system for precision medicine.* Current opinion in pediatrics, 2016. **28**(3): p. 312-317.

137. Lopes-Pacheco, M., *CFTR Modulators: Shedding Light on Precision Medicine for Cystic Fibrosis.* Frontiers in pharmacology, 2016. **7**(NA): p. 275-275.

138. Van Goor, F., et al., *Rescue of CF airway epithelial cell function in vitro by a CFTR potentiator, VX-770.* Proceedings of the National Academy of Sciences of the United States of America, 2009. **106**(44): p. 18825-18830.

139. Van Goor, F., et al., *Correction of the F508del-CFTR protein processing defect in vitro by the investigational drug VX-809.* Proceedings of the National Academy of Sciences of the United States of America, 2011. **108**(46): p. 18843-18848.

140. Awatade, N.T., et al., *Measurements of Functional Responses in Human Primary Lung Cells as a Basis for Personalized Therapy for Cystic Fibrosis.* EBioMedicine, 2014. **2**(2): p. 147-153.

141. Pranke, I., et al., *Correction of CFTR function in nasal epithelial cells from cystic fibrosis patients predicts improvement of respiratory function by CFTR modulators.* Scientific reports, 2017. **7**(1): p. 7375-7375.

142. Manunta, M., et al., *Delivery of ENaC siRNA to epithelial cells mediated by a targeted nanocomplex: a therapeutic strategy for cystic fibrosis.* Scientific reports, 2017. **7**(1): p. 700-700.

143. Tagalakis, A.D., et al., *Effective silencing of ENaC by siRNA delivered with epithelial-targeted nanocomplexes in human cystic fibrosis cells and in mouse lung.* Thorax, 2018. **73**(9): p. 847-856.

144. d'Angelo, I., et al., *Hybrid lipid/polymer nanoparticles for pulmonary delivery of siRNA: development and fate upon in vitro deposition on the human epithelial airway barrier.* Journal of aerosol medicine and pulmonary drug delivery, 2018. **31**(3): p. 170-181.

145. Mitchell, G., et al., *Infection of Polarized Airway Epithelial Cells by Normal and Small-Colony Variant Strains of Staphylococcus aureus Is Increased in Cells with Abnormal Cystic Fibrosis Transmembrane Conductance Regulator Function and Is Influenced by NF-κB.* Infection and immunity, 2011. **79**(9): p. 3541-3551.

146. Kiedrowski, M.R., et al., *Staphylococcus aureus Biofilm Growth on Cystic Fibrosis Airway Epithelial Cells Is Enhanced during Respiratory Syncytial Virus Coinfection.* mSphere, 2018. **3**(4): p. NA-NA.

147. Di Paola, M., et al., *SLC6A14 is a genetic modifier of cystic fibrosis that regulates Pseudomonas aeruginosa attachment to human bronchial epithelial cells.* MBio, 2017. **8**(6): p. e02073-17.

148. Hasan, S., P. Sebo, and R. Osicka, *A guide to polarized airway epithelial models for studies of host–pathogen interactions.* The FEBS journal, 2018. **285**(23): p. 4343-4358.

149. Yonker, L.M., et al., *Development of a Primary Human Co-Culture Model of Inflamed Airway Mucosa.* Scientific reports, 2017. **7**(1): p. 8182-8182.

150. Halldorsson, S., et al., *Azithromycin maintains airway epithelial integrity during Pseudomonas aeruginosa infection.* American journal of respiratory cell and molecular biology, 2009. **42**(1): p. 62-68.

151. Moreau-Marquis, S., G.A. O'Toole, and B.A. Stanton, *Tobramycin and FDA-Approved Iron Chelators Eliminate Pseudomonas aeruginosa Biofilms on Cystic Fibrosis Cells.* American journal of respiratory cell and molecular biology, 2009. **41**(3): p. 305-313.

152. Lashua, L.P., et al., *Engineered cationic antimicrobial peptide (eCAP) prevents Pseudomonas aeruginosa biofilm growth on airway epithelial cells.* The Journal of antimicrobial chemotherapy, 2016. **71**(8): p. 2200-2207.

153. Morales, E., *The Global Asthma Report 2018*. 2018.

154. Kudo, M., Y. Ishigatsubo, and I. Aoki, *Pathology of asthma.* Frontiers in microbiology, 2013. **4**(NA): p. 263-263.

155. Wegmann, M., *Th2 cells as targets for therapeutic intervention in allergic bronchial asthma.* Expert review of molecular diagnostics, 2009. **9**(1): p. 85-100.

156. Barnes, P.J., *Targeting cytokines to treat asthma and chronic obstructive pulmonary disease.* Nature reviews. Immunology, 2018. **18**(7): p. 454-466.

157. Lambrecht, B.N. and H. Hammad, *The airway epithelium in asthma.* Nature medicine, 2012. **18**(5): p. 684-692.

158. Barnes, P.J., *Immunology of asthma and chronic obstructive pulmonary disease.* Nature reviews. Immunology, 2008. **8**(3): p. 183-192.

159. Blume, C. and D.E. Davies, *In vitro and ex vivo models of human asthma.* European journal of pharmaceutics and biopharmaceutics : official journal of Arbeitsgemeinschaft fur Pharmazeutische Verfahrenstechnik e.V, 2013. **84**(2): p. 394-400.

160. Xiao, C., et al., *Defective epithelial barrier function in asthma.* Journal of Allergy and Clinical immunology, 2011. **128**(3): p. 549-556. e12.

161. Gras, D., et al., *An ex vivo model of severe asthma using reconstituted human bronchial epithelium.* The Journal of allergy and clinical immunology, 2012. **129**(5): p. 1259-1266.

162. Hackett, T.-L., et al., *Induction of Epithelial–Mesenchymal Transition in Primary Airway Epithelial Cells from Patients with Asthma by Transforming Growth Factor-β1.* American journal of respiratory and critical care medicine, 2009. **180**(2): p. 122-133.

163. Carlini, F., et al., *Bronchial Epithelial Cells from Asthmatic Patients Display Less Functional HLA-G Isoform Expression.* Frontiers in immunology, 2017. **8**(NA): p. 6-6.

164. Jevnikar, Z., et al., *Epithelial IL-6 trans-signaling defines a new asthma phenotype with increased airway inflammation.* The Journal of allergy and clinical immunology, 2018. **143**(2): p. 577-590.

165. Holden, N.S., et al., *Enhancement of inflammatory mediator release by β2-adrenoceptor agonists in airway epithelial cells is reversed by glucocorticoid action.* British journal of pharmacology, 2010. **160**(2): p. 410-420.

166. Woodman, L., et al., *Synthetic Response of Stimulated Respiratory Epithelium: Modulation by Prednisolone and iKK2 Inhibition.* Chest, 2013. **143**(6): p. 1656-1666.

167. Hardyman, M.A., et al., *TNF-α-mediated bronchial barrier disruption and regulation by src-family kinase activation.* The Journal of allergy and clinical immunology, 2013. **132**(3): p. 665-675.

168. Sexton, D.J., et al., *Specific inhibition of tissue kallikrein 1 with a human monoclonal antibody reveals a potential role in airway diseases.* The Biochemical journal, 2009. **422**(2): p. 383-392.

169. Lopez-Guisa, J.M., et al., *Airway epithelial cells from asthmatic children differentially express proremodeling factors.* The Journal of allergy and clinical immunology, 2012. **129**(4): p. 990-997.

170. Healey, G.D., et al., *Evaluation of nasal epithelium sampling as a tool in the preclinical development of siRNA-based therapeutics for asthma.* Journal of cellular and molecular medicine, 2013. **17**(3): p. 356-364.

171. Gras, D., et al., *Human bronchial epithelium orchestrates dendritic cell activation in severe asthma.* The European respiratory journal, 2017. **49**(3): p. 1602399-NA.

172. Jiao, D., et al., *Activation of eosinophils interacting with bronchial epithelial cells by antimicrobial peptide LL-37: implications in allergic asthma.* Scientific Reports, 2017. **7**(1): p. 1848.

173. Wawrzyniak, P., et al., *Regulation of Bronchial Epithelial Barrier Integrity by Type 2 Cytokines and Histone Deacetylases in Asthmatic Patients.* The Journal of allergy and clinical immunology, 2016. **139**(1): p. 93-103.

174. Haghi, M., et al., *Mono- and Cocultures of Bronchial and Alveolar Epithelial Cells Respond Differently to Proinflammatory Stimuli and Their Modulation by Salbutamol and Budesonide.* Molecular pharmaceutics, 2015. **12**(8): p. 2625-2632.

175. Reeves, S.R., et al., *Fibroblast-myofibroblast transition is differentially regulated by bronchial epithelial cells from asthmatic children.* Respiratory research, 2015. **16**(1): p. 21-21.

176. Paplinska-Goryca, M., et al., *The Expressions of TSLP, IL-33, and IL-17A in Monocyte Derived Dendritic Cells from Asthma and COPD Patients are Related to Epithelial–Macrophage Interactions.* Cells, 2020. **9**(9): p. 1944.

177. Siegel, R.L., K.D. Miller, and A. Jemal, *Cancer statistics, 2020.* CA: a cancer journal for clinicians, 2020. **70**(1): p. 7-30.

178. Stevens, J.L. and T.K. Baker, *The future of drug safety testing: expanding the view and narrowing the focus.* Drug discovery today, 2009. **14**(3): p. 162-167.

179. Weigelt, B., C.M. Ghajar, and M.J. Bissell, *The need for complex 3D culture models to unravel novel pathways and identify accurate biomarkers in breast cancer.* Advanced drug delivery reviews, 2014. **69**(NA): p. 42-51.

180. Jakiela, B., et al., *Eicosanoid biosynthesis during mucociliary and mucous metaplastic differentiation of bronchial epithelial cells.* Prostaglandins & other lipid mediators, 2013. **106**(NA): p. 116-123.

181. Shaykhiev, R., et al., *EGF shifts human airway basal cell fate toward a smoking-associated airway epithelial phenotype.* Proceedings of the National Academy of Sciences of the United States of America, 2013. **110**(29): p. 12102-12107.

182. Lee, J., et al., *Prevention of bronchial hyperplasia by EGFR pathway inhibitors in an organotypic culture model.* Cancer prevention research (Philadelphia, Pa.), 2011. **4**(8): p. 1306-1315.

183. Horie, M., et al., *Characterization of human lung cancer-associated fibroblasts in three-dimensional in vitro co-culture model.* Biochemical and biophysical research communications, 2012. **423**(1): p. 158-163.

184. Correia, L.L., et al., *SOX2 Drives Bronchial Dysplasia in a Novel Organotypic Model of Early Human Squamous Lung Cancer.* American journal of respiratory and critical care medicine, 2017. **195**(11): p. 1494-1508.

185. Zanoni, M., et al., *3D tumor spheroid models for in vitro therapeutic screening: a systematic approach to enhance the biological relevance of data obtained.* Scientific reports, 2016. **6**(1): p. 19103-19103.

186. Kim, M., et al., *Patient-derived lung cancer organoids as in vitro cancer models for therapeutic screening.* Nat Commun, 2019. **10**(1): p. 3991.

187. Han, K., et al., *CRISPR screens in cancer spheroids identify 3D growth-specific vulnerabilities.* Nature, 2020. **580**(7801): p. 136-141.

188. Di Liello, R., et al., *Ex vivo lung cancer spheroids resemble treatment response of a patient with NSCLC to chemotherapy and immunotherapy: case report and translational study.* ESMO open, 2019. **4**(4): p. e000536-NA.

189. Meenach, S.A., et al., *Development of three-dimensional lung multicellular spheroids in air- and liquid-interface culture for the evaluation of anticancer therapeutics.* International journal of oncology, 2016. **48**(4): p. 1701-1709.

190. Gupta, S.K., E.A.T. Guzmán, and S.A. Meenach, *Coadministration of a tumor-penetrating peptide improves the therapeutic efficacy of paclitaxel in a novel air-grown lung cancer 3D spheroid model.* International journal of cancer, 2017. **141**(10): p. 2143-2153.

191. Movia, D., et al., *Multilayered Cultures of NSCLC cells grown at the Air-Liquid Interface allow the efficacy testing of inhaled anti-cancer drugs.* Scientific reports, 2018. **8**(1): p. 12920-12920.

192. Movia, D., D. Bazou, and A. Prina-Mello, *ALI multilayered co-cultures mimic biochemical mechanisms of the cancer cell-fibroblast cross-talk involved in NSCLC MultiDrug Resistance.* BMC Cancer, 2019. **19**(1): p. 854.

193. Zhang, Y.M., et al., *Co-culture with lung cancer A549 cells promotes the proliferation and migration of mesenchymal stem cells derived from bone marrow.* Experimental and therapeutic medicine, 2017. **14**(4): p. 2983-2991.

194. Gagnadoux, F., et al., *Aerosolized chemotherapy.* Journal of aerosol medicine and pulmonary drug delivery, 2008. **21**(1): p. 61-70.

195. Lee, W.-H., et al., *Inhalation of nanoparticle-based drug for lung cancer treatment: Advantages and challenges.* Asian Journal of Pharmaceutical Sciences, 2015. **10**(6): p. 481-489.

196. Rosiere, R., et al., *New Folate-Grafted Chitosan Derivative To Improve Delivery of Paclitaxel-Loaded Solid Lipid Nanoparticles for Lung Tumor Therapy by Inhalation.* Molecular pharmaceutics, 2018. **15**(3): p. 899-910.

197. Almuqbil, R.M., et al., *Dendrimer Conjugation Enhances Tumor Penetration and Efficacy of Doxorubicin in Extracellular Matrix-Expressing 3D Lung Cancer Models.* Molecular pharmaceutics, 2020. **17**(5): p. 1648-1662.

198. Joshi, N., et al., *Endogenous lung surfactant inspired pH responsive nanovesicle aerosols: Pulmonary compatible and site-specific drug delivery in lung metastases.* Scientific Reports, 2014. **4**(1): p. 7085.

199. Mehta, A., et al., *Targeting KRAS Mutant Lung Cancer Cells with siRNA-Loaded Bovine Serum Albumin Nanoparticles.* Pharm Res, 2019. **36**(9): p. 133.

200. Zhang, C., et al., *Co-delivery of paclitaxel and survivin siRNA with cationic liposome for lung cancer therapy.* Colloids and Surfaces A: Physicochemical and Engineering Aspects, 2020. **585**(NA): p. 124054-NA.

201. Brandsma, C.-A., et al., *Recent advances in chronic obstructive pulmonary disease pathogenesis: from disease mechanisms to precision medicine.* The Journal of pathology, 2019. **250**(5): p. 624-635.

202. Marin, L., et al., *Chronic obstructive pulmonary disease: patho-physiology, current methods of treatment and the potential for simvastatin in disease management.* Expert opinion on drug delivery, 2011. **8**(9): p. 1205-1220.

203. Tuder, R.M. and I. Petrache, *Pathogenesis of chronic obstructive pulmonary disease.* The Journal of clinical investigation, 2012. **122**(8): p. 2749-2755.

204. MacNee, W., *Pathogenesis of chronic obstructive pulmonary disease.* Proceedings of the American Thoracic Society, 2005. **2**(4): p. 258-266.

205. Gao, W., et al., *Bronchial epithelial cells: The key effector cells in the pathogenesis of chronic obstructive pulmonary disease?* Respirology (Carlton, Vic.), 2015. **20**(5): p. 722-729.

206. Schamberger, A.C., et al., *Cigarette Smoke–Induced Disruption of Bronchial Epithelial Tight Junctions Is Prevented by Transforming Growth Factor-β.* American journal of respiratory cell and molecular biology, 2014. **50**(6): p. 1040-1052.

207. Haswell, L.E., et al., *Cigarette smoke total particulate matter increases mucous secreting cell numbers in vitro: A potential model of goblet cell hyperplasia.* Toxicology in vitro : an international journal published in association with BIBRA, 2010. **24**(3): p. 981-987.

208. Gohy, S., et al., *Imprinting of the COPD airway epithelium for dedifferentiation and mesenchymal transition.* The European respiratory journal, 2015. **45**(5): p. 1258-1272.

209. Heijink, I.H., et al., *Cigarette smoke-induced epithelial expression of WNT-5B: implications for COPD.* The European respiratory journal, 2016. **48**(2): p. 504-515.

210. Comer, D.M., et al., *Airway epithelial cell apoptosis and inflammation in COPD, smokers and nonsmokers.* The European respiratory journal, 2012. **41**(5): p. 1058-1067.

211. Amatngalim, G.D., et al., *Antibacterial Defense of Human Airway Epithelial Cells from Chronic Obstructive Pulmonary Disease Patients Induced by Acute*

Exposure to Nontypeable Haemophilus influenzae: Modulation by Cigarette Smoke. Journal of innate immunity, 2017. **9**(4): p. 359-374.

212. Azzopardi, D., et al., *Evaluation of an air–liquid interface cell culture model for studies on the inflammatory and cytotoxic responses to tobacco smoke aerosols.* Toxicology in vitro : an international journal published in association with BIBRA, 2015. **29**(7): p. 1720-1728.

213. Zarcone, M.C., et al., *Diesel exhaust alters the response of cultured primary bronchial epithelial cells from patients with chronic obstructive pulmonary disease (COPD) to non-typeable Haemophilus influenzae.* Respiratory research, 2017. **18**(1): p. 27-27.

214. Ladjemi, M.Z., et al., *Increased IgA production by B-cells in COPD via lung epithelial interleukin-6 and TACI pathways.* The European respiratory journal, 2014. **45**(4): p. 980-993.

215. Osei, E.T., et al., *Interleukin-1α drives the dysfunctional cross-talk of the airway epithelium and lung fibroblasts in COPD.* The European respiratory journal, 2016. **48**(2): p. 359-369.

216. Gindele, J.A., et al., *Opposing effects of in vitro differentiated macrophages sub-type on epithelial wound healing.* PloS one, 2017. **12**(9): p. e0184386-NA.

217. Marin, L., et al., *Multiple dosing of simvastatin inhibits airway mucus production of epithelial cells: Implications in the treatment of chronic obstructive airway pathologies.* European journal of pharmaceutics and biopharmaceutics : official journal of Arbeitsgemeinschaft fur Pharmazeutische Verfahrenstechnik e.V, 2013. **84**(3): p. 566-572.

218. Tatsuta, M., et al., *Effects of cigarette smoke on barrier function and tight junction proteins in the bronchial epithelium: protective role of cathelicidin LL-37.* Respiratory research, 2019. **20**(1): p. 251-251.

219. Schmid, A., et al., *Roflumilast partially reverses smoke-induced mucociliary dysfunction.* Respiratory research, 2015. **16**(1): p. 135-135.

220. Bucher, H., et al., *Neutralization of both IL-1alpha/IL-1beta plays a major role in suppressing combined cigarette smoke/virus-induced pulmonary inflammation in mice.* Pulm Pharmacol Ther, 2017. **44**: p. 96-105.

221. Reus, A.A., et al., *Feasibility of a 3D human airway epithelial model to study respiratory absorption.* Toxicology in vitro : an international journal published in association with BIBRA, 2013. **28**(2): p. 258-264.

222. Huang, S., et al., *Potential of in vitro reconstituted 3D human airway epithelia (MucilAir™) to assess respiratory sensitizers.* Toxicology in vitro : an international journal published in association with BIBRA, 2012. **27**(3): p. 1151-1156.

223. Mercier, C., et al., *Pharmacological characterization of the 3D MucilAir™ nasal model.* European journal of pharmaceutics and biopharmaceutics : official journal of Arbeitsgemeinschaft fur Pharmazeutische Verfahrenstechnik e.V, 2019. **139**(NA): p. 186-196.

224. Rotoli, B.M., et al., *Characterization of ABC Transporters in EpiAirway™, a Cellular Model of Normal Human Bronchial Epithelium.* International journal of molecular sciences, 2020. **21**(9): p. 3190-NA.

225. HoffmannWiebke, et al., *Establishment of a Human 3D Tissue-Based Assay for Upper Respiratory Tract Absorption.* Applied In Vitro Toxicology, 2018. **4**(2): p. 139-148.

226. Furubayashi, T., et al., *Comparison of Various Cell Lines and Three-Dimensional Mucociliary Tissue Model Systems to Estimate Drug Permeability Using an In Vitro Transport Study to Predict Nasal Drug Absorption in Rats.* Pharmaceutics, 2020. **12**(1): p. 79-NA.

227. Iskandar, A.R., et al., *Impact Assessment of Cigarette Smoke Exposure on Organotypic Bronchial Epithelial Tissue Cultures: A Comparison of Mono-Culture and Coculture Model Containing Fibroblasts.* Toxicological sciences : an official journal of the Society of Toxicology, 2015. **147**(1): p. 207-221.

228. Kooter, I.M., et al., *Factors of concern in a human 3D cellular airway model exposed to aerosols of nanoparticles.* Toxicology in vitro : an international journal published in association with BIBRA, 2017. **44**(NA): p. 339-348.

229. Sancey, L., et al., *Multiparametric investigation of non functionalized-AGuIX nanoparticles in 3D human airway epithelium models demonstrates preferential targeting of tumor cells.* Journal of nanobiotechnology, 2020. **18**(1): p. 129-129.

230. Mistry, A., et al., *Development of an in vitro approach to point-of-contact inhalation toxicity testing of volatile compounds, using organotypic culture and air-liquid interface exposure.* Toxicology in vitro : an international journal published in association with BIBRA, 2020. **69**(NA): p. 104968-NA.

231. Outlaw, V.K., et al., *Inhibition of Coronavirus Entry In Vitro and Ex Vivo by a Lipid-Conjugated Peptide Derived from the SARS-CoV-2 Spike Glycoprotein HRC Domain.* mBio, 2020. **11**(5): p. 1-14.

232. Huang, S., et al., *Establishment and characterization of an in vitro human small airway model (SmallAir.* European journal of pharmaceutics and

biopharmaceutics : official journal of Arbeitsgemeinschaft fur Pharmazeutische Verfahrenstechnik e.V, 2016. **118**(NA): p. 68-72.

233. Barosova, H., et al., *Use of EpiAlveolar Lung Model to Predict Fibrotic Potential of Multiwalled Carbon Nanotubes.* ACS nano, 2020. **14**(4): p. 3941-3956.

234. BolmarcichJennifer, N.A., et al., *In Vitro Human Airway Models for Study of Goblet Cell Hyperplasia and Mucus Production: Effects of Th2 Cytokines, Double-Stranded RNA, and Tobacco Smoke.* Applied In Vitro Toxicology, 2018. **4**(4): p. 332-346.

235. De Matos, R., et al., *Inhibitor-conjugated harmonic nanoparticles targeting fibroblast activation protein.* RSC Adv, 2019. **9**(54): p. 31659-31669.

236. Signer, J., et al., *In vitro virucidal activity of Echinaforce®, an Echinacea purpurea preparation, against coronaviruses, including common cold coronavirus 229E and SARS-CoV-2.* Virology journal, 2020. **17**(1): p. 136-136.

237. Mas, C., et al., *Antitumour efficacy of the selumetinib and trametinib MEK inhibitors in a combined human airway–tumour–stroma lung cancer model.* Journal of biotechnology, 2015. **205**(NA): p. 111-119.

238. Kilin, V., et al., *Health state dependent multiphoton induced autofluorescence in human 3D in vitro lung cancer model.* Scientific reports, 2017. **7**(1): p. 16233-NA.

239. Schimek, K., et al., *Human multi-organ chip co-culture of bronchial lung culture and liver spheroids for substance exposure studies.* Scientific reports, 2020. **10**(1): p. 7865-NA.

240. Shrestha, J., et al., *Lung-on-a-chip: the future of respiratory disease models and pharmacological studies.* Critical Reviews in Biotechnology, 2020. **40**(2): p. 213-230.

241. Dellaquila, A., et al., *Organ-on-a-Chip*. 2020, Academic Press Cambridge, MA, USA:.

242. Zamprogno, P., et al., *Second-generation lung-on-a-chip with an array of stretchable alveoli made with a biological membrane.* Communications biology, 2021. **4**(1): p. 168-168.

243. Huh, D., et al., *Reconstituting Organ-Level Lung Functions on a Chip.* Science (New York, N.Y.), 2010. **328**(5986): p. 1662-1668.

244. Liu, Z., et al., *Co-cultured microfluidic model of the airway optimized for microscopy and micro-optical coherence tomography imaging.* Biomedical optics express, 2019. **10**(10): p. 5414-5430.

245. Kızılkurtlu, A.A., et al., *Lung on a Chip for Drug Screening and Design.* Current pharmaceutical design, 2019. **24**(45): p. 5386-5396.

246. Lenz, A.-G., et al., *Efficient Bioactive Delivery of Aerosolized Drugs to Human Pulmonary Epithelial Cells Cultured in Air–Liquid Interface Conditions.* American journal of respiratory cell and molecular biology, 2014. **51**(4): p. 526-535.

247. Schmid, O., et al., *Biokinetics of Aerosolized Liposomal Ciclosporin A in Human Lung Cells In Vitro Using an Air-Liquid Cell Interface Exposure System.* Journal of aerosol medicine and pulmonary drug delivery, 2017. **30**(6): p. 411-424.

248. Klein, S.G., et al., *An improved 3D tetraculture system mimicking the cellular organisation at the alveolar barrier to study the potential toxic effects of particles on the lung.* Particle and fibre toxicology, 2013. **10**(1): p. 31-31.

249. Tsoutsoulopoulos, A., et al., *Validation of the CULTEX® Radial Flow System for the assessment of the acute inhalation toxicity of airborne particles.* Toxicology in vitro : an international journal published in association with BIBRA, 2019. **58**(NA): p. 245-255.

250. Aufderheide, M., et al., *A new computer-controlled air-liquid interface cultivation system for the generation of differentiated cell cultures of the airway epithelium.* Experimental and toxicologic pathology : official journal of the Gesellschaft fur Toxikologische Pathologie, 2015. **68**(1): p. 77-87.

251. Polk, W.W., et al., *Aerosol generation and characterization of multi-walled carbon nanotubes exposed to cells cultured at the air-liquid interface.* Particle and fibre toxicology, 2016. **13**(1): p. 20-20.

252. Ji, J., et al., *Development of Combining of Human Bronchial Mucosa Models with XposeALI® for Exposure of Air Pollution Nanoparticles.* PloS one, 2017. **12**(1): p. e0170428-NA.

253. Upadhyay, S. and L. Palmberg, *Air-Liquid Interface: Relevant In Vitro Models for Investigating Air Pollutant-Induced Pulmonary Toxicity.* Toxicological sciences : an official journal of the Society of Toxicology, 2018. **164**(1): p. 21-30.

254. Jeannet, N., et al., *Nano Aerosol Chamber for In-Vitro Toxicity (NACIVT) studies.* Nanotoxicology, 2014. **9**(1): p. 34-42.

255. Ihalainen, M., et al., *Design and validation of an air-liquid interface (ALI) exposure device based on thermophoresis.* Aerosol Science and Technology, 2018. **53**(2): p. 133-145.

256. Ding, Y., et al., *Quartz crystal microbalances (QCM) are suitable for real-time dosimetry in nanotoxicological studies using VITROCELL®Cloud cell exposure systems.* Particle and fibre toxicology, 2020. **17**(1): p. 1-20.

257. Mitragotri, S., P.A. Burke, and R. Langer, *Overcoming the challenges in administering biopharmaceuticals: formulation and delivery strategies.* Nature Reviews Drug Discovery, 2014. **13**(9): p. 655-672.

258. Vargason, A.M., A.C. Anselmo, and S. Mitragotri, *The evolution of commercial drug delivery technologies.* Nature Biomedical Engineering, 2021. **5**(9): p. 951-967.

259. Albarran, B., A.S. Hoffman, and P.S. Stayton, *Efficient intracellular delivery of a pro-apoptotic peptide with a pH-responsive carrier.* Reactive and Functional Polymers, 2011. **71**(3): p. 261-265.

260. Blanco, E., H. Shen, and M. Ferrari, *Principles of nanoparticle design for overcoming biological barriers to drug delivery.* Nature Biotechnology, 2015. **33**(9): p. 941-951.

261. Agrahari, V., V. Agrahari, and A.K. Mitra, *Nanocarrier fabrication and macromolecule drug delivery: challenges and opportunities.* Therapeutic Delivery, 2016. **7**(4): p. 257-278.

262. Samaridou, E., J. Heyes, and P. Lutwyche, *Lipid nanoparticles for nucleic acid delivery: Current perspectives.* Advanced Drug Delivery Reviews, 2020. **154-155**: p. 37-63.

263. Rui, Y., et al., *Carboxylated branched poly(β-amino ester) nanoparticles enable robust cytosolic protein delivery and CRISPR-Cas9 gene editing.* Science Advances, 2019. **5**(12): p. eaay3255.

264. Kandil, R., et al., *T Cell Transfection: Coming in and Finding Out: Blending Receptor-Targeted Delivery and Efficient Endosomal Escape in a Novel Bio-Responsive siRNA Delivery System for Gene Knockdown in Pulmonary T Cells (Adv. Therap. 7/2019).* Advanced Therapeutics, 2019. **2**(7): p. 1970015.

265. Yasar, H., et al., *Kinetics of mRNA delivery and protein translation in dendritic cells using lipid-coated PLGA nanoparticles.* Journal of Nanobiotechnology, 2018. **16**(1): p. 72.

266. Mitchell, M.J., et al., *Engineering precision nanoparticles for drug delivery.* Nature Reviews Drug Discovery, 2021. **20**(2): p. 101-124.

267. Zielińska, A., et al., *Polymeric nanoparticles: production, characterization, toxicology and ecotoxicology.* Molecules, 2020. **25**(16): p. 3731.

268. Choukaife, H., et al., *Current Advances in Chitosan Nanoparticles Based Oral Drug Delivery for Colorectal Cancer Treatment.* International Journal of Nanomedicine, 2022: p. 3933-3966.

269. Bodmeier, R., K.-H. Oh, and Y. Pramar, *Preparation and evaluation of drug-containing chitosan beads.* Drug development and industrial pharmacy, 1989. **15**(9): p. 1475-1494.

270. Dudhani, A.R. and S.L. Kosaraju, *Bioadhesive chitosan nanoparticles: Preparation and characterization.* Carbohydrate Polymers, 2010. **81**(2): p. 243-251.

271. Gabold, B., et al., *Transferrin-modified chitosan nanoparticles for targeted nose-to-brain delivery of proteins.* Drug Delivery and Translational Research, 2022.

272. Kaur, S., et al., *Bioengineered PLGA-chitosan nanoparticles for brain targeted intranasal delivery of antiepileptic TRH analogues.* Chemical Engineering Journal, 2018. **346**: p. 630-639.

273. Piazzini, V., et al., *Chitosan coated human serum albumin nanoparticles: A promising strategy for nose-to-brain drug delivery.* International Journal of Biological Macromolecules, 2019. **129**: p. 267-280.

274. Rinaldi, F., et al., *Different instrumental approaches to understand the chitosan coated niosomes/mucin interaction.* Journal of Drug Delivery Science and Technology, 2020. **55**: p. 101339.

275. Ho, D.-K., et al., *Farnesylated Glycol Chitosan as a Platform for Drug Delivery: Synthesis, Characterization, and Investigation of Mucus–Particle Interactions.* Biomacromolecules, 2018.

276. Wu, X., et al., *Cationic chitosan-modified silica nanoparticles for oral delivery of protein vaccine.* Journal of Biomedical Materials Research Part A, 2021. **109**(11): p. 2111-2119.

277. Bashir, S.M., et al., *Chitosan Nanoparticles: A Versatile Platform for Biomedical Applications.* Materials, 2022. **15**(19): p. 6521.

278. Mikušová, V. and P. Mikuš, *Advances in Chitosan-Based Nanoparticles for Drug Delivery.* International Journal of Molecular Sciences, 2021. **22**(17): p. 9652.

279. Chiesa, E., et al., *The Microfluidic Technique and the Manufacturing of Polysaccharide Nanoparticles.* Pharmaceutics, 2018. **10**(4): p. 267.

280. Shepherd, S.J., D. Issadore, and M.J. Mitchell, *Microfluidic formulation of nanoparticles for biomedical applications.* Biomaterials, 2021. **274**: p. 120826.

281. Whitesides, G.M., *The origins and the future of microfluidics.* Nature, 2006. **442**(7101): p. 368-373.

282. Valencia, P.M., et al., *Microfluidic technologies for accelerating the clinical translation of nanoparticles.* Nature Nanotechnology, 2012. **7**(10): p. 623-629.

283. Zhao, X., et al., *Microfluidic Generation of Nanomaterials for Biomedical Applications.* Small, 2020. **16**(9): p. 1901943.

284. Garg, S., et al., *Microfluidics: a transformational tool for nanomedicine development and production.* Journal of Drug Targeting, 2016. **24**(9): p. 821-835.

285. Hartl, N., et al., *The impact of Nylon-3 copolymer composition on the efficiency of siRNA delivery to glioblastoma Cells.* Nanomaterials, 2019. **9**(7): p. 986.

286. Nečas, D. and P. Klapetek, *Gwyddion: an open-source software for SPM data analysis.* Open Physics, 2012. **10**(1): p. 181-188.

287. Zhang, Z., et al., *Encapsulation of lactase (β-galactosidase) into κ-carrageenan-based hydrogel beads: Impact of environmental conditions on enzyme activity.* Food Chemistry, 2016. **200**: p. 69-75.

288. Estevinho, B.N., et al., *Microencapsulation of β-galactosidase with different biopolymers by a spray-drying process.* Food Research International, 2014. **64**: p. 134-140.

289. Chiesa, E., et al., *Staggered Herringbone Microfluid Device for the Manufacturing of Chitosan/TPP Nanoparticles: Systematic Optimization and Preliminary Biological Evaluation.* International Journal of Molecular Sciences, 2019. **20**(24): p. 6212.

290. de la Fuente, M., et al., *Chitosan-based nanostructures: A delivery platform for ocular therapeutics.* Advanced Drug Delivery Reviews, 2010. **62**(1): p. 100-117.

291. Marsili, L., et al., *Thermoresponsive Chitosan-Grafted-Poly(N-vinylcaprolactam) Microgels via Ionotropic Gelation for Oncological Applications.* Pharmaceutics, 2021. **13**(10): p. 1654.

292. Chiesa, E., et al., *CD44-Targeted Carriers: The Role of Molecular Weight of Hyaluronic Acid in the Uptake of Hyaluronic Acid-Based Nanoparticles.* Pharmaceuticals, 2022. **15**(1): p. 103.

293. Chiesa, E., et al., *Hyaluronic Acid-Based Nanoparticles for Protein Delivery: Systematic Examination of Microfluidic Production Conditions.* Pharmaceutics, 2021. **13**(10): p. 1565.

294. Chiesa, E., et al., *On-Chip Synthesis of Hyaluronic Acid-Based Nanoparticles for Selective Inhibition of CD44+ Human Mesenchymal Stem Cell Proliferation.* Pharmaceutics, 2020. **12**(3): p. 260.

295. Hussain, M.T., et al., *Microfluidic production of protein loaded chimeric stealth liposomes.* International Journal of Pharmaceutics, 2020. **590**: p. 119955.

296. Xiao, B., et al., *Effects of tripolyphosphate on cellular uptake and RNA interference efficiency of chitosan-based nanoparticles in Raw 264.7 macrophages.* Journal of Colloid and Interface Science, 2017. **490**: p. 520-528.

297. Jiang, T., et al., *Dual targeted delivery of statins and nucleic acids by chitosan-based nanoparticles for enhanced antiatherosclerotic efficacy.* Biomaterials, 2022. **280**: p. 121324.

298. Jeandupeux, E., et al., *Poly(2-Propylacrylic Acid) Increases In Vitro Bioactivity of Chitosan/mRNA Nanoparticles.* Journal of Pharmaceutical Sciences, 2021. **110**(10): p. 3439-3449.

299. Wang, M., et al., *Tumor-targeted nano-delivery system of therapeutic RNA.* Materials Horizons, 2022. **9**(4): p. 1111-1140.

300. Guo, D., et al., *RNA interference therapy for glioblastoma.* Expert Opinion on Biological Therapy, 2010. **10**(6): p. 927-936.

301. Cordeiro, A.S., et al., *Carboxymethyl-β-glucan/chitosan nanoparticles: new thermostable and efficient carriers for antigen delivery.* Drug Delivery and Translational Research, 2021. **11**(4): p. 1689-1702.

302. Morales-Cruz, M., et al., *Smart targeting to improve cancer therapeutics.* Drug design, development and therapy, 2019: p. 3753-3772.

303. Morachis, J.M., E.A. Mahmoud, and A. Almutairi, *Physical and Chemical Strategies for Therapeutic Delivery by Using Polymeric Nanoparticles.* Pharmacological Reviews, 2012. **64**(3): p. 505-519.

304. Choi, H.S., et al., *Renal clearance of nanoparticles.* Nature biotechnology, 2007. **25**(10): p. 1165.

305. Chen, Z., *Small-molecule delivery by nanoparticles for anticancer therapy.* Trends in Molecular Medicine, 2010. **16**(12): p. 594-602.

306. Huang, J., et al., *Radiosensitivity enhancement by combined treatment of nimotuzumab and celecoxib on nasopharyngeal carcinoma cells.* Drug Design, Development and Therapy, 2018: p. 2223-2231.

307. Kamaly, N., et al., *Degradable Controlled-Release Polymers and Polymeric Nanoparticles: Mechanisms of Controlling Drug Release.* Chemical Reviews, 2016. **116**(4): p. 2602-2663.

308. Bohrey, S., V. Chourasiya, and A. Pandey, *Polymeric nanoparticles containing diazepam: preparation, optimization, characterization, in-vitro drug release and release kinetic study.* Nano Convergence, 2016. **3**(1): p. 3.

309. Scott, C.C., F. Vacca, and J. Gruenberg, *Endosome maturation, transport and functions.* Seminars in Cell & Developmental Biology, 2014. **31**: p. 2-10.

310. Herrera, M., et al., *Illuminating endosomal escape of polymorphic lipid nanoparticles that boost mRNA delivery.* Biomaterials Science, 2021. **9**(12): p. 4289-4300.

311. Donahue, N.D., H. Acar, and S. Wilhelm, *Concepts of nanoparticle cellular uptake, intracellular trafficking, and kinetics in nanomedicine.* Advanced Drug Delivery Reviews, 2019. **143**: p. 68-96.

312. dos Santos, T., et al., *Effects of Transport Inhibitors on the Cellular Uptake of Carboxylated Polystyrene Nanoparticles in Different Cell Lines.* PLOS ONE, 2011. **6**(9): p. e24438.

313. Malhotra, M., et al., *Ultrafine chitosan nanoparticles as an efficient nucleic acid delivery system targeting neuronal cells.* Drug Development and Industrial Pharmacy, 2009. **35**(6): p. 719-726.

314. Chellat, F., et al., *Metalloproteinase and cytokine production by THP-1 macrophages following exposure to chitosan-DNA nanoparticles.* Biomaterials, 2005. **26**(9): p. 961-970.

315. Nasti, A., et al., *Chitosan/TPP and Chitosan/TPP-hyaluronic Acid Nanoparticles: Systematic Optimisation of the Preparative Process and Preliminary Biological Evaluation.* Pharmaceutical Research, 2009. **26**(8): p. 1918-1930.

316. Aranaz, I., et al., *Chitosan: An overview of its properties and applications.* Polymers, 2021. **13**(19): p. 3256.

317. Jin, T., et al., *Chitin and chitosan on the nanoscale.* Nanoscale Horizons, 2021. **6**(7): p. 505-542.

318. Rashki, S., et al., *Chitosan-based nanoparticles against bacterial infections.* Carbohydrate Polymers, 2021. **251**: p. 117108.

319. Weiss, M., et al., *Density of surface charge is a more predictive factor of the toxicity of cationic carbon nanoparticles than zeta potential.* Journal of Nanobiotechnology, 2021. **19**(1): p. 5.

320. Garaiova, Z., et al., *Cellular uptake of DNA–chitosan nanoparticles: The role of clathrin- and caveolae-mediated pathways.* International Journal of Biological Macromolecules, 2012. **51**(5): p. 1043-1051.

321. Zaki, N.M., A. Nasti, and N. Tirelli, *Nanocarriers for Cytoplasmic Delivery: Cellular Uptake and Intracellular Fate of Chitosan and Hyaluronic Acid-Coated Chitosan Nanoparticles in a Phagocytic Cell Model.* Macromolecular Bioscience, 2011. **11**(12): p. 1747-1760.

322. Ibba, M.L., et al., *Advances in mRNA non-viral delivery approaches.* Advanced Drug Delivery Reviews, 2021. **177**: p. 113930.

323. Buschmann, M.D., et al., *Nanomaterial Delivery Systems for mRNA Vaccines.* Vaccines, 2021. **9**(1): p. 65.

324. Chuah, L.H., et al., *Cellular uptake and anticancer effects of mucoadhesive curcumin-containing chitosan nanoparticles.* Colloids and Surfaces B: Biointerfaces, 2014. **116**: p. 228-236.

325. Ma, Z. and L.-Y. Lim, *Uptake of Chitosan and Associated Insulin in Caco-2 Cell Monolayers: A Comparison Between Chitosan Molecules and Chitosan Nanoparticles.* Pharmaceutical Research, 2003. **20**(11): p. 1812-1819.

326. Nowak, M., M.E. Helgeson, and S. Mitragotri, *Delivery of Nanoparticles and Macromolecules across the Blood–Brain Barrier.* Advanced Therapeutics, 2020. **3**(1): p. 1900073.

327. Furtado, D., et al., *Overcoming the Blood–Brain Barrier: The Role of Nanomaterials in Treating Neurological Diseases.* Advanced Materials, 2018. **30**(46): p. 1801362.

328. S Hersh, D., et al., *Evolving drug delivery strategies to overcome the blood brain barrier.* Current pharmaceutical design, 2016. **22**(9): p. 1177-1193.

329. Hartl, N., F. Adams, and O.M. Merkel, *From Adsorption to Covalent Bonding: Apolipoprotein E Functionalization of Polymeric Nanoparticles for Drug Delivery Across the Blood–Brain Barrier.* Advanced Therapeutics, 2021. **4**(1): p. 2000092.

330. Graff, C.L. and G.M. Pollack, *Nasal Drug Administration: Potential for Targeted Central Nervous System Delivery.* Journal of Pharmaceutical Sciences, 2005. **94**(6): p. 1187-1195.

331. Tashima, T., *Shortcut Approaches to Substance Delivery into the Brain Based on Intranasal Administration Using Nanodelivery Strategies for Insulin.* Molecules, 2020. **25**(21): p. 5188.

332. Reger, M.A., et al., *Effects of intranasal insulin on cognition in memory-impaired older adults: Modulation by APOE genotype.* Neurobiology of Aging, 2006. **27**(3): p. 451-458.

333. Lee, D. and T. Minko, *Nanotherapeutics for Nose-to-Brain Drug Delivery: An Approach to Bypass the Blood Brain Barrier.* Pharmaceutics, 2021. **13**(12): p. 2049.

334. Borrajo, M.L. and M.J. Alonso, *Using nanotechnology to deliver biomolecules from nose to brain — peptides, proteins, monoclonal antibodies and RNA.* Drug Delivery and Translational Research, 2021.

335. Md, S., et al., *Bromocriptine loaded chitosan nanoparticles intended for direct nose to brain delivery: Pharmacodynamic, Pharmacokinetic and Scintigraphy study in mice model.* European Journal of Pharmaceutical Sciences, 2013. **48**(3): p. 393-405.

336. Piazza, J., et al., *Haloperidol-loaded intranasally administered lectin functionalized poly(ethylene glycol)–block-poly(d,l)-lactic-co-glycolic acid (PEG–PLGA) nanoparticles for the treatment of schizophrenia.* European Journal of Pharmaceutics and Biopharmaceutics, 2014. **87**(1): p. 30-39.

337. Dodane, V., M. Amin Khan, and J.R. Merwin, *Effect of chitosan on epithelial permeability and structure.* International Journal of Pharmaceutics, 1999. **182**(1): p. 21-32.

338. Felt, O., P. Buri, and R. Gurny, *Chitosan: A Unique Polysaccharide for Drug Delivery.* Drug Development and Industrial Pharmacy, 1998. **24**(11): p. 979-993.

339. Sinha, V.R., et al., *Chitosan microspheres as a potential carrier for drugs.* International Journal of Pharmaceutics, 2004. **274**(1): p. 1-33.

340. Gorshkova, N., et al., *Preparation of bioactive aerogel material based on sodium alginate and chitosan for controlled release of levomycetin.* Polymers for Advanced Technologies, 2021. **32**(9): p. 3474-3482.

341. Cisneros, K., et al., *Long-Term Controlled Release of Simvastatin from Photoprinted Triple-Networked Hydrogels Composed of Modified Chitosan and PLA–PEG Micelles.* Macromolecular Bioscience, 2021. **21**(8): p. 2100123.

342. Affes, S., et al., *Chitosan derivatives-based films as pH-sensitive drug delivery systems with enhanced antioxidant and antibacterial properties.* International Journal of Biological Macromolecules, 2021. **182**: p. 730-742.

343. Gan, Q. and T. Wang, *Chitosan nanoparticle as protein delivery carrier—Systematic examination of fabrication conditions for efficient loading and release.* Colloids and Surfaces B: Biointerfaces, 2007. **59**(1): p. 24-34.

344. Aderibigbe, B.A. and T. Naki, *Chitosan-Based Nanocarriers for Nose to Brain Delivery.* Applied Sciences, 2019. **9**(11): p. 2219.

345. Keller, L.-A., O. Merkel, and A. Popp, *Intranasal drug delivery: opportunities and toxicologic challenges during drug development.* Drug Delivery and Translational Research, 2021.

346. Wu, H., K. Hu, and X. Jiang, *From nose to brain: understanding transport capacity and transport rate of drugs.* Expert Opinion on Drug Delivery, 2008. **5**(10): p. 1159-1168.

347. Erdő, F., et al., *Evaluation of intranasal delivery route of drug administration for brain targeting.* Brain Research Bulletin, 2018. **143**: p. 155-170.

348. Gizurarson, S., *Anatomical and Histological Factors Affecting Intranasal Drug and Vaccine Delivery.* Current Drug Delivery, 2012. **9**(6): p. 566-582.

349. Harkema, J.R., S.A. Carey, and J.G. Wagner, *The Nose Revisited: A Brief Review of the Comparative Structure, Function, and Toxicologic Pathology of the Nasal Epithelium.* Toxicologic Pathology, 2006. **34**(3): p. 252-269.

350. Gao, X., et al., *Brain delivery of vasoactive intestinal peptide enhanced with the nanoparticles conjugated with wheat germ agglutinin following intranasal administration.* Journal of Controlled Release, 2007. **121**(3): p. 156-167.

351. Chen, J., et al., *Solanum tuberosum lectin-conjugated PLGA nanoparticles for nose-to-brain delivery: in vivo and in vitro evaluations.* Journal of Drug Targeting, 2012. **20**(2): p. 174-184.

352. Liu, Z., et al., *Lactoferrin-modified PEG-co-PCL nanoparticles for enhanced brain delivery of NAP peptide following intranasal administration.* Biomaterials, 2013. **34**(15): p. 3870-3881.

353. Bi, C., et al., *Intranasal delivery of rotigotine to the brain with lactoferrin-modified PEG-PLGA nanoparticles for Parkinson's disease treatment.* International journal of nanomedicine, 2016. **11**: p. 6547-6559.

354. Yan, X., et al., *Lactoferrin-modified rotigotine nanoparticles for enhanced nose-to-brain delivery: LESA-MS/MS-based drug biodistribution, pharmacodynamics, and neuroprotective effects.* International journal of nanomedicine, 2018. **13**: p. 273-281.

355. Akita, T., et al., *Usefulness of cell-penetrating peptides and penetration accelerating sequence for nose-to-brain delivery of glucagon-like peptide-2.* Journal of Controlled Release, 2021. **335**: p. 575-583.

356. Kanazawa, T., H. Taki, and H. Okada, *Nose-to-brain drug delivery system with ligand/cell-penetrating peptide-modified polymeric nano-micelles for intracerebral gliomas.* European Journal of Pharmaceutics and Biopharmaceutics, 2020. **152**: p. 85-94.

357. Hernando, S., et al., *Intranasal Administration of TAT-Conjugated Lipid Nanocarriers Loading GDNF for Parkinson's Disease.* Molecular Neurobiology, 2018. **55**(1): p. 145-155.

358. Huang, R.-q., et al., *Characterization of lactoferrin receptor in brain endothelial capillary cells and mouse brain.* Journal of Biomedical Science, 2007. **14**(1): p. 121-128.

359. Mann, J.F.S., et al., *Transferrin conjugation confers mucosal molecular targeting to a model HIV-1 trimeric gp140 vaccine antigen.* Journal of Controlled Release, 2012. **158**(2): p. 240-249.

360. Liu, L., et al., *Transferrin receptor antibody-modified α-cobrotoxin-loaded nanoparticles enable drug delivery across the blood–brain barrier by intranasal administration.* Journal of Nanoparticle Research, 2013. **15**(11): p. 2059.

361. Voth, B., et al., *Transferrin receptors and glioblastoma multiforme: Current findings and potential for treatment.* Journal of Clinical Neuroscience, 2015. **22**(7): p. 1071-1076.

362. Tortorella, S. and T.C. Karagiannis, *Transferrin Receptor-Mediated Endocytosis: A Useful Target for Cancer Therapy.* The Journal of Membrane Biology, 2014. **247**(4): p. 291-307.

363. Sun, H., H. Li, and P.J. Sadler, *Transferrin as a metal ion mediator.* Chemical reviews, 1999. **99**(9): p. 2817-2842.

364. Dautry-Varsat, A., *Receptor-mediated endocytosis: The intracellular journey of transferrin and its receptor.* Biochimie, 1986. **68**(3): p. 375-381.

365. Hein, C.D., X.-M. Liu, and D. Wang, *Click chemistry, a powerful tool for pharmaceutical sciences.* Pharmaceutical research, 2008. **25**(10): p. 2216-2230.

366. Meng, X. and K.J. Edgar, *"Click" reactions in polysaccharide modification.* Progress in Polymer Science, 2016. **53**: p. 52-85.

367. Meldal, M. and C.W. Tornøe, *Cu-catalyzed azide− alkyne cycloaddition.* Chemical reviews, 2008. **108**(8): p. 2952-3015.

368. Anseth, K.S. and H.-A. Klok, *Click Chemistry in Biomaterials, Nanomedicine, and Drug Delivery.* Biomacromolecules, 2016. **17**(1): p. 1-3.

369. Bao, H., et al., *Thermo- and pH-Responsive Association Behavior of Dual Hydrophilic Graft Chitosan Terpolymer Synthesized via ATRP and Click Chemistry.* Macromolecules, 2010. **43**(13): p. 5679-5687.

370. Walker, D., et al., *Facile synthesis and 18F-radiolabeling of α4β1-specific LLP2A-aryltrifluoroborate peptidomimetic conjugates.* Bioorganic & Medicinal Chemistry Letters, 2016. **26**(20): p. 5126-5131.

371. Wu, Z., et al., *Encapsulation of β-galactosidase from Aspergillus oryzae based on "fish-in-net" approach with molecular imprinting technique.* Journal of Molecular Catalysis B: Enzymatic, 2010. **63**(1): p. 75-80.

372. Tietjen, G.T., et al., *Focus on Fundamentals: Achieving Effective Nanoparticle Targeting.* Trends in Molecular Medicine, 2018. **24**(7): p. 598-606.

373. Alkilany, A.M., et al., *Ligand density on nanoparticles: A parameter with critical impact on nanomedicine.* Advanced Drug Delivery Reviews, 2019. **143**: p. 22-36.

374. Kalkhof, S. and A. Sinz, *Chances and pitfalls of chemical cross-linking with amine-reactive N-hydroxysuccinimide esters.* Analytical and bioanalytical chemistry, 2008. **392**(1): p. 305-312.

375. Chen, G., et al., *Synthesis of azide/alkyne-terminal polymers and application for surface functionalisation through a [2+ 3] Huisgen cycloaddition process,"click chemistry".* Soft Matter, 2007. **3**(6): p. 732-739.

376. Koo, H., et al., *Bioorthogonal Copper-Free Click Chemistry In Vivo for Tumor-Targeted Delivery of Nanoparticles.* Angewandte Chemie International Edition, 2012. **51**(47): p. 11836-11840.

377. Wang, C.-F., et al., *Copper-free azide–alkyne cycloaddition of targeting peptides to porous silicon nanoparticles for intracellular drug uptake.* Biomaterials, 2014. **35**(4): p. 1257-1266.

378. Schieber, C., et al., *Conjugation of Transferrin to Azide-Modified CdSe/ZnS Core–Shell Quantum Dots using Cyclooctyne Click Chemistry.* Angewandte Chemie International Edition, 2012. **51**(42): p. 10523-10527.

379. Truong, V.X., et al., *In situ-forming robust chitosan-poly(ethylene glycol) hydrogels prepared by copper-free azide–alkyne click reaction for tissue engineering.* Biomaterials Science, 2014. **2**(2): p. 167-175.

380. Chen, J.-P. and T.-H. Cheng, *Thermo-Responsive Chitosan-graft-poly(N-isopropylacrylamide) Injectable Hydrogel for Cultivation of Chondrocytes and Meniscus Cells.* Macromolecular Bioscience, 2006. **6**(12): p. 1026-1039.

381. Sun, S., et al., *A Thermoresponsive Chitosan−NIPAAm/Vinyl Laurate Copolymer Vector for Gene Transfection.* Bioconjugate Chemistry, 2005. **16**(4): p. 972-980.

382. Lieber, E., et al., *Infrared Spectra of Organic Azides.* Analytical Chemistry, 1957. **29**(6): p. 916-918.

383. Lin, X., et al., *Transferrin-Modified Nanoparticles for Photodynamic Therapy Enhance the Antitumor Efficacy of Hypocrellin A.* Frontiers in Pharmacology, 2017. **8**(815).

384. Sola, L., et al., *Synthesis of Clickable Coating Polymers by Postpolymerization Modification: Applications in Microarray Technology.* Langmuir, 2016. **32**(40): p. 10284-10295.

385. Jang, S., et al., *Development of a Simple Method for Protein Conjugation by Copper-Free Click Reaction and Its Application to Antibody-Free Western Blot Analysis.* Bioconjugate Chemistry, 2012. **23**(11): p. 2256-2261.

386. Mistry, A., S. Stolnik, and L. Illum, *Nanoparticles for direct nose-to-brain delivery of drugs.* International Journal of Pharmaceutics, 2009. **379**(1): p. 146-157.

387. Mistry, A., et al., *Effect of physicochemical properties on intranasal nanoparticle transit into murine olfactory epithelium.* Journal of Drug Targeting, 2009. **17**(7): p. 543-552.

388. Clementino, A., et al., *The nasal delivery of nanoencapsulated statins - an approach for brain delivery.* International journal of nanomedicine, 2016. **11**: p. 6575-6590.

389. Kircheis, R., et al., *Polyethylenimine/DNA complexes shielded by transferrin target gene expression to tumors after systemic application.* Gene Therapy, 2001. **8**(1): p. 28-40.

390. Lebrón, J.A., et al., *Crystal Structure of the Hemochromatosis Protein HFE and Characterization of Its Interaction with Transferrin Receptor.* Cell, 1998. **93**(1): p. 111-123.

391. Lebrón, J.A., A.P. West, and P.J. Bjorkman, *The hemochromatosis protein HFE competes with transferrin for binding to the transferrin receptor11Edited by I. A. Wilson.* Journal of Molecular Biology, 1999. **294**(1): p. 239-245.

392. Kleven, M.D., S. Jue, and C.A. Enns, *Transferrin Receptors TfR1 and TfR2 Bind Transferrin through Differing Mechanisms.* Biochemistry, 2018. **57**(9): p. 1552-1559.

393. Giannetti, A.M., et al., *Mechanism for Multiple Ligand Recognition by the Human Transferrin Receptor.* PLOS Biology, 2003. **1**(3): p. e51.

394. Hamilton, T.A., H.G. Wada, and H.H. Sussman, *Identification of transferrin receptors on the surface of human cultured cells.* Proceedings of the National Academy of Sciences, 1979. **76**(12): p. 6406-6410.

395. Wadajkar, A.S., et al., *Tumor-targeted nanotherapeutics: overcoming treatment barriers for glioblastoma.* WIREs Nanomedicine and Nanobiotechnology, 2017. **9**(4): p. e1439.

396. Yang, T., et al., *A liquid chromatography-tandem mass spectrometry-based targeted proteomics approach for the assessment of transferrin receptor levels*

in breast cancer. PROTEOMICS – Clinical Applications, 2014. **8**(9-10): p. 773-782.

397. Baldassi, D., B. Gabold, and O.M. Merkel, *Air−Liquid Interface Cultures of the Healthy and Diseased Human Respiratory Tract: Promises, Challenges, and Future Directions.* Advanced NanoBiomed Research, 2021. **1**(6): p. 2000111.

398. Farhat, J., I. Pandey, and M. AlWahsh, *Transcending toward Advanced 3D-Cell Culture Modalities: A Review about an Emerging Paradigm in Translational Oncology.* Cells, 2021. **10**(7): p. 1657.

399. Mercier, C., et al., *Pharmacological Characterization of the RPMI 2650 Model as a Relevant Tool for Assessing the Permeability of Intranasal Drugs.* Molecular Pharmaceutics, 2018. **15**(6): p. 2246-2256.

400. Pavinatto, F.J., et al., *Interaction of Chitosan with Cell Membrane Models at the Air−Water Interface.* Biomacromolecules, 2007. **8**(5): p. 1633-1640.

401. Lin, J. and A. Alexander-Katz, *Cell Membranes Open "Doors" for Cationic Nanoparticles/Biomolecules: Insights into Uptake Kinetics.* ACS Nano, 2013. **7**(12): p. 10799-10808.

402. Wang, J., et al., *The Complex Role of Multivalency in Nanoparticles Targeting the Transferrin Receptor for Cancer Therapies.* Journal of the American Chemical Society, 2010. **132**(32): p. 11306-11313.

403. Wengst, A. and S. Reichl, *RPMI 2650 epithelial model and three-dimensional reconstructed human nasal mucosa as in vitro models for nasal permeation studies.* European Journal of Pharmaceutics and Biopharmaceutics, 2010. **74**(2): p. 290-297.

404. Charlton, S.T., S.S. Davis, and L. Illum, *Evaluation of bioadhesive polymers as delivery systems for nose to brain delivery: In vitro characterisation studies.* Journal of Controlled Release, 2007. **118**(2): p. 225-234.

405. Jones, S.K., et al., *Revisiting the value of competition assays in folate receptor-mediated drug delivery.* Biomaterials, 2017. **138**: p. 35-45.

406. Papademetriou, J., et al., *Comparative binding, endocytosis, and biodistribution of antibodies and antibody-coated carriers for targeted delivery of lysosomal enzymes to ICAM-1 versus transferrin receptor.* Journal of Inherited Metabolic Disease, 2013. **36**(3): p. 467-477.

407. Hirst, J. and M.S. Robinson, *Clathrin and adaptors.* Biochimica et Biophysica Acta (BBA) - Molecular Cell Research, 1998. **1404**(1): p. 173-193.

408. Banerjee, D., et al., *Multivalent display and receptor-mediated endocytosis of transferrin on virus-like particles.* Chembiochem : a European journal of chemical biology, 2010. **11**(9): p. 1273-1279.

409. Tosi, G., J.T. Duskey, and J. Kreuter, *Nanoparticles as carriers for drug delivery of macromolecules across the blood-brain barrier.* Expert Opinion on Drug Delivery, 2020. **17**(1): p. 23-32.

410. Casettari, L. and L. Illum, *Chitosan in nasal delivery systems for therapeutic drugs.* Journal of Controlled Release, 2014. **190**: p. 189-200.

411. Yoo, J., et al., *Active Targeting Strategies Using Biological Ligands for Nanoparticle Drug Delivery Systems.* Cancers, 2019. **11**(5): p. 640.

412. Schwarz, B. and O.M. Merkel, *Nose-to-brain delivery of biologics.* Therapeutic Delivery, 2019. **10**(4): p. 207-210.

413. Ali, A. and S. Ahmed, *A review on chitosan and its nanocomposites in drug delivery.* International Journal of Biological Macromolecules, 2018. **109**: p. 273-286.

414. Hendrix, J., et al., *Live-cell observation of cytosolic HIV-1 assembly onset reveals RNA-interacting Gag oligomers.* J Cell Biol, 2015. **210**(4): p. 629-46.

415. Schrimpf, W., et al., *PAM: A Framework for Integrated Analysis of Imaging, Single-Molecule, and Ensemble Fluorescence Data.* Biophys J, 2018. **114**(7): p. 1518-1528.

416. Ivanchenko, S. and D.C. Lamb. *Fluorescence Correlation Spectroscopy: Principles and Developments*. in *Supramolecular Structure and Function 10*. 2011. Dordrecht: Springer Netherlands.

417. Digman, M.A., et al., *The Phasor Approach to Fluorescence Lifetime Imaging Analysis.* Biophysical Journal, 2008. **94**(2): p. L14-L16.

418. Messer, P.K., et al., *A multiscale wavelet algorithm for atom tracking in STM movies.* New Journal of Physics, 2022. **24**(3): p. 033016.

419. van de Weert, M., W.E. Hennink, and W. Jiskoot, *Protein Instability in Poly(Lactic-co-Glycolic Acid) Microparticles.* Pharmaceutical Research, 2000. **17**(10): p. 1159-1167.

420. Mistry, A., S. Stolnik, and L. Illum, *Nose-to-Brain Delivery: Investigation of the Transport of Nanoparticles with Different Surface Characteristics and Sizes in Excised Porcine Olfactory Epithelium.* Molecular Pharmaceutics, 2015. **12**(8): p. 2755-2766.

421. Asadian-Birjand, M., et al., *Transferrin Decorated Thermoresponsive Nanogels as Magnetic Trap Devices for Circulating Tumor Cells.* Macromolecular Rapid Communications, 2016. **37**(5): p. 439-445.

422. Nag, M., et al., *Transferrin functionalized chitosan-PEG nanoparticles for targeted delivery of paclitaxel to cancer cells.* Colloids and Surfaces B: Biointerfaces, 2016. **148**: p. 363-370.

423. Kumar, V., et al., *Shielding of Lipid Nanoparticles for siRNA Delivery: Impact on Physicochemical Properties, Cytokine Induction, and Efficacy.* Molecular Therapy - Nucleic Acids, 2014. **3**: p. e210.

424. Gulati, N.M., P.L. Stewart, and N.F. Steinmetz, *Bioinspired Shielding Strategies for Nanoparticle Drug Delivery Applications.* Molecular Pharmaceutics, 2018. **15**(8): p. 2900-2909.

425. Kandil, R., et al., *Coming in and Finding Out: Blending Receptor-Targeted Delivery and Efficient Endosomal Escape in a Novel Bio-Responsive siRNA Delivery System for Gene Knockdown in Pulmonary T Cells.* Adv Ther (Weinh), 2019. **2**(7).

426. Jafek, B.W., *Ultrastructure of human nasal mucosa.* The Laryngoscope, 1983. **93**(12): p. 1576-1599.

427. Bansil, R. and B.S. Turner, *Mucin structure, aggregation, physiological functions and biomedical applications.* Current Opinion in Colloid & Interface Science, 2006. **11**(2): p. 164-170.

428. Tomazic, P.V., B. Darnhofer, and R. Birner-Gruenberger, *Nasal mucus proteome and its involvement in allergic rhinitis.* Expert Review of Proteomics, 2020. **17**(3): p. 191-199.

429. Tu, Y., et al., *Mucus composition abnormalities in sinonasal mucosa of chronic rhinosinusitis with and without nasal polyps.* Inflammation, 2021. **44**(5): p. 1937-1948.

430. Griffiths, P.C., et al., *Probing the interaction of nanoparticles with mucin for drug delivery applications using dynamic light scattering.* European Journal of Pharmaceutics and Biopharmaceutics, 2015. **97**: p. 218-222.

431. Morgan, K.T., et al., *The Nasal Mucociliary Apparatus.* American Review of Respiratory Disease, 1984. **130**(2): p. 275-281.

432. Olmsted, S.S., et al., *Diffusion of Macromolecules and Virus-Like Particles in Human Cervical Mucus.* Biophysical Journal, 2001. **81**(4): p. 1930-1937.

433. Khanvilkar, K., M.D. Donovan, and D.R. Flanagan, *Drug transfer through mucus.* Advanced Drug Delivery Reviews, 2001. **48**(2): p. 173-193.

434. Chatzitaki, A.-T., et al., *Chitosan-coated PLGA nanoparticles for the nasal delivery of ropinirole hydrochloride: In vitro and ex vivo evaluation of efficacy and safety.* International Journal of Pharmaceutics, 2020. **589**: p. 119776.

435. M. Ways, T.M., W.M. Lau, and V.V. Khutoryanskiy, *Chitosan and Its Derivatives for Application in Mucoadhesive Drug Delivery Systems.* Polymers, 2018. **10**(3): p. 267.

436. Wang, Y.-Y., et al., *Addressing the PEG Mucoadhesivity Paradox to Engineer Nanoparticles that "Slip" through the Human Mucus Barrier.* Angewandte Chemie International Edition, 2008. **47**(50): p. 9726-9729.

437. Lai, S.K., et al., *Drug carrier nanoparticles that penetrate human chronic rhinosinusitis mucus.* Biomaterials, 2011. **32**(26): p. 6285-6290.

438. Murgia, X., et al., *The role of mucus on drug transport and its potential to affect therapeutic outcomes.* Advanced Drug Delivery Reviews, 2018. **124**: p. 82-97.

439. Amidi, M., et al., *Preparation and characterization of protein-loaded N-trimethyl chitosan nanoparticles as nasal delivery system.* Journal of Controlled Release, 2006. **111**(1): p. 107-116.

440. Yang, W., et al., *Chitosan/Sodium Tripolyphosphate Nanoparticles: Preparation, Characterization and Application as Drug Carrier.* Journal of Biomedical Nanotechnology, 2009. **5**(5): p. 591-595.

441. d'Angelo, I., et al., *Overcoming barriers in Pseudomonas aeruginosa lung infections: Engineered nanoparticles for local delivery of a cationic antimicrobial peptide.* Colloids and Surfaces B: Biointerfaces, 2015. **135**: p. 717-725.

442. Friedl, H., et al., *Development and Evaluation of a Novel Mucus Diffusion Test System Approved by Self-Nanoemulsifying Drug Delivery Systems.* Journal of Pharmaceutical Sciences, 2013. **102**(12): p. 4406-4413.

443. Baldrick, P., *The safety of chitosan as a pharmaceutical excipient.* Regulatory Toxicology and Pharmacology, 2010. **56**(3): p. 290-299.

444. Sonin, D., et al., *Biological Safety and Biodistribution of Chitosan Nanoparticles.* Nanomaterials, 2020. **10**(4): p. 810.

445. Huang, M., E. Khor, and L.-Y. Lim, *Uptake and Cytotoxicity of Chitosan Molecules and Nanoparticles: Effects of Molecular Weight and Degree of Deacetylation.* Pharmaceutical Research, 2004. **21**(2): p. 344-353.

446. Crisler, R., et al., *Chapter 4 - Functional Anatomy and Physiology*, in *The Laboratory Rat (Third Edition)*, M.A. Suckow, et al., Editors. 2020, Academic Press. p. 91-132.

447. Treuting, P.M., S. Dintzis, and K.S. Montine, *Comparative anatomy and histology: a mouse, rat, and human atlas*. 2017: Academic Press.

448. Qian, Z.M., et al., *Targeted Drug Delivery via the Transferrin Receptor-Mediated Endocytosis Pathway.* Pharmacological Reviews, 2002. **54**(4): p. 561-587.

449. Wagner, E., D. Curiel, and M. Cotten, *Delivery of drugs, proteins and genes into cells using transferrin as a ligand for receptor-mediated endocytosis.* Advanced Drug Delivery Reviews, 1994. **14**(1): p. 113-135.

450. Widera, A., F. Norouziyan, and W.C. Shen, *Mechanisms of TfR-mediated transcytosis and sorting in epithelial cells and applications toward drug delivery.* Advanced Drug Delivery Reviews, 2003. **55**(11): p. 1439-1466.

451. Traub, L.M., *Regarding the Amazing Choreography of Clathrin Coats.* PLOS Biology, 2011. **9**(3): p. e1001037.

452. Ghadiri, M., P.M. Young, and D. Traini, *Strategies to Enhance Drug Absorption via Nasal and Pulmonary Routes.* Pharmaceutics, 2019. **11**(3): p. 113.

453. Vllasaliu, D., et al., *Tight junction modulation by chitosan nanoparticles: Comparison with chitosan solution.* International Journal of Pharmaceutics, 2010. **400**(1): p. 183-193.

454. El Leithy, E.S., H.M. Abdel-Bar, and R.A.-M. Ali, *Folate-chitosan nanoparticles triggered insulin cellular uptake and improved in vivo hypoglycemic activity.* International Journal of Pharmaceutics, 2019. **571**: p. 118708.

455. Nam, H.Y., et al., *Cellular uptake mechanism and intracellular fate of hydrophobically modified glycol chitosan nanoparticles.* Journal of Controlled Release, 2009. **135**(3): p. 259-267.

456. Zhang, J., et al., *Mechanism Study of Cellular Uptake and Tight Junction Opening Mediated by Goblet Cell-Specific Trimethyl Chitosan Nanoparticles.* Molecular Pharmaceutics, 2014. **11**(5): p. 1520-1532.

457. Chauhan, M.B. and N.B. Chauhan, *Brain Uptake of Neurotherapeutics after Intranasal versus Intraperitoneal Delivery in Mice.* Journal of neurology and neurosurgery, 2015. **2**(1): p. 009.

458. Pokharkar, V., S. Suryawanshi, and V. Dhapte-Pawar, *Exploring micellar-based polymeric systems for effective nose-to-brain drug delivery as potential neurotherapeutics.* Drug Delivery and Translational Research, 2019.

459. Rajput, A.P. and S.B. Butani, *Resveratrol anchored nanostructured lipid carrier loaded in situ gel via nasal route: Formulation, optimization and in vivo characterization.* Journal of Drug Delivery Science and Technology, 2019. **51**: p. 214-223.

460. Pardeshi, C.V. and V.S. Belgamwar, *Improved brain pharmacokinetics following intranasal administration of N,N,N-trimethyl chitosan tailored mucoadhesive NLCs.* Materials Technology, 2020. **35**(5): p. 249-266.

461. Fonseca, L.C., et al., *Intranasal drug delivery for treatment of Alzheimer's disease.* Drug Delivery and Translational Research, 2021. **11**(2): p. 411-425.

Acknowledgements

This work could not have been achieved without the support and guidance of my supervisors, colleagues, collaboration partners, friends, and, in particular, my family. Therefore, I want to express my deepest gratitude and appreciation to them in the following lines.

First and foremost, I would like to sincerely thank Prof. Dr. Olivia Merkel for her constant support starting from mentoring my master internship abroad and my master thesis up to all my PhD work. Thank you for giving me the opportunity to work in your group on an exciting, interdisciplinary and innovative project. I am deeply grateful for your guidance, dedication, enthusiasm, scientific advice, trust and encouragement throughout all the highs and lows of my time as a PhD student. Your immense knowledge and plentiful experience have encouraged me in all the time of my academic research and daily life.

This work was funded by AbbVie Deutschland GmbH. I would especially like to thank Dr. Christian Ried for his unwavering support in every stage of the research project. Thank you to Dr. Rebecka Wombacher, Dr. Andreas Popp and Dr. Thomas Merdan for the many fruitful discussions and scientific input. Without you, the project and me wouldn’t have come this far.

Special thank goes to Prof. Dr. Gerhard Winter for kindly agreeing to be the co-referee on this thesis.

Furthermore, I would like to thank both Prof. Dr. Gerhard Winter and Prof. Dr. Wolfgang Frieß for providing a great working atmosphere within the three groups of pharmaceutical technology. Thank you for your advice as well as for encouraging and supporting me and treating me as one of your own students.

I highly appreciate the help and scientific input of several colleagues and collaboration partners, such as Dr. Antonietta Greco for her superior engagement with optimizing the

microfluidic mixing procedure, Irene Gialdini for spending countless hours in a small dark room and Prof. Dr. Don Lamb for his expert knowledge, Dr. Igor Khalin and Prof. Dr. Nikolaus Plesnila for performing the mouse experiments, Dr. Friederike Adams, who taught me not to be afraid of chemistry, Dr. Sophie Brameyer for supporting me with SPR measurements, and everyone else, who kindly offered help or materials.

I would moreover like to thank my friends and former colleagues from the LMU, especially the AK Merkel-Team: Thank you Aditi, Gabriella, Rike, Ben, Rima, Tobi, Tasch, Lorenz, Domizia, Christoph, Yao, David, Siyu and FPV for all the fun times in the lab, the discussions and deep talks and for always offering a helping hand. Gabi, thank you for always keeping up and being patient with us chaotic PhD students. You really keep the team together.
As well, I would like to thank all the members of AK Frieß and AK Winter for their support, fun parties, outdoor activities, great lunch and coffee breaks. Thank you, Sabine Kohler, for being the heart and the soul of this department and with helping with every problem, no matter how big or small.
Additionally, I would like to thank all my students, who gave me the chance to teach them and supported this thesis with their excellent work.

Finally, I would like to express my gratitude to my family and my husband. Without their tremendous understanding and encouragement in the past few years, it would be impossible for me to complete my study. This thesis is dedicated to you!

List of Publications

Bettina Schwarz and Olivia M. Merkel (2017). “Functionalized PEI and its role in gene therapy”, Material Matters 12.2

Bettina Schwarz and Olivia M. Merkel (2019). "Nose-to-brain delivery of biologics.", Therapeutic Delivery 10(4): 207-210. DOI: 10.4155/tde-2019-0013

Domizia Baldassi†, **Bettina Gabold†** and Olivia M. Merkel (2021), “Air−Liquid Interface Cultures of the Healthy and Diseased Human Respiratory Tract: Promises, Challenges, and Future Directions.” Advanced NanoBiomed Research, 1: 2000111. DOI: 10.1002/anbr.202000111

Bettina Gabold, Friederike Adams, Sophie Brameyer, Kirsten Jung, Christian L. Ried, Thomas Merdan, Olivia M. Merkel (2023) “Transferrin-modified chitosan nanoparticles for targeted nose-to-brain delivery of proteins.” Drug Delivery and Translational Research 13, 822–838. DOI: 10.1007/s13346-022-01245-z

Irene Gialdini, **Bettina Gabold**, Antonietta Greco, Gemma Conte, Xiaoxuan Wang, Olivia M. Merkel, Don C. Lamb (2023) “Combining fluorescence correlation spectroscopy and lifetime imaging to study the dynamics of drug delivery nanoparticles in mucus”. Biophysical Journal, Volume 122, Issue 3, 427a. DOI: 10.1016/j.bpj.2022.11.2313

Antonietta Greco†, **Bettina Gabold†**, Siyu Chen, Xiaoxuan Wang, Zehua Xu, Achim Hartschuh, Enrica Chiesa, Ida Genta, Christian L. Ried, Thomas Merdan, Olivia M. Merkel. (2023) "Microfluidic mixing as platform technology for production of chitosan nanoparticles loaded with different macromolecules." European Journal of Pharmaceutics and Biopharmaceutics 188: 170-181. DOI: 10.1016/j.ejpb.2023.05.010

Natascha Hartl, **Bettina Gabold**, Friederike Adams, Philipp Uhl, Sabrina Oerter, Sabine Gätzner, Marco Metzger, Ann-Christine König, Stefanie M. Hauck, Antje Appelt-

Menzel, Walter Mier, Gert Fricker, Olivia M. Merkel. (2023). "Overcoming the blood-brain barrier? - prediction of blood-brain permeability of hydrophobically modified poly ethylenimine polyplexes for siRNA delivery into the brain with *in vitro* and *in vivo* models." Journal of Controlled Release 360: 613-629. DOI: 10.1016/j.jconrel.2023.07.019

†*shared first author*